Neutron scattering studies of the dynamics of biological systems as a function of hydration, temperature and pressure

Marcus Trapp

Université de Grenoble

Thèse

Pour obtenir le grade de

DOCTEUR DE L'UNIVERSITE DE GRENOBLE
Spécialité : Physique pour les sciences du vivant

Arrêté ministériel : 7 août 2006

Présentée et soutenue publiquement par

MARCUS TRAPP

le 9 décembre 2010

Neutron scattering studies of the dynamics of biological systems as a function of hydration, temperature and pressure

La dynamique des systèmes biologiques en fonction de l'hydratation, de la température et de la pression étudiée par diffusion neutronique

---

Thèse dirigée par Prof. Dr. Judith Peters

Membres du Jury

Prof. Dr. Gerald Kneller	Rapporteur
Prof. Dr. Maikel C. Rheinstädter	Rapporteur
Uni. Doz. Dr. Ruth Prassl	Examinateur
Dr. Thomas Gutberlet	Examinateur
Dr. Francesca Natali	Examinateur
Dr. Moeava Tehei	Président

Thèse préparée à l'Institut de Biologie Structurale J.-P. Ebel, CEA/CNRS/UJF, Grenoble et a l'Institut Laue-Langevin, Grenoble dans l'Ecole Doctorale de Physique

Contents

Acknowledgment

First of all, I would like to thank my supervisor Prof. Dr. Judith Peters, for her support, encouragement and guidance, without which this work would not have been possible.

I am grateful to the members of the jury, Prof. Dr. Gerald Kneller and Prof. Dr. Maikel C. Rheinstädter, who accepted to be the referees of this work, and also Uni. Doz. Dr. Ruth Prassl, Dr. Thomas Gutberlet, Dr. Moeava Tehei and Dr. Francesca Natali for being part of the jury.

Of course this was not an isolated work but has to been seen in the larger context, so I would like to thank all co-workers on the DMPC project: Thomas for his support during the hardest time of my Ph.D., Fanni for many questions and help for the data analysis, Moeava for many challenging questions, which made me learn a lot.
In the course of the AChE project I am grateful for the support I received from Marie Trovalet, Florian Nachon and Patrick Masson.

I want to thank IN13 team, which I had the pleasure to be a part of during the last three years. The two responsible, Francesca and Judith, but also the other students Chiara, Wiebke and Carlotta. Not to forget the technicians Ismaël, Teddy and Mathieu.

All of my experiments would not have been possible without the help of the local contacts, even if it was not always apparent. Therefore I want to thank Bruno Demé, Tobias Unruh, Karin Schmalzl, Marek Michael Koza and Lambert van Ejick for their support.

Support from ILL is very much appreciated. To name all people would clearly exceed the remit of these acknowledgment, therefore only some are mentioned here. I want to thank Jérôme Locatelli for the help when LAMP was not doing what I wanted, Franck Rey for many hardware checks and reversing two important cables and for the cryo team Xavier Tonon. A big thank you goes to the high pressure experts Jean-Luc Laborier and Claude Payre, who were heavily involved in the development and testing of the high pressure cell.

I am grateful to Hanna Wacklin and Giovanna Fragneto, who help me out with DMPC for the high pressure experiment on IN13.

I am thankful to Anna, Stu, Peggy, Jochen, Martin, Bastian and Marek for the company, sometimes in the middle of the night, and a lot of after hours coffee breaks and the company at rainy barbecues. A special thank you goes to Audrey and Kent for their enthusiasm during our term as student representatives. For proofreading and correcting my French and English I want to say thank you to Estelle and Anna.

For for answering many questions from a physicist entering the field of biophysics, and for many fruitful discussions I want to say thank you to Andreas, Marion, Sebastian and Julia.

I am grateful for my grant from the French Ministry for Research and Technology. The project to study the dynamics of human achetylcholinesterase was partly funded by DGA under the contract REI n° 2009340023. I acknowledge also the financial support from the Access to Major Research Facilities Program which is a component of the International Science Linkages Program established under the Australian Government's innovation statement, Backing Australia's Ability.

I want to thank all my friends in Viernheim, especially Anja and Anke for their friendship and two amazing weddings.

A big thank you go to Eva proof-reading, motivation, supporting and standing me during beam times and writing up and for many, many other things.

Last but not least I want to thank my parents for the possibility to study abroad and the encouragement during this time. And also my uncle, aunt, cousins and their families for very warm welcomes every time I came home.

Chapter 1

Introduction

For a long time lipids, and membranes made out of these lipids, were thought of as building blocks of cells, having not so prominent tasks as e.g. proteins. Fulfilling their function as cell boundaries, they cover a total surface area of about 100 km^2 in a single human being. In recent years the knowledge about their role has been extended. It was found that lipids act not only as passive solvents for membrane proteins, but play also an integral part of cellular function. They can act as enzymes, receptors, drugs as well as regulators.
Real cell membranes are highly complex systems, which consist not only of several different kinds of lipids, but also of membrane proteins and membrane active molecules such as cholesterol. Therefore model membrane systems such as 1,2-dimyristoyl-*sn*-glycero-3-phosphocholine (DMPC) are often used to mimic their more complex natural counterparts, because they show a similar thermodynamical behaviour. Depending on temperature, pressure or amount of water in the system the dynamic behaviour of these model systems can be effected. Hence, knowledge of these interactions are crucial to better understand the parameters necessary for the functioning of biological membranes and what precisely are their effects.
In the first part of this work the results of elastic and quasi-elastic neutron scattering experiments on DMCP multilayers as a function of hydration will be discussed in more detail. Analogous to the investigation of lipid dynamics, in the second part of this thesis the investigation of a protein under various external conditions via neutron scattering is described. This ansatz forms an extension of the methodology already described in the chapters dealing with DMPC.
Molecular dynamics of pure recombinant human acetylcholinesterase (hAChE) and inhibited by Huperzine A using elastic, quasi-elastic and inelastic neutron scattering will be described. This enzyme plays an important role in the termination of nerve impulses via the hydrolysis of the neurotransmitter acetylcholin. Therefore it is a primary target of neurotoxins.

In recent years the investigation of AChE has also gained interest in the treatment of neural diseases such as Alzheimer's disease or myasthenia gravis, where the hydrolysis of ACh is defective.

The energy E and wavelength λ of cold and thermal neutrons lies in the millielectron volt and Ångstrom range, therefore neutron scattering is very well suited to investigate dynamics in the pico- to nanosecond timescale and on a atomic length scale. A big advantage of neutron scattering over other techniques is the fact that it is isotope selective, this means there is a large difference of the incoherent scattering cross section of hydrogen and deuterium (about one order of magnitude). Samples such as proteins or membranes comprise about 50% hydrogen atoms, thus neutron scattering probes an average over the whole sample and perdeuteration can eventually be used to "mask" some parts.

After an introduction to the general properties of the neutron, in chapter 3 an overview of the theory of thermal neutron scattering is given, herein section 3.6 introduces the models for elastic (section 3.6.1) and quasi-elastic (section 3.6.2) incoherent neutron scattering used for data treatment in chapters 6 - 9. A brief presentation of research neutron sources and the principle of spectrometers used for this work, namely backscattering and time-of-flight spectrometers, is also part of this chapter.

The thermal backscattering spectrometer IN13 is presented in detail in chapter 4. In the course of my Ph.D. work I was highly involved in the operation and the maintenance of this collaborating research group (CRG) instrument. The chapter starts with a description of the design of the instrument. Examples of the instrument development, which led to a significant improvement of the instrument's performance, are given also.

After a short historical introduction, the model lipid DMPC and its thermodynamical characteristics are reviewed in chapter 5, thereafter the sample preparation for the experiments described in the chapters 6 and 7 is outlined.

The neutron scattering experiments performed on DMPC are described in detail in chapters 6 and 7. Chapter 6 deals with the elastic experiments contains results from two different sets of measurements, one performed on IN13 (section 6.2), the second one done on IN16 (section 6.3), both instruments are situated at the Institut Laue-Langevin in Grenoble, France. In total samples with four different hydration levels were prepared on a solid support of silicon wafers. Thanks to their very good alignment, in-plane and out-of-plane dynamics of the membranes could be probed. Results obtained during the IN13 experiments showed a clear shift to higher temper-

atures of the lipid main phase transition for decreasing water content and served also as preparation for the quasi-elastic measurements performed at the Munich research reactor FRM II.

The experiments performed on IN16 and described in section 6.3 allowed a comparison between summed intensities and mean square displacements (msd) of two samples at low hydration. It was shown that the decrease of the elastic intensity, which occurs at the main phase transition, is correlated with an increased mobility, indicated by a change of slope of the mean square displacements. The results from this experiment were published in the journal "*Spectroscopy*" as part of the proceedings of the XIII European Conference on the Spectroscopy of Biological Molecules, where this work was presented, and are part of the appendix of this manuscript (cf section D.1).

The quasi-elastic experiments performed on the time-of-flight spectrometer TOFTOF of the FRM II research reactor in Munich are outlined in chapter 7. The same samples employed for the elastic experiments on IN13 were also used for these measurements. Elastic incoherent structure factors (EISF) could be extracted. Different models had to be fitted to the data to take into account the effects of hydration. The obtained findings from the TOFTOF and IN13 experiments resulted in a paper, which is published in "*The Journal of Chemical Physics*" and can be found in the appendix to this work in section D.2.

Temperature scans are nowadays routinely used to investigate dynamics of biomolecules by neutron scattering. In contrast high hydrostatic pressure is under represented in combination with neutron scattering due to engineering difficulties. With the investigation of high pressure, a second thermodynamical variable can be explored apart from temperature scans. Pressure has a similar effect on membranes as to reduce the hydration of lipid bilayers, thus the experiments described in chapter 6 and 7 are complementary to the high pressure investigations started now. The development of a new high pressure equipment and first diffraction and spectroscopic measurements on DMPC are described in chapter 8.

The investigation on AChE is described in chapter 9. After a general introduction to AChE and depiction of the sample preparation, the elastic experiments are delineated in section 9.3. This section is based on a paper, which has been submitted to "*Physical Chemistry Chemical Physics*". Covering two orders of magnitude in instrumental resolution allows to observe mean square displacements on different time scales, ranging from about 10-1000 ps. In section 9.4 a comparison with results obtained on human butyrylcholinesterase (BChE) is drawn. The data published by Gabel and

co-workers show remarkable differences to our results on AChE, even if the function and structure of both enzymes are quite similar.
Finally in section 9.5 the results of quasi-elastic measurements on AChE at IN6 are elaborated.

Chapter 2

Résumé de la thèse en français

Pendant longtemps, les lipides et les membranes, qui sont elle-même constituées de lipides, ont été considérés comme simples composantes des cellules, n'ayant pas autant de fonctions que les protéines, par exemple. En tant que limites des cellules biologiques, ils couvrent une surface totale d'environ 100 km^2 dans un être humain. Ces dernières années, la connaissance de leurs fonctions a pourtant bien évolué. On a constaté que les lipides n'agissent pas seulement comme solvants passifs pour les protéines membranaires, mais font partie de la fonction cellulaire. Ils peuvent agir en tant qu'enzymes, récepteurs, médicaments ainsi que régulateurs.
Les membranes cellulaires biologiques sont des systèmes très complexes qui ne contiennent pas seulement plusieurs types de lipides, mais aussi des protéines membranaires et des molécules actives telles que le cholestérol. C'est pourquoi les systèmes modèles de membranes comme le 1,2-dimyristoyl-sn-glycéro-3-phosphocholine (DMPC) sont souvent utilisés pour imiter leurs homologues naturels plus complexes, car ils ont un comportement thermodynamique similaire. Selon la température, la pression ou la quantité d'eau dans le système le comportement dynamique de ces modèles peut être effectuée. Par conséquent, la connaissance de ces interactions est cruciale pour mieux comprendre les paramètres nécessaires au fonctionnement des membranes biologiques et quels sont exactement leurs effets.
Dans la première partie de ce travail, les résultats de la diffusion élastique et quasi-élastique de neutrons sur les multicouches DMCP en fonction de l'hydratation seront discutés. Analogue à l'investigation de la dynamique des lipides, dans la deuxième partie de cette thèse l'investigation d'une protéine dans diverses conditions externes par la diffusion neutronique est décrite. Cette approche formes une extension de la méthode déjà décrite dans les chapitres sur DMPC.
La dynamique moléculaire de l'acétylcholinestérase humaine recombinante (hAChE), pure et inhibée par HuperzineA, sera décrite utilisant la diffusion

de neutrons élastique, quasi-élastique et inélastique. Cette enzyme joue un rôle important dans l'achèvement des impulsions nerveuses par l'hydrolyse du neurotransmetteur acétylcholine. Par conséquent, c'est une cible primaire des neurotoxines. Ces dernières années, l'étude de l'AChE a également suscité l'intérêt dans le cadre du traitement des maladies neurologiques, comme la maladie d'Alzheimer ou la myasthénie grave, où l'hydrolyse de l'acétylcholine est défectueuse.

L'énergie E et la longueur d'onde λ des neutrons froids et thermiques se situent dans le domaine des milli-électronvolts et des Ångstroms, la diffusion de neutrons est donc très bien adaptée à l'étude de la dynamique dans le domaine de la pico- à la nanoseconde et sur une échelle de longueur atomique. Un grand avantage de la diffusion neutronique par rapport à d'autres techniques provient du fait qu'elle est sélective entre différents isotopes, cela signifie qu'il ya une grande différence entre la section efficace incohérente de l'hydrogène et du deutérium (environ un ordre de grandeur). Les échantillons tels que les protéines ou les membranes comportent environ 50% d'atomes d'hydrogène, les neutrons mesurent donc une moyenne sur l'ensemble de l'échantillon. La deutériation peut éventuellement être utilisée pour "masquer" certaines parties.

Après une introduction des propriétés générales des neutrons dans le chapitre 3, un aperçu de la théorie de la diffusion des neutrons thermiques est donnée. Dans la section 3.6 des modèles sont présentés pour décrire la diffusion incohérente neutronique élastique (section 3.6.1) et quasi-élastique (section 3.6.2), qui seront utilisés pour le traitement des données dans les chapitres 6 - 9. Une brève présentation des sources de neutrons pour la recherche et du principe des spectromètres utilisés pour ce travail, à savoir des spectromètres à rétrodiffusion et des spectromètres en temps de vol, fait aussi partie de ce chapitre.

Le spectromètre thermique à rétrodiffusion IN13 est présenté en détails dans le chapitre 4. Au cours de mon travail doctoral, j'ai été très impliqué dans l'opération et le maintien de cet instrument d'un "collaborating research group" (CRG). Le chapitre commence par une description de la conception de l'instrument. Des exemples du développement de l'instrument, qui a entraîné une importante amélioration de sa performance, sont exposés dans la suite.

Après une brève introduction historique, le lipide DMPC et ses caractéristiques thermodynamiques sont présentés dans le chapitre 5, puis la préparation des échantillons pour les expériences sont décrites dans les chapitres 6 et 7.

Les expériences de diffusion de neutrons effectuées sur DMPC sont décrites en détails dans les chapitres 6 et 7. Le chapitre 6 sur les expériences élastiques contient les résultats de deux séries de mesures différentes, l'une effectuée sur IN13 (section 6.2), l'autre sur IN16 (section 6.3). Les deux instruments se trouvent à l'Institut Laue-Langevin à Grenoble, France. Au total, quatre échantillons avec des niveaux d'hydratation différents ont été préparés sur un support solide de plaquettes en silicium. Grâce à leur excellent alignement, la dynamique des bicouches dans le plan et perpendiculaire à la normale des bichouches pouvait être sondée. Les résultats obtenus lors des expériences sur IN13 ont clairement montré un déplacement de la transition de phase lipidique principale vers des températures plus élevées pour des hydratations plus basses et ils ont également servi pour préparer les mesures quasi-élastiques réalisées à Munich au réacteur de recherche FRM II.

Les expériences réalisées sur IN16 et décrites dans la section 6.3 ont permis de faire une comparaison entre les intensités sommées et les déplacements carrés moyens (msd) de deux échantillons à faible hydratation. Il a été montré que la diminution de l'intensité élastique à la transition de phase principale est corrélée avec une mobilité accrue, qui se manifeste par un changement du coefficient directeur des déplacements carrés moyens. Les résultats de cette expérience ont été publiés dans la revue "*Spectroscopy*" dans les actes de la conférence "XIII European Conference on the Spectroscopy of Biological Molecules", où ce travail a été présenté, et font partie de l'annexe de ce manuscrit (cf article D.1).

Les expériences quasi-élastiques réalisées sur le spectromètre en temps de vol TOFTOF du réacteur de recherche FRM II à Munich sont décrites dans le chapitre 7. Les mêmes échantillons utilisés pour les expériences élastiques sur IN13 ont aussi servis pour ces mesures. Des facteurs de structure élastiques incohérents (EISF) ont pu être extraits des données. Différents modèles ont été comparés aux données pour prendre en compte les effets de l'hydratation. Les résultats obtenus à partir des expériences faites sur TOFTOF et IN13 ont abouti à une publication dans "*The Journal of Chemical Physics*" qui se trouve dans l'annexe de ce travail dans la section D.2.
Les deux chapitres commencent par une caractérisation de l'échantillon par diffraction neutronique, suivie par une description des expériences et du traitement des données est donnée suivie par l'interprétation et la discussion des résultats obtenus sont exposés en fin de chapitre.

Des balayages en température sont aujourd'hui couramment utilisés pour étudier la dynamique des biomolécules par diffusion de neutrons. Au contraire, la haute pression hydrostatique est sous-utilisée en combinaison avec la diffusion neutronique en raison des difficultés technologiques. Or,

en considerant la haute pression, une seconde variable thermodynamique peut être explorée. La pression a un effet similaire sur les membranes que la réduction de l'hydratation des bicouches lipidiques, ainsi les expériences décrites dans les chapitres 6 et 7 sont complémentaires aux études en fonction de la haute pression démarrées récemment. Le développement d'un équipement de haute pression et les premières mesures de diffraction et de spectroscopie de DMPC sont décrites dans le chapitre 8.

L'étude de l'AChE est décrite dans le chapitre 9. Après une introduction générale de l'AChE et la présentation de la préparation des échantillons, les expériences élastiques sont détaillées dans la section 9.3. Cette section est basée sur une publication soumise à "*Physical Chemistry Chemical Physics*". L'exploitation de deux ordres de grandeur de la résolution instrumentale permet d'observer les déplacements carrés moyens sur des échelles de temps très différentes, allant de 10-1000 ps environ.
Dans la section 9.4 une comparaison avec les résultats obtenus sur la butyrylcholinestérase humaine (BChE) est entreprise. Les données publiées par Gabel et ses collaborateurs montrent des différences significatives par rapport à nos résultats avec l'AChE, même si la structure et la fonction des deux enzymes sont très similaires.
Enfin dans la section 9.5 les résultats des mesures quasi-élastiques de l'AChE sur IN6 sont présentés.

Chapter 3

Thermal neutron scattering

3.1 General introduction and properties of the neutron

The neutron was discovered by Chadwick in 1932 [1]. Together with the proton it is the building block of the nucleus. Bound in the nucleus the neutron is stable, whereas the free neutron undergoes a beta decay into a proton, an electron and an anti-neutrino. The particle data group (PDG) average value of the lifetime of the free neutron is (885.7 ± 0.8) s [2]. The use of neutrons in the field of condensed matter was first introduced by Brockhouse and Shull [3]. In 1994 both were awarded the Nobel Prize in physics "for pioneering contributions to the development of neutron scattering techniques for studies of condensed matter" [4].
In terms of the wave-particle dualism neutrons can be described as waves through their wave vector $\vec{k}$ defined in equation 3.1

$$\left|\vec{k}\right| = \frac{2\pi}{\lambda}, \tag{3.1}$$

where λ is the wavelength of the neutron. Neutrons can be treated non-relativistically because their velocity is small compared to the speed of light and their kinetic energy E_{Kin} can be transformed using de Broglie's relation $\vec{p} = \hbar\vec{k} = m_n\vec{v}$ as shown in equation 3.2

$$E_{kin} = \frac{1}{2}m_n v^2 = \frac{\hbar^2 k^2}{2m_n} = \frac{h^2}{2m_n\lambda^2}. \tag{3.2}$$

Here h is Planck's constant and $\hbar = \frac{h}{2\pi}$. For exact values see the appendix (chapter B). m_n is the mass of the neutron (see table 3.1 for some characteristics of the neutron.).
In a neutron scattering experiment the energy transfer ΔE (cf equation 3.3a)

and the momentum transfer $\vec{Q}$ (cf equation 3.3b) are the observed quantities, as visualised in figure 3.1.

$$\Delta E = E_f - E_i = \hbar\omega = \frac{\hbar^2}{2m_n}(k_f^2 - k_i^2) \tag{3.3a}$$

and

$$\vec{Q} = \vec{k_f} - \vec{k_i}. \tag{3.3b}$$

For inelastic processes the energy dependence of $\vec{Q}$ has to be taken into account. The corresponding formula (equation 3.16) can be found in section 3.5.2.

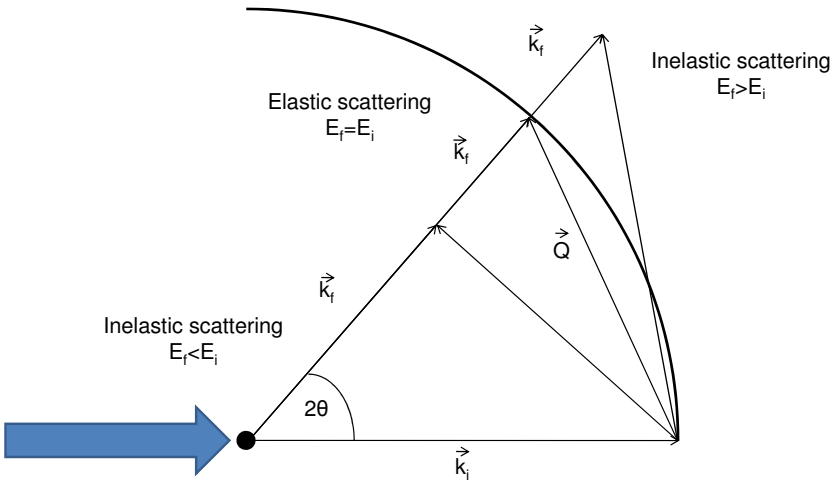

Figure 3.1: Schematic representation of a scattering event. The incoming wave is characterised by its wave vector $\vec{k_i}$ and its corresponding wavelength λ_i and energy E_i. Both elastic ($E_f = E_i$) and inelastic scattering ($E_f \neq E_i$) are shown. Also conservation of momentum $\vec{Q} = \vec{k_f}$ - $\vec{k_i}$ is depicted. 2θ is the scattering angle.

3.2 Interaction between neutrons and matter

Electromagnetic radiation interacts with the electrons in the atomic shell. Therefore the interaction strongly depends on the atomic number. The

charge	0
mass	1.008 66 u = 1.675 10 $\times 10^{-27}$ kg
spin	$\frac{1}{2}$
magnetic moment	-1.923 nuclear magnetons

Table 3.1: Properties of the neutron.

higher the atomic number, the stronger the interaction. In contrast to electromagnetic radiation no such general statement about neutrons can be made, since neutrons interact via the short range strong interaction with the nucleus of the atoms and therefore the interaction is not as systematic as in the eletromagnetic case. The scattering processes will be treated in more detail in section 3.3.
The difference in the scattering cross sections of hydrogen and its isotope deuterium is employed in biophysical neutron scattering (cf. table 3.2). About 50% of the atoms in biological macromolecules are hydrogens, thus their incoherent scattering dominates the recorded signal.
Hydration plays a crucial role in the dynamics of biomolecules such as lipids [5], proteins [6], RNA and whole cells [7], too. In order to focus on the water dynamics, deuterated macromolecules are used so that the only hydrogen atoms in the sample are those of the solvent [8]. If in contrast the interest of the performed study lies in the dynamics of the biomolecule, D_2O is used for hydration [9]. However, it has been shown that the elastic energy resolution and therefore the accessible space-time window of the employed instrument also plays a role. For example in the space-time frame observed on IN13, bulk H_2O contributes to the data only as a flat background [10].

3.3 Scattering law

In the following section the basic principles of neutron scattering are presented. As biological samples are normally non magnetic, only nuclear scattering is considered below.
In any neutron experiment the double differential cross section $\frac{d^2\sigma}{d\Omega dE}$ is measured. This quantity is the number of neutrons scattered per second into a given solid angle $d\Omega$ with a final energy E between $\hbar\omega$ and $\hbar\omega + \hbar d\omega$ divided by the incoming flux. When the perturbation of the scatterer by the incident neutron is small, the Born approximation holds [12] and the double differential cross section can be written as:

$$\frac{d^2\sigma}{d\Omega dE} = \frac{k_f}{k_i}\frac{1}{2\pi\hbar}\sum_{i,j}\left\langle b_i b_j\right\rangle \int_{-\infty}^{\infty}\left\langle e^{-i\vec{Q}\vec{r}_i(0)}e^{i\vec{Q}\vec{r}_j(t)}\right\rangle \cdot e^{-i\omega t}dt, \qquad (3.4)$$

Isotope	σ_{coh} [barn]	σ_{inc} [barn]	σ_{abs} [barn]
H	1.76	80.26	0.33
^{1}H	1.76	80.27	0.33
^{2}H	5.59	2.05	0.0
^{3}He	4.42	1.53	5333.0
^{4}He	1.34	0.0	0.0
Li	0.45	0.92	70.50
^{6}Li	0.51	0.46	940.0
^{7}Li	0.62	0.78	0.05
B	3.54	1.70	767.0
^{10}B	0.14	3.0	3835.0
C	5.55	0.0	0.0
N	11.01	0.50	1.90
O	4.23	0.0	0.0
Al	1.50	0.01	1.50
Si	2.16	0.0	0.17
P	3.31	0.0	0.17
Cd	3.04	3.46	2520.0
Gd	29.30	151.0	49700.0
^{157}Gd	650.0	394.0	259000.0

Table 3.2: Scattering cross sections σ. The table gives the coherent (σ_{coh}), incoherent (σ_{inc}) and absorption (σ_{abs}) cross section for the most common elements in biological samples (H,C,O,N,P,S). From the high absorption cross section of ^{6}Li, ^{10}B, Cd and Gd it is obvious that these elements are used for shielding purposes. Where no isotope is specified the numbers refer to the ratio occurring in nature [11].

where $\vec{r}_i$(t) is the position of scatterer i at a time t and b_i the scattering length of atom i. The sum runs over all possible pairs (i,j) of scatterers in the sample. b is related to the scattering cross sections given in table 3.2 as follows:

$$\sigma_{coh} = 4\pi \langle b \rangle^2 = 4\pi b_{coh}^2 \tag{3.5a}$$

$$\sigma_{inc} = 4\pi(\langle b^2 \rangle - \langle b \rangle^2) = 4\pi b_{inc}^2 \tag{3.5b}$$

Equation 3.4 contains two contributions: A first part concerning the time correlation between different scatterers (i,j) and a self-correlation part where i=j. A separation of these two parts leads to:

$$\begin{aligned} \frac{d^2\sigma}{d\Omega dE} = &\frac{\sigma_{coh}}{4\pi}\frac{k_f}{k_i}\frac{1}{2\pi\hbar}\sum_{i,j}\int_{-\infty}^{\infty}\left\langle e^{-i\vec{Q}\vec{r}_i(0)}e^{i\vec{Q}\vec{r}_j(t)}\right\rangle \cdot e^{-i\omega t}dt \\ &+ \frac{\sigma_{inc}}{4\pi}\frac{k_f}{k_i}\frac{1}{2\pi\hbar}\sum_{i}\int_{-\infty}^{\infty}\left\langle e^{-i\vec{Q}\vec{r}_i(0)}e^{i\vec{Q}\vec{r}_i(t)}\right\rangle \cdot e^{-i\omega t}dt \end{aligned} \tag{3.6}$$

With the coherent $S_{coh}(\vec{Q},\omega)$ and incoherent $S_{inc}(\vec{Q},\omega)$ dynamic scattering functions defined as follows:

$$S_{coh}(\vec{Q},\omega) = \frac{\sigma_{coh}}{N}\frac{1}{2\pi\hbar}\sum_{i,j}\int_{-\infty}^{\infty}\left\langle e^{-i\vec{Q}\vec{r}_i(0)}e^{i\vec{Q}\vec{r}_j(t)}\right\rangle \cdot e^{-i\omega t}dt \tag{3.7a}$$

$$S_{inc}(\vec{Q},\omega) = \frac{\sigma_{inc}}{N}\frac{1}{2\pi\hbar}\sum_{i}\int_{-\infty}^{\infty}\left\langle e^{-i\vec{Q}\vec{r}_i(0)}e^{i\vec{Q}\vec{r}_i(t)}\right\rangle \cdot e^{-i\omega t}dt \tag{3.7b}$$

the double differential cross section can be written as:

$$\frac{d^2\sigma}{d\Omega dE} = N\frac{1}{4\pi}\frac{k_f}{k_i}(S_{coh}(\vec{Q},\omega) + S_{inc}(\vec{Q},\omega)). \tag{3.8}$$

Introducing the intermediate scattering functions

$$I_{coh}(\vec{Q},t) = \frac{\sigma_{coh}}{N}\sum_{i,j}\left\langle e^{-i\vec{Q}\vec{r}_i(0)}e^{i\vec{Q}\vec{r}_j(t)}\right\rangle \tag{3.9a}$$

$$I_{inc}(\vec{Q},t) = \frac{\sigma_{inc}}{N}\sum_{i}\left\langle e^{-i\vec{Q}\vec{r}_i(0)}e^{i\vec{Q}\vec{r}_i(t)}\right\rangle \tag{3.9b}$$

equations 3.7 can be written as time Fourier transforms:

$$S_{coh}(\vec{Q},\omega) = \frac{1}{2\pi\hbar}\int_{-\infty}^{\infty} I_{coh}(\vec{Q},t)\cdot e^{-i\omega t}dt \tag{3.10a}$$

$$S_{inc}(\vec{Q},\omega) = \frac{1}{2\pi\hbar}\int_{-\infty}^{\infty} I_{inc}(\vec{Q},t)\cdot e^{-i\omega t}dt. \tag{3.10b}$$

Performing a Fourier transform with respect to space on the intermediate scattering functions leads to the Van Hove pair correlation function in the case of coherent scattering and to the self correlation function in the case of incoherent scattering [13]:

$$G(\vec{r},t) = \frac{1}{(2\pi)^3}\int I_{coh}(\vec{Q},t)\cdot e^{-i\vec{Q}\vec{r}}d\vec{Q} \tag{3.11a}$$

$$G_S(\vec{r},t) = \frac{1}{(2\pi)^3}\int I_{inc}(\vec{Q},t)\cdot e^{-i\vec{Q}\vec{r}}d\vec{Q}. \tag{3.11b}$$

G($\vec{r}$,t) is the probability that, given a particle at the origin a time t = 0, any particle (including the original particle) can be found at $\vec{r}$ at a time t. In contrast $G_S(\vec{r},t)$ gives the probability of finding the same particle, which was at t = 0 at the origin at a time t at the position $\vec{r}$. Therefore G($\vec{r}$,t) includes $G_S(\vec{r},t)$.
Coherent scattering thus contains the correlation of the position of different atoms at different times. Hence information on structure and collective motions can be deduced from coherent scattering. In contrast the incoherent part contains information about the evolution in time of one and the same atom, thus the local dynamics of the sample can be probed with incoherent scattering.

3.4 Neutron sources and transport

About 50% of all matter is made up of neutrons but they are bound to the nucleus. In order to produce free neutrons two methods are employed in research institutes: fission (Institut Laue-Langevin (ILL), Grenoble, France, Forschungsreaktor München II (FRMII), Munich, Germany) and spallation (Spallation neutron source (SNS) in Oak Ridge, US, Paul Scherrer Institut (PSI), Villigen, Switzerland or ISIS, Didcot, UK). Laser induced fusion has been proposed lately [14], but will not be available in the near future, due to technological difficulties.
In the fission process ^{235}Uranium nuclei are split into two lighter parts and release energy (see figure 3.2a). Apart from the fission fragments in average 2.5 neutrons with energies in the MeV range are produced per fission event. This technology is limited to a relatively low flux (maximum 1×10^{14}-1×10^{15} n cm^2/s), due to heat production in the reactor core and

the difficulty of heat dissipation in short times.
In the case of spallation sources a heavy metal target (liquid or solid) is hit by an accelerated proton (up to several GeV). The excitation of the target leads to an evaporation of 20 to 30 neutron in the MeV range per event (cf figure 3.2b). Therefore more neutrons can be produced per proton pulse in a spallation source, but these sources are normally operated in a discontinuous way. Thus absolute flux values are difficult to compare.

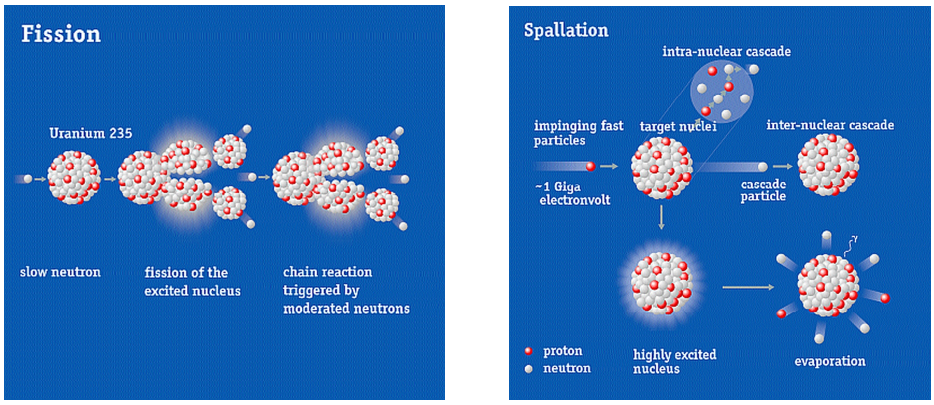

(a) (b)

Figure 3.2: Schematic representation of the fission 3.2a and spallation 3.2b process [15].

The energy of the liberated neutrons (in the order of MeV) is too high by far for scattering experiments for which energies in the meV range are needed to probe excitations within the sample. Moderators are generally used to shift the energy of the neutrons to lower values. In reactor sources they are in particular needed to slow down the fast neutrons created in the fission process and thus sustain the chain reaction. In neutron scattering moderation is also employed to move the energy of the fission neutrons into the range used for the experiments ($\approx$ meV). Typically materials used as moderators have a high scattering cross section (cf table 3.2). At ambient temperature water or heavy water is often used. To slow down the neutrons even further liquid hydrogen or deuterium at temperatures around 20 K can be employed. The neutrons have Maxwellian energy distribution after the moderation with a maximum which corresponds to the temperature of the moderator. An overview of characteristic temperatures and energies typically employed in neutron scattering can be found in table 3.3. Neutron guides are used to transport the free neutrons from where they are created to the experiments. Nowadays the longest transport distance is about 100 m at neutron centres, so beam loss due to neutron decay can be neglected. As neutrons carry no charge, they cannot be deflected by

electro-magnetic fields. Therefore total reflection is employed to transport the neutrons. Often nickel is used for the coating of neutron guides due to its high refraction index n. Below a critical angle of $\theta_C = \lambda[\text{Å}] \times 0.1°$ total reflection occurs [16]. It can be improved even further by using ^{58}Ni due to its larger coherent scattering length and multilayer coating of the guides [17].

	E [meV]	T [K]	v [m s^{-1}]	λ [Å]
cold	0.1 - 10	1 - 120	130 - 1300	30 - 3
thermal	10 - 100	120 - 1200	1300 - 4000	3 - 1
hot	100 - 500	1200 - 6000	4000 - 10000	1 - 0.4

Table 3.3: Characteristic neutron energies, temperatures, velocities and corresponding wavelengths. Values can be calculated using the relation E = k_BT and equation 3.2.

3.5 Spectrometers

Via Heisenberg's uncertainty principle:

$$\Delta E \Delta t \geq \frac{\hbar}{2} \tag{3.12}$$

the observation time is directly related to the energy resolution of the employed instrument. Thus using spectrometers with different energy resolutions gives access to different time scales probed within the sample.
A whole hierarchy of energy resolutions is covered by the different types of spectrometers currently available in neutron scattering centres.
The highest energy resolution (in the order of neV) is obtained by the Neutron spin echo (NSE) technique [18]. Backscattering spectrometers give access to energy resolutions between 0.9 µeV and 10 µeV. This type of instrument will be discussed in more detail in section 3.5.1 and the IN13 spectrometer will be especially highlighted in chapter 4. The energy resolution of disk chopper time-of-flight spectrometers can be varied almost continuously between 10 µeV and 3 meV by adjusting the speed of the choppers. Resolutions of the instruments used in this work are shown in figure 3.3 for comparison. The resolution functions normally have Gaussian or Lorentzian shapes, but can also have a triangular shape, depending on the chopper alignment. Three axis spectrometers are employed mainly in solid state physics to study collective excitations (phonons). They will not be discussed here.

In neutron spectroscopy not only the spatial deviation of the neutron, but also the energy exchanged with the sample is measured. Via the scat-

tering vector $\vec{Q}$ information on the length scales under investigation can be extracted. The energy transfer ΔE provides information on the dynamics of the samples. Therefore the incident wave vector $\vec{k_i}$ of the neutrons has to be well defined.
Two methods are employed in backscattering and time-of-flight instruments to select a given wavelength out of the polychromatic neutron beam:

1. Bragg reflection of crystals. In this case the reflection of a single crystal is used to select a wavelength, which is determined by the lattice constant of the crystal. This method is mainly employed in backscattering spectrometers (see section 3.5.1), but also on some time-of-flight instruments (e.g. IN6).

2. Time-of-flight. A set of choppers is used to create neutron pulses with a given energy resolution (cf section 3.5.2). Choppers are disks rotating with a speed up to 20000 rpm. They are coated with a neutron absorbing material (e.g. gadolinium), only a small fraction is untreated and therefore lets neutrons pass.

In the following sections backscattering and time-of-flight spectrometers will be discussed in greater detail, because these two types of instruments were employed in the presented work.

Spectrometer	IN6	IN6	IN13	IN16	TOFTOF
Wavelength [Å]	5.12	5.90	2.23	6.27	6.00
Accessible Q-range [$Å^{-1}$]	0.4-2.2	0.4-1.9	0.2-4.9	0.02-1.9	0.4-1.6
Length scale [Å]	2.9-15.7	3.3-15.7	1.3-31.4	3.3-314.2	3.9-15.7
Resolution FWHM [μeV]	90	50	8	0.9	56
Timescale [ps]	4	7	40	365	6

Table 3.4: Characteristics of the spectrometers used in this work. IN6, IN13 and IN16 are situated at the ILL, TOFTOF at the FRMII.
The length scale was calculated using equation 6.2. Following Heisenberg's uncertainty principle (equation 3.12) the elastic energy resolution can be converted into a timescale using the relation: $\Delta t = 329\ \mu eV\ ps/\Delta E$.

3.5.1 Backscattering spectrometers

In this section some general remarks on backscattering spectrometers will be given and two spectrometers (IN13, IN16), used in this work will be highlighted in more detail.
The backscattering technique was proposed 1966 by Maier-Leibnitz [19].

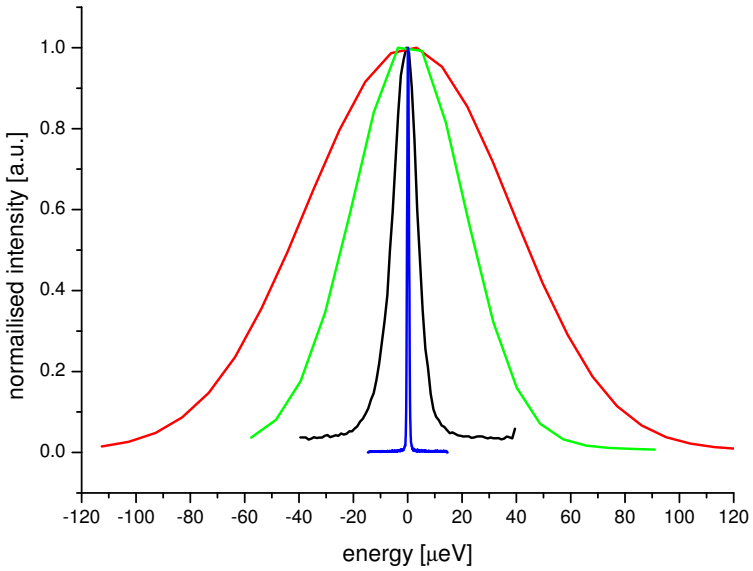

Figure 3.3: Comparison of the elastic energy resolutions of three different instruments and four different resolutions used for this work. The resolutions cover a range from 0.9 μeV to 90 μeV (FWHM). Shown in red IN6 (5.1 Å = 90 μeV), in green IN6 (5.9 Å = 50 μeV) is displayed, in black IN13 (8 μeV) is presented and IN16 (0.9 μeV) is depicted in blue. More information on the characteristics of the single instruments can be found in table 3.4.

In this technique crystal reflections are used according to Bragg's law (see equation 3.13) to select a given wavelength:

$$n\lambda = 2d \sin\theta_B. \tag{3.13}$$

In this equation d stand for the repeat distance of the crystal lattice, θ_B for the Bragg angle and n for the order of the reflection. It takes advantage of the fact, that the energy resolution in backscattering geometry ($2\theta = 180°$) becomes very narrow. This can be seen by taking the derivative of Bragg's Law:

$$\frac{\Delta E}{E} = \frac{2\Delta\lambda}{\lambda} = \frac{2\Delta d}{d} + 2\cot\theta_B \Delta\theta_B. \tag{3.14}$$

For θ_B=90° the cotangent term in eq. 3.14 becomes zero and only the first term, which solely depends on the crystal quality, dominates the energy resolution of the spectrometer. This setup is realised within the secondary spectrometer (see pictures 3.4 and 4.1). The analyser crystals are mounted in perfected backscattering geometry, so only neutrons with the corresponding resolution are collected by the neutron detectors.
Until the invention of the spin echo technique, backscattering spectrometers provided the finest energy resolution available. Furthermore the first inelastic studies revealing the dynamical transition with neutrons were performed on a backscattering spectrometer [9].

IN13

During my thesis I was involved in the development and the operation of the thermal backscattering spectrometer IN13, therefore the instrument and its characteristics will be discussed in more detail in chapter 4.

IN16

The backscattering spectrometer IN16 is situated on a guide looking at one of the cold sources of the ILL. Therefore the Si (111) reflection is used to select a wavelength of λ = 6.27 Å of the incoming neutrons. This instrumental setup results in a very narrow elastic energy resolution of 0.9 µeV. In contrast to IN13, where the energy of the impinging neutrons is changed by heating or cooling the monochromator, IN16 uses a Doppler drive. For elastic measurements this drive is at rest, in the quasi-elastic mode it moves with a given speed resulting in an accessible energy range of $\pm$ 15 µeV. The schematic layout of IN16 can be found in figure 3.4.

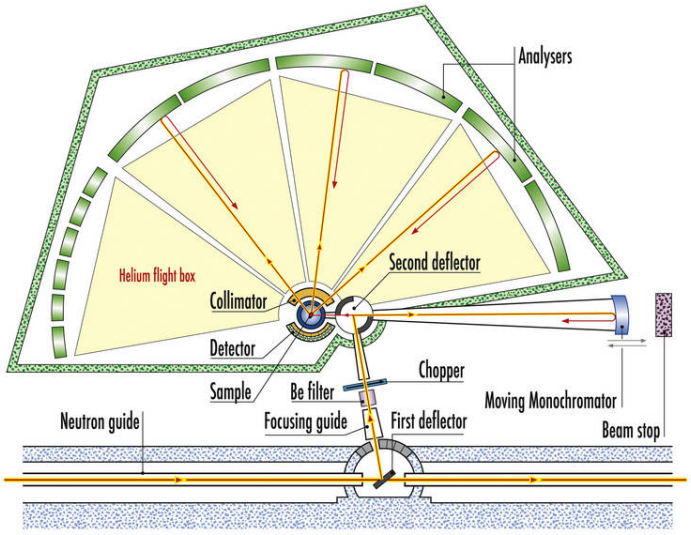

Figure 3.4: Schematic layout of the cold neutron backscattering spectrometer IN16 at ILL [20].

3.5.2 Time-of-Flight spectrometers

This type of spectrometer uses the time-of-flight of the scattered neutrons for energy discrimination. Monochromatisation is done by either using Bragg reflection, then the spectrometer is called XTL-TOF (crystal-time-of-flight) spectrometer. If a system of choppers is used to select a wavelength, the instrument is called TOF-TOF spectrometer. At least two choppers are needed to perform this task. A schematic representation of this setup is shown in figure 3.5. The first chopper (P-chopper in figure 3.5) divides the continuous beam into discrete packages. These packages still contain neutrons with different wavelengths, i.e. different velocities. The second chopper (M-chopper in figure 3.5), installed at a certain distance to the first one (typically one to several meters), is used to select one wavelength out of the now dispersed package. Additional choppers can be put in place between these two choppers, to avoid e.g. that very slow neutrons from the reactor also pass and distort the recorded signal.

The scattered neutrons are detected as a function of time. Neutrons which gained energy during the scattering process will arrive before elastically scattered neutrons. Neutrons which have lost energy during the interaction with the sample will arrive last in the detectors. The recorded time difference Δt then permits to recalculate the energy difference to the elastically scattered neutrons through:

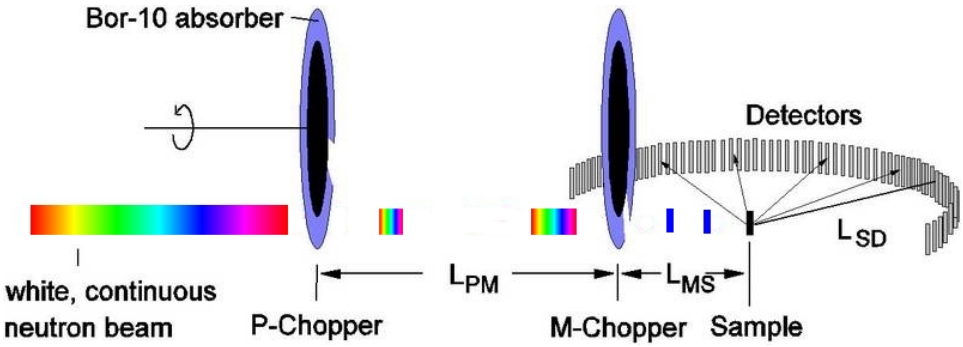

Figure 3.5: Sketch of the time-of flight principle. The different wavelengths of the polychromatic beam are presented by different colours. Adapted from [21].

$$\begin{aligned}\Delta E = \hbar\Delta\omega &= \frac{1}{2}m_n(\Delta v)^2 \\ &= \frac{1}{2}m_n L_{SD}^2\left(\frac{1}{t_0}-\frac{1}{t}\right)^2 = \frac{1}{2}m_n L_{SD}^2\left(\frac{\Delta t}{t_0^2+t_0\Delta t}\right)^2\end{aligned} \tag{3.15}$$

where L_{SD} denotes the distance between sample and detector (cf figure 3.5), t_0 is the flight time of the elastically scattered neutrons and Δt the difference in the time of flight: $\Delta t = t - t_0$.

In contrast to backscattering spectrometers, where only small energy transfers are probed, on a time-of-flight instrument the energy dependence of $\vec{Q}$ cannot be neglected. Hence equation 3.3b has to be rewritten as equation 3.16

$$Q^2 = k_i^2 + k_f^2 - 2k_i k_f \cos 2\theta. \tag{3.16}$$

Together with the energy transfer (eq. 3.2) this leads to the fundamental relation between scattering vector $\vec{Q}$, incident wave vector $\vec{k_i}$ and scattering angle 2θ which is shown in equation 3.17 and visualised for different scattering angles in figure 3.6:

$$Q^2 = 2k_i^2 - \frac{2m_n\omega}{\hbar} - 2k_i\sqrt{k_i^2 - \frac{2m_n\omega}{\hbar}}\cos 2\theta. \tag{3.17}$$

In the following sections, the two time-of-flight spectrometers which have been used during this work, will be described in more detail.

IN6

IN6 is an example of a time focusing XTL-TOF spectrometer. It uses crystal reflections of three pyrolytic graphite monochromator arrays to monochro-

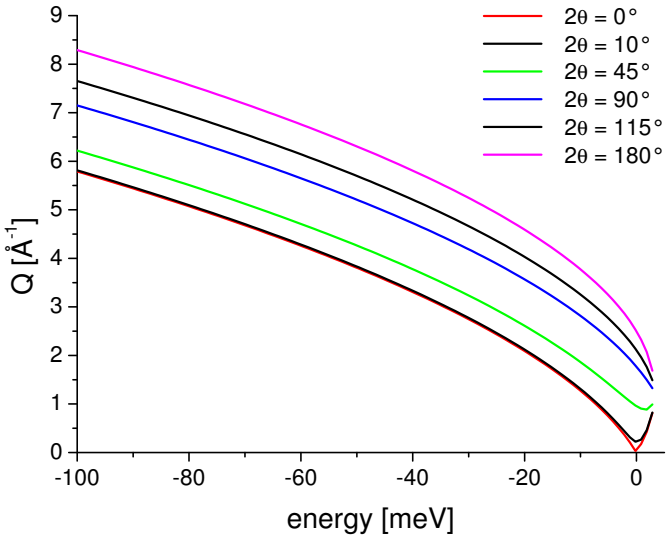

Figure 3.6: Dynamic range for a given k_i=1.23 $Å^{-1}$ (corresponding to a wavelength of 5.1 Å) and different scattering angles 2θ. The black lines indicate the angular range covered with detectors on the IN6 spectrometer at ILL.

matise the incident beam. By changing the angle of the secondary spectrometer with respect to the monochromator, four discrete wavelengths (4.1, 4.6, 5.1, 5.9 Å) can be selected on this spectrometer. Higher order reflections are removed by a beryllium filter. The schematic layout of the instrument can be found in figure 3.7. For the experiments described in the following chapters only incident wavelengths of 5.1 and 5.9 Å were used, resulting in elastic energy resolutions of 90 and 50 µeV, respectively (cf figure 3.3). In order to get the neutrons from all three monochromators at the same time on the sample, this corresponds to the so called time-focusing condition, the beam is pulsed by a Fermi chopper (a fast rotating assembly of curved slits). To prevent frame-overlap when the chopper is rotating faster than 7500 rpm, a suppressor chopper is placed before the Fermi chopper and rotates in phase with the latter at a lower speed. The secondary spectrometer is filled with helium and equipped with 337 ^{3}He counters covering an angular range from 10° to 115° and a total surface of about 6 m^2.
The accessible dynamic range of IN6 for an incident wavelength of 5.1 Å is shown as a black line in figure 3.6.

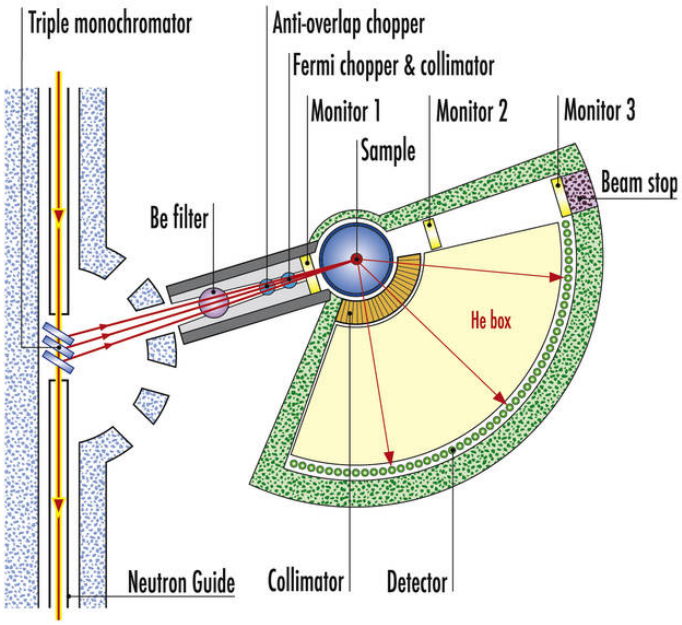

Figure 3.7: Schematic layout of the cold time-of-flight spectrometer IN6 at ILL [22]. The four possible positions of the secondary spectrometer are indicated by the four openings of the monochromator shielding (blue).

TOFTOF

In contrast to IN6 the "TOFTOF" time-of-flight spectrometer installed at the FRMII in Munich is a TOF-TOF spectrometer. In total seven choppers are used to monochromatise the beam of cold neutrons [23]. The elastic energy resolution can be varied between about 4 µeV to 3000 µeV. Due to a special S-shaped neutron guide with an increased reflectivity towards the sample, the spectrometer provides a high flux and at the same time a good signal to noise ratio. After interacting with the sample, the scattered neutrons are detected by 603 ^{3}He gas detectors installed 4 m from the sample position. They cover an angular range from $-15°$ to $-140°$.

3.6 Energy resolved neutron scattering

A schematic representation of a typical scattering spectrum is shown in figure 3.8a. Elastic, quasi-elastic and inelastic scattering are presented. The elastic scattering ($\Delta E = 0$) has always a finite width Γ_{res} given by the elastic energy resolution of the spectrometer. From the evolution of the elastic intensity with Q (see figure 3.8b) information about the geometry of the observed motion can be inferred.

The quasi-elastic broadening with width H_1 is caused by diffusive motions. It can be described by a sum of Lorentzians [24]. According to the employed model different parameters such as diffusion constants D or residence times τ can be extracted from the half width at half maximum (HWHM) of the curve.

Inelastic excitations are generated by e.g. phonons and give rise to a satellite peak at a given energy value. They are often investigated by three axis spectroscopy [25] and will not be discussed in detail in this framework.

In the following section more details about elastic (Section 3.6.1) and quasi-elastic neutron scattering (section 3.6.2) will be given.

3.6.1 Elastic neutron scattering

Elastic incoherent scans as a function of temperature provide a fast way to characterise average molecular dynamics of the sample, because the elastic intensity is by far larger than in the quasi-elastic or inelastic regime.
The incoherent intermediate scattering function 3.9b can be rewritten in terms of the Gaussian approximation [27, 28]. The approximation assumes that displacement of the atoms around their rest position $\vec{r}_i(0)$ is Gaussian. It yields:

$$I_{inc}(\vec{Q},t) = \frac{1}{N}\sum_i e^{-\frac{1}{3}Q^2\left\langle u_i^2\right\rangle} \tag{3.18}$$

where the displacements $\vec{u}_i(t)$ are defined as follows:

$$\vec{u}_i(t) = \vec{r}_i(t) - \vec{r}_i(0). \tag{3.19}$$

The intermediate scattering function can be separated into a time-dependent and a time-independent part [24]:

$$I_{inc}(\vec{Q},t) = I_{inc}(\vec{Q},\infty) + I'_{inc}(\vec{Q},t). \tag{3.20}$$

Fourier transformation of this expression results in:

$$S_{inc}(\vec{Q},\omega) = S(\vec{Q},0) + S'_{inc}(\vec{Q},\omega) \tag{3.21}$$

with:

$$S(\vec{Q},0) = \delta(\omega) I_{inc}(\vec{Q},\infty). \tag{3.22}$$

Hence $S(\vec{Q},\omega)$ can again be separated in an elastic and an inelastic contribution. Below the elastic component will be examined in more detail.
After performing the average over i, $S(\vec{Q},0)$ reads:

$$S(\vec{Q},0) \approx e^{-\frac{1}{3}Q^2\langle u^2\rangle} \tag{3.23}$$

The average mean square displacement can be extracted from a linear fit to the logaritm of S($\vec{Q}$,0) versus Q^2 according to :

$$\langle u^2\rangle = -3\frac{\partial \ln S(\vec{Q},0)}{\partial Q^2}. \tag{3.24}$$

The same formalism is used in small angle scattering and known as Guinier approximation [29]. The approximation is strictly valid for $Q \to 0$, but it was shown, that it hold up to $\langle u^2\rangle$ $Q^2 \approx 1$ [30].

3.6.2 Quasi-elastic neutron scattering

Analysing the quasi-elastic scattering gives a more detailed picture about the observed dynamics. From the elastic incoherent structure factor (EISF) the geometry of the motion can be inferred. The theoretical scattering function $S_{theo}(\vec{Q},\omega)$ reads [24]:

$$S_{theo}(\vec{Q},\omega) = e^{-\langle x^2\rangle Q^2}\left[A_0(\vec{Q})\delta(\omega) + \sum_n A_n(\vec{Q})L_n(\vec{Q},\omega)\right] \tag{3.25}$$

where $e^{-\langle x^2\rangle Q^2}$ is the Debye-Waller factor, representing vibrations. The delta function δ accounts for dynamics that cannot be resolved by the instruments' resolution. The amplitude $A_0(\vec{Q})$ is the elastic incoherent structure factor (EISF) and contains information about the geometry of the movement. The quasi-elastic contributions are mimicked by a sum of Lorentzian functions $L_n(\vec{Q},\omega)$ and the corresponding quasi-elastic incoherent structure factors (QISF) $A_n(\vec{Q})$.

$$L_n(\vec{Q},\omega) = \frac{1}{\pi}\frac{\Gamma_n(\vec{Q})}{\omega^2 + \Gamma_n(\vec{Q})^2}. \tag{3.26}$$

For data analysis the theoretical scattering law S_{theo} has to be convoluted with the instrumental energy resolution, which can be mimicked by e.g. vanadium:

$$S_{meas}(\vec{Q},\omega) = S_{theo}(\vec{Q},\omega) \otimes S_{res}(\vec{Q},\omega). \tag{3.27}$$

Diffusion in a sphere model

For the description of diffusion in confined space, such as hydrogen atoms in a lipid or in proteins, Volino and Dianoux developed the model of diffusion in a sphere. Here diffusive motion are allowed only inside a sphere

with radius r and impervious walls [31]. The scattering law can be written as:

$$S(\vec{Q},\omega) = A_0^0(\vec{Q})\delta(\omega) + \sum_{(l,n)\neq(0,0)} (2l+1)A_n^l(\vec{Q})\frac{1}{\pi}\frac{\lambda_n^l D}{\pi\omega^2 + (\lambda_n^l D)^2}. \quad (3.28)$$

The authors found an analytical expression for the EISF, which reads:

$$A_0^0(\vec{Q}) = \left[\frac{3j_1(\vec{Q}r)}{\vec{Q}r}\right]^2, \quad (3.29)$$

where $j_1(x) = \frac{\sin x}{x^2} - \frac{\cos x}{x}$ is the first order spherical Bessel function and r the radius of the sphere, which can be extracted from fitting equation 3.29 to the obtained data. Bellisent-Funel and co-workers [32] expanded the model for the EISF by an immobile fraction p, where p denotes strongly bound proton. Equation 3.29 then reads:

$$A_0^0(\vec{Q}) = p + (1-p) \times \left[\frac{3j_1(\vec{Q}r)}{\vec{Q}r}\right]^2. \quad (3.30)$$

Figure 3.9a shows the HWHM of the quasi-elastic component of the scattering law as a function of $(RQ)^2$. For continuous diffusion a linear dependence is expected [24] as drawn in the graph 3.9. However, for small Q-values ($Q < \frac{\pi}{r}$) Γ tends towards a constant value Γ_0, what is a signature of motion in confinement. Γ is then related to the Diffusion constant D and the radius of the sphere via:

$$\Gamma_0 = \frac{4.33D}{r^2}. \quad (3.31)$$

Hall and Ross [33] extended this model to a random jump diffusion within the restricted geometry of a sphere. For small Q-values, it shows the same behaviour as the diffusion in a sphere model, but for large values of Q it converges towards the jump-diffusion model introduced by Singwi and Sjölander [34]. The half width at half maximum can be described by equation 3.32, where D is the diffusion constant and τ the residence time between two jumps. τ can be described in the limit of large Q as $\Gamma_\infty = 1/\tau$:

$$\Gamma = \frac{DQ^2}{1 + DQ^2\tau}. \quad (3.32)$$

Carpentier model

A modification of the Volino-Dianoux model assumes not only one fix radius but allows increasing radii for the diffusion volumes of the hydrogen

atoms along a linear chain (see equation (3.33a)). This model was introduced by Carpentier et al. for the study the dynamics of alkyl chain of dicopper tetrapalmitate [35] and was already employed to describe the dynamics of lipid chains by König et al. [36] and also by Doxastakis et al. [37]. In this case the EISF can be written as:

$$A_0(\vec{Q}) = \frac{1}{N}\sum_{n=1}^{N}\left[\frac{3j_1(QR_n)}{QR_n}\right]^2 \tag{3.33a}$$

with

$$R_n = \frac{n-1}{N-1} \times [R_N - R_1] + R_1. \tag{3.33b}$$

N stands for the total number of hydrogen atoms along a chain and R_n gives the corresponding radii for the running index n. The line width in this model shows a similar behaviour as in the case of the "diffusion in a sphere" model.

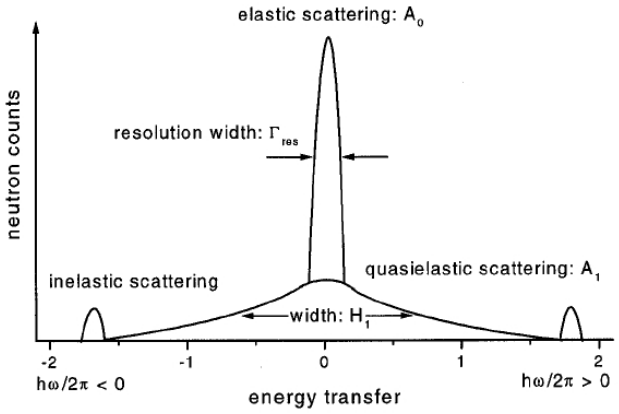

(a)

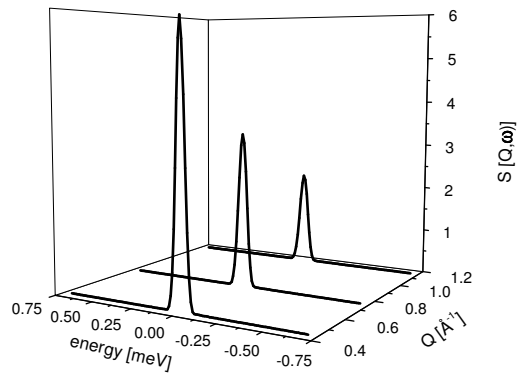

(b)

Figure 3.8: Figure 3.8a shows a schematic representation of a scattering spectrum is shown. Elastic, quasi-elastic and inelastic scattering are indicated (Taken from [26]). The evolution of the elastic peak as a function of Q is shown in figure 3.8b.

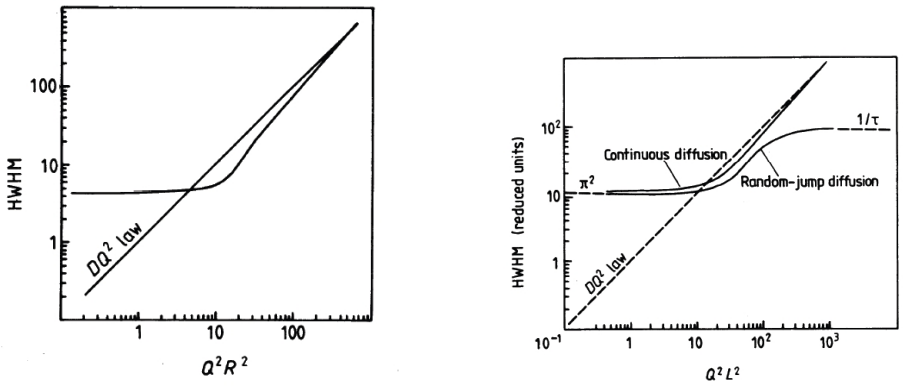

(a) (b)

Figure 3.9: Schematic representations of the HWHM of the function representing the quasi-elastic component of the scattering law in the case of the diffusion in a sphere model (3.9a) [31] and the model introduced by Hall and Ross (3.9b) [33].

Chapter 4

The backscattering spectrometer IN13

The backscattering (BS) spectrometer IN13 was designed in the 1980s at the ILL for the study of tunnelling effects [38]. The instrument was built in order to achieve a good energy resolution with a large Q-range, as these are the important characteristics for tunnelling experiments. It also fills the gap in ($\vec{Q}$, ω) space between the backscattering spectrometers with even finer energy resolution (IN10 and IN16) and the time-of flight instruments IN5 and IN6. The shorter wavelength allows especially to access a much larger Q-range compared to a cold instrument. In the case of IN13 a scattering vector Q of up to 4.9 Å^{-1} is available.
After redesigning and the installation of some modifications the thermal neutron backscattering spectrometer IN13 is operated since 1998 by a Collaborating research group (CRG) [39]. 50% of the available beamtime is allocated by the CRG partners (Italy and France) and the other half by the ILL subcommittees. The CRG time is dedicated to the investigation of dynamics of biological systems such as proteins, lipids or whole cells.

4.1 Detailed instrument description

A schematic layout of the spectrometer is displayed in figure 4.1. The instrument is situated on the H24 guide of the ILL which is fed with thermal neutrons coming from the reactor core. The neutrons have a Maxwellian distribution centered around 2 Å due to the moderator temperature of 300K. A monochromator made out of CaF_2 crystals is employed to extract neutrons with a wavelength of 2.23 Å from the guide. For this purpose the (422) reflection of the crystals is used. Several types of scans can be performed on the spectrometer. For elastic scans, the energy of the incoming neutrons is kept fix. To perform inelastic scans, the energy of the neutrons hitting the sample is changed. This is achieved by heating or cooling the monochro-

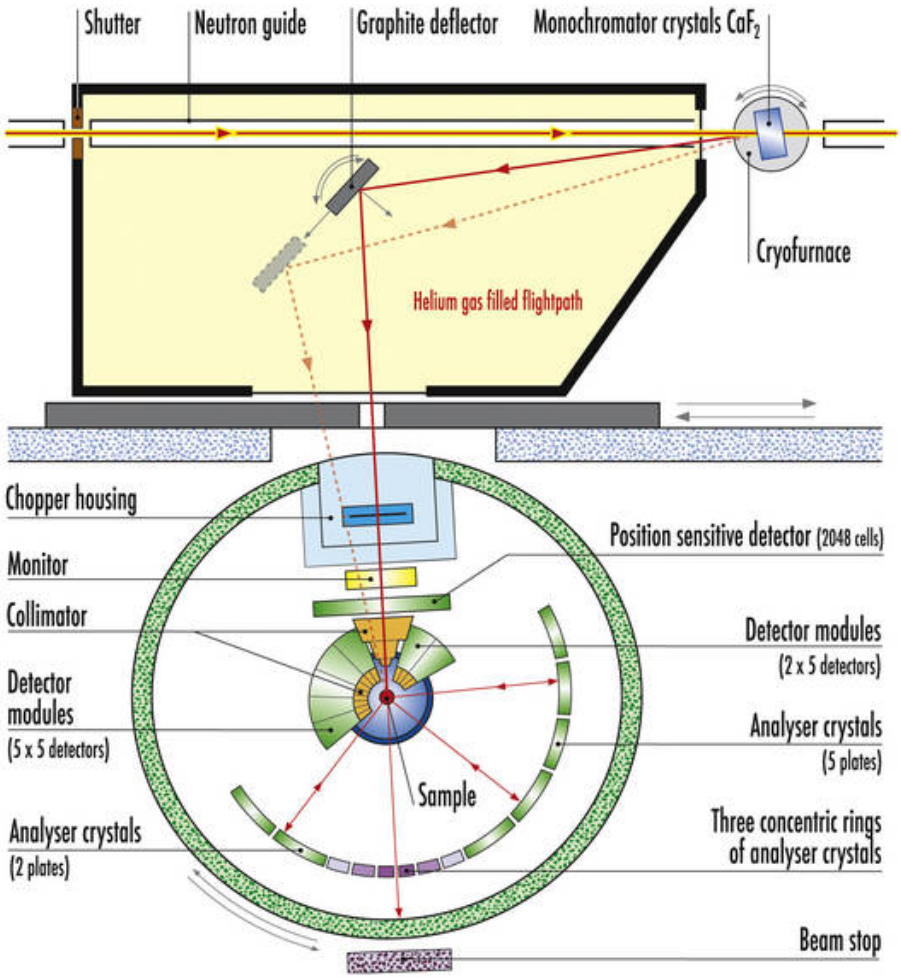

Figure 4.1: Schematic layout of the IN13 backscattering spectrometer [40].

mator, which results in a change of the lattice constant of the monochromator crystals. To obtain a good energy resolution an almost backscattering condition is employed already at this stage. With a take-off angle of typically 1.8° a deflector is needed to deviate the neutrons. For this purpose an array of nine rows of pyrolytic graphite crystals deflects and focuses the neutron beam into the secondary spectrometer. To avoid beam loss due to air scattering (for a flight path of 1 m in air approximately 10% of the neutrons are lost) the deflector is housed in a sealed box which is filled with helium gas. The box is additional faced with cadmium to avoid parasitic scattering.
The sample is normally contained in a closed cycle cryostat (displex) or a cryofurnace for temperature control. The displex allows experiments in a temperature range from 3 K to 550 K. A set of seven analyser crystals (again CaF_2, (422) reflection) installed in perfect backscattering condition selects the neutrons of the right energy, which pass a second time through the sample before reaching the detectors. A sample transmissions in the order of 90% or higher avoids that the neutrons are scatterd again while they pass a second time through the sample. Finally the neutrons are detected by 35 ^{3}He counters and in the small angle region by a Position Sensitive Detector (PSD). In order to suppress the neutrons which are scattered directly from the sample onto the detectors and thus do not fulfil the backscattering condition and to suppress higher orders of the refelction of the monochromator ($\lambda/2$, etc), a chopper is used. Operating at a speed of 6756 rpm, it chops the neutron beam into discrete packages. Because the velocity of the neutrons is well-known, a discrimination via the time-of-flight is possible. Neutrons scattered directly into the detectors are suppressed by the electronics. Finally only neutrons which were selected by the analysers are counted, whereas.
Neutrons that pass the sample without being scattered are stopped by a cadmium coated beam stop, which can be replaced by a monitor to measure transmission. In total IN13 makes use of two monitors. The first one is permanently installed in the beam, positioned between chopper and sample. It is used to normalise the scattered intensity to the incoming flux. It has a low efficiency in order to keep the impinging flux on the sample as high as possible. The second one is used to measure transmission and is mounted on a linear stage after the sample position. During data acquisition it is moved out of the beam, for transmission measurements it is put in.

4.2 Instrument development

During my PhD I was also highly involved in the user support, maintenance and running of the IN13 spectrometer. In this section some of the

recent technical developments are highlighted.

- In order to guide and focus the beam perfectly onto the sample, the deflector can be moved by five axes. It is mounted on two linear stages, through which the x- and y-direction can be controlled. Furthermore it can be rotated (ω), tilted (χ) and its curvature can be changed (ρ) in order to focus the beam on the sample position.
  During inelastic scans the temperature of the monochromator is varied in order to change the energy of the incoming neutrons. Therefore, the deflector has to be moved to the new position of the beam. Even during elastic scans its position has to be checked regularly and corrected when needed. This can be necessary when the temperature of the analyser crystals changes due to environmental reasons. In this case the temperature of the monochromator is changed while the temperature of the deflector is kept fixed. Thus a precise positioning and monitoring of the deflector is essential for the experiment.
  The motors performing the motions are controlled by encoders which allow the absolute determination of the position of the motors. Because of a malfunction of one of the encoders and aging due to radiation, it was decided to replace all of them. During the work a displacement of the linear stage, on which the deflector is mounted, was discovered. Thereupon a re-alignment of the complete instrument, starting with the monochromator became necessary.

Energy [µeV]	x_{DF}[mm]	y_{DF}[mm]	ω_{DF}[°]	ω_{BA}[°]
-100	78.20	419.64	45.21	7.11
-50	72.70	414.22	45.28	6.88
-25	69.97	411.52	45.32	6.84
-10	68.32	409.89	45.34	6.84
1.8	67.04	408.62	45.36	6.81
10	66.14	407.72	45.37	6.77
25	64.52	406.09	45.39	6.74
50	61.84	403.41	45.43	6.69
100	56.38	398.03	45.51	6.52

Table 4.1: Deflector positions as a function of energy transfer on IN13. 1.8 µeV corresponds to the elastic position.

  During a long shutdown in 2010, in a first step a laser setup was used to find the optically correct position of the deflector and the corresponding position of the secondary spectrometer. The alignment using neutrons was done in the beginning of the first cycle 2010. Scans

of the four axes x_{DF}, y_{DF}, ω_{DF}, ω_{BA} (where "DF" stands for deflector and "BA" for the secondary spectrometer) were performed to find the position of the maximal flux. First a scan with large step width of the x_{DF}- and y_{DF}-axis of the deflector was performed in order to locate the elastic position. These two axes are less sensible to changes than ω_{DF} and ω_{BA}, as it can be seen from table 4.1. A second scan using all four axes around the intensity maximum found in the first scan then allowed to exactly determine the position of the maximal flux. An example of the scan of x_{DF} and y_{DF} is shown in figure 4.2. The re-alignment resulted in a gain in flux of about 7%.

- A second improvement was the installation of a new CCD camera to check the sample alignment [41]. The position of the sample in the beam has to be verified for every user. In the old configuration a Polaroid camera was used to verify the sample position with respect to the beam. Both systems use scintillators to convert neutrons into photons, which are then recorded either by a photo sensitive chip or an emulsion. Typical exposure times for the Polaroid camera were in the order of 5 min whereas with the CCD camera the exposure time could be reduced to 20 s. Figure 4.3 shows an example where the length of the sample stick had to be adapted. With the old setup this simple operation took at least ten minutes whereas it can be done in less than a minute now. Furthermore, the picture taken can be easily archived for comparison.

- Finally the development and testing of a high pressure cell dedicated to biological samples was also part of my work. The cell was originally designed in the group of M.-C. Bellisent-Funel at the Laboratoire Léon Brillouin (LLB) in Saclay [42] (see figure 4.4). The pressure cell used in this work was manufactured by J.-L. Laborier and C. Payre at the ILL. It is made out of an aluminium cylinder (7049T6) with an inner diameter of 6 mm and an outer diameter of 15 mm, what leads to a thickness of 9 mm. A piston transmits the pressure of up to 6.5 kbar (1 bar = 0.1 MPa) with a precision of 3% to the sample inside. In order to avoid multiple scattering the sample volume in the beam can be further reduced by an aluminum insert of 4 mm diameter. The cell has been tested with powder (hydrated lysozyme) and liquid samples (DMPC in D_2O). Some of the results obtained on DMPC will be presented in more detail in chapter 8.

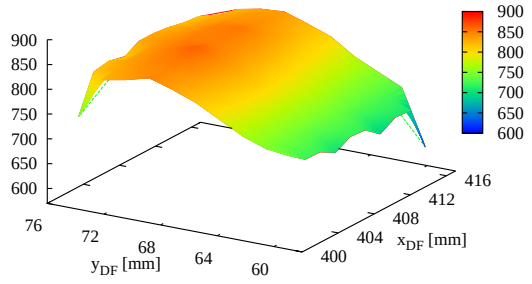

(a)

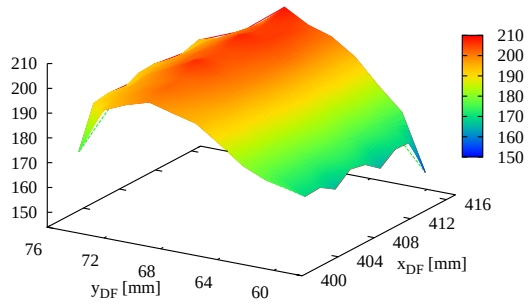

(b)

Figure 4.2: Wide scan of the x and y axes of the deflector. Figure 4.2a shows the intensity measured at the position of the monitor 1, 4.2b shows the summed intensity of all detectors. The sample used, was a 2 mm thick vanadium reference.

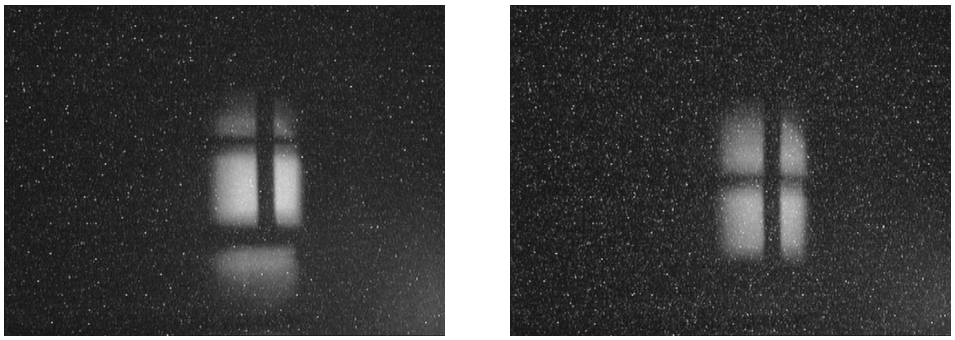

(a) (b)

Figure 4.3: Example for the adjustment of the length of the sample stick using the new CCD camera. Picture 4.3a shows the initial position of the sample with respect to the incident neutron beam. Picture 4.3b displays the adjusted position. Exposure times were 20 s per image. To visualise the center of the sample cell a cross made out of cadmium is screwed to the sample stick.

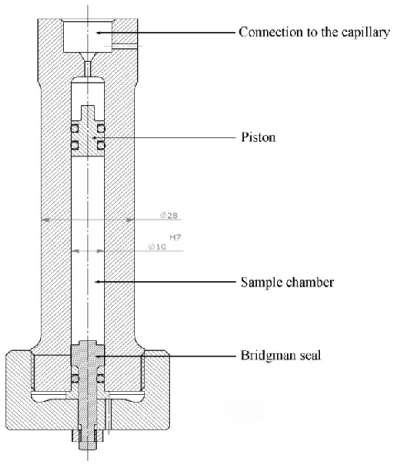

Figure 4.4: Schematic design of the high pressure cell. The cell can be filled and emptied via the bottom. To reduce the sample volume, an aluminum insert can be used.

Chapter 5

Model lipids

5.1 Historical overview

Biological membranes are complex systems containing not only different kinds of lipids, they incorporate also membrane proteins, membrane active molecules such as, e.g., cholesterol or ethanol etc. The membrane composition varies not only from organism to organism but it differs also for different organelles. A myelin membrane contains about 80% lipids and 20% proteins, whereas the mitochondrial inner membranes contain about 75% proteins and only 25% lipids.

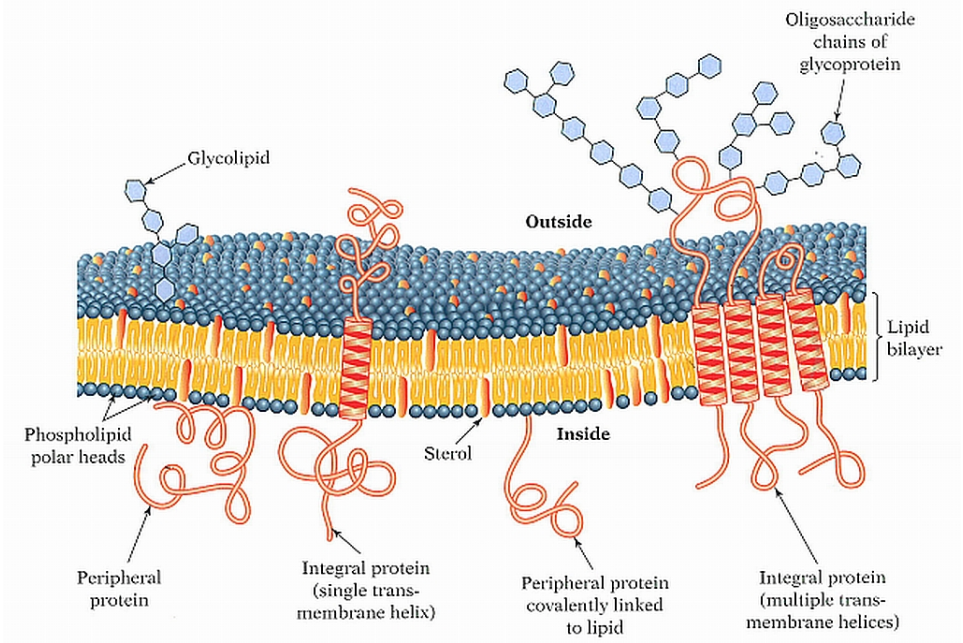

Figure 5.1: Schematic composition of a membrane containing lipids, proteins and other molecules [43].

The exact knowledge about membrane structure is not very old and it turned out that it was not an easy task to come to this picture. The first time an existence of a plasma membrane was proposed was in 1877 by Pfeffer [44]. The bilayered structure was introduced by Gorter and Gredel in 1925 [45]. But it took until 1972 to come to a more complete picture when Singer and Nicolson [46] suggested in their fluid-mosaic model that proteins are not simply bound to the membrane, but that they can also be incorporated in it. To account for mismatches within the lipid bilayer caused by lipids with different chain length or by lipid protein interactions, Mouritsen and Bloom proposed a modified version of the Singer model, the mattress model [47]. Here interfacial tension can lead to a deformation of the bilayer and to the aggregation of lipids of a similar kind. A schematic assembly of a membrane and its components is shown in figure 5.1.
Even if the investigation of membrane dynamics using neutron scattering started about 15 years ago [36, 48–50], there is still discussion about the types of motion observed [51]. In recent years not only local dynamics [36, 51] using time-of-flight instruments, but also collective dynamics [25, 52] using three-axis and spin-echo spectrometers have been studied.

5.2 Model lipid DMPC and its phase behaviour

Phospholipids are amphiphilic molecules, which means they posses both hydrophobic and hydrophilic parts. In the case of phospholipids the polar head group is the hydrophilic part and the acyl chains are hydrophobic. Therefore they tend to form aggregates when inserted into water with the trend to form larger aggregates at higher lipid concentrations. The first crystal structure of DMPC, the lipid used in this work, was published in 1979 [53].

As a function of shape, temperature and concentration they can form different kinds of phases, such as micelles, lamellar, cubic or hexagonal phases. In the following description we will concentrate on the lamellar phases. Depending on the sample preparation they were employed as oriented bilayers (when prepared on a solid support 5.3.1) or vesicles, which can be subdivided into unilamellar (formed out of only one bilayer) or multilamellar (made out of several bilayers). Below, the different phases are described in more detail and displayed in figure 5.2. Phase transitions can be determined e.g. by calorimetric measurements, the corresponding data for DMPC are shown in figure 5.5.

- $L_{\beta'}$ phase: In this so called 'gel' phase the lipid chains are ordered in the all-trans configuration. The prime indicates that the alkyl chains are tilted with respect to the bilayer normal, in the case of DMPC an angle of about 30° is observed. The high degree of chain order leads to

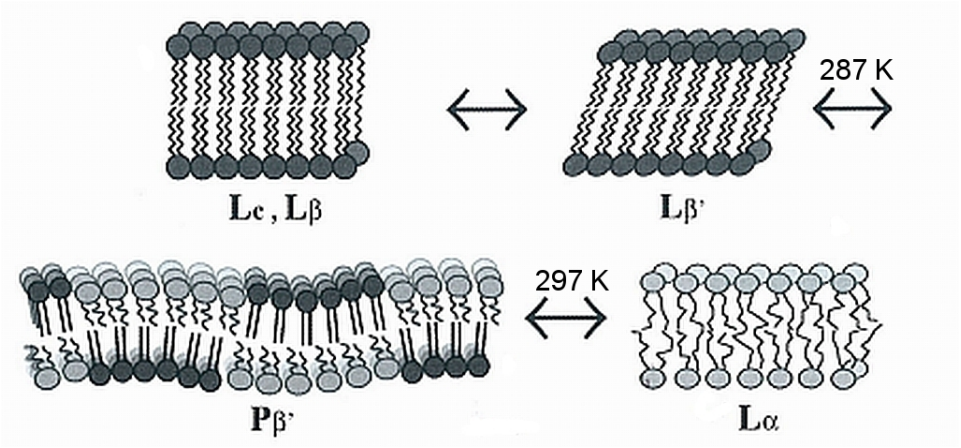

Figure 5.2: Schematic representation of the different phases that occur as a function of temperature [54]. The higher the temperature, the higher the chain disorder. Transition temperatures are given for protonated DMPC.

a quasi-crystalline order. This order can be recognised in the neutron data by the appearance of a coherent peak. This quasi-Bragg peak at Q=1.48 $Å^{-1}$ corresponds to the inter-chain distance of about 4.25 Å in real space.

- $P_{\beta'}$ phase: the 'ripple' phase. This phase is formed prior to the main phase transition. It exhibits one dimensional ripples on the membrane surface.

- L_α phase: the liquid-disordered or fluid phase. The long-range in-plane order is lost. Due to the disorder of the lipid chains, the quasi-Bragg peak caused by the chain ordering vanishes. This effect can be used for determination of the temperature of the main phase transition T_M.

Generally speaking the degree of chain ordering gets lower as you go through the different phases starting with the low temperature $L_{\beta'}$ phase. Figure 5.3 shows the phase behaviour of DMPC which was used in this study as a function of temperature and hydration.
The transition temperature shifts with increasing chain length to higher temperatures and can be approximated linearly. Table 5.1 gives values for T_M for some common lipids. The lower T_M for the deuterated lipids was associated by Guard-Friar and coworkers to a lower degree of ordering in the gel phase of the deuterated hydrocarbon chains [56].

During this work two kinds of DMPC were used for experiments: fully protonated DPMC and chain deuterated DMPC-d54 (see figure 5.4). Both coherent and incoherent scattering lengths for the two species are found

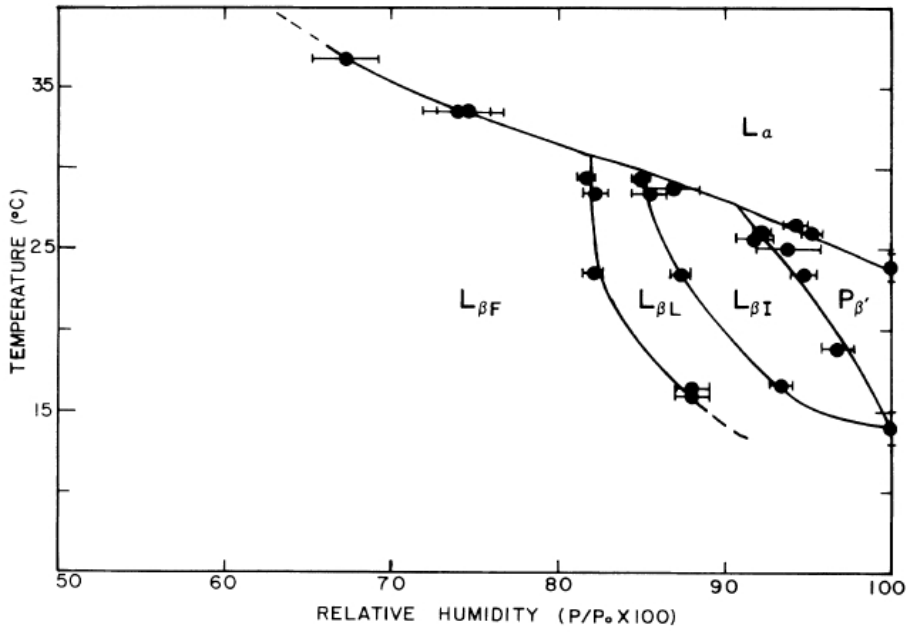

Figure 5.3: Phase diagram of DMPC as a function of temperature and relative humidity [55].

Lipid	chain length	T_M [K]
DMPC	14:0	296.75
DMPC-d54	14:0	293.30
DPPC	16:0	314.45
DPPC-d62	16:0	310.27
DSPC	18:0	327.85
DSPC-d70	18:0	323.67

Table 5.1: Transition temperatures T_M of some common lipids. Values for the protonated lipids are adapted from [54]. The chain deuterated lipids are marked as "-d" where the number indicates the total number of deuterium atoms present in both alkyl chains. T_M for the chain deuterated lipids are taken from [56].
Note that there is a shift of 3-5 K for the deuterated lipids. This shift was associated by Guard-Friar et al. [56] with a less well ordering of the chains in the gel phase in the case of chain deuterated lipids compared to their nondeuterated counterparts.

in table 5.2. The experiments done with DMPC-d54 are described in the chapters 6 and 7, fully protonated DMPC was used for the high pressure studies presented in chapter 8.

	σ_{coh} [barn]	σ_{inc} [barn]
DMPC	373.97	5779.98
DMPC (tails) ($H_{54}C_{26}$)	239.34	4315.17
DMPC (head group) ($C_{10}H_{18}NO_8P$)	135.32	1445.38
DMPC-d54 (tails) ($D_{54}C_{26}$)	446.29	110.73
DMPC-d54 total	581.61	1556.11

Table 5.2: Scattering lengths σ for fully protonated DMPC and chain deuterated DMPC-d54. The head group comprises the choline and phosphate groups as well as the glycerol backbone. The chain includes the CD_2 and CD_3 groups.

5.3 Sample preparation

5.3.1 Oriented samples

The chain deuterated lipids were purchased from Avanti Polar Lipids (Alabaster, AL., USA) and used without any further purification. The DMPC powder was dissolved in a 3:1 chloroform-trifluoroethanol (TFE) mixture [59]. This solution was kept at $-20\,^{\circ}C$ overnight and then sprayed onto cleaned Si-wafers. The wafers were purchased from Siltronix, Archamps, France. Its specifications are listed in table 5.4. Each Si-wafer was cut to a size of about 30 mm x 40 mm to fit perfectly the dimensions of the IN13 sample holders. The sample holders are made out of aluminium and were coated with 0.5 µm gold and 3 µm nickel to avoid chemical interacting between the holder and the sample. About 30 mg of lipid was deposited on a single wafer. After the preparation the wafers were dried for two days in a desiccator.

The samples were rehydrated from pure D_2O or saturated salt solutions at 40 °C. The corresponding relative humidities can be found in table 5.3. Each sample was made out of six such wafers, to achieve a sample amount of about 200 mg per sample. In order to reduce contact with the sample holder to a minimum, the wafers are inserted into the holder in a way that

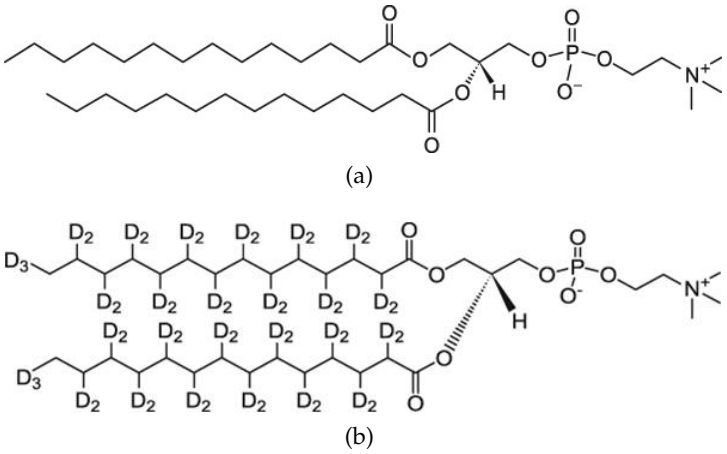

Figure 5.4: Schematic structure of the both types of DMPC employed in this work. Fully protonated DMPC is shown in figure 5.4a, chain deuterated DMPC-d54 in figure 5.4b, respectively. Both pictures are taken from [57].

salt	relative humidity [%]	max. dissolved salt [g/100 g H_2O]
K_2SO_4	96	14.8
KCl	82	40.3
NaCl	75	36.4

Table 5.3: Salts used for rehydration. All values are given for a temperature of 40 °C.

the sprayed sides face each other. After closing the sample holders, the weight of both samples was monitored. No mass loss was observed after the experiments.

5.3.2 DMPC in solution for the high pressure experiments

When applying high pressure to the membranes, oriented sample can no longer be used, simply because the silicon wafers will not support the high pressure and break. Therefore the samples for the high pressure investigation of the dynamics of DMPC cannot be prepared on silicon wafers but have to be in solution.
For the high pressure experiments completely protonated DMPC purchased at Lipoid (Ludwigshafen, Germany), was used. To avoid water inclusions in vesicles formed during the preparation, DMPC powder was hydrated from D_2O vapor pressure at 40 °C for two days. To ensure a fully hydrated sample, additional heavy water was added when filling the sample holder

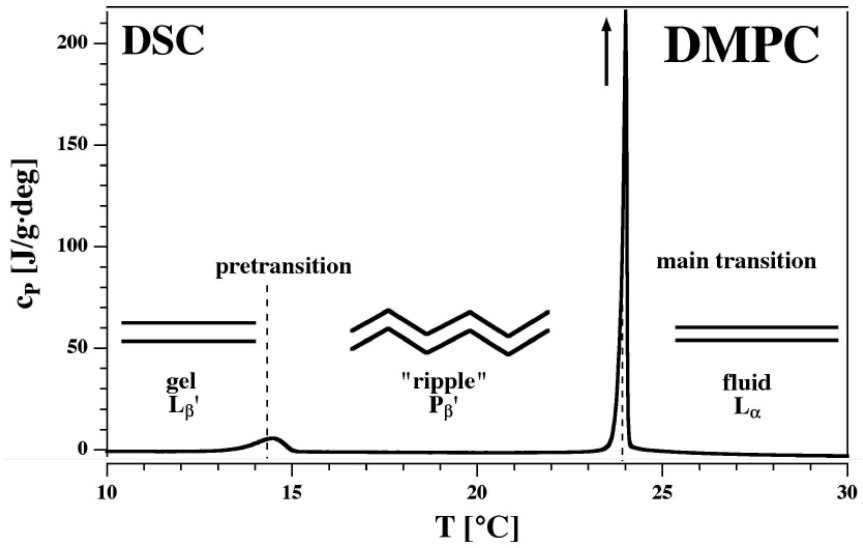

Figure 5.5: Calorimetric melting profile of DMPC [58]. Here, the heat capacity Δc_p as a function of temperature is shown. It increases slightly around 287 K at the pretransition from the gel phase to the ripple phase. Around 297 K Δc_p shows a drastic and sharp increase due to the main phase transition from the ripple to the liquid-disordered phase.

Diameter	3 inch
Orientation	<111>
Thickness	(380 ± 25) µm
Doping	N-Phos
Resistivity	$> 10\,\Omega$
Surface	polished one side

Table 5.4: Characteristics of Si-wafer.

for the high pressure experiments.

Chapter 6

Elastic measurements

Native biological systems are always found in aqueous environments. Therefore, it is not surprising that dynamics of such systems are influenced by the hydration level, as it has been confirmed by several neutron scattering studies [6, 60–64] and molecular dynamics (MD) simulations [65–68]. A dynamical transition for proteins appears around 200 K. This marks the crossover from a regime in which only vibrational motions of the atoms, around their stationary position, are observed to a regime where anharmonic motions emerge. Below a certain level of hydration (typically 0.2-0.4 g water/g protein) corresponding to one complete water layer bound to the protein surface, the protein shows no dynamical transition and as a consequence does not become active [6].
In the case of membranes a transition due to the structural transition into the liquid-crystalline L_α phase is observed (cf chapter 5). Depending on the chain length and the degree of hydration of the lipid it occurs around room temperature or even higher temperatures [54]. In contrast to proteins where the hydration of individual amino acids allows local motions of the protein, in phospholipid bilayers only the hydration of the hydrophilic head group triggers the dynamic response of the hydration shielded hydrophobic alkyl chains, due to the increased surface available with increased hydration. For membranes a shift of the main phase transition to higher temperatures with decreasing water content is already known for quite some time [55]. In recent years numerous neutron scattering studies of membrane dynamics focused on highly hydrated samples [36, 48, 69, 70], but only a few of these studies took hydration effects explicitly into consideration, e.g., König et al. [48].
In the following chapters the investigation of the influence of hydration on the dynamics of model membranes by elastic incoherent (EINS) (chapter 6) and quasi-elastic (QENS) (chapter 7) neutron scattering is discussed in more detail. Dynamics in such lipid systems span a large range in time and space and have been investigated not only by neutron scattering [25, 36,

48, 52, 69], but also by nuclear magnetic resonance (NMR) [50, 71], inelastic x-ray scattering [72], dielectric spectroscopy [73], differential scanning calorimetry (DSC) [74], dynamic light scattering (DLS) [75], single particle tracking [76] and other methods. In addition to the experimental results there are also simulations dealing with membrane dynamics available [65–68]. To mimic membrane behaviour in biological systems the fully hydrated state is the one of interest because this resembles physiological conditions. On the other hand also the dried state is of interest, e.g. for food science [37]. Therefore an exact knowledge of the hydration and the resulting dynamics of the investigated sample are crucial for the understanding of the system.

6.1 Sample characterisation at D16

In this section the characterisation of the DMPC-d54 multilayer samples at the small momentum transfer diffractometer D16 (see figure 6.1) for the elastic measurements performed on IN13 is described.
D16 is situated, like IN16, on the H53 guide of the ILL. Via a focusing pyrolytic graphite monochromator two wavelengths (4.7 Å or 5.6 Å) can be selected. A beryllium filter is used to eliminate higher orders and a set of slits to adapt the beam size to the individual sample size is available. The diffracted neutrons are recorded with a two dimensional area detector.
As mentioned in chapter 3, structural information about the sample can be extracted from diffraction data. From the scattering angle θ, the wave vector transfer Q can be calculated following eq. 6.1 (λ being the incident wavelength and θ the scattering angle).

$$Q = \frac{4\pi}{\lambda}\sin(\theta). \tag{6.1}$$

Combining equation 6.1 with Bragg's law (eq. 3.13) leads to:

$$d = \frac{2\pi}{Q}. \tag{6.2}$$

where d stands for the atomic distance corresponding to a given Q-value.

In the case of solid supported membranes, the characteristic repeat distance d of the bilayers and the alignment of the multilayer with respect to each other were checked. The first can be done by scanning the scattering angle θ (θ - 2θ scan). From the positions of the Bragg peaks in reciprocal space the repeat distance can be calculated using equation 6.2. As the repeat distance depends on the hydration, the degree of hydration can be extracted from this value [78].

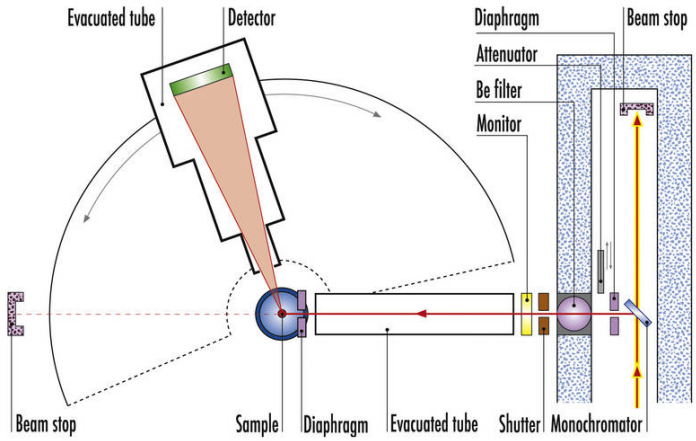

Figure 6.1: Schematic layout of the small momentum transfer diffractometer D16 at ILL [77].

The mosaic spread can be deduced from a rocking scan where the sample is rotated with respect to the incoming beam (ω-axis). From the full width at half maximum (FWHM) of the first order Bragg reflections the mosaic spread of the samples was calculated. The mosaic spread is an indication of the relative orientation of the membranes. A typical value of the mosaic spread for solid supported membranes is in the order of 1° or less.
With this two methods a d-spacing of 62.5 Å and a mosaicity of $(0.22 \pm 0.02)°$ (FWHM) were found for the sample hydrated from pure D_2O. In the course of this work, it will be referred to as the "higher hydrated sample".
The sample hydrated from saturated salt solution (D_2O + NaCl) showed a d-spacing of 54.9 Å and a mosaic spread of $(0.25 \pm 0.02)°$. It will be referred to as "less hydrated sample".
Comparing the measured values with the values obtained by Kucerka et al. using X-ray diffraction [78], the hydration of the first sample corresponds to a fully hydrated sample. The latter one corresponds to the hydration used by Rheinstädter et al. for their investigations of collective membrane dynamics e.g [25,79].
Figures 6.2a and 6.2b show the fits to evaluate the mosaic spread. The θ-2θ scans for the evaluation of the repeat distance are shown in figures 6.3a and 6.3b. The incident wavelength for these measurements was λ = 4.75 Å.

6.2 Elastic measurements at IN13

A detailed description of the instrument can be found in chapter 4. Transmission for both samples was measured and found to be in the order of 90%, so multiple scattering effects were not taken into consideration for the

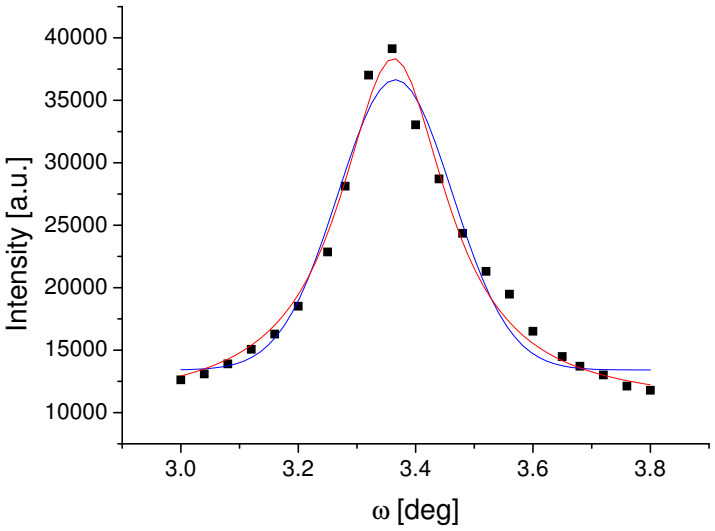

(a) Higher hydrated DMPC-d54 sample. The sample contains about 12 water molecules per lipid.

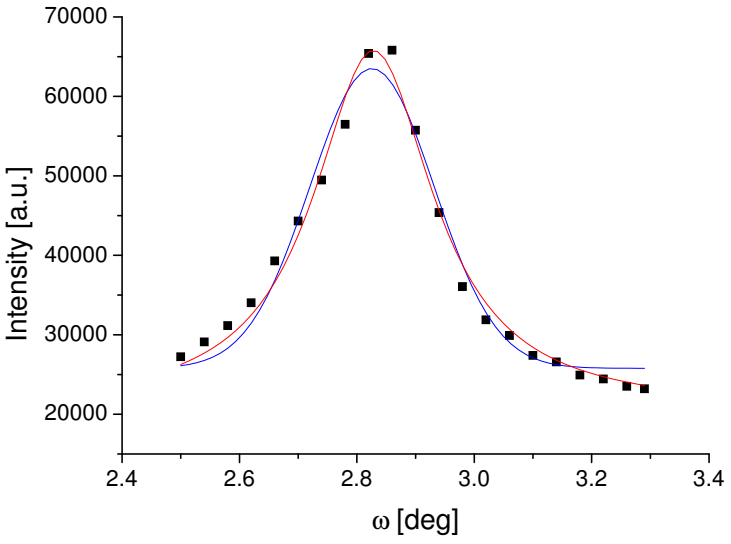

(b) Less hydrated DMPC-d54 sample. The sample contains approximately 9 water molecules per lipid

Figure 6.2: Rocking scans of the fully hydrated sample (6.2a) and the less hydrated sample (6.2b) of DMPC-d54 oriented on silicon wafers, respectively. In red Lorentzians fits to the data are shown, in blue Gaussian fits. For the evaluation of the repeat distance and the mosaic spread, the values obtained with the Lorentzian fit curve have been used.

data treatment. For both samples fixed energy window (FEW) scans were recorded in the temperature range between 250 K and 310 K in steps of 5 K to cover both the phase transition from the lamellar gel to the fluid phase at 295 K and also the transition from the gel to the crystalline phase around 285 K. Special care was taken for the sample alignment so that the scattering vector $\vec{Q}$ at the lipid peak maximum lies in the plane of the membrane bilayers for the parallel orientation. Using equation 6.1 the corresponding angles of 75° and 165° with respect to the incoming beam were calculated for the parallel and perpendicular orientation of the scattering vector towards the membrane surface, respectively.
Strictly speaking the terms "parallel" and "perpendicular" are only true for these particular values, nevertheless we are using these designations in the course of this work to distinguish the orientations where these alignments are best visible. Both orientations $\vec{Q}_{||}$ and $\vec{Q}_{\perp}$ to the membrane surface were measured, but we focused on the parallel orientation ($2\theta = 75°$) in order to investigate the in plane diffusion. Three hours per temperature were measured to favor good data statistic collection for this orientation. For the perpendicular orientation the acquisition time varied between 45 minutes and one hour (at higher temperatures in particular). For data correction purposes an empty cell, a cell with six cleaned wafers and for normalization a 2 mm Vanadium sample were measured. The data evaluation was carried out using the LAMP software available at ILL [80].
Normalised intensities as a function of Q for both orientations are shown in figure 6.4. Here the clear difference between the two orientations is obvious. The quasi-Bragg peak arising from the ordering of the alkyl chains is clearly visible in the parallel setup (figure 6.4a), whereas in the perpendicular orientation (figure 6.4b) ordering out of the plane is probed and therefore the peak around 1.5 Å^{-1} is no longer observed.

6.2.1 Results and discussion

Figure 6.5 shows the normalized summed intensity taken on IN13 (Q-range: $0.19\,\text{Å}^{-1} < Q < 1.67\,\text{Å}^{-1}$) as a function of temperature for both samples. The representation of the data offers a simple and model-free approach to detect transitions as changes in the elastic intensity decay [81]. In the chosen setup, the influence of the coherent scattering coming from the chain ordering is mainly seen in the parallel orientation. Summed intensities are then shown only for the parallel orientation. The phase transition for the fully hydrated sample is found to lie around 294 K which coincides very well with the value of 293.30 K found by Guard-Friar et al. [56] by differential scanning microcalorimetry for DMPC-d54. Whereas for the less hydrated sample a transition temperature around 298 K is found.
It is known from e.g. FTIR spectroscopy [82] that dehydration increases the transition temperature. Following the procedure used by Pfeiffer et

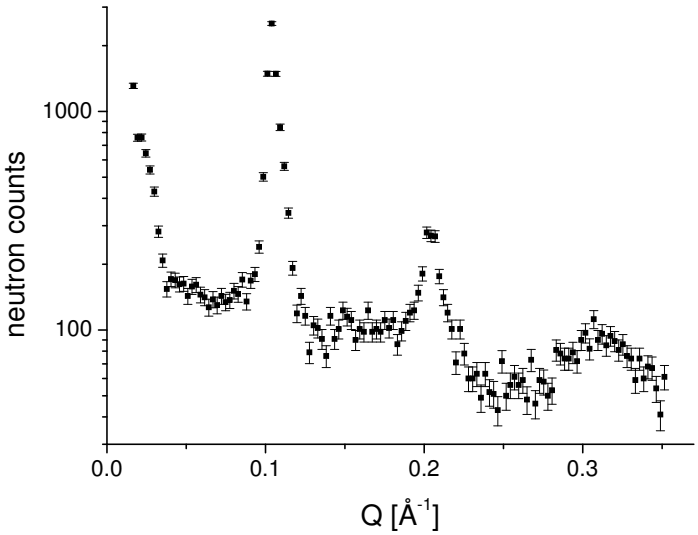

(a) Higher hydrated DMPC-d54 sample.

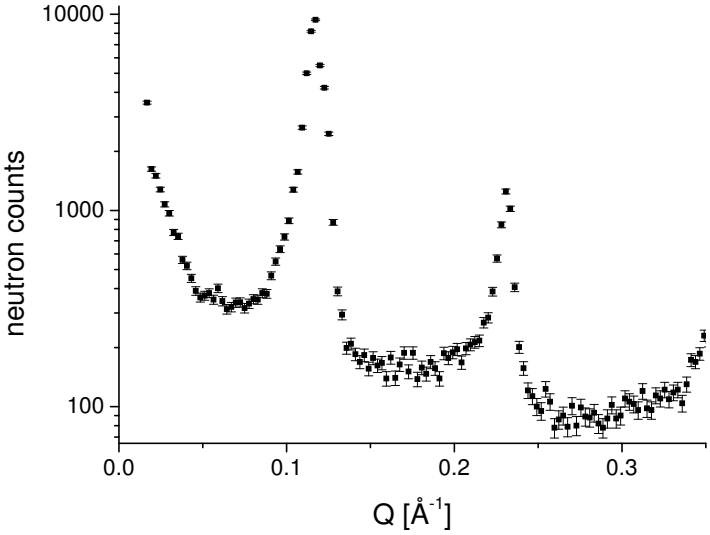

(b) Less hydrated DMPC-d54 sample.

Figure 6.3: θ-2θ scans of the two samples. From the peak position the repeat distance of the bilayers was calculated using equation 6.2.

al. [83] we estimated the water content from the shift of the main phase transition temperature. We can extract the parameter R_W=n_W/n_A where R_W expresses the molar ratio of water (n_W) and amphiphile (n_A) [82, 83]. The calculated R_W for the fully hydrated sample is $R_W \approx 12$ and $R_W \approx 9$ for the less hydrated sample. Pfeiffer et al. find for DMPC multilayers a value of $R_W \approx 12$ for fully hydrated membranes [83]. Therefore the elastic measurements on IN13 provide a solid basis to characterize the system for the quasi-elastic experiment at TOFTOF. The quasi-elastic experiments will be described in more detail in chapter 7.
Due to the coherent scattering arising from the ordering of the lipid chains below the main phase transition and the relatively broad Q resolution of IN13 only three detectors were left to evaluate the mean square displacements (msd) [28], therefore, it was not possible to obtain msd's with reasonable error bars. A detailed comparison between mean square displacements and summed intensities for DMPC can be found elsewhere [84].

6.3 Elastic measurements at IN16

Because it was not possible to extract mean square displacements from the elastic scans on IN13, another set of measurements on the IN16 backscattering spectrometer, where more detectors in the low Q-range and a higher flux are available, was performed. This time two hydration levels that were different from the ones used on IN13 and TOFTOF were used. For the sample rehydration saturated salt solution made out of D_2O + K_2SO_4 and D_2O + KCl, resulting in relative humidities of 96 % and 82 %, respectively (cf table 5.3). As for the previous experiment also in this case the level of hydration, the mosaicity of the 1D lamellar order and the evolution of the repeat distance (d-spacing) of the bilayers with temperature were checked by neutron diffraction measurements on the small momentum transfer diffractometer D16 [77]. After heating to 330 K to allow annealing of defects, scans were performed to obtain the repeat distance of the membranes at three different temperatures, namely 330 K, 310 K and 280 K. During the temperature changes data were taken to identify the temperature of the main phase transition. An example of the evolution of the d-spacing with temperature is shown in figure 6.6a.

Elastic temperature scans in the range of 280-330 K were performed on the cold neutron backscattering spectrometer IN16 at ILL at an energy resolution of $\Delta E = 0.9$ μeV (full width half maximum) and an accessible Q-range of 0.19-1.93 $Å^{-1}$ [20]. The investigated temperature range covers both the main phase transition from the P_β ripple to the liquid-crystalline L_α phase which occurs around 297 K for DMPC at full hydration and also the pretransition from the L_β gel phase to the P_β ripple phase about 10 degrees below the main phase transition. Special care was taken on the orienta-

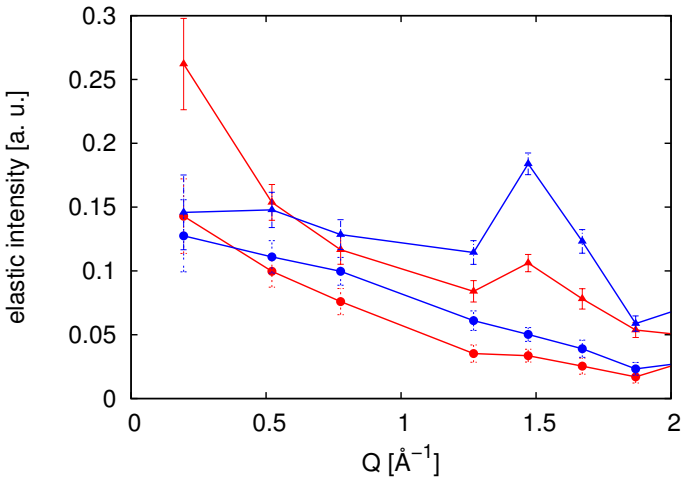

(a) Parallel orientation $\vec{Q}_{||}$. Triangles represent data taken in the $L_{\beta'}$ at 280 K, circle data in the L_α phase at 300 K. The higher hydrated sample is drawn in red, the less hydrated in blue.

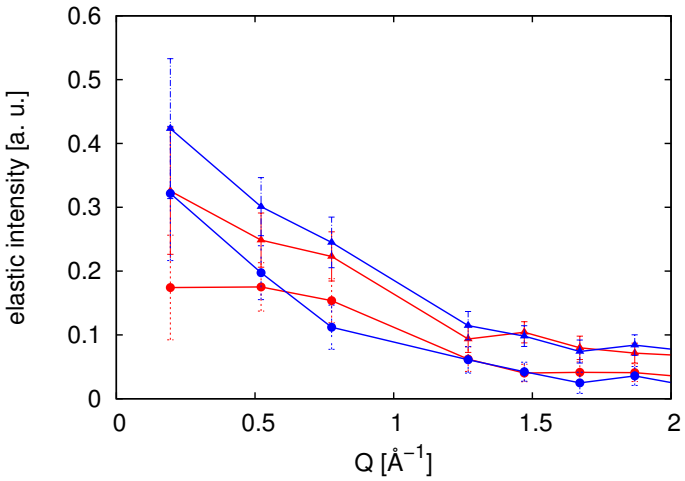

(b) Perpendicular orientation $\vec{Q}_\perp$. Again triangles show data recorded in the $L_{\beta'}$ at 280 K. The data in the L_α phase are given for the higher hydrated sample at 300 K, for the less hydrated sample at 305 K. The higher hydrated sample is drawn in red, the less hydrated in blue.

Figure 6.4: Normalised elastic intensities for both DMPC-d54 samples under investigation in the parallel (6.4a) and perpendicular (6.4b) orientation.

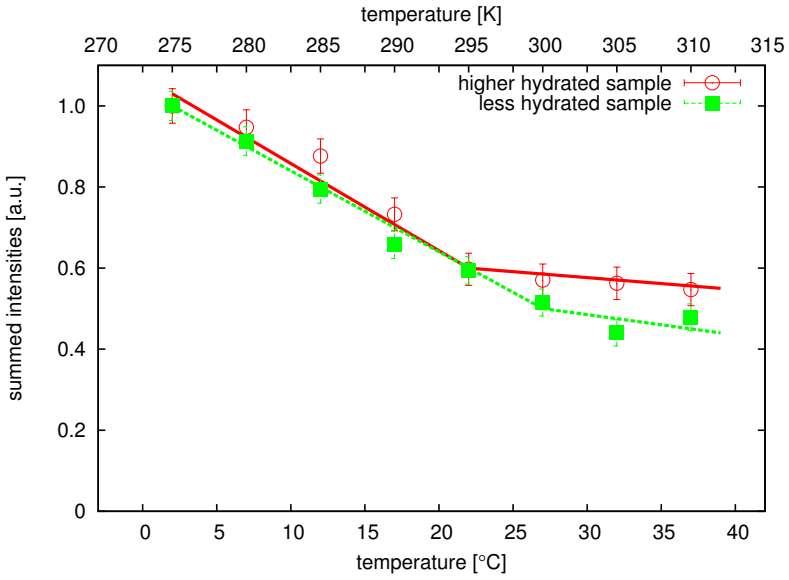

Figure 6.5: Summed intensities for both samples DMPC-d54 in the parallel orientation measured on IN13. Used Q-range: $0.19\,\text{Å}^{-1} < Q < 1.67\,\text{Å}^{-1}$.

tion of the sample to probe motions around the chain correlation peak at Q=1.48 Å^{-1} parallel and perpendicular to the membrane surface. Via the relation 6.1 the angle of the sample with respect to the incoming beam was calculated to be 135° for the orientation parallel to the membrane surface and 45° for the perpendicular orientation, respectively. From the obtained data an empty cell was subtracted and the data were normalised by the scattering of a 1mm Vanadium sample.
Figure 6.7 (using the left y-axis) shows the summed elastic intensities measured for the parallel orientation at 135° with respect to the incoming beam for the two samples on IN16. At the temperature of the main phase transition a drastic decrease in the elastic intensity occurs. The phase transition temperature moves to higher temperatures for the sample with lower water content.
In order to compare the results obtained from the mean square displacement (using the right y-axis in figure 6.7) with the summed elastic intensities, the intensities shown in figure 6.7 (using the left y-axis) were summed over the same Q-range ($0.43\,\text{Å}^{-1} \leq Q \leq 1.16\,\text{Å}^{-1}$) which was used in the evaluation of the msd's. The effect is stronger for the summed intensities due to adding up the signals from all detectors in the used Q-range. From hydration dependent studies of e.g. bacteriorhodopsin [55] it is known that with increasing hydration the msd's show a steeper slope only at high rel-

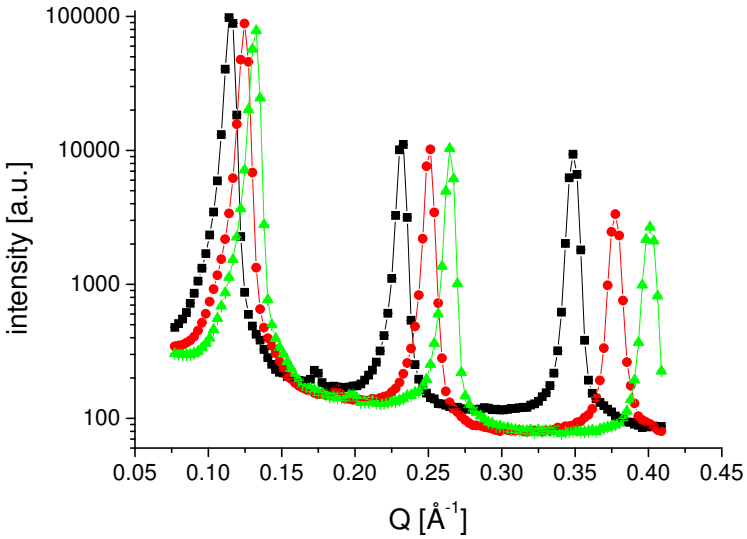

(a) DMPC-d54 sample hydrated from D_2O + K_2SO_4.

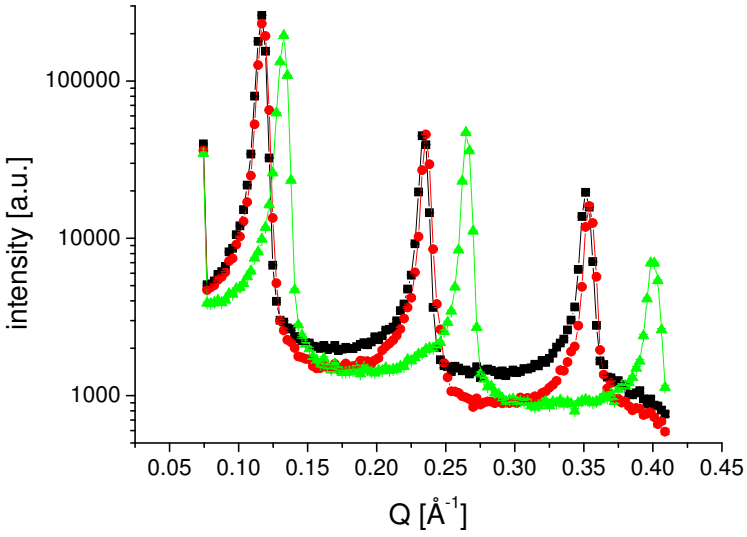

(b) DMPC-d54 sample hydrated from D_2O + KCl.

Figure 6.6: θ-2θ data taken on D16 at ILL. Data for both samples are shown for three different temperatures: 280K (black), 310K (red) and 330K (green). The less hydrated sample (6.6b) shows no change of the lamellar d-spacing below 310 K, whereas a continuous change is observed for the higher hydrated sample 6.6a.

ative humidities in contrast to proteins where a steady rice of the msd is observed [28].

6.3.1 Results and discussion

From the shift of the main phase transition temperature to higher temperatures with decreasing water content (see section 1 and figure 1 in [5]), it is possible to evaluate the water content between the phospholipid surfaces. We can extract the parameter R_W=n_W/n_A where R_W expresses the molar ratio of water (n_W) and amphiphile (n_A) [82, 83]. The calculated R_W for the higher hydrated sample is $R_W \approx 6$ (transition temperature: 305 K) and $R_W \approx 4$ for the less hydrated sample (transition temperature: 310 K). A values of $R_W \approx 12$ was found by Pfeiffer et al. for DMPC multilayers for a fully hydrated sample [83].
To characterise the local dynamics from the elastic neutron scattering intensity, the so called atomic mean square displacements (msd) $<u^2>$ were calculated. The elastic scattering function S(Q, ω=0) can be approximated by $S(Q, \omega=0) \approx \exp(-<u^2>Q^2/3)$, as explained in section 3.6.1. From the slope of a linear fit to the logarithm of the normalised data as a function of Q^2 the $<u^2>$ were extracted. Below the temperature of the main phase transition, coherent scattering arising from the ordering of the alkyl chain, gives rise to the so called "chain correlation peak" around a characteristic Q value of 1.48 $Å^{-1}$. Therefore the fit range was limited to 0.18-1.33 $Å^{-2}$ in our data analysis. As shown in figure 6.7 (using the right y-axis) the $<u^2>$ show transitions at 305 K and 310 K for the higher and lower hydrated sample, respectively. At first sight the evaluated mean square displacements are very large above temperature of the main phase transition, but $<u^2>$ in the same order of magnitude have been observed in a previous study which aimed to investigate the influence of the myelin basic protein (MBP) on the dynamics of model membranes (DMPA in this study) [85].
A recently published molecular-dynamics simulation performed on fully hydrated DMPC bilayers in the L_α phase (at 303 K) also shows very large $<u^2>$ at this temperature, even larger then the two partially hydrated samples used in our study [86]. Hence we attribute the difference in the values of the mean square displacements to the different hydrations of the samples, ranging from the highest $<u^2>$-value for the simulation ($\approx 8\,Å^2$ for the centre of mass) to the sample with the lowest hydration of $R_W \approx 4$ ($\approx 1.5\,Å^2$). The authors differentiate three different diffusion regimes in time: 1. a ballistic region where $<u^2> \approx t^2$; 2. a subdiffusive domain where $<u^2> \approx t^\beta$ with $\beta < 1$ and 3. a domain of Fickian diffusion with $<u^2> \approx t$. According to this simulation, the time window of IN16 of about 700 picoseconds probes length scales in the subdiffusive regime. A detailed analysis of quasi-elastic data taken on IN13 in both the L_β gel and liquid-crystalline L_α phase is still in progress [87].

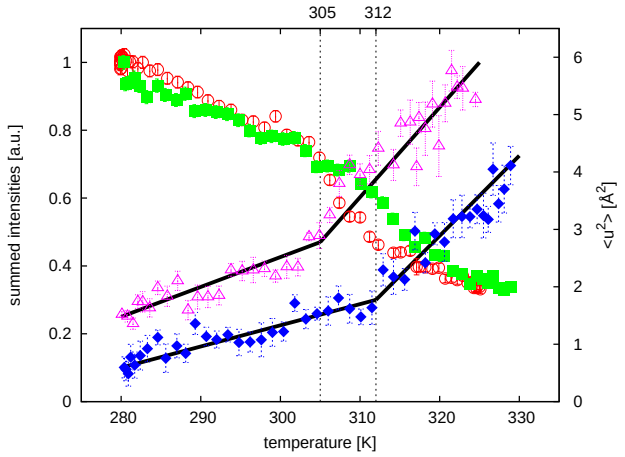

Figure 6.7: Summed elastic intensity (Q-range: 0.43-1.16 $Å^{-1}$) measured at 135° (left y-scale, filled squares $R_W \approx 4$, empty circles: $R_W \approx 6$) and mean square displacements $\langle u^2 \rangle$ (right y-scale, filled diamonds $R_W \approx 4$, empty triangles: $R_W \approx 6$). Drawn lines are guides to the eyes to follow the evolution of the mean square displacements. Data taken on the cold neutron spectrometer IN16 at ILL (energy resolution: 0.9 µeV). Intensities are normalised to the lowest temperature.

Rheinstädter et al. [79] analyzed the elastic intensity at various Q-values of DMPC to map out the transition of the different molecular components from immobile to mobile as a function of temperature. The effect of hydration on the membrane dynamics was neglected in their analysis. Our study reveals the strong influence hydration has on the membrane systems, not only on the structure but also on the dynamics. Similar to hydrated protein powders also phospholipids show a dynamic transition in the mean square displacements $\langle u^2 \rangle$ and a shift of the temperature of the main phase transition depending on their hydration. The transition for proteins occurs around 200 K and is often called "dynamical transition" [9]. In the case of membranes this transition is due to the structural transition into the liquid-crystalline L_α phase at 297 K. In contrast to proteins were the individual amino acid is hydrated to allow local motions of the proteins in phospholipid bilayers only the hydration of the hydrophilic head group of the phospholipid triggers the dynamic response of the hydration shielded hydrophobic alkyl chains. In conclusion special care should be taken for the hydration control to avoid a mixing of effects, which could be partly due to the hydration state of the sample.

Chapter 7

Quasi-elastic measurements

7.1 Sample characterisation at TREFF

The same two samples used for the elastic measurements in May 2008 at IN13 (see chapter 6) were used for the measurements at the time-of-flight instrument TOFTOF. In the time between the two measurements the samples were kept in a cold room at 8 °C. To see if the two samples kept their good alignment, diffraction data was taken at the TREFF diffractometer at FRM II (see figure 7.1). The higher hydrated sample showed a lamellar d-spacing of 62.96 Å, which reproduced the values calculated from the earlier measurements at D16 (see section 6.1). The mosaicity of this sample was 0.1°. With 52.25 Å the d-spacing of the less hydrated sample was 2.6 Å smaller then during the elastic measurements on IN13. The mosaicity for this sample was also 0.1° (This value of 52.25 Å corresponds to the value of 53 Å of the sample used by Rheinstädter et al. [25]). Fits for the diffraction data is shown in figures 7.2a and 7.2b.

7.2 The measurement

Quasi-elastic neutron scattering experiments (QENS) have been performed on the same samples at the time-of-flight spectrometer TOFTOF [23] at the Munich research reactor FRM II in Garching, Germany. Other results obtained on of the spectrometer in the field of membrane biophysics can be found in e.g. Busch et al. [51]. The incident wavelength was set to λ=6 Å, the chopper speed to 12000 rpm, resulting in an energy resolution of the elastic line of 56 µeV (FWHM of the elastic line). The setup was chosen in order to compare the results with previous measurements obtained by another group [36]. Both samples were measured in a temperature range from 278 K to 298 K to cover both phase transitions, the pre-transition from the L_β gel phase to the P_β ripple phase at 285 K as well as the main phase transition from the P_β phase to the L_α liquid phase at 295 K [55]. Spectra

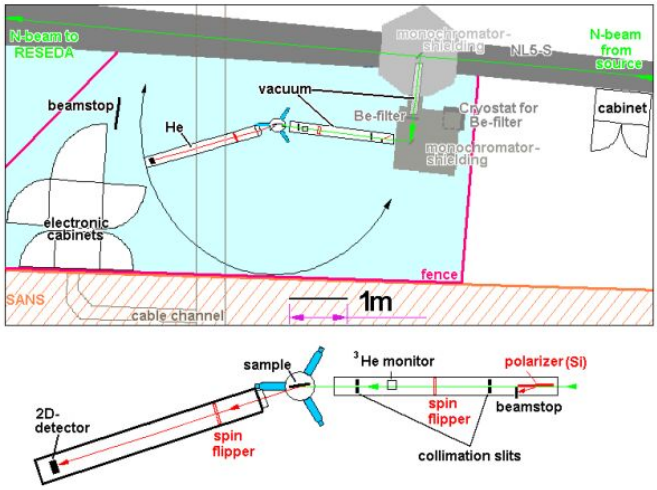

Figure 7.1: Setup of the diffractometer TREFF at FRM II.

were taken every 5 K. The measuring time per temperature was five hours. All samples, including a 1.5 mm vanadium sample and a sample holder with six empty wafers and pure D_2O needed for corrections, were measured in one orientation (at 45° with respect to the incident beam), only. The D_2O hardly contributes to the scattering signal of the empty cell at this wavelength as it was shown by Busch et al. [51], therefore the empty cell scattering can be subtracted from the sample signal. In the case of 2θ = 45°, $\vec{Q}$ is mainly parallel to the membrane surface at the alkyl chain correlation peak position (Q=1.48 Å^{-1}) for low energy transfers. Earlier QENS experiments on 1,2-dipalmitoyl-*sn*-glycero-3-phosphocholine (DPPC) [36] observed no significant differences in the elastic incoherent structure factor (EISF) for $\vec{Q}$ oriented parallel or perpendicular to the membrane surface in this time window. This fact was confirmed by our elastic data, and consequently the QENS data were recorded only for the parallel orientation. From the measured spectra the scattering of the empty can was subtracted, then they were normalized to vanadium and transformed into (Q,E)-space. The data were binned into 15 groups with Q ranging from 0.44 Å^{-1} to 1.56 Å^{-1}. Data reduction was performed with IDA package available onsite [88], data analysis was done using the PAN package from DAVE software [89].

7.3 Results and discussion

A detailed description of the analysis of quasi-elastic neutron scattering data can be found in Bée [24]. For applications in the context of lipid dy-

namics see e.g. Busch et al. [51] and for water dynamics in lipid systems e.g. Swenson et al. [90].
The obtained data are a convolution of the theoretical scattering law $S_{theo}(\vec{Q},\omega)$ and the instrumental resolution $S_{res}(\vec{Q},\omega)$ given by a measured vanadium sample (cf equation 3.27). The theoretical scattering law can be expressed by a delta function for the elastic contribution and a sum of Lorentzians for the quasi-elastic contributions coming from the dynamics of the investigated sample [24]. It is shown in equation 3.25. In our study, an elastic peak and two Lorentzian functions (narrow and broad components) were necessary to reasonably fit the obtained data. In figure 7.3 the fits to the data are shown for two Q values. $S(\vec{Q},\omega)$ can be written as shown in equation 3.25 with n = 2.
Keeping in mind that chain-deuterated lipids were used in our experiments, the narrow and the broad Lorentzians were associated with slow and fast motions of the head groups, respectively. The geometry of the motion can be extracted from the elastic incoherent structure factor (EISF) as defined in equation (7.1)

$$EISF(\vec{Q}) = \frac{A_0(\vec{Q})}{A_0(\vec{Q}) + A_1(\vec{Q}) + A_2(\vec{Q})}. \tag{7.1}$$

For both samples the EISF does not decay to zero for large Q-values, which indicates an immobile fraction in the examined time-space window. Two different models were applied to fit the EISFs. First we used the "diffusion in a sphere" model introduced by Volino and Dianoux [31], where free diffusion in the restricted volume of a sphere is permitted. Bellissent-Funel and co-workers [32] established as an addition to this model an immobile fraction. Here p and $(1-p)$ denote the populations of hydrogen atoms that appear immobile and mobile in the observed space and time window, respectively. The corresponding EISFs are described by equations 3.29 and 3.30.
A modification of the Volino-Dianoux model allows increasing radii for the diffusion volumes of the hydrogen atoms along the head group (see equation (3.33a)). This model was introduced by Carpentier et al. for the study of dicopper tetrapalmitate [35] and is described by equations 3.33a and 3.33b. N stands for the total number of atoms in the chain to which hydrogen atoms are bound (in the case of this study N=3). The index n starts with the carbon atom the closest to the oxygen of the phosphorus group which connects the lipid chains with the head group and ends with the nitrogen of the choline group (see fig. 5.4). R_n gives the radius of the diffusion volume for the corresponding hydrogen atoms. In equation (3.33b) linear increasing radii are assumed. It turned out during the fitting procedure that the choice of N=3 yields physically reasonable results, whereas for values bigger than N=3 the radius for R_1 became negative.

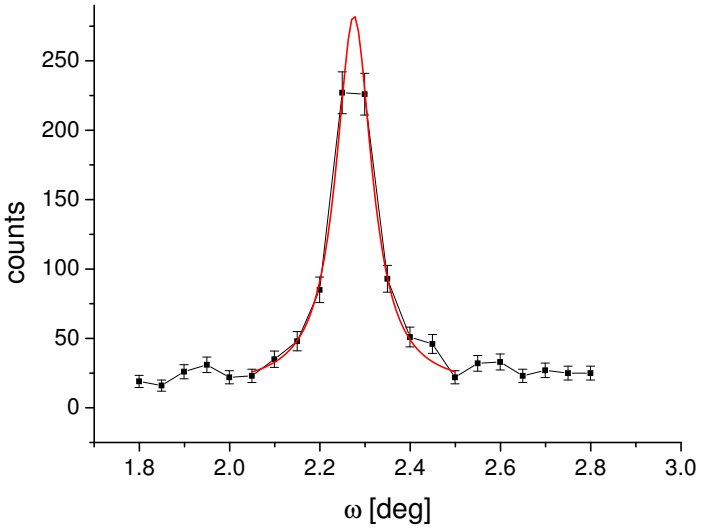

(a) Higher hydrated sample with a repeat distance of 62.96 Å and a mosaic spread of 0.1°.

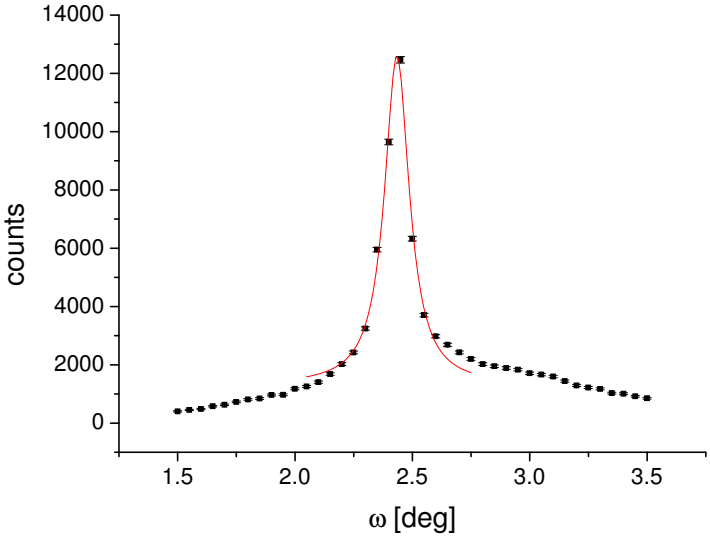

(b) Less hydrated sample with a repeat distance of 52.25 Å and a mosaic spread of 0.1°.

Figure 7.2: Rocking scan of the two DMPC-54 samples measured at TREFF (FRMII). The samples were exactly the same samples used for the experiments on D16 and IN13 and described in chapter 6.2.

Around $1.48\,\text{Å}^{-1}$ the coherent scattering rising from the ordering of the lipid chains, the so called "chain correlation peak", is clearly visible. To exclude its influence on the EISF fits, the fit range was restricted to a range of $0.44\,\text{Å}^{-1} < Q < 1.32\,\text{Å}^{-1}$. Figures 7.4a and 7.4b show the obtained data for two temperatures, one below (278 K) and one above (298 K) the main phase transition for the fully hydrated sample and the less hydrated sample, respectively. Fits corresponding to the diffusion in a sphere model are shown as solid blue lines, the Carpentier model as dashed green lines. In the case of the less hydrated sample the diffusion in a sphere model fits the data sufficiently well within the experimental errors, leading to values of $a = (2.64 \pm 0.10)$ Å and $a = (2.91 \pm 0.06)$ Å for the radii at 278 K and 298 K, respectively. For the higher hydrated sample the simple model of diffusive motion in a sphere is not longer sufficient. Here the Carpentier model gives definitely better results, especially at higher temperatures. In the L_β gel phase at 278 K the fits result in values of $R_{min} = (0.36 \pm 0.04)$ Å for the displacement of the proton bound in the methylene groups near the phosphorus atoms of the lipid and of $R_{max} = (5.05 \pm 0.06)$ Å for the hydrogens of the methyl groups in the choline group. At 298 K in the liquid L_α phase corresponding values of $R_{min} = (1.14 \pm 0.03)$ Å and $R_{max} = (6.42 \pm 0.11)$ Å were obtained. The fact that the EISF is not going to zero for large Q-values is an indication that not all of the protons take part in the movements observed in the chosen time-space window of the experiment, as it has been seen e.g. for protein-membrane complexes [85, 91]. However for a detailed investigation a broader Q-range would be preferable to clearly distinguish trends. In this context we want to emphasize that both employed models have only two fit parameters, namely in the case of the diffusion in a sphere model the radius a and the immobile fraction p, and in the Carpentier model the first radius R_1 and the last radius R_N. We tried also to fit other models to the EISF (with more than two fit parameters) which are often used to analyze methyl group reorientation because of the three head group methyl groups. Namely the threefold jump model [24] and a variant of this model (applied to the methyl reorientation on trimethyloxosulphonium [92]) have also been fitted to the data, but they do not sufficiently well fit the experimental data (not shown).

Our experiments demonstrate nicely the influence of hydration on the mobility of the protons. The difference in the EISF values shows a strong dependence on the level of hydration. For the "diffusion in a sphere" model the percentage of immobile protons can be inferred directly from the fit parameter p (see formula 3.30)), in the case of the Carpentier model different radii for the volume of rotation can be extracted. Thus, for the less hydrated sample the values of the strongly bound protons for 278 K amount to $p_{278\,K} = (61.9 \pm 1.4)$ % and $p_{298\,K} = (42.0 \pm 0.8)$ % for 298 K, respectively.

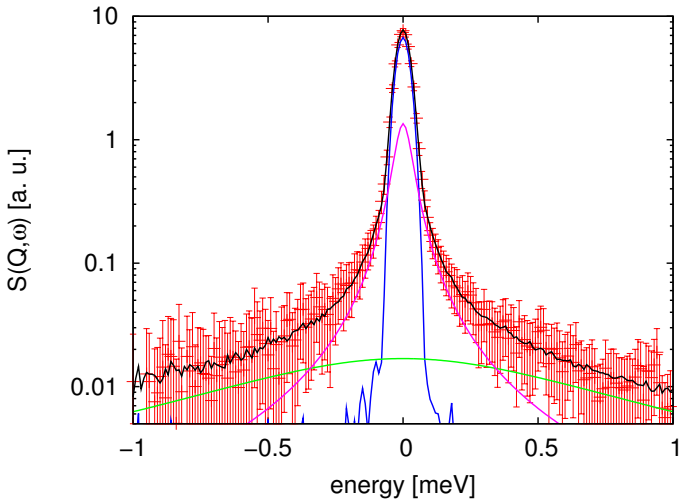

(a) Q = 0.44 Å^{-1}.

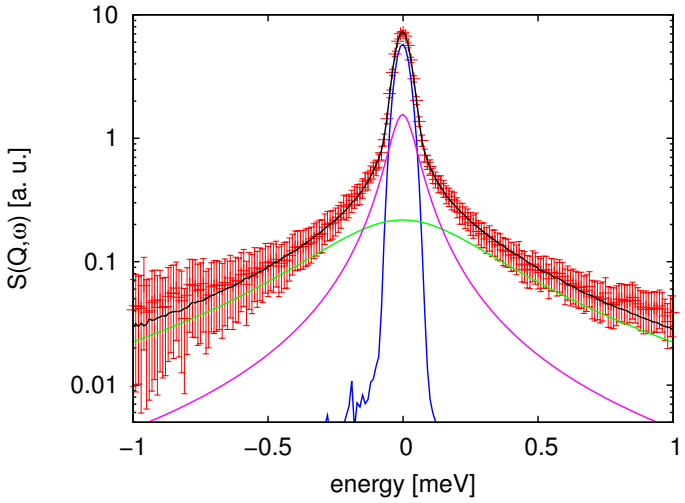

(b) Q = 1.48 Å^{-1}.

Figure 7.3: Plot of S($\vec{Q}$,ω) for the higher hydrated sample ($R_W \approx 12$) at two discrete Q-values at a temperature of 278 K. The resulting fit is shown (black line) as well as the single contributions. As blue line the delta function is drawn, the two Lorentzians are plotted as green and pink lines, respectively.

Even if the "diffusion in a sphere" model cannot be applied to the higher hydrated sample, it is already clear from comparing figures 7.4a and 7.4b that the immobile fraction for the latter sample is lower. With the obtained results, we are able to directly associate different models of motions to a given hydration of the lipids.
The line width of the broad Lorentzian is about a factor of ten larger than the narrow one and it shows Q independent, constant values of Γ for both hydrations (data shown in figure 7.6), indicating some rotational motions. As this contribution is so noisy, it will not be discussed in more detail.

Figures 7.5 and 7.7 show the line widths Γ of the narrower Lorentzian as a function of Q^2.

For small Q-values ($Q \to 0$), the data do not go to zero as for free diffusion, then they increase and asymptotically reach a constant value Γ_∞ for large Q. A constant value at small Q was assigned by Volino and Dianoux [31] to a confinement effect at large radii. A similar behaviour is assumed and has also been observed by Carpentier et al. [35].
However we find a discrete kink only for the lowest measured temperature (red points in figure 7.5 and in more detail shown in figure 7.7). At this temperature the confinement radius R_{conf} obtained from the crossover of the two regimes at a Q^2-value of about $0.55\,\text{Å}^{-2}$ following formula 7.2 was calculated to be (4.2 ± 0.4) Å. This values is in between R_{min} and R_{max} obtained from the EISF fits for the corresponding sample at 278 K and therefore consistent with these values according to

$$Q = \frac{\pi}{R_{conf}}. \tag{7.2}$$

No pronounced plateau is visible for higher temperatures, but a Γ which does not decay to zero for small Q values is still an indication for restricted motion as it has also been observed for proteins [93,94]. As we find several radii for the diffusion volumes in the Carpentier model, a superposition of different kinks leads to the observed behaviour, especially at high temperatures. At larger Q-values, the line width Γ follows the "random jump diffusion" model [95].
As for the EISF also for the line width the influence of the coherent scattering arising from the chain ordering around Q=1.48 Å^{-1} occurs below the main phase transition, whereas for 298 K the predicted plateau is observed. Therefore the data are drawn in the same range as for the EISF.

7.4 Conclusions

In this chapter the hydration dependent behavior of model membrane systems above and below the main phase transition of DMPC with a focus on

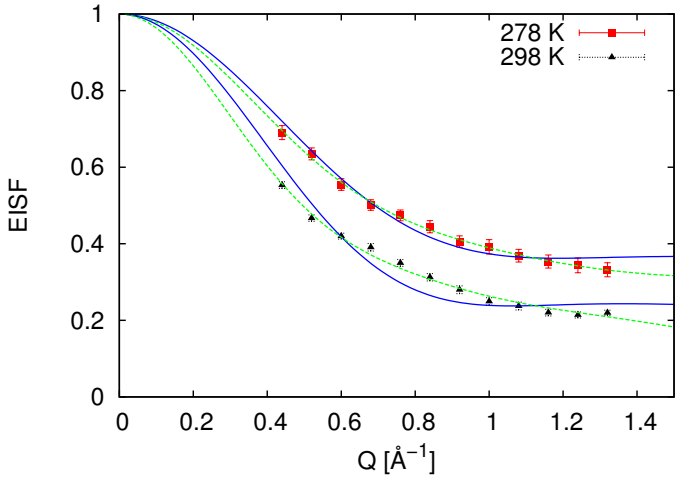

(a) Sample hydrated with 12 water molecules per lipid.

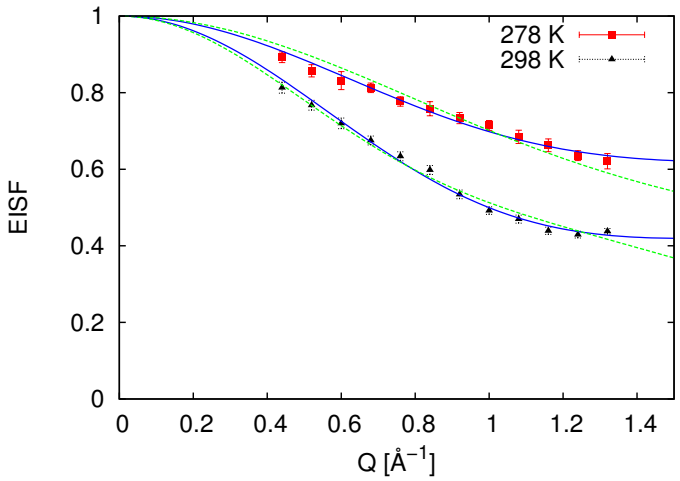

(b) Sample hydrated with 9 water molecules per lipid.

Figure 7.4: Elastic incoherent structure factors for both samples. The lowest, 278 K (red squares), and highest temperature measures 298 K (black triangles) are shown. Data for the higher hydrated DMPC-d54 sample ($R_W \approx 12$) are given in figure 7.4a, the less hydradted samples ($R_W \approx 9$) is shown in figure 7.4b. Fits according to the diffusion in a sphere model (equation 3.30) are shown in blue. The fits corresponding to the Carpentier model (equation 3.33) are shown as dashed green lines.

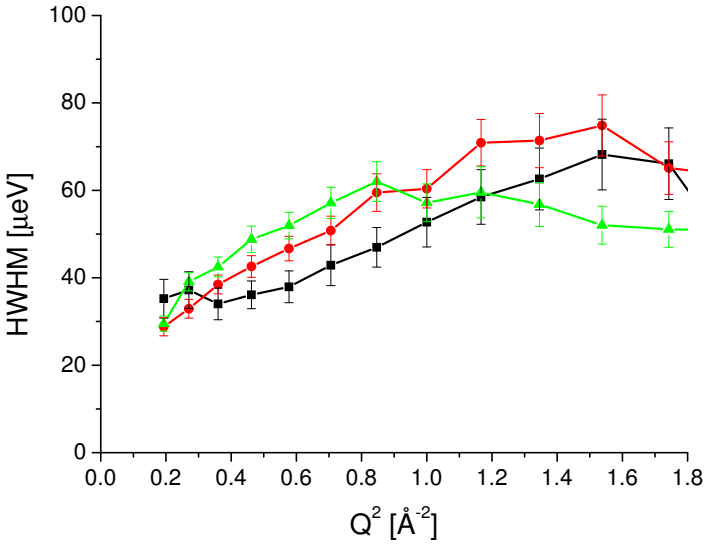

Figure 7.5: Comparison of the line width for the higher hydrated sample for selected temperatures (278 K (black sqaures), 288 K (red circles) and 298 K (green triangles)). For the display of the data, the same Q-range was used as for the EISFs.

the head group motion has been investigated using quasi-elastic neutron scattering. In contrast to existing studies, hydration effects on the dynamics of model membrane systems were explicitly taken into account. Therefore, different models for the motions of the hydrogen atoms in the head group could be associated to different degrees of hydration. The influence of hydration in the observed time and space window is clearly assigned by the different models necessary to fit the obtained elastic incoherent structure factors for the different hydrations and the resulting radii.

7.5 Conclusion en français

Dans ce chapitre, nous avons étudié par diffusion quasi-élastique de neutrons le comportement des systèmes modèles de membranes en fonction de l'hydratation. Nous mesurons au-dessus et en-dessous de la transition de phase principale de DMPC en mettant l'accent sur les mouvements du groupe de tête des lipides. Contrairement aux études existantes, les effets de l'hydratation sur la dynamique des systèmes membranaires modèles ont été explicitement pris en compte. Par conséquent, des modèles différents pour les mouvements des atomes d'hydrogène dans le groupe de tête pouvaient être associés à des degrés différents d'hydratation. Dans la

fenêtre espace-temps définie par l'instrument, l'influence de l'hydratation peut clairement être attribuée aux différents modèles nécessaires à l'affinement des facteurs de structure incohérents élastiques pour des hydratations différentes et les rayons de confinement qui en résultent.

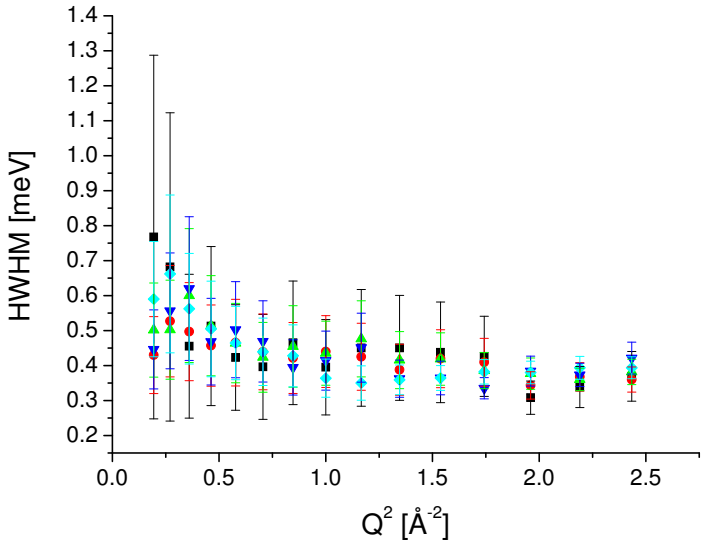

(a) Line width of the broad Lorentzian for the higher hydrated sample.

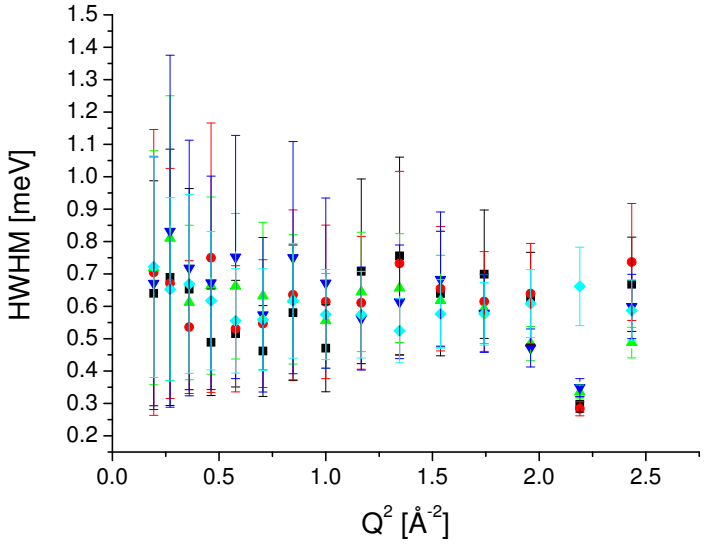

(b) Line width of the broad Lorentzian for the less hydrated sample.

Figure 7.6: Lorentzian width of the broader Lorentzian. All measured temperature are shown: 278 K (black squares), 283 K (red circles), 288 K (green triangles), 293 K (dark blue inverse triangles) and 298 K (light blue diamonds). The line width is Q independent. Note that line width is also constant in the investigated temperature range. A further analysis was not performed, due to the large errors of the obtained values.

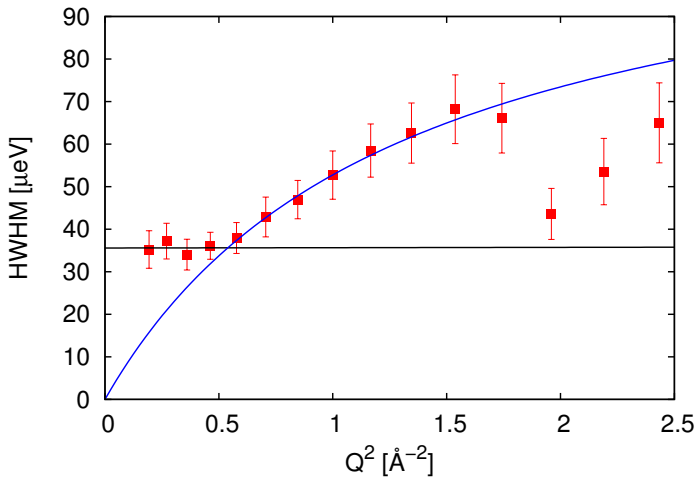

Figure 7.7: Line width of the smaller Lorentzian for the higher hydrated sample at 278 K. A plateau (marked with a black line) indicating a confinement is observed at small Q-values. For high Q-values the data follow a behaviour according to equation 3.32 of the random jump diffusion model (blue curve). Data are fitted up to Q^2-values of 1.5 $Å^{-2}$ to exclude the influence of the coherent scattering arising from the chain ordering in the gel phase around 2 $Å^{-2}$.

Chapter 8

High pressure experiments on DMPC

In order to establish a complete picture of the energy landscape of the biomolecule under investigation, as many thermodynamical variables as possible have to be employed. Besides temperature, which is routinely used in neutron scattering studies, high pressure opens access to a complementary parameter.
A recent development within our research group was the construction and testing of a high pressure cell dedicated to biological samples. For several reasons it was decided to use DMPC as a benchmark in order to test the performance of the cell. About 200 mg are needed for (in-)elastic neutron scattering experiments in order to achieve good counting statistics. Due to constrains resulting from the design of the high pressure cell, an even higher amount of several hundreds of milligram of specimen are needed to fill the cell. Because of their large variety of applications not only in research but also for industrial e.g. pharmaceutical and cosmetic industry, lipids are available in large quantities, therefore they are ideally suited to test the performance of the high pressure cell.
From a scientific point of view the use of lipids is interesting for two reasons. First, there are already SAXS/SANS experiments showing a shift of the temperature of the main phase transition of about 22 K per 1000 bar [96], therefore these experiments can serve as a reference. Secondly, only a few dynamical studies under high pressure of lipid model systems exist, that were performed using NMR [97]. No neutron scattering study dealing with the influence of high pressure on lipid dynamics has been published so far. Thus already from the first experiments, relevant data can be extracted.
After a general introduction, a brief description of the diffraction experiments performed on D16 are described, followed by a series of EINS measurements done on IN13.

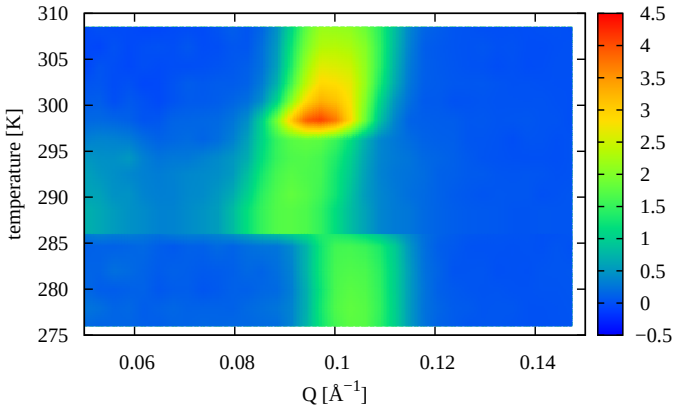

(a) Radial integrated scattering intensity of a θ-2θ scan at atmospheric pressure.

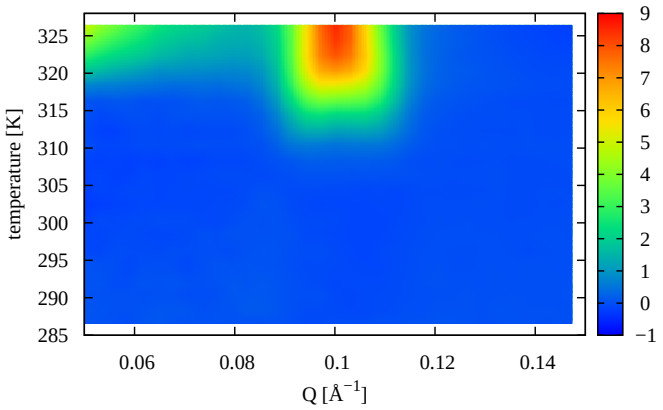

(b) Radial integrated scattering intensity of a θ-2θ scan at 600 bar.

Figure 8.1: Sample characterisation of DMPC in the excess of D_2O at D16. In figure 8.1a the scattered intensity at atmospheric pressure as a function of temperature is shown. The phase transitions are clearly visible as changes of the peak position and hence of the repeat distance of the lipid multilayers. Picture 8.1b shows the scattered intensity at 600 bar.

8.1 Introduction

About 75% of the marine biosphere lies in the deep sea below 1000 m. Therefore, it is exposed to 100 bar or higher pressure [98]. In the Mariana Trench, depth up to 11 000 m, corresponding to 110 bar are reached. In food industry high hydrostatic pressure (HHP) is used as a nonthermal food processing technology, whereby foods are subjected to pressure, generally in the range of 100-600 MPa at or around room temperature [99]. Pressures between 300 and 600 MPa can inactivate yeasts, moulds and most vegetative bacteria including most infectious food-borne pathogens. Thus, pressure is a potential alternative to heat pasteurization as pressure leaves small molecules such as many flavour compounds and vitamins intact [100].
Even if the structure and composition of deep-sea life form is under investigation for quite a while [101], the recently completed "census of marine life" [102] quarried numerous, so far unknown, life forms from all three domains of life [103]. Somero and co-workers [98] found that membranes are very sensitive to pressure effects, in the sense that the main phase transition is shifted to higher temperatures with increasing pressure, therefore pressure has a similar effect on the transition temperature as a decreased hydration. The observed effect is independent of the chain length.
In order to maintain membrane fluidity at physiological temperatures organisms exposed to high pressure change the ratio between saturated and unsaturated lipid chains toward the latter. Unsaturated chains are known to lower transition temperature [104, 105], this counteracts the ordering effect induced by the applied pressure.
Lipids can form additional hexagonal phases, so called "mesophases", while applying pressure. However this behaviour is only observed for lipids with a chain length longer than 16 carbon atoms [106]. So DMPC with only 14 carbon atoms per chain is ideally suited to probe the dynamics of pure lamellar phases (L_β gel and L_α liquid phase, respectively).
Also from a biomedical point of view the investigation of pressure effects on membranes is interesting. Anaesthetics are known to lower the temperature of the main phase transition and whereas pressure increases T_M. It was shown that the effect of alcohol and other anaesthetics on tadpoles can be reversed by applying pressure up to 5000 psi (1 psi $\approx$ 0.069 bar) [107]. Even if there are models which try to explain the impact of anaesthetics by a thermodynamical approach [108], a general description how anaesthetics act on membranes is still not existing.

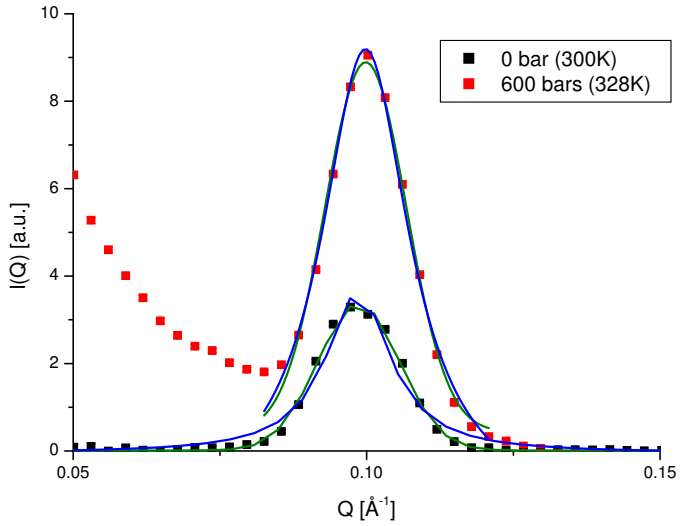

(a) Peak positions in the L_α phase at 0 bar and 600 bar. Lorentzian (in blue) and Gaussian (in green) fits to evaluate the repeat distance are also shown.

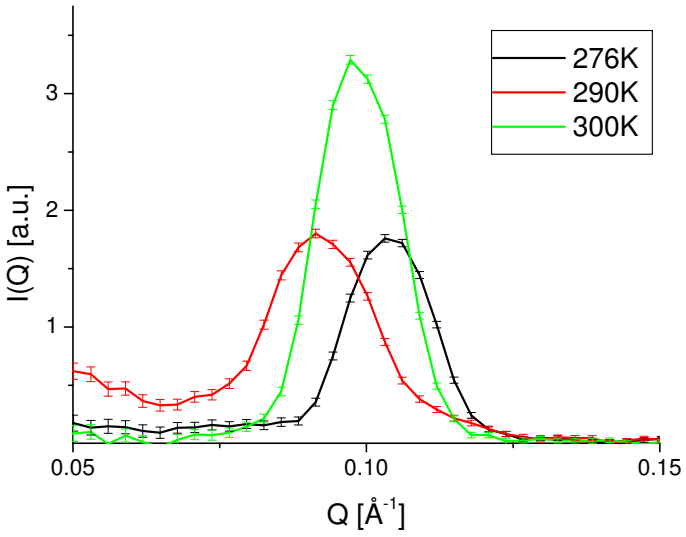

(b) Repeat distance in the $L_{\beta'}$ (black curve), in the $P_{\beta'}$ (red curve) and in the L_α (green curve) phases.

Figure 8.2: The peak position at both investigated pressure values is shown in figure 8.2a. Figure 8.2b shows a comparison of the repeat distance of the different lipid phases at atmospheric pressure.

8.2 Diffraction experiments on D16

In a first step and as a test of the newly developed pressure cell (see chapter 4) we performed diffraction experiments on D16 to follow the predicted shift of the temperature of the main phase transition of 22 K per 1000 bar [96].
To avoid water inclusions in lipid vesicles the sample was prepared to form lamellar bilayers by hydrating dry lipid powder from D_2O vapour at 310 K for two days (cf chapter 5). Additional heavy water was added to ensure a full hydration of the sample. As reference a temperature scan from 276 K to 310 K at atmospheric pressure was performed (steps of 2 K). Figure 8.1a shows a reference scan taken at atmospheric pressure. As expected for fully hydrated DMPC, the two phase transitions are apparent and occur at the same temperatures, namely 287 K and 297 K, as in the oriented samples in the fully hydrated state (see chapter 6) or e.g. DSC. Even if no correction for multiple scattering has been applied so far, this is an encouraging result from the first test.
In a next step a second temperature scan from 280-330 K (steps of 2 K) was recorded, this time a pressure of 600 bar was applied to the sample. The observed temperature for the main phase transition at this pressure was 310 K, corresponding exactly to a shift of 13 K (cf figure 8.1b) and thus in agreement with what was reported by Winter et al. [96]. Below the temperature of the main phase transition neither the ripple phase nor the gel phase was observed. As pressure has a similar effect on the lipids as a decreased hydration, the absence of the $P_{\beta'}$ phase is in agreement with observations made by Smith et al. [55] at hydrations below 85 % relative humidty. The surprising feature of the absence of the gel phase is under further investigation.
Figure 8.2a shows a comparison of the peak position of the L_α phase for both investigated pressure values. They agree within errors and show a repeat distance around 63 Å, which is in agreement with literature values for fully hydrated DMPC. The fact that the repeat distance of the bilayers stays constant when applying pressure is an indication that the lateral structure persists in the investigated pressure range.

8.3 Elastic experiments on IN13

First experiments on IN13 were performed using the high pressure cell in the course of 2010. Due to an exceptional reactor shut down during the third cycle in 2010, it was so far only possible to perform a temperature scan at atmospheric pressure, which will serve as reverence. Figure 8.3a shows the summed elastic intensity normalised to 290 K. Due to the high counting time per point (approximately 12 hours) only a limited temper-

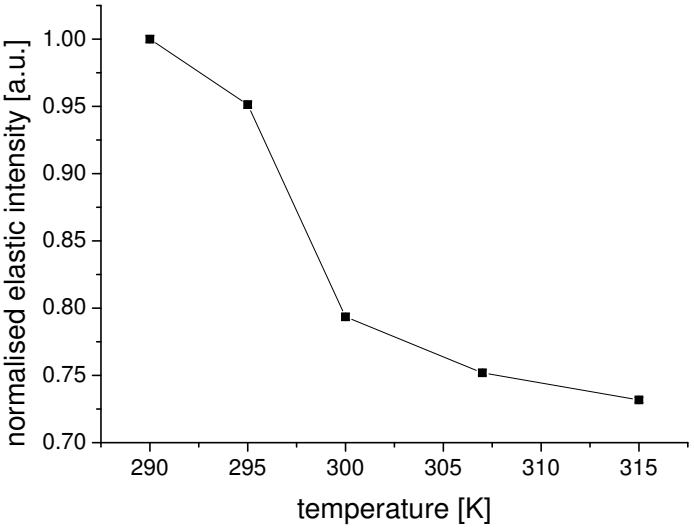

(a) Normalised summed elastic intensities at atmospheric pressure.

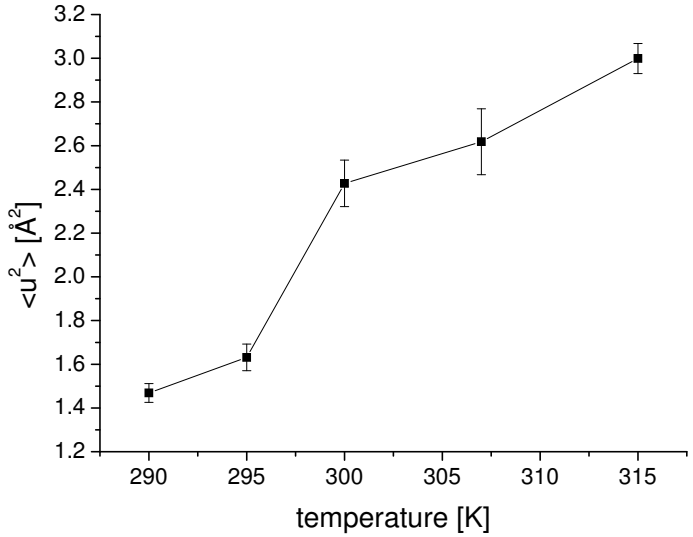

(b) Mean square displacements obtained from fitting the data in a Q-range of $0.52\,\text{Å}^{-1} \leq Q \leq 1.47\,\text{Å}^{-1}$.

Figure 8.3: Elastic intensities and mean square displacements of DMPC in excess of heavy water at atmospheric pressure.

ature range can be scanned during an experiment. The calculated mean square displacements are shown in figure 8.3b, so far no correction of multiple scattering has been applied.
Nevertheless the extracted $<u^2>$ show already good agreement with a recent MD simulation at 303 K and atmospheric pressure [86]. Figure 8.4 shows the results of the simulation. The time resolution of IN13 is drawn as dashed red line. Values for the mean square displacements at different position of the lipid molecule were extracted from the simulation. For the carbon atom of the methyl group at the end of the lipid chain (CT) a value of about 11 $Å^2$ is found, whereas for the centre of mass (CM) a value of about 1 $Å^2$ was deduced. The value obtained from the IN13 experiment is 5 $Å^2$ (cf figure 8.3b) and thus lies in between the two simulation values.
The data obtained on IN13 with the cylindrical high pressure cell show the well known behaviour of a kink at the main phase transition indicating an increased mobility. The same characteristics were observed on IN16 with the solid supported DMPC in flat sample holders (see chapter 6.3).
In addition to the reference scan at atmospheric pressure, temperature scans at two more pressure values, namely 300 bar and 600 bar are planned. The applied pressure should lead to a shift of 6.6 K for 300 bar and 13.2 K for 600 bar, respectively.

8.4 Future perspectives

For the fourth reactor cycle in 2010 high pressure elastic and quasi-elastic neutron scattering experiments on the time-of-flight spectrometers IN5 and IN6 on fully hydrated DMPC in the range between 0 bar and 600 bar will be performed. They will enlarge the already started elastic investigations on IN13.
It is known from the investigation of deep-sea organisms that the composition of membranes changes as a function of pressure. The higher the pressure, the more lipids with unsaturated chains are found [109].
The effect of unsaturated chains on the phase transition temperature will be investigated by elastic temperature scans on IN13. In the autumn proposal round 2010 a project was submitted to perform EINS experiments on mixtures of saturated DMPC (14:0) with (Δ9-Trans) PC (1,2-dimyristelaidoyl-sn-glycero-3-phosphocholine) and (Δ9-Cis) PC (1,2-dimyristoleoyl-sn-glycero-3-phosphocholinelipids). These lipids have the same chain length and head group as DMPC but they have one unsaturated carbon bond per chain (14:1) at the ninth position of the chain. The temperature range between 275 K and 330 K will be investigated in order to detect any shift of the main phase transition temperature. In addition to the neutron experiments, DSC measurements are envisaged to follow the shift transition temperature with a complementary method.

On a long scale perspective comparative measurements of cell membranes from organisms living at different depths can give insight on how lateral diffusion processes in the membrane under physiological pressure conditions happen.

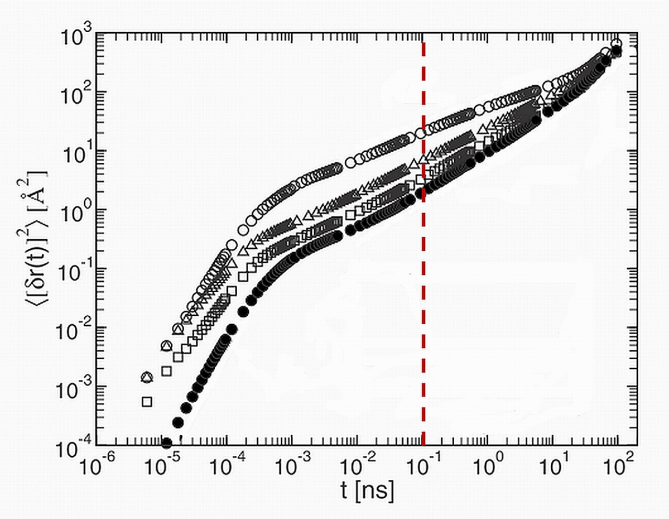

Figure 8.4: Values of MSDs extracted from MD simulations. Data are given for four different positions within the lipid. The open square represent the MSDs of the phosphorus atom, open triangles the carbon of the methyl groups in the head group of the lipid, open circles the carbon of the terminal methyl group of the lipid chain and the closed circles represent the centre of mass MSDs. The time resolution of IN13 is depicted as dashed red line. Figure is adapted from [86].

8.5 Perspectives

Dûrant le quatrième cycle du réacteur en 2010, des expériences à haute pression élastique et quasi-élastique sont prévues sur les spectromètres en temps de vol IN5 et IN6. Des échantillons DMPC complètement hydratés seront étudiés dans la gamme entre 0 et 600 bars pour élargir les investigations déjà commencées sur IN13.
L'effet des chaînes non saturées sur la température de la transition de phase sera étudié par balayages élastiques sur IN13. En automne 2010, un projet a été soumis à l'ILL pour effectuer des expériences EINS sur des mélanges de DMPC saturé (14 :0) avec (Δ9-Trans) PC (1,2-dimyristelaidoyl-sn-glycéro-3-phosphocholine) et (Δ9- Cis) PC (1,2-dimyristoleoyl-sn-glycéro-3-phosphocholinelipids). Ces lipides ont la même longueur de chaîne et le même groupemebnt de tête que DMPC, mais ils ont une liaison insaturée

par chaîne (14 :1) à la neuvième position de la chaîne. La gamme de température entre 275 K et 330 K a été choisie afin de détecter tout changement de la température de transition de phase principale. En plus des expériences neutroniques, des mesures DSC sont envisagées pour suivre le décalage de la température de transition par une méthode complémentaire.
A plus longue échelle des mesures de comparaison de membranes cellulaires d'organismes vivants à des profondeurs différentes peuvent donner des indications à savoir comment des processus de diffusion latérale ont lieu dans une membrane sous des conditions de pression physiologique.

Chapter 9

Neutron scattering studies of human acetylcholinesterase

In the following chapter a second project, in which I have participated in the course of my PhD thesis, is described. Neutron scattering studies on pure human acetylcholinesterase and in complex with the non-covalent binding inhibitor Huperzine A have been performed. In total three different spectrometers (IN6, IN13, IN6) and four different energy resolutions have been employed to study the dynamics of AChE and its inhibited counterpart on a pico- to nanosecond timescale.
After a general introduction (section 9.1) and the description of the sample preparation (section 9.2), the elastic experiments are described in section 9.3, this section is based on a research paper submitted to "*Physical Chemistry Chemical Physics*" for publication. In section 9.4 the mean square displacements of AChE are compared to those of the second cholinesterase, which can be found in humans, butyrylcholinesterase (BChE). Both enzymes fulfil similar tasks and have therefore a high structural similarity, nevertheless our findings show significant differences on the pico- to nanosecond timescale between them. The results from the quasi-elastic measurements are introduced in section 9.5. Concluding remarks and an outlook for further investigations are given in section 9.6.

9.1 Introduction

Cholinesterases (ChEs) belong to the hydrolase class of enzymes (Enzyme Commission (E.C.) class 3) and are fundamental for cholinergic and non-cholinergic functioning of the nervous system and are presumably involved in various diseases. It has been proposed that they have additional functions as bioscavengers for poisons, as protection against the toxicity of nerve agents or in mutant forms as therapeutic treatment of cocaine overdose [111, 112]. Acetylcholinesterase (AChE, E.C. 3.1.1.7, see figure 9.1 for

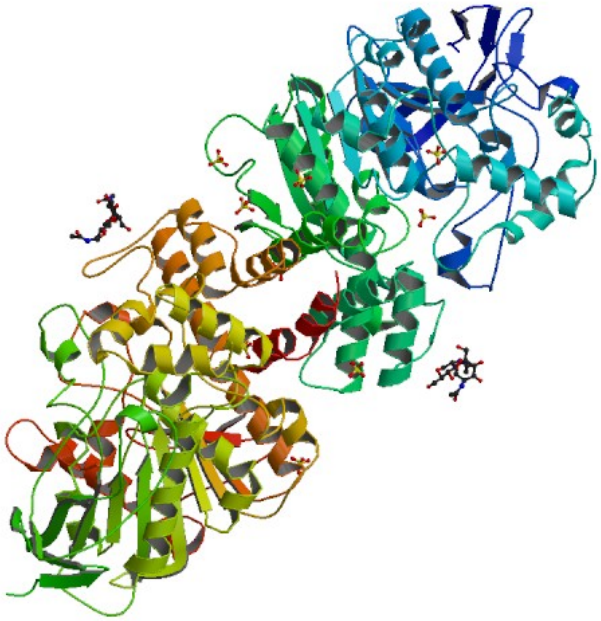

Figure 9.1: Crystal structure of human AChE (PDB code 3LII). Data were taken at a resolution of 3.2 Å. The size of the unit cell was determined to a = b = 210.90 Å and c = 115.27 Å (angles: $\alpha = \beta = 90°$, $\gamma = 120°$) [110].

the crystal structure), which is one of the two ChEs found in mammals, hydrolyses the neurotransmitter acetylcholine (ACh) (see figure 9.2), thereby regulating the concentration of the transmitter at the synapse. An abrupt blockade of acetylcholine-mediated neurotransmission is lethal. Clinically, moderate inhibition of AChE is effective in treatment of certain diseases to prolong the action of ACh on the receptor. Such a treatment is desirable either if there are fewer ACh-receptors, as in the case of myasthenia gravis, or if there is reduced production of ACh, as in the case of Alzheimer's disease. Huperzine A (HupA) is a naturally occurring alkaloid isolated from the Chinese medicinal herb Huperzia serrata. As it is a powerful reversible inhibitor of AChE, it was envisaged for the symptomatic treatment of Alzheimer's disease.

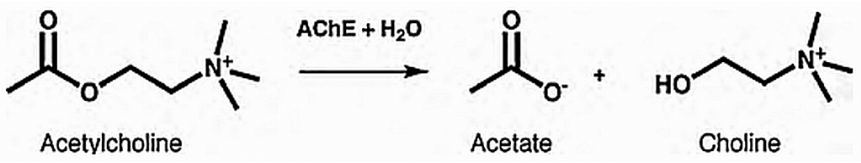

Figure 9.2: Enzymatic hydrolysis of Acetylcholin by AChE.

AChE is one of the fastest enzymes known [113], operating nearly at the diffusion limit. The first crystallographic structure of *Torpedo Californica* AChE (*Tc*AChE) [114] revealed a surprising feature, which is at odds with the speed of the enzyme: the active site is located at the bottom of a deep and narrow gorge lined by 14 conserved aromatic residues. Due to the restrictive dimensions of the active site gorge (20 Å deep, Ø $\approx$ 5 Å), substrate hydrolysis takes place in a closed space virtually isolated from the bulk solvent. In parts, the gorge appears to be so narrow that only water molecules could fit through, and substrates or inhibitors would have no access to the active site if the enzyme was rigid. Thus large amplitude fluctuations are necessary to explain the entry of molecules like substrates and inhibitors.
Experimentally neutron spin echo experiments have been used to investigate large scale fluctuations covering a time range up ton several 100 ns [115]. In the case of alcohol dehydrogenase the collective motion of domains were related to a cleft opening dynamics between the binding and the catalytic domains enabling binding and release of a functional important cofactor [116].
In addition molecular dynamics simulations (MD) are a powerful computing tool to analyse dynamics in more detail and such efforts have revealed a whole hierarchy of motions acting together on different timescales. Studies of the enzyme's dynamics, using MD simulations [117, 118] and quantum mechanical-molecular mechanical (QM/MM) simulations [119], indicate the presence of such motions. The groups of J.A. McCammon and

Y. Xu [120] have undertaken simulations of mouse AChE (mAChE), unliganded and in complex with HupA [121–124]. The first two simulations of McCammons' group dealt with a liganded mAChE at 300 K over 500 ps and 1 ns (with slightly different starting structures). The next simulations investigated the unliganded form at 300 K over 1 and 10 ns. The authors analyzed the dynamics of the breathing mode of the gorge and the possible opening of a so-called backdoor and other possible side channels in detail. These studies revealed in particular the dynamical complexity of the fluctuations: the latter fact seems to be a general characteristic of macromolecules due to their rough energy landscapes [125]. Xu et al. concentrated on the motions of specific residues and studied amongst others the question how one could explain the fact that the association time with HupA is much shorter than the dissociation time [124].
Within complex dynamical systems such as proteins, diffusive motions are often confined in space. Therefore they can be described as diffusion processes in presence of systematic forces. The corresponding autocorrelation functions exhibit long-term memory effects and lead to a non-exponential decay in time. This effect is the signature of a linking of the time scales of fast and slow functional relaxation dynamics [126], resulting from different scales of interactions that each have important but competitive contributions. The analysis of the variation of the gorge radius over 10 ns showed clearly that the corresponding autocorrelation function complies with a non-exponential relaxation [123]. For instance, the local motions of side chains seem to contribute significantly to the opening of the gorge, but they are strongly correlated to larger domains of collective dynamics. At least half the protein was found to be involved in large-scale fluctuations. The authors are speaking about a hierarchy of relaxations divided into tiers of faster and slower motions, where the relaxations in the slower tiers only become accessible when the faster tiers have moved into the required conformations. A similar interpretation was given by K. Henzler-Wildman & D. Kern [125], stating that transitions are slow if they are improbable, arising from many individual attempts by local groups to overcome the energy barrier separating the conformational states. The low success rate results from the collective nature of such large-scale motions.
More recently, a combined MD simulation and experimental study has shown that picosecond mean square displacements, as measured by elastic incoherent neutron scattering (EINS), satisfy a universal scaling law with respect to viscosity measured over much longer time scales (up to seconds or more). Such universal correlation was observed to be valid for a wide range of simple liquids, supercooled liquids and glass formers, and thus confers on picosecond MSDs a more general and intriguing role of fast predictor for slower dynamical processes governed by viscosity and relaxations [127, 128]. In fact, the protein solvation shell exhibits a regular glass transition, so that such effects are probably also correlated to protein dy-

namics.
Members of the ChE family differ from each other in catalytic activity, oligomerisation state and glycosylation [129]. The question of whether there exists a correlation between these characteristics and dynamics is still an unresolved matter [130]. Catalytic activities lie on the millisecond timescale, which are comparable to those required for protein folding. Can differences in catalytic activities be reflected in variations in atomic thermal fluctuations on the pico- to nanosecond time-scale? By blocking or not enzymatic activity with an inhibitor, could this be a way to trigger it and to probe its effects on the dynamics? The inhibitor HupA was chosen for the experiments because it is a small molecule. Due to its low hydrogen content, the molecule itself will be almost invisible in the neutron dynamics studies, but when bound to AChE, it switches off the enzyme activity.
Elastic, quasi-elastic and inelastic neutron scattering was used to probe experimentally and quantitatively the molecular dynamics of human AChE (hAChE), with or without HupA inhibition, in order to investigate the relationships between molecular dynamics, activity, inhibitor-binding, and unfolding.
We used three different spectrometers (IN6, IN13 and IN16) [20, 22, 40, 131] at the ILL. The energy resolution of the spectrometers corresponds to different time scales, which permitted to probe dynamics between a few picoseconds up to about one nanosecond (cf table 3.4), corresponding to movements from very fast internal motions to slow global motions. In section 9.3 elastic intensity changes upon temperature variation are reported. The application of approximate relations assuming a Gaussian distribution of the atoms around their equilibrium positions permits the extraction of average atomic mean square displacements. They are the reflection of the sampling of conformational sub-states and of vibrational amplitudes. The wavelength of the incident neutrons corresponds to inter-atomic distances and, contrary to the energy of X-ray or synchrotron radiation, the corresponding neutron energy is of the order of the energy of vibrational and conformational states. Therefore EINS is well suited for experimental investigations of thermal fluctuations within biological macromolecules under different biochemical conditions on timescales that match those of MD calculations and permit direct comparisons.

9.2 Sample preparation and characterisation

9.2.1 Purification of recombinant human AChE

The full cDNA of hAChE was inserted into pGS vector carrying the glutamine synthetase gene marker and expressed in Chinese hamster ovary cells (CHO-K1 cells). The cells were maintained in BioWhittaker® Ultra-

cultureTM medium (Lonza, Belgium) and transfected using DNA-calcium phosphate co-precipitation. Transfected clones were selected by incubation in media containing methionine sulfoximide (50 M). The enzyme, secreted into the culture medium, was purified by affinity chromatography as previously described [132]. hAChE was concentrated to 13 mg ml^{-1} using a Centricon-30 ultrafiltration microconcentrator (30,000 MW cutoff from Amicon (Millipore, USA)). Enzyme concentration was determined from its absorbance at 280 nm using a molar extinction coefficient of 1.7 for 1 mg ml^{-1} of protein [133].
Activity measurements were carried out at 298 K according to Ellman method [134] using 1 mM acetylthiocholine (ATC) as substrate and 0.5 mM 5-5'-dithio-bis (2-nitrobenzoic acid) (DTNB) in 0.1 M phosphate buffer pH 7. Circular dichroism (CD) spectra of recombinant hAChE (0.1 mg ml^{-1} in ammonium acetate buffer 5 mM pH 7) were collected on a JASCO-810 CD spectrometer in the spectral range 190 nm–240 nm (at 0.5 nm intervals) at room temperature. Baseline was performed with ammonium acetate buffer 5 mM pH 7. The spectra analyses were performed using the DichroWeb server (Dichro).

9.2.2 Sample preparation for neutron scattering

A batch of about 300 mg of hAChE was dialyzed against 25 mM ammonium acetate dissolved in D_2O, pD 7.0 (corresponding to a pH 6.6). Since the buffer is completely volatile, an over-night lyophilisation at 220 K under vacuum resulted in salt free protein powder. About 140 mg of hAChE in D_2O solution was mixed with 2 molar equivalents of (-)-HuperzineA before lyophilisation. About the same amount of hAChE was lyophilised without inhibitor. Both lyophilised powders (free hAChE and hAChE-HupA complex) were placed in aluminium sample containers of dimensions $30 \times 40 \times 1$ mm^3 to match the size of the neutron beam available on the instruments. The samples were dried at atmospheric pressure over phosphorus pentoxide (P_2O_5) and weighed. The measured weights were taken as their dry weights (h = 0 g D_2O/g dry powder, denoted by g/g below). For neutron experiments, samples were hydrated by vapour exchange over D_2O, at ambient temperature, in a desiccator. A final water content of 0.4g/g for both samples was achieved. To verify that no loss of material had occurred, all samples were weighed before and after the neutron scattering experiments. No losses were detected for any sample.

9.3 Elastic experiments

Incoherent neutron scattering is dominated by the signal of hydrogen scattering intensity. This is due to the hydrogen incoherent scattering cross sec-

tion which is one order of magnitude larger than that of all other elements usually occurring in biological matter, and also of its isotope deuterium (see table 3.2). The technique probes average protein dynamics because hydrogen atoms are uniformly distributed in the protein. The wild type form of hAChE contains a high proportion of hydrogen, 4673 of a total of 9470 atoms. The incoherent cross section of the hydrogen atoms thus corresponds to 99.8% of the total incoherent cross section and to 92.6% of the total scattering. The exact number of amino acids and the atomic composition of hAChE can be found in the tables C.1 and C.2 in appendix C.

9.3.1 Instrumental aspects and data analysis

The characteristics of the used spectrometers in terms of incident wavelength, accessible Q-range, detectable length-scale, energy resolution and timescale are already outlined in table 3.4. The timescale can be calculated from the energy resolution using the Heisenberg uncertainty relation (equation 3.12) or eq. 21 in the paper by Zorn [135], assuming a Gaussian shape of the resolution function. As the edges of the time window are not sharp, rounded values in between both results are given in the table.
The cold neutron time-of-flight spectrometer IN6 [22] is sensitive to motions with associated times of a few ps. Two different wavelengths corresponding to two different energy resolutions of $\Delta E \approx 50$ and $90\,\mu eV$ were measured. IN13 [40] is the only thermal neutron backscattering spectrometer worldwide with an intermediate energy resolution of $\Delta E \approx 8\,\mu eV$. Finally IN16 [20] is a high resolution cold neutron backscattering spectrometer with an energy resolution of $\Delta E \approx 0.9\,\mu eV$, corresponding to a time window ranging up to $\approx 1\,ns$. A comparison of the different elastic resolution functions was already shown in figure 3.3 of section 3.5.2. Thus, the three instruments are sensitive to motions on different time scales. The different contributions to atomic motions (lattice and internal molecular vibrations, reorientations, translations) are assumed to be completely decoupled, because they occur on significantly different time scales, what was also shown by MD simulations [136]. In this sense the instruments can be seen as a motion filter to focus on certain aspects of the sample dynamics only. Internal motions are within the window for all three spectrometers. The contribution of global protein diffusion is negligible for all instruments apart from IN16, which has the broadest time window. Water diffusion is outside the window of IN13 and IN16 and appears as a smooth background. It does, however, contribute significantly on IN6. Especially the length-time window of IN13 is well suited to measure internal dynamics, without 'pollution' of the scattering by contributions from global or bulk water diffusion [137].
Transmission values were measured on IN13 and corresponded to 0.94 and 0.95 for the wild type and the inhibited form of AChE, respectively. Mul-

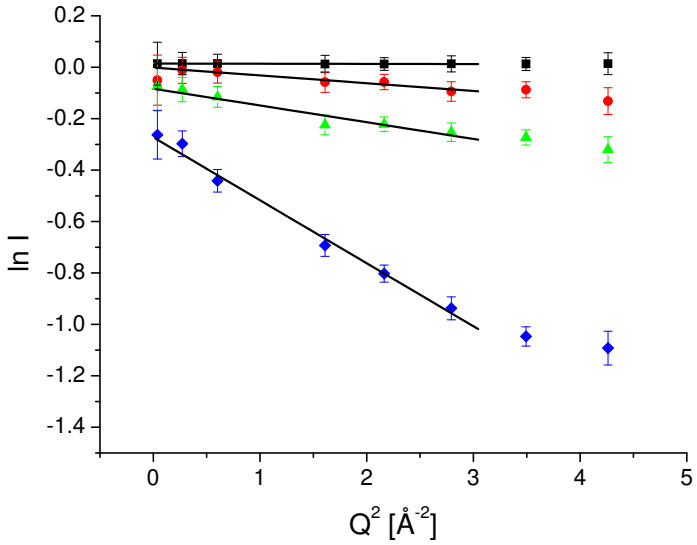

(a) Data taken on IN13.

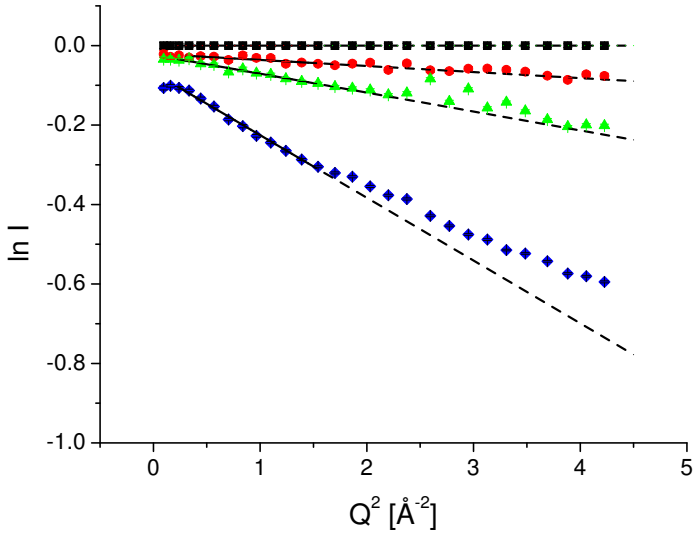

(b) Data taken on IN6 (90 µeV resolution).

Figure 9.3: Logarithm of the normalised intensities of hAChE plotted versus Q^2 for 20 (black squares), 100 (red circles), 200 (green triangles) and 300 K (blue diamonds) with corresponding error bars. The full lines correspond to the linear fits used to extract the MSDs. The dashed lines in the right figure are extrapolations of the linear fits to higher Q-values and show a clear deviation from Gaussian behaviour at higher temperatures.

tiple scattering effects were therefore not taken into consideration for the data treatment. To obtain the scattered intensities of the sample, scattering from the empty sample holder was subtracted. The data were normalized to the lowest temperature (20 K), where molecular motions are strongly reduced. Absorption correction was based on the correction formula of Paalman-Pings coefficients [138]. Data evaluation was carried out using the LAMP software available at ILL [80].

9.3.2 Determination of atomic mean-square displacements

The logarithm of the elastic intensity (eq 3.23) of each sample at a given temperature T is plotted against Q^2 (see e.g. figures 9.3a and 9.3b). As IN6 is a time-of-flight instrument, the whole accessible energy range is measured simultaneously. The elastic data were thus extracted by integrating over an energy range of [-0.11, 0.12] meV for the 90 µeV resolution and of [-0.06, 0.09] meV for the 50 µeV resolution. This corresponds to the whole elastic peak and not only the full width half maximum (FWHM). Whereas at low temperatures intensities decreased linearly over the whole Q-range, a dynamical transition appeared in the plots above $\approx$ 200 K (see figure 9.3), consistent with the well-known deviation from the Gaussian behaviour at higher temperatures [9]. The mean square displacements can be obtained from the slope of the logarithm of the scattered intensities according to equation 3.24. This approach is formally similar to the Guinier approximation in small angle scattering experiments [29]. MSDs were extracted from the Q-ranges where the linearity was clearly visible. The corresponding Q-ranges, used during the fitting procedure are given in table 9.1.

Spectrometer	IN6	IN6	IN13	IN16
Resolution FWHM [µeV]	90	50	8	0.9
used Q-range [$Å^{-1}$]	0.49 - 1.24	0.42 - 1.13	0.52 - 1.67	0.54 - 1.10

Table 9.1: Q-range used in order to extract mean square displacements.

The criterion for validity of the Gaussian approximation $\langle u^2 \rangle Q^2 \leq 1$ was checked a posteriori: it is slightly exceeded at IN16 and IN13 (values up to 2.9), but the curves are still linear for these Q-values and thus the approximation is justified [139].

9.3.3 Results

Some complementary tests were performed to characterise the samples before and after the neutron scattering experiments. The enzyme solutions were stable at 277 K and hAChE activity was partially preserved after a

lyophilisation step (only 20-25% of activity was lost - data not shown). The CD spectrum of hAChE in 5 mM ammonium acetate buffer (pH 7) indicated the presence of a large amount of alpha-helix structures and beta-sheets. However, after the neutron scattering study, dissolution of hAChE sample was not possible and neither activity nor CD measurements could be performed as a final temperature exceeding the denaturation temperature was reached during the experiments (cf section 9.3.3).

IN13: Correlation between heat denaturation and MSDs

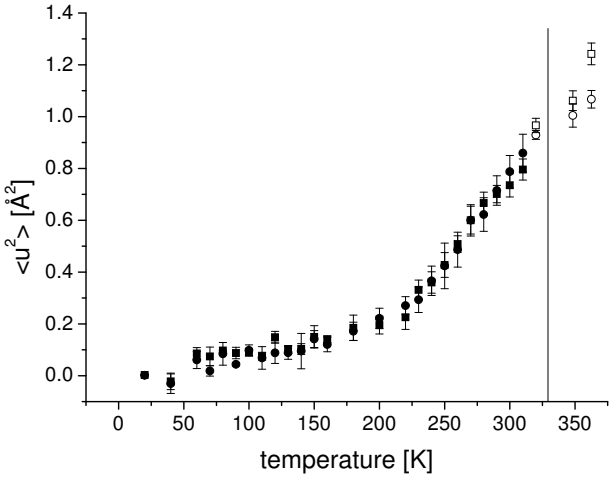

Figure 9.4: MSDs measured on IN13 of hAChE (squares) and hAChE with HupA (circles), hydrated from D_2O in the temperature ranges 20-310 K (filled symbols) and 310-365 K (open symbols). The seal of the sample holder had to be exchanged between the two temperature ranges. The mid-point denaturation temperature of the native (non-inhibited) enzyme in solution is indicated by the vertical line.

The denaturation temperature of recombinant hAChE is known to be 329 K in HEPES 20 mM NaCl 150 mM at pH 7.5 [140] and 334 K in 50 mM sodium phosphate at pH 8.0 [141]. Therefore we measured both samples (hAChE with and without HupA) first in the temperature range from 20-310 K (measured on all instruments) and in a second experiment from 310-365 K (measured only on IN13). One difficulty was related to the fact, that the used indium alloy seal to make the sample holder tight melts around 350 K. So the sample holders for higher temperature measurements had to be re-opened in order to take away the indium and replace it by a seal of silicon Motorsil D. The samples were then carefully dried and rehydrated

again.

The behaviour of the protein on IN13 under denaturing conditions by heating it up to 365 K was investigated.
Here a reference to a former study on IN16, which reported about enzyme dynamics in the presence of a covalent inhibitor (the organophosphonate soman) on hydrated powders [142] as function of temperature is inserted. The protein under investigation was a ChE without known function, present in human blood plasma: human butyrylcholinesterase (hBuChE, E.C. 3.1.1.8)). hBuChE and AChE have a close structure of the active site and a similar a/b fold [111, 129], hence both share a similar catalytic function, only hBuChE can hydrolyse butyrylcholine in addition to acetylcholine. For instance, the size of the catalytic subunit of hBuChE is almost identical to that of *Tc*AChE, the residues 1 - 574 and 1 - 575 for the tailed molecular forms and their sequences are 54% identical.
Neutron dynamics studies revealed identical behaviour of the wild type and the inhibited enzyme in the temperature range below 334 K, but above that temperature the soman phosphonylated BChE was more rigid than the native enzyme. Furthermore the inhibited enzyme had a denaturation midpoint temperature in both H_2O- and D_2O-solution shifted by 10 K from 337.5 to 347.5 K [143, 144]. In the present study, similar effects were addressed using the non-covalent inhibitor HupA on hAChE.
Figure 9.4 shows MSDs obtained on IN13 as function of temperature. Since HupA has only 18 hydrogen atoms compared to the 4673 H-atoms of hAChE, the measured signal represents essentially the enzyme dynamics, even in presence of the ligand. The MSDs increase smoothly and display the well-known dynamical transition at around 220K [9]. Within the error bars, no differences are visible between both samples below the denaturation temperature at around 330 K. The error bars increase above 300 K, due to the reduced data acquisition time available. Only above 360 K a slight difference between the curves appears. Such a small effect cannot be valued as a proof, but it is also not contradicting earlier observations of Rochu et al. [145] and Gabel et al. [142], i.e. a covalently or non-covalently bound inhibitor stabilizes the enzyme and shifts the denaturation temperature to a higher value.
The results can be compared with MD simulations from Tara et al. [122] of pure mAChE and mAChE in the presence of HupA. These simulations found overall lower structural MSDs for residues in the gorge of the unliganded form. In a first impression, this fact could seem to be at variance with the presented data, because hardly any difference between the wild type and the inhibited form is seen. Neutron scattering averages over all residues in the protein and cannot differentiate between gorge residues and others in a completely protonated protein. Simulations can easily disentangle such small effects. Their observation is in accordance with an ex-

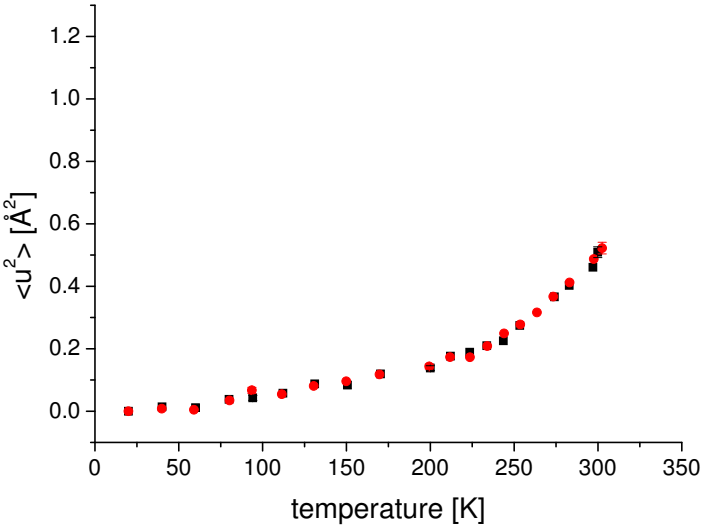

(a) IN6, 90 µeV, $t_{max} \approx 10$ ps.

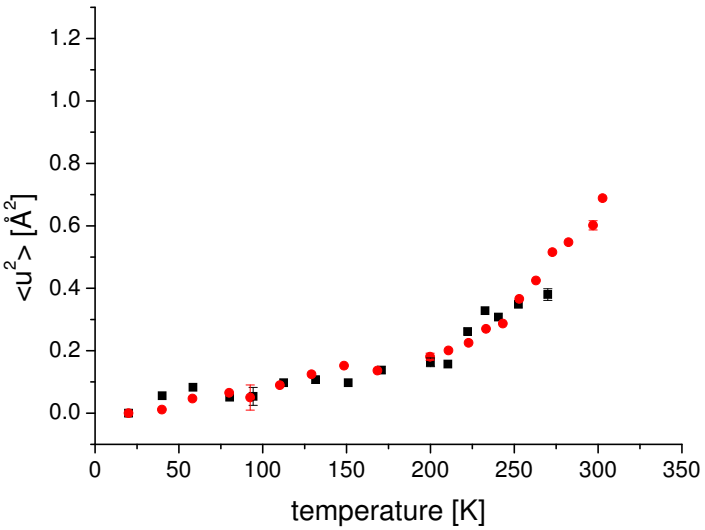

(b) IN6, 50 µeV, $t_{max} \approx 20$ ps. Due to limited beamtime the native AChE sample could only be measured up to a temperature of 270 K.

Figure 9.5: MSDs of pure hAChE (black squares) and with HupA (red circles), hydrated from D_2O vapor and measured at IN6. For a better visibility error bars are given only for a few data points. They are highest at high temperature. t_{max} gives the maximal resolved observation time of the corresponding spectrometer. Figure is continued on the next page

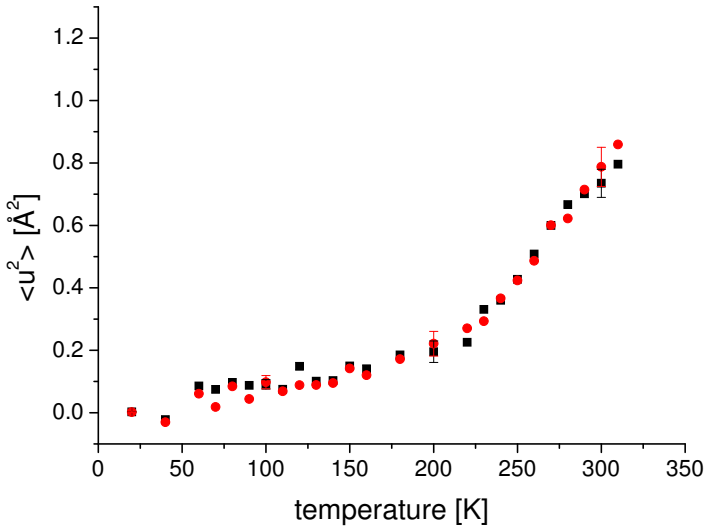

(c) IN13, 8 µeV, $t_{max} \approx 100$ ps.

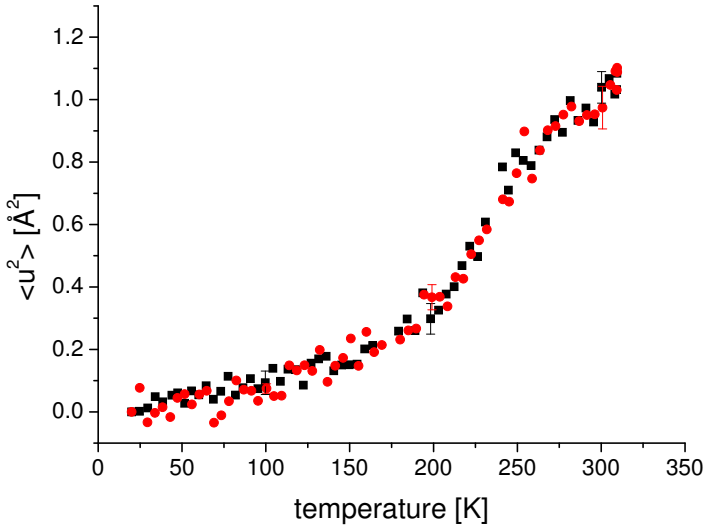

(d) IN16, 0.9 µeV, $t_{max} \approx 1$ ns.

Figure 9.5: MSDs of pure hAChE (black squares) and with HupA (red circles), hydrated from D_2O vapor and measured at IN13 and IN16. For a better visibility error bars are given only for a few data points. They are highest at high temperature. t_{max} gives the maximal resolved observation time of the corresponding spectrometer.

perimental study by S. Sacquin-Mora et al. [146], where they investigated by neutron scattering the purple bacterium *Rhodobacter sphaeroides* in parallel with two nonfunctional mutants and showed that the active sites are among the rigid parts of proteins.

MSDs of folded hAChE with and without inhibitor HupA

In order to compare the elastic data measured on each spectrometer, the MSDs were extracted from all elastic measurements as described in section 3.6.1 (see figure 9.5). For all three instruments and all four energy resolutions there is no difference detectable in the MSDs between the liganded and the wild type form of AChE. With an improving instrumental energy resolution and thus an increasing time window the MSDs increase continuously by more than a factor of two between the smallest and the largest time window (see figure 9.6). Such a tendency is in accordance with other comparative measurements on different spectrometers [147], showing that specific motions occur on each time domain.
The dynamical transition appears in all four figures, but becomes more pronounced with finer instrumental resolution. The corresponding onset of anharmonic motions is shifted with the time window from 180 K at IN16 to 230 K for the broadest resolution at IN6, as shown in figure 9.6. This means that between 180 and 230 K the elastic peak of the underlying relaxation process is situated in between the energy resolution of IN6 and IN16 and thus can be seen on IN16 and not on IN6. Doster [9] and Cordone [148] emphasized the importance of the protein environment on its dynamics, which influences the onset transition temperatures depending on the experimental time scale and particularly including the viscosity of the solvent (hydration water and buffer). In a recent publication, Doster [149] describes the mechanism of the dynamical transition as a first appearance of local dynamics in the cage of nearest neighbours, corresponding to the fast β-process. This process is the precursor of a main structural relaxation, the α-relaxation, which is a collective dynamics process corresponding to slower motions. Again we find here the idea of a hierarchy of motions, which appear in different instrumental time windows.
As long as their motions can be considered as harmonic, i.e. below the dynamic transition, particles perform only vibrations around their equilibrium positions and do not change between one local minimum of the energy landscape and another. Hence no energy barrier is passed and no energy is exchanged upon collision with neutrons. The harmonic motions induce purely elastic scattering processes with no quasi-elastic contribution. This means that the MSDs measured at all three instruments must coincide up to at least 150 K (see figure 9.6) and the elastic intensities must follow a linear drop off with Q^2 up to the highest Q values (see figure 9.3). Our results verify this for both intensities and MSDs within the accuracy of

the measurements.

Figure 9.5 shows the MSDs measured on all three instruments over the whole investigated temperature range. It indicates that the MSDs are possibly converging for all instruments at higher temperatures, as it was reported by Daniel et al. [150]. Unfortunately this fact could not be verified experimentally due to the protein denaturation and the associated irreversible structural changes at temperatures above 334 K. The MSD values measured at IN13 are thus between the data of IN16 and IN6, including the relaxation processes of the lower energy resolution and indicating that there must be a certain overlap between the measurable motions on the three instruments. To make this effect even more visible, Daniel et al. [150, 151] mention the possibility of subtracting the IN6 (or IN13) data from the IN16 data to study the change in dynamics in different time windows.
The observed decrease in slope of the MSDs at IN16 (figure 9.5 and 9.6) for temperatures higher than 280 K can be explained by the limitation of the instrumental resolution in relation to the measurement of large-scale motions [142]. The influence of a finite instrument resolution was simulated within the framework of the neutron frequency window model [152]. The transition observed by a spectrometer depends on the relationship between the timescales of the relaxation processes activated and the timescale accessible to the instrument. Two extreme scenarios were considered: firstly if the characteristic relaxation frequencies lie all within the energy resolution of the instrument, the observed dynamical transition is completely dependent on the temperature changes of the corresponding atomic MSDs, probing the energy levels of different conformational substates. The difference in energy of the substates corresponds to the free energy difference ΔG, which is furnished by the increase in thermal energy [9]. Secondly, it could be possible to have no change of the MSDs with temperature, which could be conceivable if there is no difference in energy for different local minima of the energy landscape. In the latter case, the various local minima are separated by a potential barrier corresponding to the activation energy E_a. Comparing data taken on IN6 and IN16 with simulations, McCammon et al. [117] demonstrated that such effects lead to a shift of the dynamic transition temperature and can explain the change of slope of the MSDs measured on IN16. Such an apparent dynamical transition can arise if the relaxation frequencies increase with temperature, e.g. the density of states is changing, such that they move into the frequency window of the instrument, giving therefore information about the timescales of motions crossing the resolution window of the instrument.
In a complex protein energy landscape it is likely to find a combination of both scenarios. The increase of the MSDs with the time scale together with the deviation of the intensities from Gaussian behaviour indicates

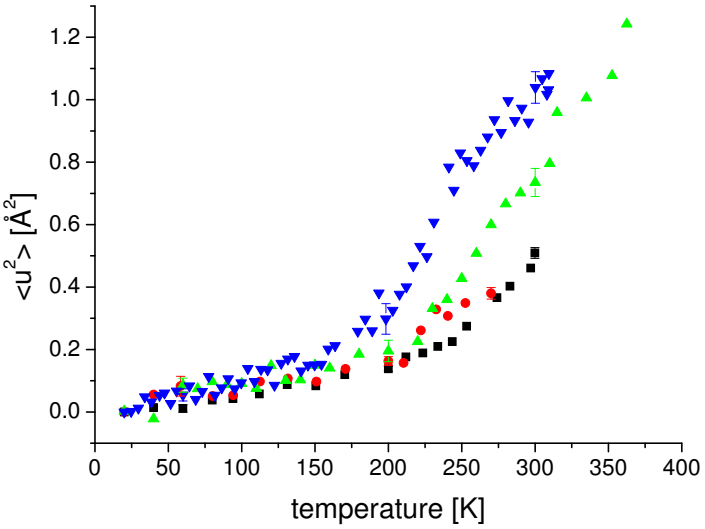

(a) $\langle u^2 \rangle$ of the pure hAChE.

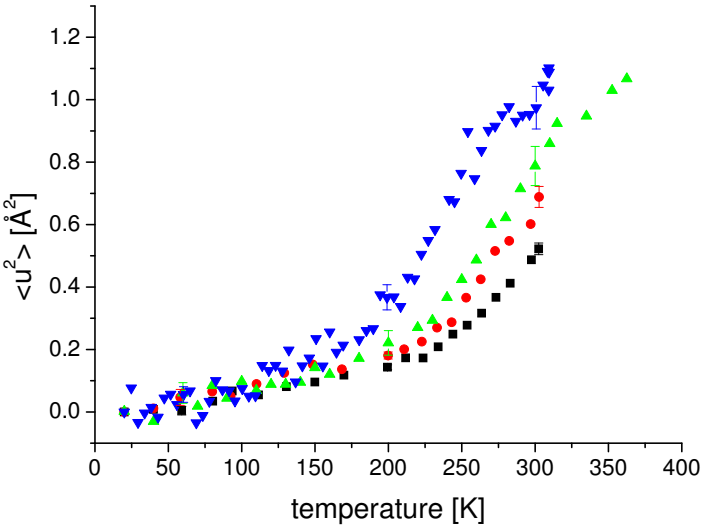

(b) $\langle u^2 \rangle$ of hAChE + HupA.

Figure 9.6: Compilation of the obtained mean square displacements. IN16 (blue diamonds), IN13 (green triangles) and IN6 (50 µeV: red circles, 90 µeV: black squares). For clarity characteristic error bars are only given at 50 K, 200 K and 300 K.

the existence of more than a single relaxation process (G. Kneller, unpublished work). This leads necessarily to an autocorrelation function I(Q,t), the Fourier transform of the scattering function S(Q, ω), with long-term memory effects and a non-exponential decay in time. As mentioned in the introduction, it is the signature of a linking of the time scales of fast and slow functional relaxation dynamics [126] and was already found by molecular dynamics simulations [123].

In fact, this can be verified by the experimental data. Using the "Fourier Transform Toolkit" (FFT) included in the DAVE program suite [89], the recorded scattering functions S(Q, ω) have been transformed into intermediate scattering functions I(Q,t). When only one relaxation process is observed, I(Q,t) shows an exponential decay, corresponding to $\beta = 1$ in equation 9.1. If several processes lie in the examined space and time window, I(Q,t) can be described by a stretched exponential or Kohlrausch-Williams-Watts (KWW) function, where $0 \leq \beta \leq 1$ and τ represents the relaxation time of the system.

$$I(t) \propto \exp\left[-\left(\frac{t}{\tau}\right)^{\beta}\right] \tag{9.1}$$

The β extracted from fits to the data shown in figure 9.7 resulted in values of $\beta \approx 0.3$ for both resolutions.

Conclusions

A series of elastic incoherent neutron scattering experiments were carried out on native and HupA inhibited hAChE at different spectrometers to probe different motions contributing to the functioning of the enzyme. Although no difference in MSDs of the wild type and the inhibited form until 350 K was detected, a indication of a small shift of the denaturation temperature due to the ligand appears around 360 K and could indicate stabilization by the inhibitor.
The MSDs recorded on the different instruments increase continuously with the enlargement of the observation time window from about 1.0 $Å^2$ for ΔE = 90 μeV to about 2.3 $Å^2$ for ΔE = 0.9 μeV. In agreement with MD simulation the results confirm the concept that a hierarchy of local and subdomain motions is necessary for the breathing movement of the enzyme's gorge.
Another effect of the influence of the instrumental resolution can be seen on the basis of the shift of the dynamical transition temperature from 230 K at IN6 (90 μeV) to 180 K at IN16 (0.9 μeV). It can be explained in the light of the so-called 'frequency-window model' where the motion enter the resolution window of the corresponding instrument at different temperatures.

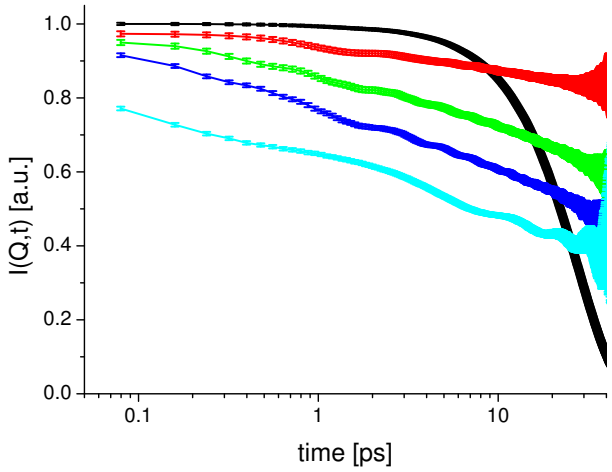

(a) Intermediate scattering function I(Q,t) at a given wavelength of 5.1 Å for AChE + HupA. The figure shows curves for Q-values of 0.5 $Å^{-1}$ (red), 1.0 $Å^{-1}$ (green), 1.5 $Å^{-1}$ (dark blue) and 2.0 $Å^{-1}$ (light blue) at 300 K.

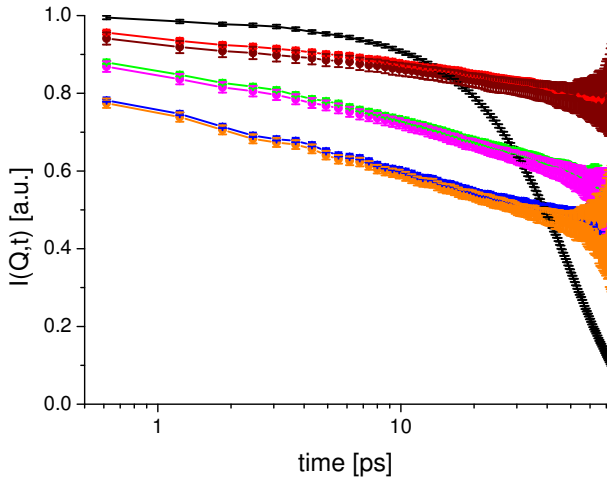

(b) Comparison of I(Q,t) of pure AChE and AChE + HupA (λ = 5.9 Å). Data for the pure AChE is depicted with squares, AChE + HupA with circles, respectively. Again selected Q-values of 0.5 $Å^{-1}$ (red and brown), 1.0 $Å^{-1}$ (green and pink) and 1.5 $Å^{-1}$ (blue and orange) are shown.

Figure 9.7: Intermediate scattering functions for both resolutions measured on IN6. The increasing error bars for long correlation times indicate the resolution limit of the given setup. The black curves represents the instrumental resolution.

In this context also the observed decrease in slope of the MSDs on IN16 for temperatures higher than 280 K can be explained by the limitation of the instrumental resolution. The stretched exponential behaviour of I(Q,t) indicates the existence of more than a single relaxation process [123].

9.4 Comparison between AChE and BChE

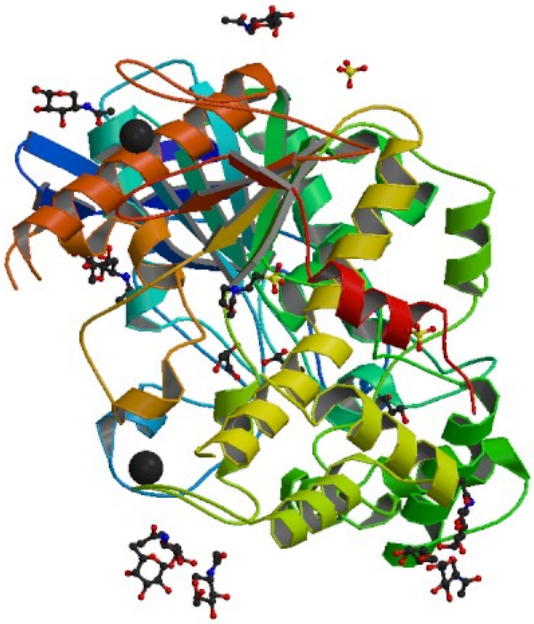

Figure 9.8: Crystal structure of human BChE (PDB code 1P01). Data were taken to a resolution of 2.0 Å. The size of the unit cell was determined to a = b = 154.66 Å and c = 127.89 Å (angles: $\alpha = \beta = \gamma = 90°$) [129].

The second member of the choline family which can be found in mammalians is BChE (E.C. 3.1.1.8). Human BChE is a tetrameric protein, whose crystal structure is shown in figure 9.8. It was solved by the group of P. Masson [129]. As already mentioned in the introduction, it fulfils similar tasks as AChE, but is mainly found in the plasma, whereas AChE is mainly located in the muscle nervous tissue. Nevertheless also BChE is found in small amounts in nervous tissue.
The mean square displacements of native BChE and in the presence of its covalent binding inhibitor soman, have been investigated by Gabel et al. [142], using the backscattering spectrometer IN16.

For the comparison of the two data sets, the data recorded by Gabel et

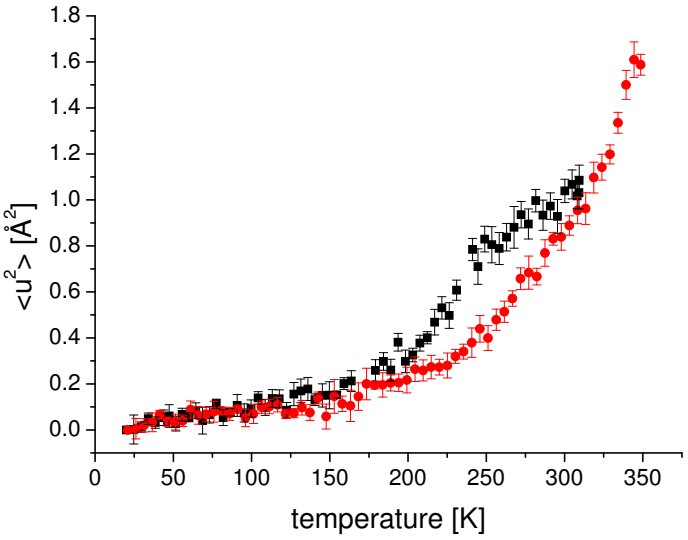

(a) Native AChE and BChE.

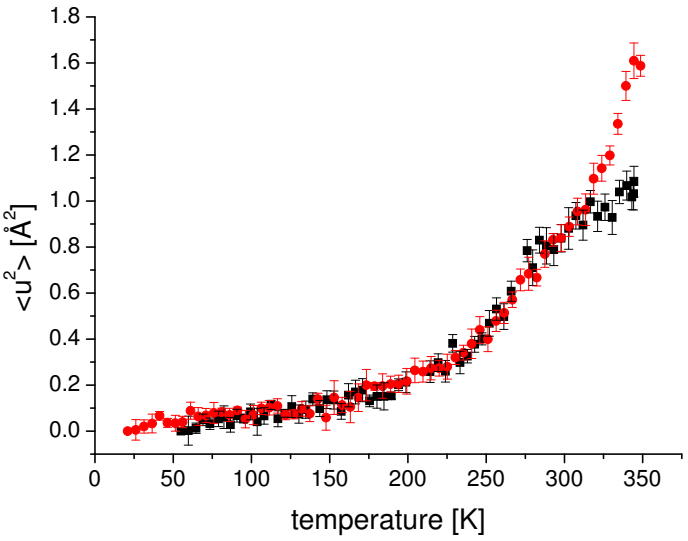

(b) Same data as shown in 9.9a but with a shift of the x-axis for AChE data of 35 K.

Figure 9.9: Comparison of the mean square displacements of native AChE and BChE taken on IN16. In black the AChE data are shown, in red the corresponding BChE data, respectively. To demonstrate that both data sets show the same slope, the x-axis of the AChE data is shifted by 35 K in figure 9.9b.

al. [142] have been retreated using exactly the same LAMP routines as for the evaluation of the AChE data in order to avoid any differences coming from the data treatment. No discrepancies between the old and the new data treatment were found.
At first glance, it appears that AChE shows a steeper slope in comparison to BChE after the dynamical transition. Figures 9.9a and 9.10a show the original data, whereas figures 9.9b and 9.10b show, for comparison, the same data, but with the temperature axis shifted empirically by 35 K in the case of AChE and AChE + HupA. From the latter it is obvious that both, AChE and BChE, show the same slope, and therefore the same resilience [153].
In order to extract thermodynamical variables from the elastic data a model, introduced by Becker et al. [152, 154], was used to fit the mean square displacements as a function of temperature. The corresponding equation used for the fitting procedure is given as:

$$< \Delta u^2 >=< \Delta u^2 >_{fast} + < \Delta u^2 >_{\bar{A}_0} \left(1 - \frac{2}{\pi} \arctan \frac{\Delta\omega}{\kappa}\right). \qquad (9.2)$$

Following the description of Becker et al. $<\Delta\ u^2>_{fast}$ was assumed to depend linearly on temperature, can be expressed as $<\Delta\ u^2>_{fast} = \alpha T$ and can be obtained by fitting the data at low temperatures with a straight line. $<\Delta\ u^2>_{\bar{A}_0}$ is a fit parameter, accounting for slow motions. $\Delta\omega$ is given by the half width at half maximum of the elastic energy resolution of the corresponding spectrometer. In the case of IN16 $\Delta\omega_{IN16} = 0.5\,\mu eV \mathrel{\widehat{=}} 7.595 \times 10^8\,s^{-1}$ and in the case of IN13 $\Delta\omega_{IN13} = 4\,\mu eV \mathrel{\widehat{=}} 6.076 \times 10^9\,s^{-1}$. κ is the relaxation frequency of the observed process.

Assuming an Arrhenius behaviour for κ, it can be expressed as:

$$\kappa(T) = a \cdot e^{-E_a/RT}, \qquad (9.3)$$

where a is a prefactor, E_a the activation energy, R the ideal gas constant and T the temperature. The resulting fits to the elastic data of the AChE samples are shown in figure 9.11 for the data obtained on IN16 and in figure 9.13 for the IN13 data, respectively. The fits to the BChE sample are given in figure 9.12.
During the analysis of the elastic neutron data it was found that the values of E_a for BChE are about a factor of two larger the the values obtained for the activation energy E_a of AChE (cf tables 9.2 for AChE and 9.3 for BChE). This tendency is in agreement with results obtained by activity measurements of hAChE and hBChE. About a factor of two between the two enzymes was found [155].
The degree of glycolisation differs between the two enzymes. As sugars are known to slow down dynamics on the pico- to nanosecond range [156], this could be one reason for the difference see between AChE and BChE.

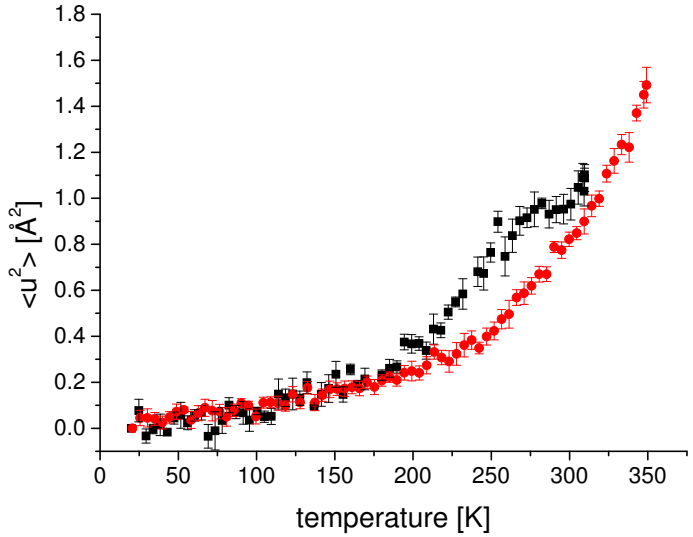

(a) AChE inhibited with HupA, BChE inhibited with soman.

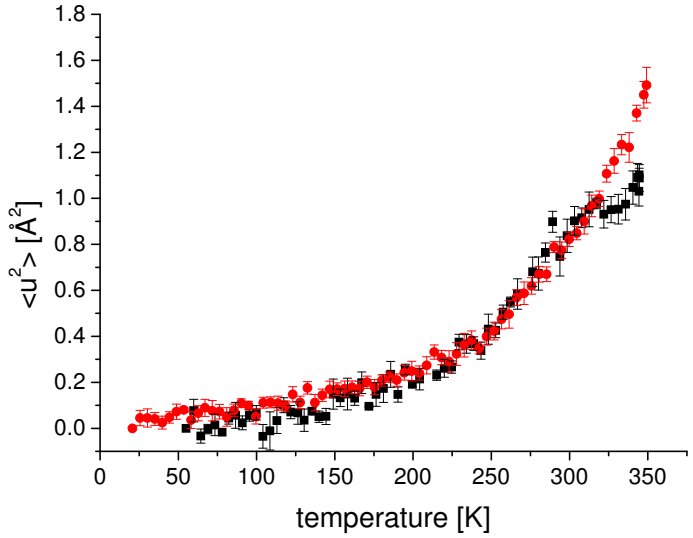

(b) same data as shown in 9.10a but with a shift of the x-axis for AChE + HupA data of 35 K.

Figure 9.10: Comparison of the mean square displacements of AChE and BChE in the presence of their inhibitors on IN16. In black the AChE + HupA data are shown, in red the corresponding BChE + soman, respectively. As for figure 9.9b also in figure 9.10b the x-axis of the AChE + HupA data is shifted by 35 K.

	fit parameters	AChE	AChE + HupA
IN16	α [Å^2 K^{-1}]	0.00106 ± 0.00005	0.00100 ± 0.00007
	$<\Delta u^2>_{\bar{A}_0}$ [Å^2]	0.83 ± 0.02	0.84 ± 0.03
	a [s^{-1}]	1×10^{12}	1×10^{12}
	E_a [kJ mol^{-1}]	14.20 ± 0.11	14.27 ± 0.16
IN13	α [Å^2 K^{-1}]	0.00083 ± 0.00007	0.00074 ± 0.00005
	$<\Delta u^2>_{\bar{A}_0}$ [Å^2]	0.97 ± 0.10	1.18 ± 0.09
	a [s^{-1}]	1×10^{12}	1×10^{12}
	E_a [kJ mol^{-1}]	12.55 ± 0.39	12.88 ± 0.30
IN6 50 µeV	α [Å^2 K^{-1}]	0.00069 ± 0.00012	0.00078 ± 0.00005
	$<\Delta u^2>_{\bar{A}_0}$ [Å^2]	0.88 ± 0.78	0.99 ± 0.15
	a [s^{-1}]	1×10^{12}	1×10^{12}
	E_a [kJ mol^{-1}]	9.40 ± 22.20	14.46 ± 0.54
IN6 90 µeV	α [Å^2 K^{-1}]	0.00056 ± 0.00004	0.00058 ± 0.00004
	$<\Delta u^2>_{\bar{A}_0}$ [Å^2]	4.78 ± 1.80	5.65 ± 1.93
	a [s^{-1}]	1×10^{12}	1×10^{12}
	E_a [kJ mol^{-1}]	12.25 ± 0.99	12.62 ± 0.90

Table 9.2: Values obtained from fitting formula 9.2 to the mean square displacements of AChE and AChE + HupA. Values are given for data obtained on all spectrometers. a was fixed to a value of 1×10^{12} s^{-1} in order to allow the fit to converge. The value can be found in the literature as a typical value for barrier crossing in condensed-phase molecular systems [24, 152]. Due to the limited acquisition time on IN6 the native AChE sample elastic data could only be measured up to 270 K in the 50 µeV setup, therefore the obtained fit results show large errors compared to the other data sets.

	BChE	BChE + Soman
α [Å^2 K^{-1}]	0.00104 ± 0.00005	0.00119 ± 0.00003
$<\Delta u^2>_{\bar{A}_0}$ [Å^2]	1.78 ± 0.10	1.57 ± 0.06
a [s^{-1}]	1×10^{12}	1×10^{12}
E_a [kJ mol^{-1}]	19.39 ± 0.26	19.56 ± 0.18

Table 9.3: Values obtained from fitting formula 9.2 to the mean square displacements of BChE and BChE + Soman. As for the fits of the AChE data, the value for a was kept fix during the fitting procedure in order to allow a convergence of the fit.

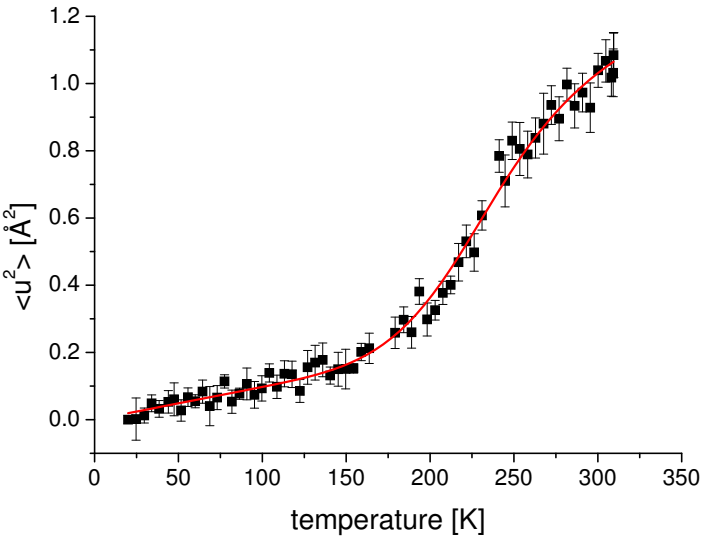

(a) MSDs of AChE with corresponding fit.

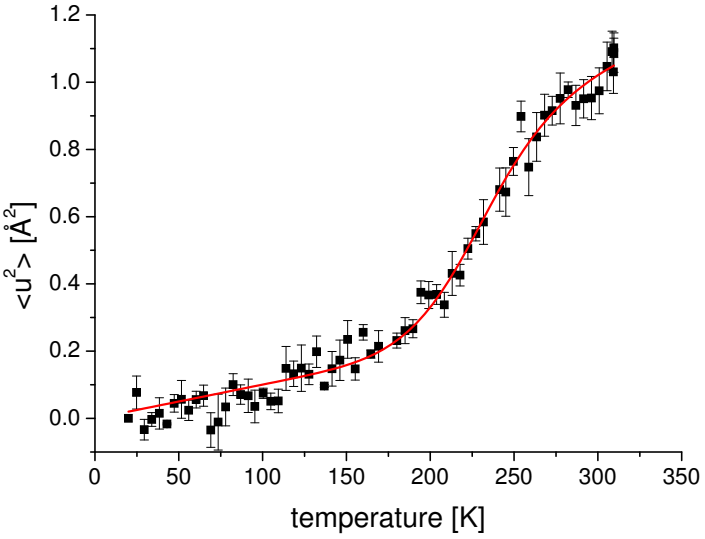

(b) MSDs of AChE + HupA with corresponding fit.

Figure 9.11: Evaluated mean square displacements of AChE and AChE + HupA on IN16 with corresponding fits according to equation 9.2. The obtained fit parameters are given in table 9.2.

With the values for a and E_a obtained by fitting equation 9.2 to the data, the resulting curves for κ are shown in figure 9.14. The elastic energy resolution of IN16 is about 1000 ps. The inverse of this value corresponds to a frequency of 0.001 ps^{-1}, which indicates the resolution limit of the spectrometer, and is drawn as horizontal line in figure 9.14a. Motions faster than this limit cannot be resolved by the spectrometer. The fact, that both, AChE and AChE + HupA, cross this line around 250 K is consistent with the finding of a kink around the same temperature in the mean square displacements.
In the case of BChE and BChE + Soman κ passes the resolution limit not until 330 K. Therefore the observed motions stay almost over the whole investigated temperature range within the resolution window of the spectrometer.
For the MSDs of AChE obtained on IN13 the situation presents itself differently. On this spectrometer the energy resolution is about 8 μeV, thus about a factor of 10 larger than the resolution of IN16. Therefore also the observation time is ten times shorter and hence the observable frequency ten times larger, respectively.
Fits to the mean square displacements are depicted in figure 9.13, they show no levelling off, as seen for IN16. Hence the κ obtained from the fits and drawn in figure 9.14b stay within the time resolution for IN13, indicated by the horizontal black line. The investigated fit range was limited to 310 K in order to exclude the influence of the protein denaturation occurring around a temperature of 330 K.

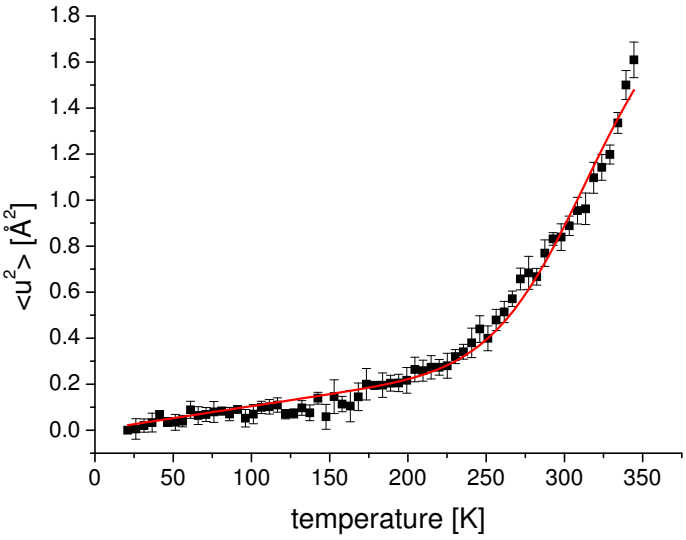

(a) MSDs of BChE with corresponding fit.

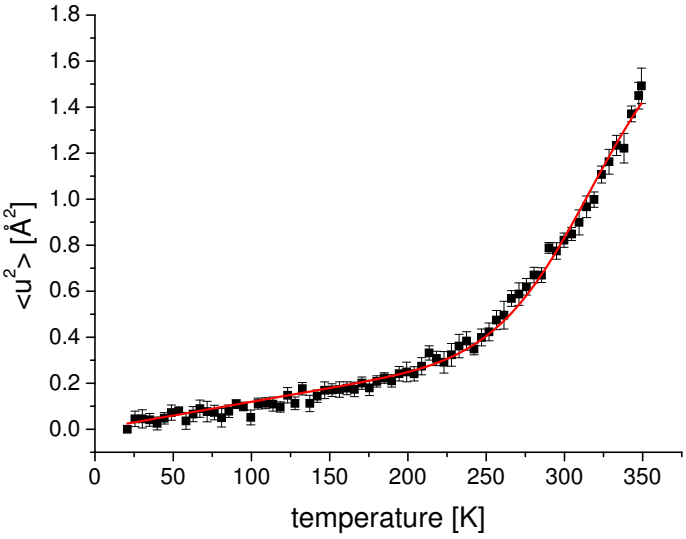

(b) MSDs of BChE + Soman with corresponding fit.

Figure 9.12: Evaluated mean square displacements of BChE and BChE + Soman on IN16 with corresponding fits according to equation 9.2. The resulting fit parameters are given in table 9.3.

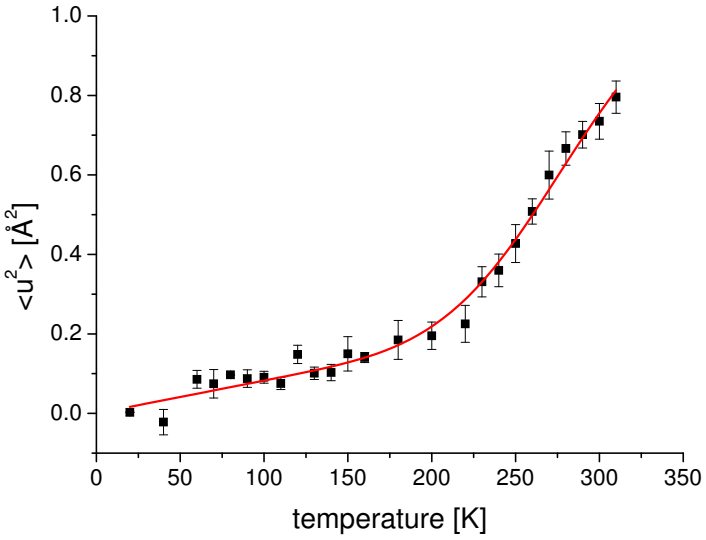

(a) MSDs of AChE with corresponding fit on IN13.

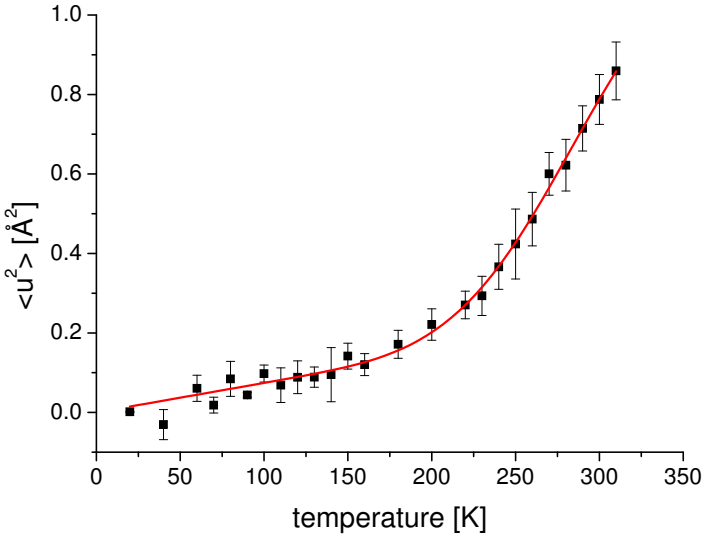

(b) MSDs of AChE + HupA with corresponding fit on IN13.

Figure 9.13: Evaluated mean square displacements of AChE and AChE + HupA with corresponding fits according to equation 9.2 on IN13. The obtained fit parameters are given in table 9.2. In order to exclude the influence of denaturation effects, the fit range was limited to a a range of 20 K–310 K.

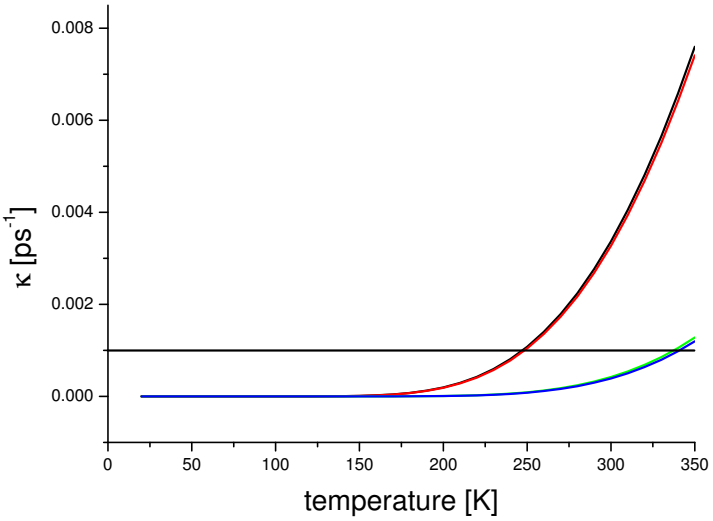

(a) Values for AChE are shown in black, AChE + HupA in red. The calculated values for BChE are given in green and for Soman in blue, respectively. The black horizontal line indicates the resolution limit of $\approx 0.001\,\mathrm{ps}^{-1}$ on IN16.

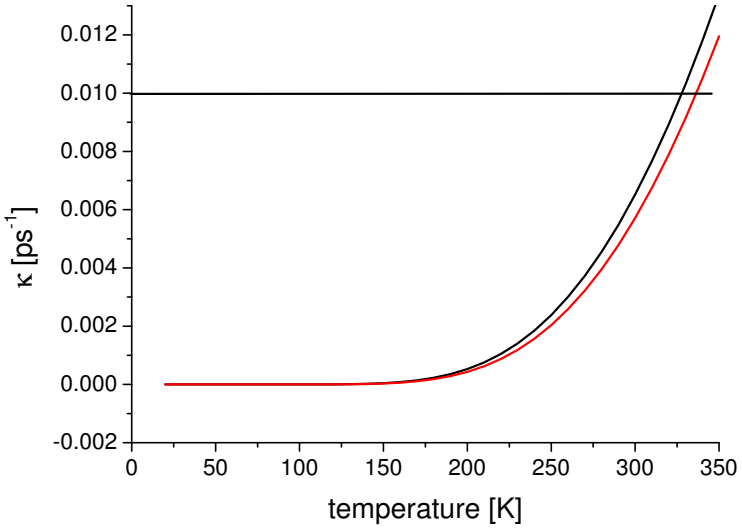

(b) Values for AChE are shown in black, AChE + HupA in red. The black horizontal line indicates the resolution limit of $\approx 0.01\,\mathrm{ps}^{-1}$ on IN13.

Figure 9.14: κ calculated according to equation 9.3 using the values obtained by fitting equation 9.2 to the MSDs for IN16 and IN13.

9.5 Quasi-elastic experiments

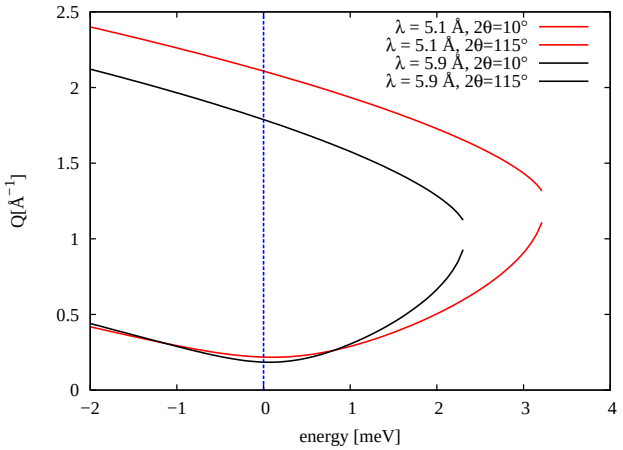

Figure 9.15: Dynamical ranges for the two wavelengths used on IN6. The dashed blue line represents the elastic line. In the data evaluation a Q-range of 0.5 Å^{-1}–1.6 Å^{-1} was chosen for a λ of 5.9 Å and 0.5 Å^{-1}–1.9 Å^{-1} for λ = 5.1 Å, respectively.

On a high flux instrument such as IN6 it is possible due to the high count rate around the elastic position to record the elastic data, during heating the samples from 20 K to room temperature. However to obtain reasonable statistics for quasi-elastic scans, longer count rates are necessary. Typical QENS measuring times lie in the order of several hours, instead of several minutes for an elastic scan.
Recorded data are corrected in the same way as elastic data for the scattering coming from the sample holder, then they are normalised to the 20 K data and grouped to increase the statistics.
Due to the two different wavelengths used in the experiments, the accessible Q-ranges differ slightly for the two resolutions, as can be seen from figure 9.15. For an incoming wavelength of λ = 5.9 Å and an energy transfer of ± 0.75 meV, the Q-range is limited to 0.5 Å^{-1}–1.6 Å^{-1}. Choosing a ΔQ of 0.1 Å^{-1} this results in 12 data points. For λ = 5.1 Å this can be extended to an energy transfer of ± 1 meV and a Q-value of 1.9 Å^{-1}. The same binning of ΔQ = 0.1 Å^{-1} was chosen, resulting in 15 groups.

The obtained data were fitted using a delta function for the elastic contribution, a single Lorentzian to mimic the quasi-elastic broadening and a slope background. The resulting fits for the native AChE sample and an

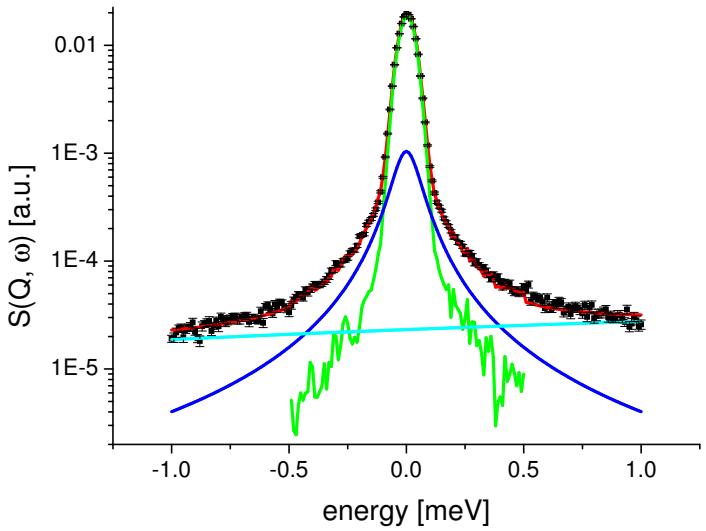

(a) Wave vector Q = 0.5 Å^{-1}.

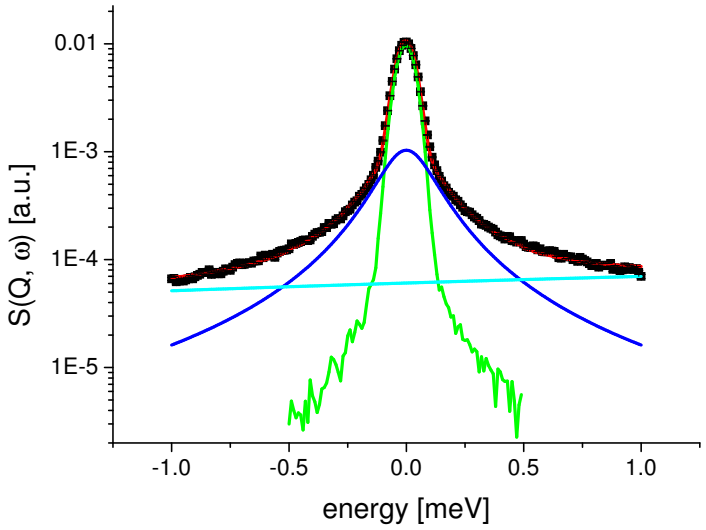

(b) Wave vector Q = 1.8 Å^{-1}.

Figure 9.16: S(Q, ω) of native AChE taken on IN6 (90 µeV energy resolution) with corresponding fits. Data are shown as black points with corresponding error bars. The delta function used as elastic line is shown in green, in blue is a single Lorentzian curve and in cyan a linear background is drawn. Due to the convolution with the experimental determined instrumental resolution, the elastic line shows noise for higher energy transfers. Data are given for the lowest and highest measured Q-value.

incident wavelength of 5.1 Å are shown in figure 9.16. Data and fits corresponding to the second measured resolution (5.9 Å $\widehat{=}$ 50 µeV) are given in figure 9.17. For comparison fits for the lowest and highest measured Q-values are given.
The half-width at half maximum Γ of the Lorentzian used in the fitting procedure are given in figure 9.18a for the 90 µeV setup and in figure 9.18b for the 50 µeV as a function of Q^2, respectively. From both figures it is obvious that in the limit of $Q \to 0$ the HWHM does not tend to zero. Γ increases with Q^2 and seems to approach asymptotically a constant value Γ_∞. The first feature indicates, as already mentioned in the theory section (section 3.6.2), that the diffusive motion is not free, but confined in space [24]. Using the "diffusion in a sphere" model introduced by Volino and Dianoux (cf. section 3.6.2) and the modification introduced by Bellissent-Funel et al., this can be taken into consideration for the data evaluation.
The radius of the sphere was extracted from fitting equation 3.30 to the Q-dependence of the EISF. The resulting fits are shown in figure 9.19 and the obtained values for the radius of the sphere and the percentage of immobile protons are given in table 9.4. For both investigated resolutions the obtained values for the EISF agree within experimental errors. The observed radius is larger for an incident wavelength of λ = 5.9 Å due to the longer observation time in comparison to an incident wavelength of λ = 5.1 Å. For the second parameter extracted from the fits, the immobile fraction, such a statement is not possible because of the large errors due to the restricted fit range at large Q-values (cf figure 9.19).
In contrast to MD simulations [121, 122] where specific sites of the enzyme can be investigated in more detail e.g. the gorge, neutron scattering probes the average over all protons present in the protein. Therefore the conclusion can be drawn that ligand binding can have a local effect on the dynamics of the gorge but a rather small impact on global dynamics.

		native AChE	AChE + HupA
λ = 5.1 Å	radius *a* [Å]	2.69 ± 0.07	2.71 ± 0.07
	immobile fraction *p* [%]	71.19 ± 3.71	69.81 ± 4.31
λ = 5.9 Å	radius *a* [Å]	2.93 ± 0.09	2.96 ± 0.06
	immobile fraction *p* [%]	69.37 ± 6.00	68.19 ± 4.23

Table 9.4: Results obtained from fitting the EISF with the "diffusion in a sphere" model. Values are given for both samples and both investigated energy resolutions.

The line widths of the Lorentzian are drawn in figure 9.18, as already

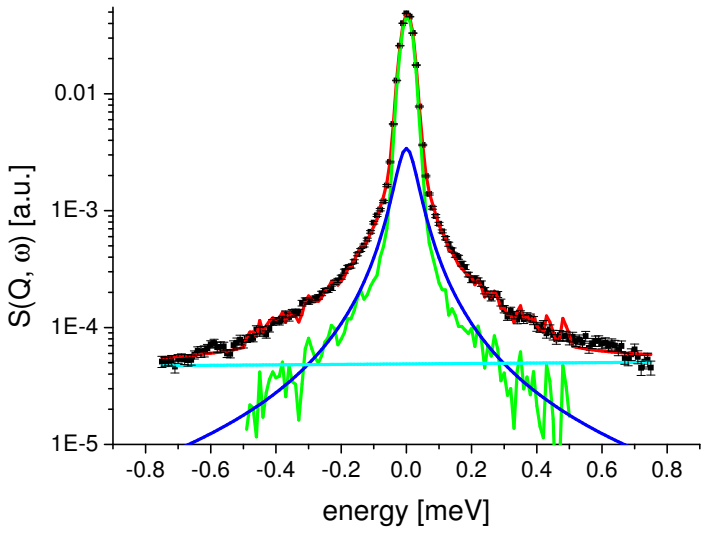

(a) Wave vector Q = 0.5 Å^{-1}.

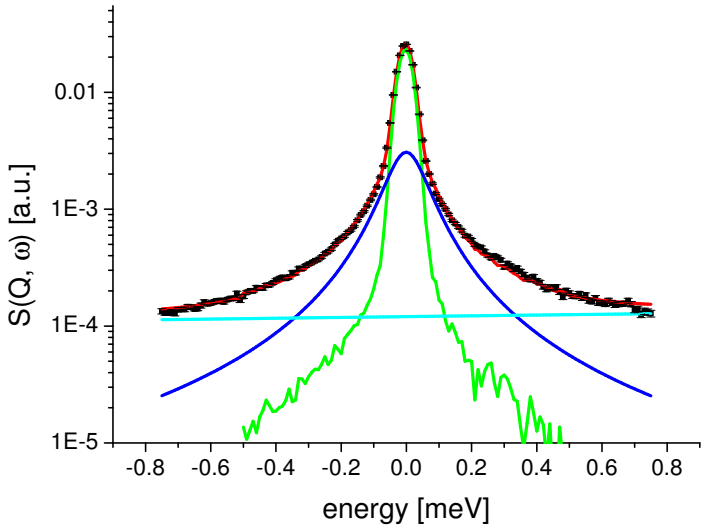

(b) Wave vector Q = 1.6 Å^{-1}.

Figure 9.17: S(Q, ω) of AChE + HupA taken on IN6 (50 µeV energy resolution) with corresponding fits. Data are shown as black points with corresponding error bars. The delta function used as elastic line is shown in green, in blue is a single Lorentzian curve and in cyan a linear background is drawn. Due to the convolution with the experimental determined instrumental resolution, the elastic line shows noise for higher energy transfers. Data are given for the lowest and highest measured Q-value.

mentioned above. For small Q-values, i.e. large distances, a confinement effect is visible. According to the "diffusion in a sphere" model (cf section 3.6.2), the diffusion coefficient D can be estimated from the limit Γ_0 for $Q \rightarrow 0$ according to equation 3.31. The resulting values are given in table 9.5 for 90 µeV. For the 50 µeV energy resolution the values for D were extracted from fitting equation 3.32 to the data, corresponding values are shown in table 9.5. Again, the obtained values match within experimental errors for both resolutions.
For large Q-values, the line width does not follow a free diffusion. For free diffusion Γ can be written as $\Gamma = DQ^2$. In the here investigated case the line width shows a jump diffusion behaviour, described by equation 3.32. High Q-values correspond to short length scales, thus local motions such as jumps of the observed protons become dominant. The residence time τ between two jumps is given by $\tau = 1/\Gamma_\infty$, where Γ_∞ can be extracted from the asymptotic behaviour of Γ for high Q, where a constant value Γ_∞ is reached.
For both resolutions the line width is still increasing at high Q-values and has not yet reached a plateau in the investigated Q-range. Therefore the values have to be extracted from fitting equation 3.32 to the data. Corresponding values for τ are also given in tables 9.5 and 9.6.
The characteristic jump distance can be calculated using:

$$l = \sqrt{D\tau}. \tag{9.4}$$

Again the obtained results are given in tables 9.5 and 9.6. As for all other parameters obtained, also the jump lengths for native AChE and AChE + HupA agree within experimental errors.
In order to perform a jump, protons have to overcome an energy barrier imposed by the surrounding energy landscape. The height of this energy barrier is linked to the residence time via the Arrhenius relation:

$$\tau = \tau_0 e^{E_a/k_B T}, \tag{9.5}$$

where τ_0 is a pre-factor and E_a the activation energy of the process. When τ_0 is assumed to be the same for native AChE and its inhibited counterpart, ΔE_a can be written as

$$\Delta E_a = k_B T \ln\left(\frac{\tau_{AChE}}{\tau_{HupA}}\right). \tag{9.6}$$

Using equation 9.6 the activation energy difference between the two investigated systems is found to be $\Delta E_{a,90\,\mu eV}$ = 10.47 ± 0.30 and $\Delta E_{a,50\,\mu eV}$ = 11,90 ± 0.43 cal/mol, respectively. Both values correspond to approximately 0.02k_BT and therefore only to very small energy differences.

In this section first quasi-elastic neutron scattering data on native AChE and AChE + HupA for two different energy resolutions are presented. Information on internal diffusion motion were extracted from fits to the quasi-elastic broadening of the experimental scattering function. The analysis of the EISF gave information on the radii in which protons diffuse according to the "diffusion in a sphere" model [31]. In addition the immobile fraction of hydrogens in the observed space-time window could be extracted. The evaluation of the HWHM of the Lorentzian broadening permits a detailed evaluation of the observed diffusive motions. In the low Q-region a confinement effect is observed as deviation from the DQ^2 law. For the higher Q-values, the diffusion can be described by jump diffusion. Both diffusion constants D and residence times τ were calculated. All results obtained in this section agree within the experimental errors for the native AChE and its inhibited counterpart. Even if the here presented results were obtained using hydrated powders, they yield values for D and τ which can be compared to values obtained on proteins in solution, e.g. [93].

9.6 Conclusion and outlook

In this chapter extensive neutron scattering studies on human AChE are described. The dynamics in the pico to nanosecond time have been explored using four different elastic energy resolutions. The results from the elastic scattering experiments (section 9.3) showed that more than one relaxation process is observed. From the fact, that the observed motions leave the time window of IN16 a maximal timescale of the motion can be inferred.
In section 9.4 the mean square displacements of human AChE and human BChE have been investigated. A clear difference in the msds has been detected. Already some explanations have been given in section 9.4, but in order to further clarify the reasons for the different behaviours, several additional investigations have to be performed.
Finally, in section 9.5 the results from the quasi-elastic experiments on IN6 are presented. The evaluation of the obtained EISFs and Lorentzian widths permits a more detailed picture of the internal diffusive motions than the elastic data but showed also no significant difference between the native and the inhibited form of AChE.
In a next step EINS studies on different kinds of AChE, especially mouse ACHE (mAChE) are planned using the same four energy resolutions as for AChE. With the results from these experiments it will be possible to show, if there is already a large variation of MSDs between AChE from different species or if the observed difference between human AChE and BChE is due structural differences between the two enzymes. Especially the results from IN16 where a comparison of all samples is possible will help to clarify this fact.

In addition to the experimental approach, MD simulations are foreseen. So far it was not possible to perform MD simulations of human AChE because there was no crystal structure available. The crystal structure of human AChE in its apo state has only been published very recently [110].
With the now available crystallographic data, MD simulations of human AChE and BChE will be performed in the ns range to cover the time window of IN16 in order to find the origin of the observed difference in the neutron data obtained on this spectrometer. The experimental data obtained on mAChE will also be included in the analysis, because there exist already MD simulations on this type of AChE [121–123], not only in the native form but also in complex with HupA.

9.7 Conclusion en français

Dans ce chapitre, des études détaillées de l'AChE humaine par diffusion de neutrons sont décrites. La dynamique dans le domaine du temps allant de la pico- à la nano -seconde a été explorée en utilisant quatre différentes résolutions pour l'énergie élastique. Les résultats des expériences de diffusion élastique (section 9.3) ont montré que plus d'un processus de relaxation est contenu dans la dynamique. Le fait que les mouvements observés sortent la fenêtre de temps de IN16 permet de déduire l'échelle de temps maximale des mouvements.
Dans la section 9.4 les déplacements carrés moyens de l'AChE humaine et de la BChE humaine ont été étudiés. Une différence considérable dans leurs MSD a été détectée. Quelques explications sont proposées dans la section 9.4, mais pour mieux comprendre les raisons des comportements différents, plusieurs études supplémentaires sont envisagées.
Nous voulons réaliser des études EINS sur différents types de AChE, en particulier l'ACHE de souris (mAChE). Avec les résultats de ces expériences nous pourrons voir si il existe déjà une grande variation entre les MSD de différentes espèces, ou si la différence observée entre l'AChE et la BChE humaines est due à des différences structurales entre les deux enzymes.
Une autre approche sera effectuée à l'aide de simulations de dynamique moléculaire. Jusqu'à présent, il n'était pas possible d'entreprendre de telles simulations de l'acétylcholinestérase humaine, parce qu'il n'existait pas de structure cristalline publiée. La structure cristalline de l'AChE humaine dans son état apo n'a été publiée que très récemment [110].
Avec les nouvelles données cristallographiques, des simulations de dynamique moléculaire de l'AChE et de la BChE humaines seront effectuées dans le domaine de la ns pour couvrir la fenêtre de temps de IN16, afin de mieux comprendre l'origine de la différence observée dans les données neutroniques obtenues sur ce spectromètre. En outre, les mesures recueillies sur mAChE pourront également être incluses dans l'analyse, car il

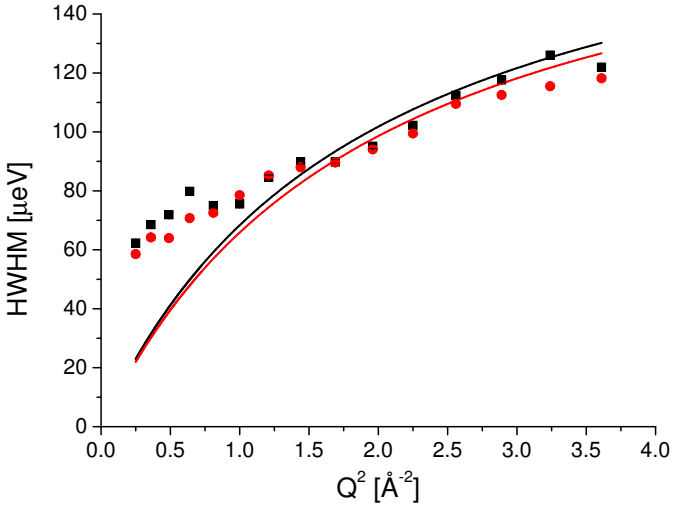

(a) Lorentzian width at a wavelength of 5.1 Å (elastic energy resolution: 90 μeV). Fit curves correspond to equation 3.32 of the jump diffusion model. A clear deviation for low Q-values, corresponding to confinement effects, is visible. The results from the fits are given in table 9.5.

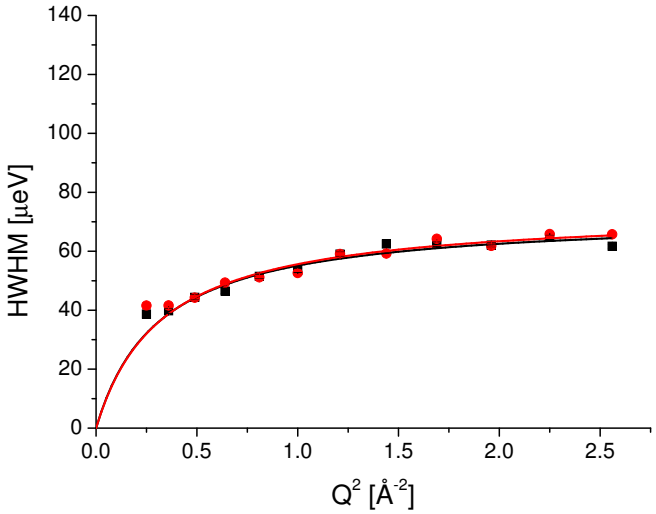

(b) Lorentzian width for the data taken at 50 μeV. Fit corresponds to the jump diffusion model (see equation 3.32). The results from the fit are given in table 9.6.

Figure 9.18: Half widths of the quasi-elastic Lorentzian as a function of Q^2 for native AChE (black squares) and AChE + HupA (red circles) for both investigated resolutions on IN6. The colors of the fit curves correspond to respective sample.

existe déjà des simulations MD sur ce type d'AChE [121–123], et non seulement dans sa forme native, mais aussi en complexe avec HupA.
Enfin, dans la section 9.5 les résultats des expériences quasi-élastiques sur IN6 sont présentés. L'évaluation des EISFs fournisse une image plus détaillée de la dynamique que les données élastiques seules.

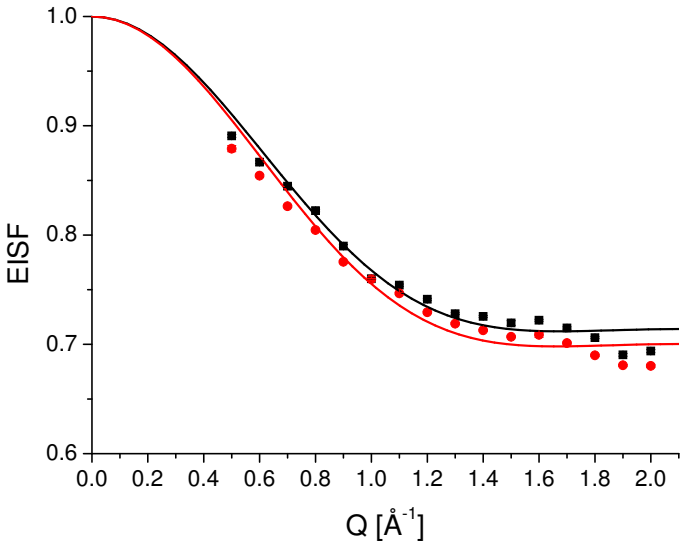

(a) EISF for an incident wavelength of 5.1 Å (elastic energy resolution : 90 µeV).

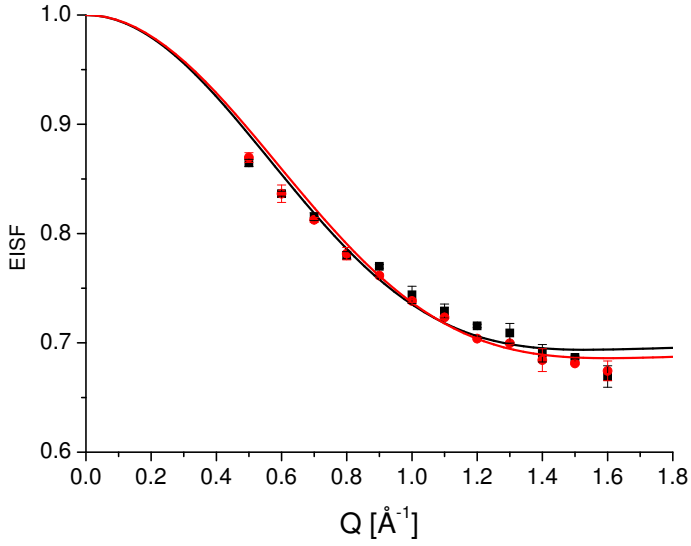

(b) EISF for an incident wavelength of 5.9 Å (elastic energy resolution : 50 µeV).

FIGURE 9.19 – Elastic incoherent structure factor for both resolutions measured on IN6. Data and corresponding fits for pure AChE are drawn in black, for AChE + HupA data and fits are depicted in red. The values extracted from the fits are given in table 9.4.

	native AChE	AChE + HupA
D $[10^{-5}\,\mathrm{cm^2\,s^{-1}}]$	1.58 ± 0.07	1.51 ± 0.06
τ [ps]	3.30 ± 0.29	3.36 ± 0.31
l [Å]	0.72 ± 0.04	0.71 ± 0.04
ΔE_a [cal/mol]	10.47 ± 0.30	

Table 9.5: Values obtained by fitting equation 3.32 to the data obtained with 90 µeV energy resolution and shown in figure 9.18a.

	native AChE	AChE + HupA
D $[10^{-5}\,\mathrm{cm^2\,s^{-1}}]$	3.53 ± 0.33	3.45 ± 0.31
τ [ps]	9.11 ± 0.23	8.93 ± 0.22
l [Å]	1.79 ± 0.17	1.76 ± 0.16
ΔE_a [cal/mol]	11.90 ± 0.43	

Table 9.6: Values obtained by fitting equation 3.32 to the data at 50 µeV energy resolution and shown in figure 9.18b. Due to the levelling of at small Q-values the, first data point was excluded from the fit.

Appendix A

Abbreviations

AChE	Acetylcholinesterase
BChE	Butyrylcholinesterase
CCD	Charge-coupled device
CRG	Collaborating research group
DMPA	1,2-dimyristoyl-*sn*-glycero-3-phosphate
DMPC	1,2-dimyristoyl-*sn*-glycero-3-phosphocholine
DMPC-d54	1,2-dimyristoyl-d54-*sn*-glycero-3-phosphocholine
DPPC	1,2-dipalmitoyl-*sn*-glycero-3-phosphocholine
EINS	Elastic incoherent neutron scattering
EISF	Elastic incoherent structure factor
eV	Electron volt
FRMII	Forschungsreaktor München II
FWHM	Full width at half maximum
HHP	High hydrostatic pressure
HupA	Huperzine A
HWHM	Half width at half maximum
IBS	Institut de Biologie Structurale
ILL	Institut Laue-Langevin
LLB	Laboratoire Léon Brillouin
MD	Molecular dynamics
msd	Mean square displacement
NSE	Neutron spin echo
PDG	Particle data group
PSD	Position Sensitive Detector
PSI	Paul Scherrer Institut
QENS	Quasi-elastic neutron scattering
QISF	Quasi-elastic incoherent structure factor
rpm	Revolutions per minute
SNS	Spallation neutron source

Appendix B

Physical constants

Planck constant:

$$\begin{aligned} h &= (6.626\,068\,96 \pm 0.000\,000\,33) \times 10^{-34}\,\mathrm{J\,s} \\ &= (4.135\,667\,33 \pm 0.000\,000\,10) \times 10^{-15}\,\mathrm{eV\,s} \end{aligned}$$

reduced Planck constant

$$\begin{aligned} \hbar = \frac{h}{2\pi} &= (1.054\,571\,628 \pm 0.000\,000\,053) \times 10^{-34}\,\mathrm{J\,s} \\ &= (6.582\,118\,99 \pm 0.000\,000\,16) \times 10^{-16}\,\mathrm{eV\,s} \end{aligned}$$

Boltzmann constant

$$\begin{aligned} k_B &= (1.380\,650\,4 \pm 0.000\,002\,4) \times 10^{-23}\,\mathrm{J\,K^{-1}} \\ &= (8.617\,343 \pm 0.000\,015) \times 10^{-5}\,\mathrm{eV\,K^{-1}} \end{aligned}$$

Avogadro constant

$$N_A = (6.022\,141\,79 \pm 0.000\,000\,30) \times 10^{30}\,\mathrm{mol^{-1}}$$

Gas constant

$$\begin{aligned} R = N_A \cdot k_B &= (8.314\,472 \pm 0.000\,015)\,\mathrm{J\,mol^{-1}\,K^{-1}} \\ &= 5.189 \times 10^{19}\,\mathrm{eV\,mol^{-1}\,K^{-1}} \end{aligned}$$

Appendix C

Amino acid composition of hAChE

Amino acid		number	percentage
Ala	(A)	55	9.0
Arg	(R)	43	7.0
Asn	(N)	17	2.8
Asp	(D)	29	4.7
Cys	(C)	8	1.3
Gln	(Q)	24	3.9
Glu	(E)	34	5.5
Gly	(G)	58	9.4
His	(H)	15	2.4
Ile	(I)	9	1.5
Leu	(L)	69	11.2
Lys	(K)	10	1.6
Met	(M)	9	1.5
Phe	(F)	29	4.7
Pro	(P)	51	8.3
Ser	(S)	36	5.9
Thr	(T)	26	4.2
Trp	(W)	17	2.8
Tyr	(Y)	21	3.4
Val	(V)	54	8.8

Table C.1: Amino acid composition of human AChE.

Atom		number in protein
Carbon	C	3074
Hydrogen	H	4673
Nitrogen	N	841
Oxygen	O	865
Sulfur	S	17

Table C.2: Atomic content of human AChE.

Appendix D

Articles

In this chapter all accepted articles are listed, I contributed to. They are quoted in the order of their publication data, staring with the earliest.

D.1 Elastic scattering studies of aligned DMPC multilayers on different hydrations

The following article was published in the proceedings of the XIII European Conference on the Spectroscopy of Biological Molecules, held in Palermo, Italy from August 28 - September 2, 2009. During the conference I presented a poster with results of a measuring campaign on IN16, ILL. The presented results are summarised in the following article.

Spectroscopy 24 (2010) 461–466
DOI 10.3233/SPE-2010-0481
IOS Press

Elastic scattering studies of aligned DMPC multilayers on different hydrations [1]

Marcus Trapp [a], Fanni Juranyi [b], Moeava Tehei [c,d], Lambert van Eijck [e], Bruno Demé [e], Thomas Gutberlet [f] and Judith Peters [a,e,g,*]

[a] *Institut de Biologie Structurale J.-P. Ebel, UMR 5075, CNRS-CEA-UJF, Grenoble, France*
[b] *LNS, ETH Zürich and Paul Scherrer Institut, Villigen, Switzerland*
[c] *Australian Institute of Nuclear Science and Engineering, Menai, Australia*
[d] *School of Chemistry and Centre for Medical Bioscience, University of Wollongong, Wollongong, Australia*
[e] *Institut Laue-Langevin, Grenoble, France*
[f] *JCNS at FRMII, Garching, Germany*
[g] *Université Joseph Fourier, Grenoble, France*

Abstract. Biological membranes, consisting mainly of phospholipids and proteins, are organized in a bilayered structure which exhibits dynamical behaviour within time regimes ranging from 10^{-12} s with the motion of alkyl chain defects and 1 s corresponding to collective excitations of the bilayer [*Europhysics Letters* **8** (1989), 201–206]. With the prominent role hydration plays on the structural phase behaviour of phospholipids membranes, it is essential for a better description of membranes to understand also the influence of hydration on the dynamics of membrane systems. In the present study we have performed neutron scattering investigations on highly oriented DMPC-d54 multilayers at two different relative humidity (rh) levels. Our results reveal the strong influence of hydration on the local membrane dynamics, i.e., head group dynamics.

Keywords: Oriented model membranes, elastic neutron scattering, dynamics, hydration effects

1. Introduction

Biological membranes consist not only of different kinds of lipids, but also of membrane proteins and molecules like, e.g., cholesterol and ethanol [18]. To investigate the physical and structural behaviour of such complex systems, lipid membranes consisting of only one type of lipid such as 1,2-Dimyristoyl-*sn*-Glycero-3-Phosphocholine (DMPC) serve as suitable model systems.

Saturated phospholipids like DMPC show two phase transitions: (1) a pre-transition from the L_β gel phase to the P_β ripple phase (DMPC at 286 K) and (2) the main phase transition from the P_β ripple phase to the liquid-crystalline L_α phase (DMPC at 296 K) where the mobility of the alkyl chains is enhanced with respect to the gel phase [10]. For chain deuterated lipids which were used in this study the temperature of the main phase transition is shifted by about 3 K to lower temperatures [6].

Lowering the water content reduces the repeating distance of the bilayers. In addition, structural investigations [20] show that a lower degree of hydration causes a shift of the main phase transition to

[1] This paper was presented at ECSBM, Palermo, Italy, August 28–September 2, 2009. Guest Editor: A. Cupane.

[*] Corresponding author: Judith Peters, Université Joseph Fourier, F-38042 Grenoble Cédex 9, France. Tel.: +33 476 20 75 60; Fax: +33 476 20 76 88; E-mail: peters@ill.fr.

higher temperatures. The effect can be observed by X-ray or neutron diffraction following the shift in the distance of the Bragg peaks of the lipid bilayers. The relation $d = \lambda/2 \times \sin(\theta)$ (λ – X-ray or neutron wavelength, θ – scattering angle) allows to calculate the repeating distance d. For a fully hydrated DMPC bilayer, the repeating distance d is around 63 Å [8]. While the influence of hydration on the structural properties of membranes is well investigated [20], its influence on dynamic behaviour is rather poor.

The diffusive motions of lipids within the bilayer have been explored by quasi-elastic neutron scattering [7,14,22]. More recently collective motions of the lipid bilayer were also studied with inelastic neutron scattering [15]. However, the hydration effects on the lipid bilayer properties were not enclosed in these investigations. In this study, we thus performed neutron scattering investigations on highly oriented DMPC multilayers at two different relative humidity (rh) levels with the aim to fill this gap. Our results reveal the strong influence of hydration on the local membrane dynamics.

2. Materials and methods

2.1. Sample preparation

To probe dynamics of lipid membranes in and out of plane, oriented samples can be prepared on very smooth surfaces such as silicon wafers or mica sheets. Solid supported bilayer systems also allow the preparation of large amount of sample (≈150–200 mg) required in inelastic and quasi-elastic neutron scattering experiments [19]. Another advantage of this preparation method is the very low mosaic spread (below 0.5°). Each Si-wafer was of size of about 30 × 40 mm which fitted perfectly the dimensions of the flat gold coated aluminium sample cells used for the experiments.

Alkyl chain deuterated 1,2-dimyristoylphosphatidylcholine-d54 (DMPC-d54) was purchased from Avanti Polar Lipids (Alabaster, AL, USA) and used without further purification. The DMPC powder was dissolved in a 3:1 chloroform–trifluoroethanol (TFE) mixture following a protocol described in [2]. This solution was then kept at -20°C overnight.

About 30 mg of lipid was deposited on a single wafer. After the deposition the wafers were dried for two days in a desiccator. One sample was rehydrated from pure D_2O with relative humidity of 100%, another one was rehydrated from a saturated salt solution (D_2O + NaCl) with reduced relative humidity of 75%. Six such wafers were placed in the sample cell and sealed to achieve an amount of about 200 mg hydrated lipid bilayers per sample. The weight of both samples was monitored and no change in weight before and after the neutron experiments was observed.

2.2. Elastic neutron experiments

The level of hydration, the mosaicity of the 1D lamellar order and the evolution of the repeat distance (d-spacing) of the bilayers with temperature were checked by neutron diffraction measurements on the small momentum transfer diffractometer D16 at the Institut Laue-Langevin (ILL), Grenoble, France [1]. After heating to 330 K to allow annealing of defects, scans were performed to obtain the repeat distance of the membranes at three different temperatures, namely, 330, 310 and 280 K. During the temperature changes data were taken to identify the temperature of the main phase transition. An example of the evolution of the d-spacing with temperature is shown in Fig. 1.

Elastic temperature scans in the range of 280–330 K were performed on the cold neutron backscattering spectrometer IN16 at ILL at an energy resolution of $\Delta E = 0.9$ μeV (full width half maximum) and an accessible Q-range of 0.19–1.93 Å^{-1} [5]. The investigated temperature range covers both the main

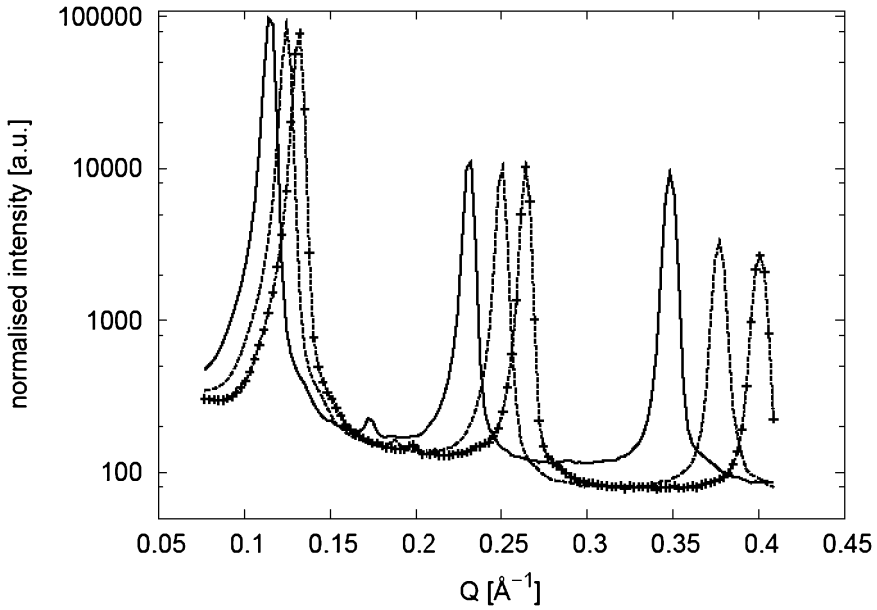

Fig. 1. Diffraction data taken on D16 at ILL. Data are shown for three different temperatures: 280 K (straight line), 310 K (broken line) and 330 K (broken line with crosses). The sample was hydrated from a saturated salt solution (D_2O + NaCl) resulting in a relative humidity of 75%.

phase transition from the P_β ripple to the liquid-crystalline L_α phase which occurs around 296 K for DMPC at full hydration and also the pre-transition from the L_β gel phase to the P_β ripple phase about 10 degrees below the main phase transition.

Special care was taken on the orientation of the sample to probe motions around the chain correlation peak at $Q = 1.48$ Å^{-1} parallel and perpendicular to the membrane surface. Via the relation $Q = 4\pi \sin(2\theta)/\lambda$ the angle of the sample with respect to the incoming beam was calculated to be 135° for the orientation parallel to the membrane surface and 45° for the perpendicular orientation, respectively. From the obtained data an empty cell was subtracted and the data were normalised by the scattering of a 1 mm vanadium sample.

3. Results and discussion

From the shift of the main phase transition temperature to higher temperatures with decreasing water content (see Section 1 and Fig. 1 in [20]), it is possible to evaluate the water content between the phospholipid surfaces. We can extract the parameter $R_w = n_W/n_A$ where R_w expresses the molar ratio of water (n_W) and amphiphile (n_A) [12,13]. Figure 2 (using the left y-axis) shows the summed elastic intensities measured for the parallel orientation at 135° with respect to the incoming beam for the two samples on IN16. At the temperature of the main phase transition a drastic decrease in the elastic intensity occurs. The phase transition temperature moves to higher temperatures for the sample with lower water content. The calculated R_w for the higher hydrated sample is $R_w \approx 6$ (transition temperature: 305 K) and $R_w \approx 4$ for the less hydrated sample (transition temperature: 310 K). Pfeiffer et al. find for DMPC multilayers a value of $R_w \geqslant 12$ for fully hydrated membranes [13].

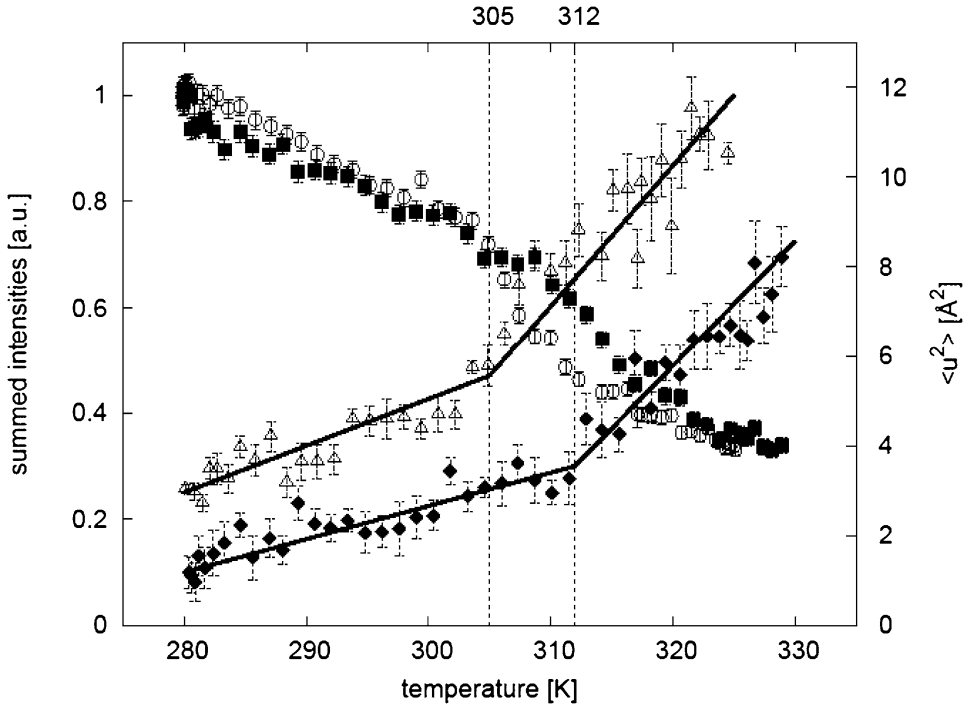

Fig. 2. Summed elastic intensity (Q-range: 0.43–1.16 Å^{-1}) measured at 135° (left y-scale, filled squares: $R_{\mathrm{w}} \approx 4$, empty circles: $R_{\mathrm{w}} \approx 6$) and mean square displacements $\langle u^2 \rangle$ (right y-scale, filled diamonds: $R_{\mathrm{w}} \approx 4$, empty triangles: $R_{\mathrm{w}} \approx 6$). Drawn lines are guides to the eyes to follow the evolution of the mean square displacements. Data taken on the cold neutron spectrometer IN16 at ILL (energy resolution: 0.9 μeV). Intensities are normalised to the lowest temperature.

To characterise the local dynamics from the elastic neutron scattering intensity, the so-called mean square displacements (msd) $\langle u^2 \rangle$ were calculated. The elastic scattering function $S(Q, \omega = 0)$ can be approximated by $S(Q, \omega = 0) \approx \exp(1/6 \times \langle u^2 \rangle Q^2)$ [21]. From the slope of a linear fit to a semi-logarithmic plot of the data one can extract the $\langle u^2 \rangle$. Below the temperature of the main phase transition, coherent scattering arising from the ordering of the alkyl chain, gives rise to the so-called "chain correlation peak" around a characteristic Q-value of 1.48 Å^{-1}. Therefore the fit range was limited to 0.18 Å$^{-2} \leqslant Q^2 \leqslant$ 1.33 Å^{-2} in our data analysis. As shown in Fig. 2 (using the right y-axis) the $\langle u^2 \rangle$ show transitions at 305 and 310 K for the higher and lower hydrated sample, respectively. At first sight the evaluated mean square displacements are very large above temperature of the main phase transition, but $\langle u^2 \rangle$ in the same order of magnitude have been observed in a previous study which aimed to investigate the influence of the myelin basic protein (MBP) on the dynamics of model membranes (DMPA in this study) [11]. A recently published molecular-dynamics simulation performed on fully hydrated DMPC bilayers in the L_α phase (at 303 K) also shows very large $\langle u^2 \rangle$ at this temperature, even larger then the two partially hydrated samples used in our study [4]. Hence we attribute the difference in the values of the mean square displacements to the different hydrations of the samples, ranging from the highest $\langle u^2 \rangle$-value for the simulation (≈8 Å^2 for the centre of mass) to the sample with the lowest hydration of $R_{\mathrm{w}} \approx 4$ (≈2.9 Å^2). The authors differentiate three different diffusion regimes in time: (1) a ballistic region where $\langle u^2 \rangle \sim t^2$; (2) a subdiffusive domain where $\langle u^2 \rangle \sim t^\beta$ with $\beta < 1$ and (3) a domain of Fickian diffusion with $\langle u^2 \rangle \sim t$. According to this simulation, the time window of IN16 of about 700 picoseconds probes length scales in the subdiffusive regime. A detailed analysis of quasi-

elastic data taken in both the L_β gel and liquid-crystalline L_α phase is still in progress [23]. In order to compare the results obtained from the mean square displacement (using the right y-axis in Fig. 2) with the summed elastic intensities, the intensities shown in Fig. 2 (using the left y-axis) were summed over the same Q-range (0.43 $\text{Å}^{-1} \leqslant Q \leqslant 1.16$ Å^{-1}) which was used in the evaluation of the msd's. The effect is stronger for the summed intensities due to adding up the signals from all detectors in the used Q-range. From hydration dependent studies of, e.g., bacteriorhodopsin [9] it is known that with increasing hydration the msd's show a steeper slope only at high relative humilities in contrast to protein where a steady rice of the msd is observed [17]. Only small difference of the calculated slopes in the L_α phase (higher hydrated sample: 0.258 ± 0.0157, less hydrated sample: 0.224 ± 0.022) of our results confirm these finding.

Rheinstaedter et al. [16] analyzed the elastic intensity at various Q-values of DMPC to map out the transition of the different molecular components from immobile to mobile as a function of temperature. The effect of hydration on the membrane dynamics was neglected in their analysis. Our study reveals the strong influence hydration has on the membrane systems, not only on the structure but also on the dynamics. Similar to hydrated protein powders [3] also phospholipids show a dynamic transition in the mean square displacements $\langle u^2 \rangle$ and a shift of the temperature of the main phase transition depending on their hydration. The transition for proteins occurs around 200 K and is often called "dynamical transition". In the case of membranes this transition is due to the structural transition into the liquid-crystalline L_α phase. In contrast to proteins were the individual amino acid is hydrated to allow local motions of the proteins in phospholipid bilayers only the hydration of the hydrophilic head group of the phospholipid triggers the dynamic response of the hydration shielded hydrophobic alkyl chains. In conclusion special care should be taken for the hydration control to avoid a mixing of effects, which could be partly due to the hydration state of the sample.

Acknowledgements

We acknowledge the ILL for the allocation of beamtime and the financial support from the Access to Major Research Facilities Programme which is a component of the International Science Linkages Programme established under the Australian Government's innovation statement, Backing Australia's Ability.

References

[1] http://www.ill.eu/d16/.
[2] L. Ding, T.M. Weiss, G. Fragneto, W. Liu, L. Yang and H.W. Huang, Distorted hexagonal phase studied by neutron diffraction: lipid components demixed in a bent monolayer, *Langmuir* **21** (2005), 203–210.
[3] W. Doster, S. Cusack and W. Petry, Dynamical transition of myoglobin revealed by inelastic neutron scattering, *Nature* **337** (1989), 754–756.
[4] E. Flenner, J. Das, M.C. Rheinstadter and I. Kosztin, Subdiffusion and lateral diffusion coefficient of lipid atoms and molecules in phospholipid bilayers, *Physical Review E – Statistical, Nonlinear, and Soft Matter Physics* **79** (2009), 011907.
[5] B. Frick and M. Gonzalez, Five years operation of the second generation backscattering spectrometer IN16 – a retrospective, recent developments and plans, *Physical Review B – Condensed Matter* **301** (2001), 8–19.
[6] D. Guard-Friar, C.H. Chen and A.S. Engle, Deuterium isotope effect on the stability of molecules: phospholipids, *The Journal of Physical Chemistry* **89** (1985), 1810–1813.
[7] S. König, W. Pfeiffer, T. Bayerl, D. Richter and E. Sackmann, Molecular dynamics of lipid bilayers studied by incoherent quasi-elastic neutron scattering, *Journal de Physique II France* **2** (1992), 1589–1615.

[8] N. Kucerka, Y. Liu, N. Chu, H.I. Petrache, S. Tristram-Nagle and J.F. Nagle, Structure of fully hydrated fluid phase DMPC and DLPC lipid bilayers using X-ray scattering from oriented multilamellar arrays and from unilamellar vesicles, *Biophysical Journal* **88** (2005), 2626–2637.
[9] U. Lehnert, V. Réat, M. Weik, G. Zaccaï and C. Pfister, Thermal motions in bacteriorhodopsin at different hydration levels studied by neutron scattering: correlation with kinetics and light-induced conformational changes, *Biophysical Journal* **75** (1998), 1945–1952.
[10] J.F. Nagle, Theory of the main lipid bilayer phase transition, *Annual Review of Physical Chemistry* **31** (1980), 157–196.
[11] F. Natali, A. Relini, A. Gliozzi, R. Rolandi, P. Cavatorta, A. Deriu, A. Fasano and P. Riccio, The influence of the lipid–protein interaction on the membrane dynamics, *Physical Review B – Condensed Matter* **350** (2004), E623–E626.
[12] H. Pfeiffer, H. Binder, G. Klose and K. Heremans, Hydration pressure and phase transitions of phospholipids: I. Piezotropic approach, *Biochimica et Biophysica Acta – Biomembranes* **1609** (2003), 144–147.
[13] H. Pfeiffer, H. Binder, G. Klose and K. Heremans, Hydration pressure and phase transitions of phospholipids: II. Thermotropic approach, *Biochimica et Biophysica Acta – Biomembranes* **1609** (2003), 148–152.
[14] W. Pfeiffer, T. Henkel, E. Sackmann, W. Knoll and D. Richter, Local dynamics of lipid bilayers studied by incoherent quasi-elastic neutron scattering, *Europhysics Letters* **8** (1989), 201–206.
[15] M.C. Rheinstädter, C. Ollinger, G. Fragneto, F. Demmel and T. Salditt, Collective dynamics of lipid membranes studied by inelastic neutron scattering, *Physical Review Letters* **93** (2004), 108107.
[16] M.C. Rheinstädter, T. Seydel, F. Demmel and T. Salditt, Molecular motions in lipid bilayers studied by the neutron backscattering technique, *Physical Review E – Statistical, Nonlinear, and Soft Matter Physics* **71** (2005), 061908.
[17] J.H. Roh, J.E. Curtis, S. Azzam, V.N. Novikov, I. Peral, Z. Chowdhuri, R.B. Gregory and A.P. Sokolov, Influence of hydration on the dynamics of lysozyme, *Biophysical Journal* **91** (2006), 2573–2588.
[18] E. Sackmann, Biological membranes architecture and function, in: *Structure and Dynamics of Membranes, Handbook of Biological Physics*, Vol. 1, R. Lipowsky and E. Sackmann, eds, Elsevier, Amsterdam, 1995, pp. 1–64.
[19] T. Salditt and M.C. Rheinstädter, Structure and dynamics of model membrane systems probed by elastic and inelastic neutron scattering, in: *Neutron Scattering in Biology, Techniques and Applications*, J. Fitter, T. Gutberlet and J. Katsaras, eds, Springer, Berlin, 2006, pp. 503–530.
[20] G.S. Smith, E.B. Sirota, C.R. Safinya and N.A. Clark, Structure of the L beta phases in a hydrated phosphatidylcholine multimembrane, *Physical Review Letters* **60** (1988), 813–816.
[21] J.C. Smith, Protein dynamics: comparison of simulations with inelastic neutron scattering experiments, *Quarterly Reviews of Biophysics* **24** (1991), 227–291.
[22] J. Swenson, F. Kargl, P. Berntsen and C. Svanberg, Solvent and lipid dynamics of hydrated lipid bilayers by incoherent quasielastic neutron scattering, *Journal of Chemical Physics* **129** (2008), 045101.
[23] M. Trapp, F. Juranyi, M. Tehei, L. van Eijck, B. Demé, T. Gutberlet and J. Peters, QENS studies on aligned DMPC multilayers at different hydrations, in preparation.

D.2 Hydration dependent studies of highly aligned multilayer lipid membranes by neutron scattering

The article entitled "Hydration dependent studies of highly aligned multilayer lipid membranes by neutron scattering" has been accepted for publication in *The Journal of Chemical Physics* and was published in October 2010. The article was also selected for the October issue of the *JCP: BioChemical Physics*. It includes the subset of articles from *The Journal of Chemical Physics* that directly deals with, or has important implications for, biologically related systems.
Elastic and quasi-elastic data are presented which where obtained during measurements on IN13 and TOFTOF. I was responsible for the sample preparation, took part in both measurement campaigns and performed the data evaluation.

Hydration dependent studies of highly aligned multilayer lipid membranes by neutron scattering

Marcus Trapp,[1,2] Thomas Gutberlet,[3] Fanni Juranyi,[4] Tobias Unruh,[5] Bruno Demé,[2] Moeava Tehei,[6] and Judith Peters[1,2,7,a)]

[1]*Institut de Biologie Structurale J.-P. Ebel, UMR 5075, CNRS-CEA-UJF, 41 rue Jules Horowitz, 38027 Grenoble, France*
[2]*TOF/HR Group, Institut Laue Langevin (ILL), 6 Avenue J. Horowitz, BP 156, F-38042 Grenoble Cedex 9, France*
[3]*Jülich Centre for Neutron Science, TU Munich, Lichtenbergstr. 1, 85747 Garching, Germany*
[4]*Laboratory for Neutron Scattering, ETH Zürich and Paul Scherrer Institut, 5232 Villigen PSI, Switzerland*
[5]*Physik Department E13 and Forschungsneutronenquelle Heinz Maier-Leibnitz FRM II, Technische Universität München, Lichtenbergstr. 1, 85747 Garching, Germany*
[6]*Australian Institute of Nuclear Science and Engineering (AINSE), Menai 2234, New South Wales, Australia and School of Chemistry and Centre for Medical Bioscience, University of Wollongong, Wollongong, New South Wales 2522, Australia*
[7]*Université Joseph Fourier, F-38041 Grenoble Cédex 9, France*

(Received 26 April 2010; accepted 12 September 2010; published online 25 October 2010)

We investigated molecular motions on a picosecond timescale of 1,2-dimyristoyl-*sn*-glycero-3-phosphocholine (DMPC) model membranes as a function of hydration by using elastic and quasielastic neutron scattering. Two different hydrations corresponding to approximately nine and twelve water molecules per lipid were studied, the latter being the fully hydrated state. In our study, we focused on head group motions by using chain deuterated lipids. Information on in-plane and out-of-plane motions could be extracted by using solid supported DMPC multilayers. Our studies confirm and complete former investigations by König *et al.* [J. Phys. II (France) **2**, 1589 (1992)] and Rheinstädter *et al.* [Phys. Rev. Lett. **101**, 248106 (2008)] who described the dynamics of lipid membranes, but did not explore the influence of hydration on the head group dynamics as presented here. From the elastic data, a clear shift of the main phase transition from the P_β ripple phase to the L_α liquid phase was observed. Decreasing water content moves the transition temperature to higher temperatures. The quasielastic data permit a closer investigation of the different types of head group motion of the two samples. Two different models are needed to fit the elastic incoherent structure factor and corresponding radii were calculated. The presented data show the strong influence hydration has on the head group mobility of DMPC. © *2010 American Institute of Physics*. [doi:10.1063/1.3495973]

I. INTRODUCTION

Native biological systems are always found in aqueous environments. Therefore, it is not surprising that the dynamics of such systems is influenced by the hydration level, as it has been confirmed by several neutron scattering studies[1–6] and molecular dynamics simulations.[7–9] The dynamical transition for proteins appears around 200 K. It marks the crossover from a regime in which only vibrational motions of the atoms are observed to a regime where anharmonic motions emerge. Below a certain level of hydration (typically 0.2–0.4 g water/g protein) corresponding to one complete water layer bound to the protein surface, the protein shows no dynamical transition and as a consequence does not become active.[4]

In the case of membranes, a transition due to the structural transition into the liquid-crystalline L_α phase is observed. Depending on the chain length and the degree of hydration of the lipid, it occurs around room temperature or even higher temperatures.[10] In contrast to proteins where the hydration of individual amino acids allows local motions of the protein, in phospholipid bilayers, only the hydration of the hydrophilic head group triggers the dynamic response of the hydration shielded hydrophobic acyl chains due to the increased surface available with increased hydration. For membranes, a shift of the main phase transition to higher temperatures with decreasing water content is already known for quite some time.[11] In recent years, neutron scattering studies of membrane dynamics focused on highly hydrated samples,[12–15] but only a few of these studies took hydration effects explicitly into consideration, e.g., König *et al.*[14]

In this work, we investigated the hydration influence on the dynamics of model membranes by quasielastic neutron scattering (QENS) and elastic incoherent neutron scattering. Model membrane systems such as 1,2-dimyristoyl-*sn*-glycero-3-phosphocholine (DMPC) show a similar thermodynamical behavior as real cell membranes[16] and are therefore often used to mimic their more complex natural counterparts.

Dynamics in such lipid systems span over a large range

a)Author to whom correspondence should be addressed. Electronic mail: peters@ill.fr.

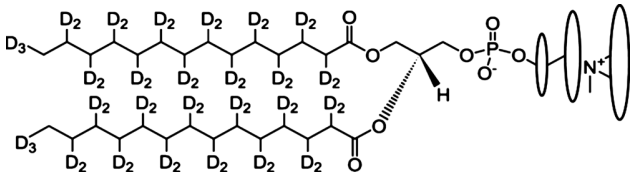

FIG. 1. Schematic view of DMPC-d54. According to the Carpentier model, three different radii are sketched in the choline head group.

in time and space, and have been investigated not only by neutron scattering,[12–14,17,18] but also by nuclear magnetic resonance,[19,20] inelastic x-ray scattering,[21] dielectric spectroscopy,[22] differential scanning calorimetry,[23] dynamic light scattering,[24] single particle tracking,[25] and other methods. To mimic membrane behavior in biological systems the fully hydrated state is the one of interest because this resembles physiological conditions. On the other hand, also the dried state is of interest, e.g., for food science.[26]

The knowledge of the dynamical behavior of these model systems as a function of hydration is then crucial to better understand the parameters necessary for the functioning of biological membranes and what precisely are their effects.[27]

II. SAMPLE PREPARATION AND CHARACTERIZATION

In neutron scattering, deuterated samples allow to take advantage of the great difference in the incoherent scattering cross sections of hydrogen [$\sigma_{inc}=80.26$ b (Ref. 28)] and its isotope deuterium ($\sigma_{inc}=2.05$ b), whereas the coherent scattering cross sections are of the same order of magnitude [$\sigma_{coh}(H)=1.76$ b and $\sigma_{coh}(D)=5.59$ b, all values are given for thermal neutron with an incident wavelength of about 1.8 Å]. So selective deuteration can be used to change the contrast between different parts of the sample. This method is especially useful for biological samples which contain a high amount of homogeneously distributed hydrogen atoms. In phospholipid model membranes, the incoherent scattering cross section is drastically decreased by deuterating the alkyl-chains of the lipids. For completely protonated DMPC, the contribution to the incoherent scattering of the head group accounts for 25% of the total incoherent scattering. However, for the chain deuterated lipid used in our experiments, 73% of the total (incoherent+coherent) scattering cross section stems from the head group. The ratio is even more striking considering only the incoherent cross section, here 93% of the scattering originates from the head group. In the gel phase, the chains are arranged in a regular manner at a characteristic distance. This ordering gives rise to the coherent scattering originating from a quasi-Bragg peak around 1.48 $Å^{-1}$, the so called "chain correlation peak," corresponding to a distance of about 4.2 Å. In the liquid phase, the motion of the lipid chains prevents their ordering, and therefore the appearance of the correlation peak.

For the experiments described in the paper, we used chain deuterated DMPC-d54 (including the methyl groups at the end of the alkyl chains, see Fig. 1). The lipids were purchased from Avanti Polar Lipids (Alabaster, AL, USA) and used without any further purification (deuteration of ≥98%). The DMPC powder was dissolved in a 3:1 chloroform-trifluoroethanol mixture following a protocol described by Ding and co-workers.[29] The dissolution was kept at −20 °C overnight. To be able to probe the in- and out-of-plane motions of the lipids in the membranes, oriented samples have to be used. Such oriented samples have to be prepared on very smooth surfaces such as silicon wafers. The wafers were purchased from Siltronix (Archamps, France) with a thickness of 380(25) μm and Si (111) orientation. Each Si-wafer was cut to a size of about 30 mm × 40 mm to fit the dimensions of the flat aluminum sample container used for the experiments. To avoid chemical interactions between the holder and the sample, the cells are coated with a layer of 3 μm nickel and 0.5 μm gold. About 30 mg of lipid solution was sprayed onto a single wafer. Using this method, bilayer stacks parallel to the wafer surface are assembled. Two samples with different hydration levels were prepared. After the deposition, the wafers were dried over silica gel for 2 days in a desiccator. One sample was rehydrated from pure D_2O at 40 °C to achieve a fully hydrated sample (corresponding to about 12 water molecules per lipid and more[30]). The other one was rehydrated from a saturated salt solution to get reduced water content compared to the fully hydrated sample (D_2O+NaCl at 40 °C resulting in a relative humidity of 75%, about 9 water molecules per lipid). For each sample, six wafers were stacked together after rehydration to achieve a total amount of about 200 mg lipid per sample. A flat cover was used to close the sample cells. The total sample thickness of the six wafers (total thickness of 2.3 mm) and deposited DMPC was 3 mm. With typical values of about 90% for the sample transmission, this amount of sample is needed to achieve sufficiently high statistics in a reasonable measuring time. The weight of both samples was monitored before and after the experiments and no change was observed.

The level of hydration and the mosaicity of the samples were characterized by neutron diffraction prior to both the quasielastic and elastic experiments. The corresponding diffraction data obtained at D16 (Ref. 31) of the Institut Laue Langevin (ILL), Grenoble, France, are shown in the supplements to this paper.[32] This allows evaluating the bilayer repeat distance for each sample and by this means the relative humidity.[33] For the sample hydrated from pure D_2O, which will be referred to as the "higher hydrated sample" in the following, the diffraction data yield a repeat distance of 62.5 Å. The mosaic spread was extracted from fitting a Lorentzian curve to the experimental data to be 0.22(2)° [full width at half maximum (FWHM)]. The sample hydrated from D_2O+NaCl showed a d-spacing of 54.9 Å and a mosaicity of 0.25(2)° (data not shown here). It will be referred to as "less hydrated sample."

III. EXPERIMENT

A. Elastic experiments at IN13

Elastic experiments were performed at the Collaborative Research Group (CRG) thermal neutron backscattering spectrometer IN13 at ILL, Grenoble. The incident wavelength was $\lambda=2.23$ Å with an incident neutron energy of about 16 meV. This setup results in a uniquely wide range of mo-

mentum transfer $Q(0.2\ \text{Å}^{-1} < Q < 4.9\ \text{Å}^{-1})$. The elastic energy resolution was 8 μeV. A detailed description of the instrument and selected applications in the field of biophysics can be found in Natali *et al.*[34] Transmission for both samples was measured and found to be in the order of 90%, so multiple scattering effects were not taken into consideration for the data treatment. For both samples, fixed energy window scans were recorded in the temperature range between −23 and 37 °C in steps of 5 °C to cover both the phase transition from the lamellar gel to the fluid phase at 22 °C and also the transition from the gel to the crystalline phase around 12 °C. Special care was taken for the sample alignment so that the momentum transfer $\hbar\vec{Q}$ at the lipid peak maximum lies in the plane of the membrane bilayers for the parallel orientation. Using Eq. (1), the corresponding angles of 75° and 165° with respect to the incoming beam were calculated for the parallel and perpendicular orientation of the scattering vector toward the membrane surface, respectively,

$$Q = \frac{4\pi}{\lambda}\sin\theta. \tag{1}$$

Strictly speaking, the terms "parallel" and "perpendicular" are only true for these particular values; nevertheless, we are using these designations in the course of this paper to distinguish the orientations where these alignments are best visible. Both orientations $\vec{Q}$ parallel and $\vec{Q}$ perpendicular to the membrane surface were measured. We mainly focused on the parallel orientation ($2\theta = 75°$). 3 h per temperature was measured to favor good data statistic collection for this orientation. For the perpendicular orientation, the acquisition time varied between 45 min and 1 h (at higher temperatures in particular). For data correction purposes, an empty cell, a cell with six cleaned wafers, and for normalization a 2 mm vanadium sample were measured. The data evaluation was carried out using the LAMP software available at ILL.[35]

B. Quasielastic neutron scattering experiments at TOFTOF

QENS experiments have been performed on the same samples at the time-of-flight spectrometer TOFTOF (Ref. 36) at the Munich research reactor FRM II in Garching. Applications of the spectrometer in the field of membrane biophysics can be found in, e.g., Busch *et al.*[37] The incident wavelength was set to $\lambda = 6$ Å, the chopper speed to 12 000 rpm, resulting in an energy resolution of the elastic line of 56 μeV (FWHM of the elastic line). The setup was chosen in order to compare the results with previous measurements obtained by another group.[13] Both samples were measured in a temperature range from 5 to 25 °C to cover both phase transitions: the pretransition from the L_β gel phase to the P_β ripple phase at 12 °C as well as the main phase transition from the P_β phase to the L_α liquid phase at 22 °C.[11] Spectra were taken every 5 °C. The measuring time per temperature was 5 h. All samples, including a 1.5 mm vanadium sample and a sample holder with six empty wafers and pure D_2O needed for corrections, were measured in one orientation (at 45° with respect to the incident beam) only. In this case $\hbar\vec{Q}$ is mainly parallel to the membrane surface at the alkyl chain correlation peak position ($Q = 1.48\ \text{Å}^{-1}$) for low energy transfers. Earlier QENS experiments on 1,2-dipalmitoyl-*sn*-glycero-3-phosphocholine[13] showed no significant differences in the elastic incoherent structure factor (EISF) for $\hbar\vec{Q}$ oriented parallel and perpendicular to the membrane surface. This fact was confirmed by our elastic data and the QENS data were recorded only for the parallel orientation. From the measured spectra, the scattering of the empty can was subtracted, then they were normalized to vanadium and transformed into (Q,E)-space. The data were binned into 15 groups with Q ranging from 0.44 to 1.56 Å^{-1}. Data reduction was performed with IDA package available onsite,[38] data analysis was done using the PAN package from DAVE software.[39]

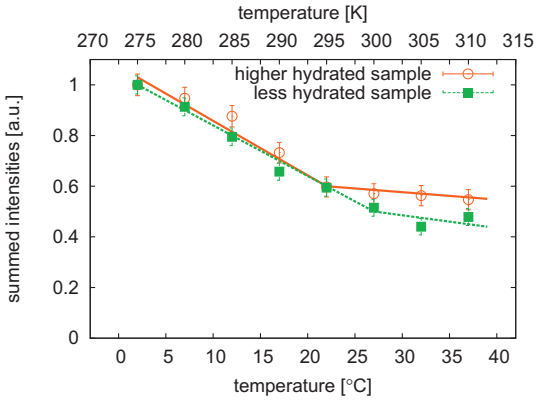

FIG. 2. Plot of the normalized summed elastic intensity vs temperature for Q aligned parallel to the membrane surface. With decreasing water content, a shift in the temperature of the main phase transition is evident. Lines are guides to the eye.

IV. RESULTS AND DISCUSSION

A. Elastic data

Figure 2 shows the normalized summed intensity taken on IN13 (Q-range: $0.19\ \text{Å}^{-1} < Q < 1.67\ \text{Å}^{-1}$) as a function of temperature for both samples. The representation of the data offers a simple and model-free approach to detect transitions as changes in the elastic intensity decay.[40] In the chosen setup, the influence of the coherent scattering coming from the chain ordering is mainly seen in the parallel orientation. Summed intensities are then shown only for the parallel orientation. The phase transition for the fully hydrated sample is found to lie around 21 °C which coincides very well with the value of 20.15 °C found by Guard-Friar *et al.*[41] Whereas for the less hydrated sample a transition temperature around 25 °C is found. It is known from, e.g., Fourier transform infrared spectroscopy (FTIR) spectroscopy[42] that dehydration increases the transition temperature. Following the procedure used by Pfeiffer *et al.*,[30] we estimated the water content from the shift of the main phase transition temperature. We can extract the parameter $R_w = n_W/n_A$ where R_w expresses the molar ratio of water (n_W) and amphiphile (n_A).[30,42] The calculated R_w for the fully hydrated sample is $R_w \approx 12$ and $R_w \approx 9$ for the less hydrated sample. Pfeiffer *et al.* found for DMPC multilayers a value of $R_w \approx 12$ for fully

hydrated membranes.[30] Therefore, the elastic measurements on IN13 provide a solid basis to characterize the system for the quasielastic experiment at TOFTOF.

Due to the coherent scattering arising from the ordering of the lipid chains, below the main phase transition and the relatively broad Q resolution of IN13, only three detectors were left to evaluate the mean square displacements (MSDs);[43] therefore, it was not possible to obtain MSDs with reasonable error bars. A detailed comparison between the mean square displacements and the summed intensities for DMPC is found elsewhere.[44]

B. Quasielastic data

A detailed description of the analysis of quasielastic neutron scattering data can be found in Bée.[45] For applications in the context of lipid dynamics, see, e.g., Busch *et al.*,[37] and for water dynamics in lipid systems, see, e.g., Swenson *et al.*[46]

The obtained data are a convolution of the theoretical scattering law $S_{\text{theo}}(\vec{Q},\omega)$ and the instrumental resolution $S_{\text{res}}(\vec{Q},\omega)$ given by a measured vanadium sample,

$$S_{\text{meas}}(\vec{Q},\omega) = S_{\text{theo}}(\vec{Q},\omega) \otimes S_{\text{res}}(\vec{Q},\omega). \tag{2}$$

The theoretical scattering law can be expressed by a delta function for the elastic contribution and a sum of Lorentzians for the quasielastic contributions coming from the dynamics of the investigated sample.[45] In our study, an elastic peak and two Lorentzian functions (narrow and broad components) were necessary to reasonably fit the obtained data. In Fig. 3 the fits to the data are shown for two Q-values. The $S(\vec{Q},\omega)$ writes

$$S_{\text{theo}}(\vec{Q},\omega) = e^{-\text{DWF}}(A_0(\vec{Q})\delta(\omega) + A_1(\vec{Q})L_1(\Gamma_1,\omega) + A_2(\vec{Q})L_2(\Gamma_2,\omega)). \tag{3}$$

$e^{-\text{DWF}}$ is the Debye–Waller factor according for vibrational motions, Γ_i represents the half width at half maximum of each Lorentzian, A_i is the corresponding amplitude with the normalization $A_0+A_1+A_2=1$. Keeping in mind that chain-deuterated lipids were used in our experiments, the narrow and the broad Lorentzians were associated with slow and fast motions of the head groups, respectively. The geometry of the motion can be extracted from the EISF as defined in

$$\text{EISF}(\vec{Q}) = \frac{A_0(\vec{Q})}{A_0(\vec{Q}) + A_1(\vec{Q}) + A_2(\vec{Q})}. \tag{4}$$

For both samples, the EISF does not decay to zero for large Q-values, which indicates an immobile fraction in the examined time-space window.

Two different models were applied to fit the EISFs. First, we used the "diffusion in a sphere" model introduced by Volino and Dianoux,[47] where free diffusion in the restricted volume of a sphere is permitted. Bellissent-Funel and co-workers[48] established as an addition to this model an immobile fraction. The corresponding EISF is described by

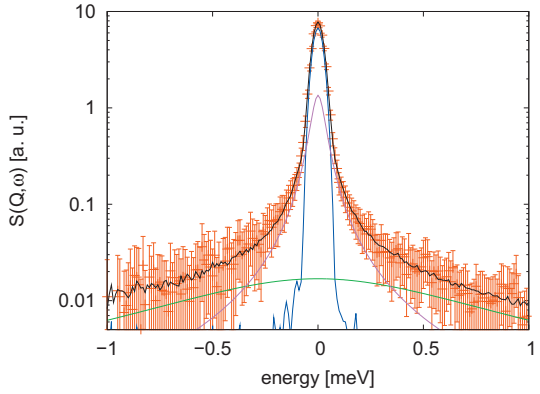

(a)

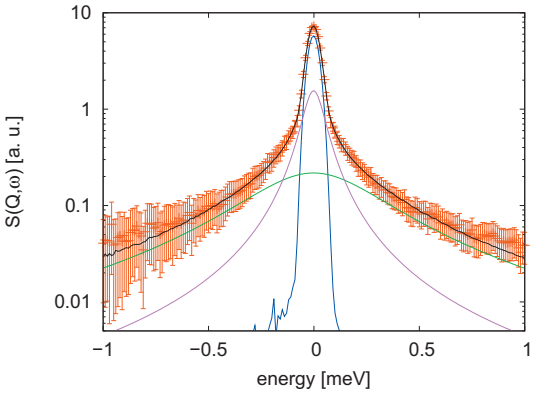

(b)

FIG. 3. Plot of $S(\vec{Q},\omega)$ for (a) Q=0.44 Å^{-1} and (b) Q=1.48 Å^{-1} at 5 °C. The resulting fit is shown (black line) as well as the single contributions. The delta function is drawn in the blue line; the two Lorentzians are plotted as green and pink lines, respectively.

$$A_0(\vec{Q}) = p + (1-p) \times \left[\frac{3j_1(Qa)}{Qa}\right]^2, \tag{5}$$

where j_1 is the first order spherical Bessel function of the first kind, a is the radius of the sphere, p denotes an immobile contribution, and $(1-p)$ is the corresponding mobile fraction.

A modification of the Volino/Dianoux model allows increasing radii for the diffusion volumes of the hydrogen atoms along the head group [see Eq. (6a)]. This model was introduced by Carpentier *et al.* for the study of dicopper tetrapalmitate[49] and is described by

$$A_0(\vec{Q}) = \frac{1}{N}\sum_{n=1}^{N}\left[\frac{3j_1(QR_n)}{QR_n}\right]^2 \tag{6a}$$

with

$$R_n = \frac{n-1}{N-1} \times [R_N - R_1] + R_1. \tag{6b}$$

N stands for the total number of atoms in the chain to which hydrogen atoms are bound (in the case of this study N=3). The index n starts with the carbon atom the closest to the oxygen of the phosphorus group which connects the lipid chains with the head group and ends with the nitrogen of the

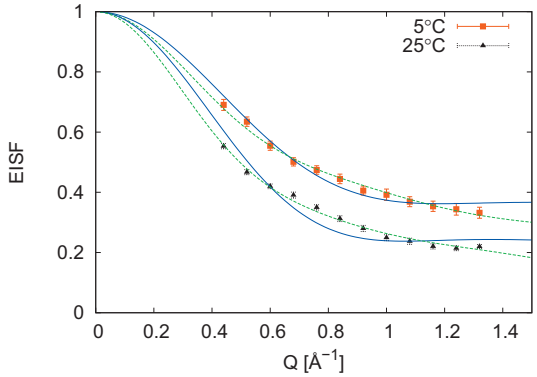

(a)

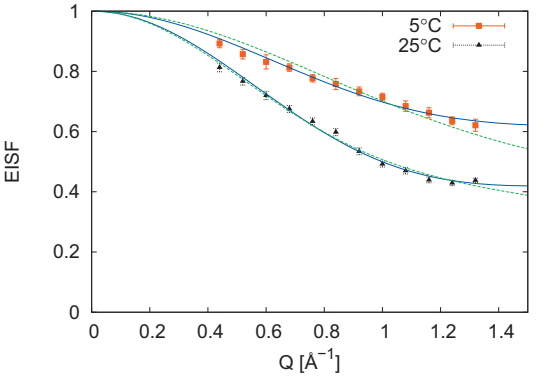

(b)

FIG. 4. EISFs with corresponding fits for the higher hydrated sample (a) and the less hydrated sample (b), respectively. Fits corresponding to the method introduced by Carpentier and co-workers (Ref. 49) are drawn as dashed green lines; fits corresponding to the diffusion in a sphere model (Ref. 47) are drawn as solid blue lines.

choline group (see Fig. 1). R_n gives the radius of the diffusion volume for the corresponding hydrogen atoms. In Eq. (6b) linear increasing radii are assumed. It turned out during the fitting procedure that the choice of $N=3$ yields physically reasonable results, whereas for values bigger than $N=3$ the radius for R_1 became negative. Around 1.48 Å^{-1}, the coherent scattering rising from the ordering of the lipid chains, the so-called chain correlation peak, is clearly visible. To exclude its influence on the EISF fits, the fit range was restricted to a range of 0.44 Å$^{-1} < Q < 1.32$ Å^{-1}. Figures 4(a) and 4(b) show the obtained data for two temperatures, one below (5 °C) and one above (25 °C), the main phase transition for the fully hydrated sample and the less hydrated sample, respectively. Fits corresponding to the diffusion in a sphere model are shown as solid blue lines, the Carpentier model as dashed green lines. In the case of the less hydrated sample, the diffusion in a sphere model fits the data sufficiently well within the experimental errors, leading to values of $a=2.64(10)$ Å and $a=2.91(06)$ Å for the radii at 5 and 25 °C, respectively. For the higher hydrated sample, the simple model of diffusive motion in a sphere is not longer sufficient. Here, the Carpentier model gives definitely better results, especially at higher temperatures. In the L_β gel phase at 5 °C, the fits result in values of $R_{min}=0.36(4)$ Å for the

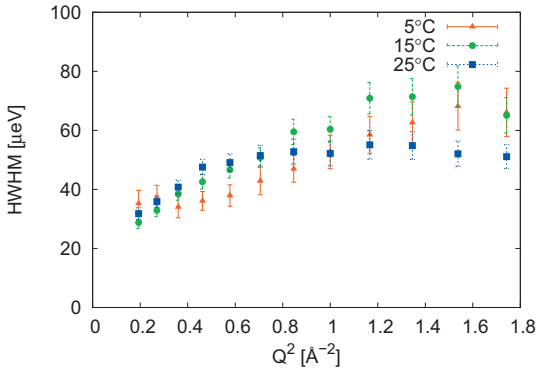

FIG. 5. Line widths for selected temperatures (5, 15, and 25 °C) for the higher hydrated sample.

displacement of the proton bound in the methylene groups near the phosphorus atoms of the lipid and of $R_{max}=5.05(6)$ Å for the hydrogens of the methyl groups in the choline group. At 25 °C in the liquid L_α, phase corresponding values of $R_{min}=1.14(3)$ Å and $R_{max}=6.42(11)$ Å were obtained. The fact that the EISF is not going to zero for large Q-values is an indication that not all of the protons take part in the movements observed in the chosen time-space window of the experiment, as it has been seen, e.g., for protein-membrane complexes.[50,51] However, for a detailed investigation, a broader Q-range would be preferable to clearly distinguish trends. In this context, we want to emphasize that both employed models have only two fit parameters, namely, in the case of the diffusion in a sphere model the radius a and the immobile fraction p, and in the Carpentier model the first radius R_1 and the last radius R_N. We tried also to fit other models to the EISF (with more than two fit parameters) which are often used to analyze methyl group reorientation because of the three head group methyl groups. Namely, the threefold jump model[45] and a variant of this model (applied to the methyl reorientation on trimethyloxosulphonium[52]) have also been fitted to the data but they do not sufficiently well fit the experimental data (data not shown).

Our experiments demonstrate nicely the influence of hydration on the mobility of the protons. The difference in the EISF values shows a strong dependence on the level of hydration. For the diffusion in a sphere model the percentage of immobile protons can be inferred directly from the fit parameter p (see formula (5)), in the case of the Carpentier model different radii for the volume of rotation can be extracted. Thus, for the less hydrated sample, the values for 5 °C amount to $p_{5\,°C}=61.9(14)\%$ and $p_{25\,°C}=42.0(8)\%$ for 25 °C, respectively. Even if the diffusion in a sphere model cannot be applied to the higher hydrated sample, it is already clear from comparing Figs. 4(a) and 4(b) that the immobile fraction for the latter sample is lower. With the obtained results, we are able to directly associate different models of motions to a given hydration of the lipids.

Figure 5 shows the line widths Γ of the narrower Lorentzian as a function of Q^2. The line width of the second Lorentzian is about a factor of 10 larger than the narrow one and it shows a Q-independent, constant value for Γ for both hydrations (data not shown here). For small Q-values

($Q \to 0$), the data do not go to zero as for free diffusion, then they increase and asymptotically reach a constant value Γ_∞ for large Q. A constant value at small Q was assigned by Volino and Dianoux[47] to a confinement effect at large radii. A similar behavior is assumed and has also been observed by Carpentier *et al.*[49]

However, we find a discrete kink only for the lowest measured temperature (red points in Fig. 5). At this temperature, the confinement radius R_{conf} obtained from the crossover of the two regimes at a Q^2-value of about 0.55 Å^{-1} following formula (7) was calculated to be 4.2 (4) Å. These values are in between R_{min} and R_{max} obtained from the EISF fits for the corresponding sample at 5 °C and therefore consistent with these values,

$$Q = \frac{\pi}{R_{\text{conf}}}. \tag{7}$$

No pronounced plateau is visible for higher temperatures, but a Γ which does not decay to zero for small Q values is still an indication for restricted motion as it has also been observed for proteins.[53,54] As we find several radii for the diffusion volumes in the Carpentier model, a superposition of different kinks leads to the observed behavior, especially at high temperatures. At larger Q-values, the line width Γ follows the "random jump diffusion" model.[55]

As for the EISF also for the line width, the influence of the coherent scattering arising from the chain ordering around $Q = 1.48$ Å^{-1} occurs below the main phase transition, whereas for 25 °C the predicted plateau is observed. Therefore, the data are drawn in the same range as for the EISF.

V. CONCLUSIONS

In the present study, we have investigated the hydration dependent behavior of model membrane systems above and below the main phase transition of DMPC with a focus on the head group motion. In contrast to existing studies, we took explicitly into account the hydration effect on the dynamics of model membrane systems. Therefore, we were able to directly associate different models for the motions of the hydrogen atoms in the head group to different hydration levels. The elastic temperature scans show a strong dependence on the hydration: the phase transition temperature is lower (related to a higher mobility of the head groups) in the L_α phase at full hydration compared to the less hydrated sample. The type of head group motions possible in the different samples has been probed in more detail by the performed QENS studies. Here, the hydration influence in the observed time and space window is clearly translated by the different models necessary to fit the obtained elastic incoherent structure factor for the different hydrations and the resulting radii. In summary, this study has shown that hydration of lipid bilayers plays a major role in understanding the dynamics of these kinds of systems and should always be properly characterized when dealing with samples containing lipids.

ACKNOWLEDGMENTS

The authors thank F. Natali and S. Busch for the fruitful discussions. M. Trapp was supported by a Ph.D. scholarship from the French Ministry for Research and Technology. This research project has been supported by the European Commission under the Sixth Framework Program through the Key Action: Strengthening the European Research Area, Research Infrastructures (Contract No. RII3-CT-2003-5059825). We acknowledge the ILL and the FRM II for the allocation of beamtime and the financial support from the Access to Major Research Facilities Program which is a component of the International Science Linkages Program established under the Australian Government's innovation statement, Backing Australia's Ability.

[1] J. Fitter, S. A. W. Verclas, R. E. Lechner, H. Seelert, and N. A. Dencher, FEBS Lett. **433**, 321 (1998).
[2] J. Zanotti, M.-C. Bellissent-Funel, and J. Parello, Biophys. J. **76**, 2390 (1999).
[3] F. Gabel, D. Bicout, U. Lehnert, M. Tehei, M. Weik, and G. Zaccai, Q. Rev. Biophys. **35**, 327 (2002).
[4] J. Roh, J. Curtis, S. Azzam, V. Novikov, I. Peral, Z. Chowdhuri, R. Gregory, and A. Sokolov, Biophys. J. **91**, 2573 (2006).
[5] J. Pieper, T. Hauß, A. Buchsteiner, and G. Renger, Eur. Biophys. J. **37**, 657 (2008).
[6] K. Wood, U. Lehnert, B. Kessler, G. Zaccai, and D. Oesterhelt, Biophys. J. **95**, 194 (2008).
[7] P. J. Steinbach and B. Brooks, Proc. Natl. Acad. Sci. U.S.A. **90**, 9135 (1993).
[8] M. Tarek and D. J. Tobias, Phys. Rev. Lett. **88**, 138101 (2002).
[9] C.-J. Högberg and A. P. Lyubartsev, J. Phys. Chem. B **110**, 14326 (2006).
[10] T. Heimburg, *Thermal Biophysics of Membranes* (Wiley-VCH, Weinheim, Germany, 2007).
[11] G. S. Smith, E. B. Sirota, C. R. Safinya, and N. A. Clark, Phys. Rev. Lett. **60**, 813 (1988).
[12] W. Pfeiffer, T. Henkel, E. Sackmann, W. Knoll, and D. Richter EPL **8**, 201 (1989).
[13] S. König, W. Pfeiffer, T. Bayerl, D. Richter, and E. Sackmann, J. Phys. II (France) **2**, 1589 (1992).
[14] S. König, T. M. Bayerl, G. Coddens, D. Richter, and E. Sackmann, Biophys. J. **68**, 1871 (1995).
[15] M. Rheinstädter, J. Das, E. Flenner, B. Brüning, T. Seydel, and I. Kosztin, Phys. Rev. Lett. **101**, 248106 (2008).
[16] *Structure and Dynamics of Membranes*, Handbook of Biological Physics Vol. 1, edited by R. Lipowsky and E. Sackmann (Elsevier, Amsterdam, The Netherlands, 1995).
[17] M. C. Rheinstädter, C. Ollinger, G. Fragneto, F. Demmel, and T. Salditt, Phys. Rev. Lett. **93**, 108107 (2004).
[18] M. C. Rheinstädter, W. Häußler, and T. Salditt, Phys. Rev. Lett. **97**, 048103 (2006).
[19] A. A. Nevzorov and M. F. Brown, J. Chem. Phys. **107**, 10288 (1997).
[20] S. König, E. Sackmann, D. Richter, R. Zorn, C. Carlile, and T. M. Bayerl, J. Chem. Phys. **100**, 3307 (1994).
[21] S. H. Chen, C. Y. Liao, H. W. Huang, T. M. Weiss, M.-C. Bellisent-Funel, and F. Sette, Phys. Rev. Lett. **86**, 740 (2001).
[22] B. Klösgen, C. Reichle, S. Kohlsmann, and K. Kramer, Biophys. J. **71**, 3251 (1996).
[23] E. Y. Shalaev and P. L. Steponkus, J. Phys. Chem. B **107**, 8734 (2003).
[24] R. Hirn, T. M. Bayerl, J. O. Rädler, and E. Sackmann, Faraday Discuss. **111**, 17 (1999).
[25] C. Eggeling, C. Ringemann, R. Medda, G. Schwarzmann, K. Sandhoff, S. Polyakova, V. Belov, B. Hein, C. von Middendorff, A. Schonle, and S. Hell, Nature (London) **457**, 1159 (2009).
[26] M. Doxastakis, V. G. Sakai, S. Ohtake, J. K. Maranas, and J. J. de Pablo, Biophys. J. **92**, 147 (2007).
[27] U. Lehnert, V. Réat, M. Weik, G. Zaccaï, and C. Pfister, Biophys. J. **75**, 1945 (1998).
[28] V. F. Sears, Neutron News **3**, 26 (1992).
[29] L. Ding, T. Weiss, G. Fragneto, W. Liu, L. Yang, and H. Huang, Langmuir **21**, 203 (2005).
[30] H. Pfeiffer, H. Binder, G. Klose, and K. Heremans, BBA-Biomembranes **1609**, 148 (2003).
[31] See http://www.ill.eu/d16/.

[32] See supplementary material at http://dx.doi.org/10.1063/1.3495973 for the diffraction data taken on D16 to evaluate the repeat distance and mosaicity of the aligned multilayer samples.
[33] N. Kucerka, Y. Liu, N. Chu, H. I. Petrache, S. Tristram-Nagle, and J. F. Nagle, Biophys. J. **88**, 2626 (2005).
[34] F. Natali, J. Peters, D. Russo, S. Barbieri, C. Chiapponi, A. Cupane, A. Deriu, M. T. Di Bari, E. Farhi, Y. Gerelli, P. Mariani, A. Paciaroni, C. Rivasseau, G. Schiró, and F. Sonvico, Neutron News **19**, 14 (2008).
[35] See http://www.ill.eu/instruments-support/computing-for-science/cs-software/all-software/lamp/.
[36] T. Unruh, J. Neuhaus, and W. Petry, Nucl. Instrum. Methods Phys. Res. A **580**, 1414 (2007).
[37] S. Busch, C. Smuda, L. C. Pardo, and T. Unruh, J. Am. Chem. Soc. **132**, 3232 (2010).
[38] See http://sourceforge.net/projects/frida/.
[39] See http://www.ncnr.nist.gov/dave.
[40] B. Frick and L. J. Fetters, Macromolecules **27**, 974 (1994).
[41] D. Guard-Friar, C. H. Chen, and A. S. Engle, J. Phys. Chem. **89**, 1810 (1985).
[42] H. Pfeiffer, H. Binder, G. Klose, and K. Heremans, BBA-Biomembranes **1609**, 144 (2003).
[43] J. C. Smith, Q. Rev. Biophys. **24**, 227 (1991).
[44] M. Trapp, F. Juranyi, M. Tehei, L. van Eijck, B. Demé, T. Gutberlet, and J. Peters, Spectroscopy **24**, 461 (2010).
[45] M. Bée, *Quasielastic Neutron Scattering: Principles and Applications in Solid State Chemistry, Biology and Materials Science* (Adam Hilger, Philadelphia, 1988).
[46] J. Swenson, F. Kargl, P. Berntsen, and C. Svanberg, J. Chem. Phys. **129**, 045101 (2008).
[47] F. Volino and A. J. Dianoux, Mol. Phys. **41**, 271 (1980).
[48] M.-C. Bellissent-Funel, J. Teixeira, K. Bradley, and S. H. Chen, J. Phys. I (France) **2**, 995 (1992).
[49] L. Carpentier, M. Bée, A. M. Giroud-Godquin, P. Maldivi, and J. C. Marchon, Mol. Phys. **68**, 1367 (1989).
[50] F. Natali, A. Relini, A. Gliozzi, R. Rolandi, P. Cavatorta, A. Deriu, A. Fasano, and P. Riccio, Chem. Phys. **292**, 455 (2003).
[51] F. Natali, A. Relini, A. Gliozzi, R. Rolandi, P. Cavatorta, A. Deriu, A. Fasano, and P. Riccio, Physica B **350**, E623 (2004).
[52] M. Bée, H. Jobic, and C. Sourisseau, J. Phys. C **18**, 5771 (1985).
[53] M. Tehei, J. Smith, C. Monk, J. Ollivier, M. Oettl, V. Kurkal, J. Finney, and R. Daniel, Biophys. J. **90**, 1090 (2006).
[54] Z. Bu, D. A. Neumann, S.-H. Lee, C. M. Brown, D. M. Engelman, and C. C. Han, J. Mol. Biol. **301**, 525 (2000).
[55] P. A. Egelstaff, *An Introduction to the Liquid State* (Academic Press, New York, 1967).

D.3 Dynamics of model membranes

In the following a chapter for the e-book entitled "Dynamics of Biological Macromolecules by Neutron Scattering" is presented (editors Salvatore Magazú and Federica Migliardo). I contributed to this review section 4 about the hydration influence on membranes.

DYNAMICS OF MODEL MEMBRANES

F. Natali[1] and M. Trapp[2]

[1]*CNR-INFM, OGG, c/o Institut Laue-Langevin, Grenoble, FR-38000, France*
[2]*Institut de Biologie Structurale J.-P. Ebel, UMR 5075, CNRS-CEA-UJF, Grenoble, FR-38027, France*

Abstract

Biological membranes are complex multicomponent systems whose dynamics and structure provide their physiological function. Many parameters interplay to determine the membrane flexibility; among them, lipid composition, lipid-protein interaction, hydration, temperature etc.
We provide here a tentative overview of recent successful neutron scattering experiments on different oriented model membranes, with the aim to demonstrate the many unique advantages that elastic and quasi-elastic neutron scattering offer for the investigation of membrane dynamics.

Introduction

Membranes are fundamental elements of all living cells, performing important active functions controlling transport of molecules and ions across them. The lipid bilayer itself is a complicated multicomponent system made up of about 100 different lipids, differing in the hydrocarbon chain and in the polar head groups. Structural properties of these bilayers are very important for their functional activity and have been investigated in detail [1]. Much less is known on bilayer dynamics.
On the other hand, it is well acknowledged that the different kinds of motions of the lipid chains are of paramount importance for the physiological function of membranes and those motions can be modulated by a number of factors like lipidic composition and protein interactions.
It is commonly accepted that at least six different lipid movements can be observed in oriented membranes, characterized by specific time scale windows [2]. In the 10^{-11}-10^{-8} s range the chain defect motions and the rotational diffusion about the lipid molecular axis and the chain defect motions can be observed. In the latter, the lipid chain oscillates forming an angle θ with respect to the molecule axis, along the normal to the membrane plane (wobbling motion). The origin of this kind of motion is still not completely understood and could be due to a fluctuating cis-trans isomerization of the acyl chains emphasized when membrane defects, such as holes due to a missing or not complete lipid, appear.
On the other hand, the 10^{-10} – 10^{-9} s time scale is characterized by the exhibition of the vertical (i.e. parallel to the membrane normal) vibrational motion of the lipid molecules. At lower times, lateral diffusion in the bilayer plane (10^{-9} s) and rotational and flip flop motion of the lipid head groups (3×10^{-9} s), take place. Finally, much slower membrane dynamics is promoted by the collective modulations of the bilayers, which, observed in the s time scale, conferees the membrane roughness.

Incoherent neutron scattering is a powerful technique to investigate dynamics of biological molecules, which are characterized by a extremely high hydrogen content, representing at least half of the total number of atoms of the system. In fact, the hydrogen incoherent neutron scattering cross section is about an order of magnitude larger than that of other atomic species typically present in biological systems. Thus, incoherent neutron scattering provides averaged information on the global dynamics of the system. In particular, elastic (ENS) and quasi-elastic incoherent neutron scattering (QENS) have been already demonstrated to represent an optimal tool to provide unique information on lipid dynamics [3-5]. For these measurements, highly ordered samples are required in order to allow selection of the direction of momentum transfer with respect to the membrane normal, and therefore separation of in-plane and out-of-plane motions (Fig. 1).

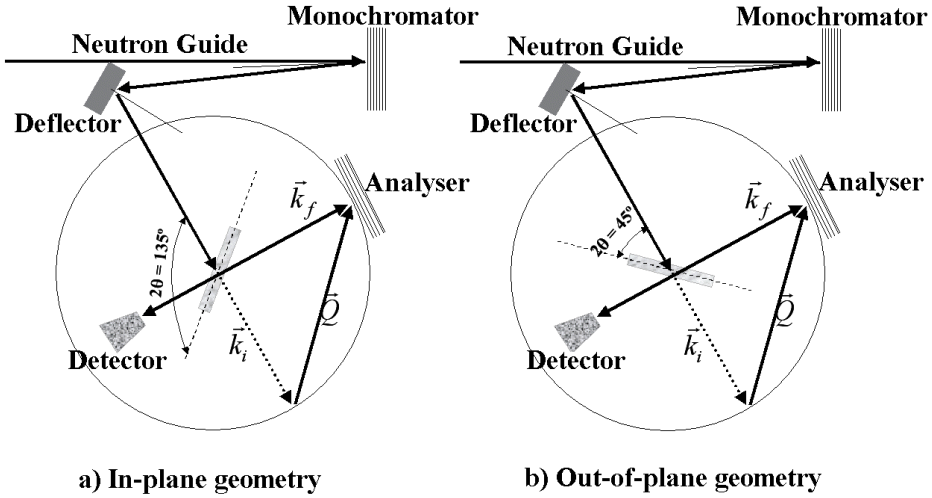

Fig. 1: By rotating the sample with respect to the incoming beam, the momentum transfer is predominantly oriented parallel (135°, panel a) and perpendicular to the membrane surface (45°, panel b)

This is achieved using oriented lipid multilayer obtained drying a thin layer of liposome suspension on a solid support, typically SiO_2 polished wafers.
We report here few selected examples of the investigation of dynamical properties of different membrane model systems.

1. Effect of Myelin Basic Protein on the Dynamics of Oriented Lipid Bilayers

Myelin is the discontinuous multibilayer membrane sheath wrapped around the nerve axon. The integrity of the myelin sheath is fundamental to optimize the action potential conduction along spike in the axon [6,7], while stacking disorder causes severe diseases like multiple sclerosis. It contains proteins which are believed to play an important role in maintaining the membrane stack order [8-11]. Among them, the Myelin Basic Protein (MBP) is the second most abundant myelin protein that counts for up to 30% of the total protein fraction in the Central Nervous System (CNS) [12].
MBP is an extrinsic protein that, when removed from its native environment in the membrane and isolated in the water-soluble form, appears as an extended, flexible, irregular coil having little secondary structure [8,13]. However, several studies have

demonstrated that MBP, according to its structural role, can interact with specific lipids to form ordered assemblies [12,14,15]. On the other hand, it is still not clear whether the absence of MBP affects the lipid dynamics. Recent elastic and quasi-elastic neutron scattering experiments, performed on highly oriented dimyristoyl phosphatidic acid (DMPA) phospholipid multilayers, simulating the myelin sheath, have demonstrated that it is possible to separate the in-plane and out-of-plane contributions of the membrane dynamics, thus to investigate the eventual appearance of membrane anisotropy [16]. It was also observed that the addition of the MBP to the DMPA membranes affects significantly the membrane dynamics. In particular the lipid mobility in the out-of-plane configuration (i.e. at 45° with respect to the incident beam) was shown to increase (Fig. 2).

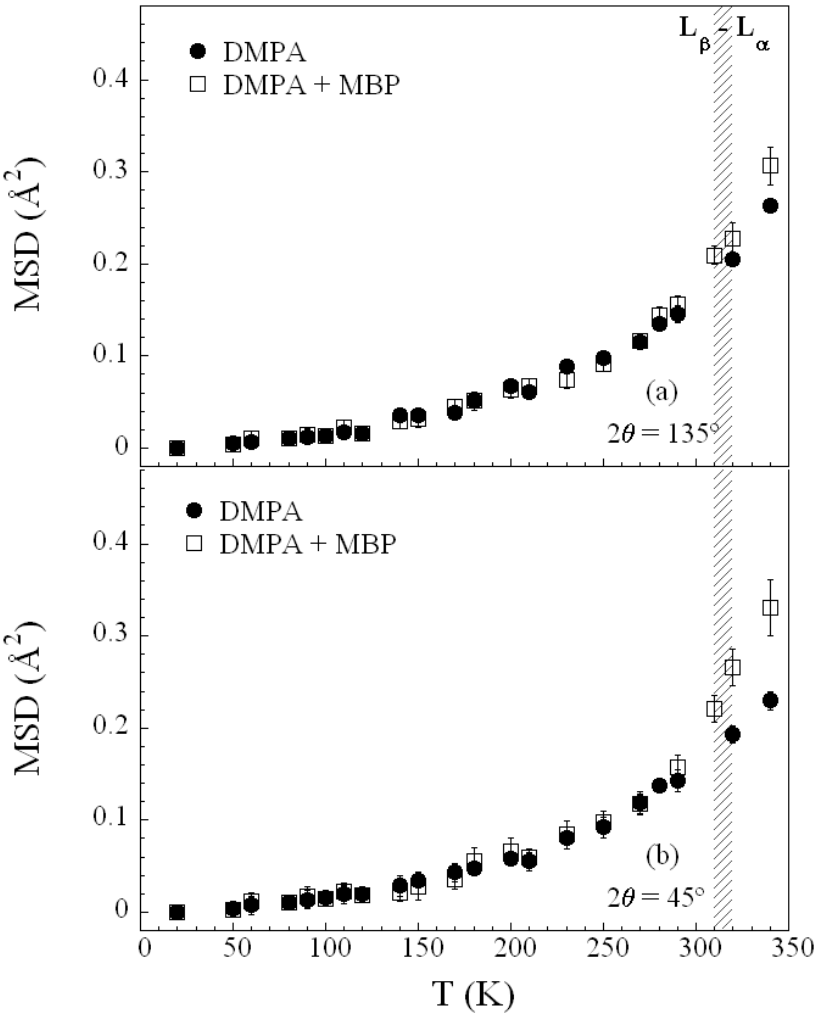

Fig. 2: Temperature dependence of the normalised Mean Square Displacements (MSD) of DMPA (filled symbols) and DMPA+MBP (empty symbols). Incoherent elastic neutron scattering data have been acquired at the high resolution backscattering spectrometer IN13 at the Institut Laue-Langevin in Grenoble - France (ILL), using an energy resolution of 8μeV, corresponding to ~100 ps time scale accessible. MSD are calculated, in agreement to the Gaussian model, as the slope of the logarithm of the elastic intensity versus squared momentum transfer Q^2, in the low-Q range fulfilling the condition of the Guinier approximation. (a) and (b) refer to the in plane (135°) and out-of-plane (45°) configurations, respectively. The lipid phase transition from gel (L_β) to liquid-crystalline (L_α), occurring at T_c close to 320 K, is also shown [16].

Moreover, the lipids are known to exhibit a complex temperature-dependent phase diagram, with at least two phase transitions from crystalline (L_c-phase), to gel (L_β-phase), and then to liquid crystalline (L_α-phase) structures, reflecting different degrees of disorder. The transition from gel to liquid-crystalline phase ($L_\beta \rightarrow L_\alpha$) in saturated lipids normally occurs at temperatures around $T_c \sim 320$ K, depending on the membrane composition.

Thus, the observed enhanced lipid flexibility in DMPA+MBP at T > 310 K (Fig. 2), that leads to higher MSD values, could be assigned to the effect of the membrane structural modification occurring across the lipid phase transition.

Moreover, the out-of-plane membrane dynamics is markedly characterized by spatially restricted vertical diffusive motions of the lipids, significantly enhanced by the MBP above the gel to liquid crystalline ($L_\beta \rightarrow L_\alpha$) DMPA phase transition (Fig.3).

On the other hand, the in-plane dynamics seems to involve predominantly the spatially restricted lateral diffusion of the lipids on the membrane surface that appears to be only slightly affected by the presence of the MBP.

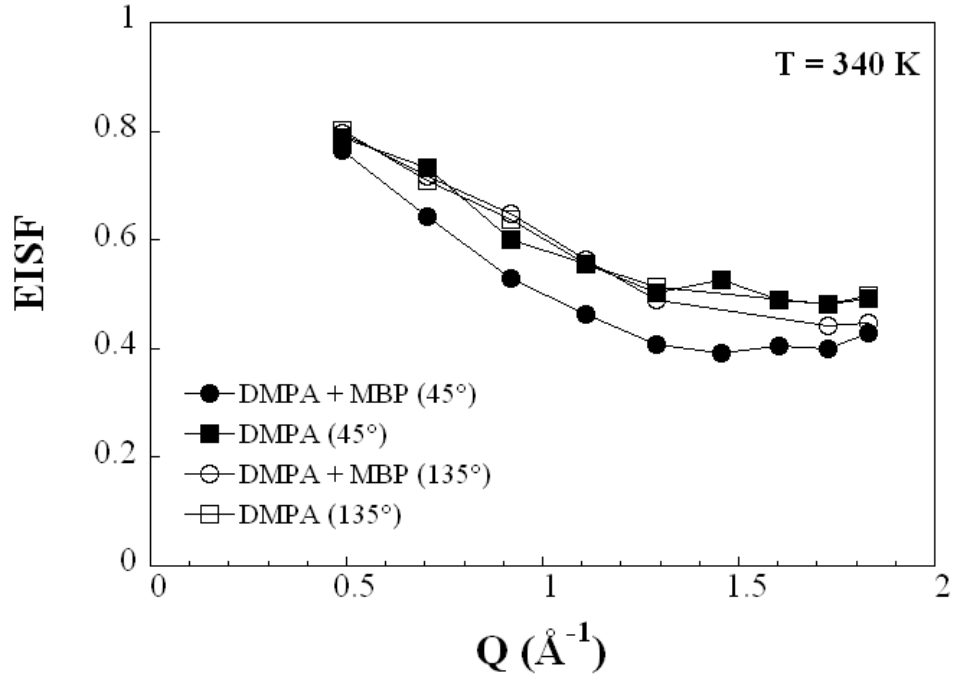

Fig. 3: Q dependence of the Elastic Incoherent Structure Factor (EISF) of DMPA and DMPA+MBP, measured in the L_α liquid phase (T = 340 K) and at both geometrical configurations (135° and 45°). Incoherent quasi-elastic neutron data have been acquired at the IN16 backscattering spectrometer at ILL, using an energy resolution of 0.9μeV, corresponding to ~2 ns time scale accessible. The presence of an EISF indicates that the observed motions have a localized diffusive nature. The EISF values at high-Q show a tendency to an asymptotic non-zero value (close to 0.5), suggeststing that about 50% of the hydrogen contributing to the spectrum perform only fast vibrational motions and do not contribute to the quasi-elastic part of the spectrum.

2. *Dynamics of lipoplex-DNA gene vectors*

Human gene therapy is defined as the transfer of nucleic acids to somatic cells of a patient providing a therapeutic effect [17,18]. Among the non-viral carriers, cationic liposomes (CL) attract a significant interest because of their unique properties and their efficiency in acting as vehicles for DNA delivery into eukariotic cells [18,19].
Many theoretical and experimental studies have been performed [20-24] to understand the factors governing the energetic, structural, and thermodynamic characteristics of CL-DNA complexes; these properties, strongly influenced by the specific composition of lipoplexes, are essential for optimizing their transfection efficiency. The cationic lipoplexes are normally constituted by the mixture of a neutral (helper) lipid and a charged lipid; the former determines a given structure (in particular lamellar or hexagonal geometry), whereas the latter is fundamental for delivering the genes into the cell [22,23-30].
The direct interaction of the positively charged lipid headgroup with the negatively charged phosphate of the DNA backbone is suggested by many authors to be the main mechanism for the complexation of DNA with cationic lipids [26,28]. This is also supported by both fluorescence techniques and differential scanning calorimetry [25] suggesting that the release of bound water and counterions is the driving force behind complex formation [26]. Besides, Choosakoonkriang and coworkers suggest that complexation with DNA induces a small increase in the disordered conformation of the lipid alkyl chain, altering the packing of the lipid (due to the alignment of the lipid headgroup with the DNA phosphate) and determining a greater fluidity of the apolar region of the membrane [27,28].
Unfortunately, very few studies have been performed on the dynamics of CLs-DNA systems to date; among them, is the recent investigation of highly oriented lamellar CLs-DNA complexes consisting of calf thymus DNA added to 1:1 ratio binary mixtures of cationic monovalent lipid DOTAP (dioleoyl trimethylammonium propane) and the neutral helper lipid DOPC (dioleoyl phosphatidylcholine), both lipids having two 18-carbon (C18) aliphatic chains per molecule [31].
The membrane dynamics is shown to be strongly dependent on the cationic lipid/DNA molar weight ratio ρ (Fig. 4). Indeed, CLs-DNA at the isoelectric point (Fig. 4, panel c), displays a marked anisotropy in the mean square displacements. In particular, higher dynamics is observed in the out-of-plane configuration.
The main result is that a minimum amount of DNA phosphate groups is not sufficient to induce modifications in membrane dynamics. On the other hand, at the isoelectric point, the balance of the total net charge inside the complex, together with the displacement of bound water molecules into solution (accompanied by counterion release), provides new degrees of freedom to the lipoplex, enhancing the apolar region fluidity and resulting in a very large increase of the out-of-plane lipid motions, mainly assigned to spatially confined vertical translation of the entire lipid molecule.
An exhaustive description of the results, together with a proposed model to interpret the data, is reported elsewhere [31].

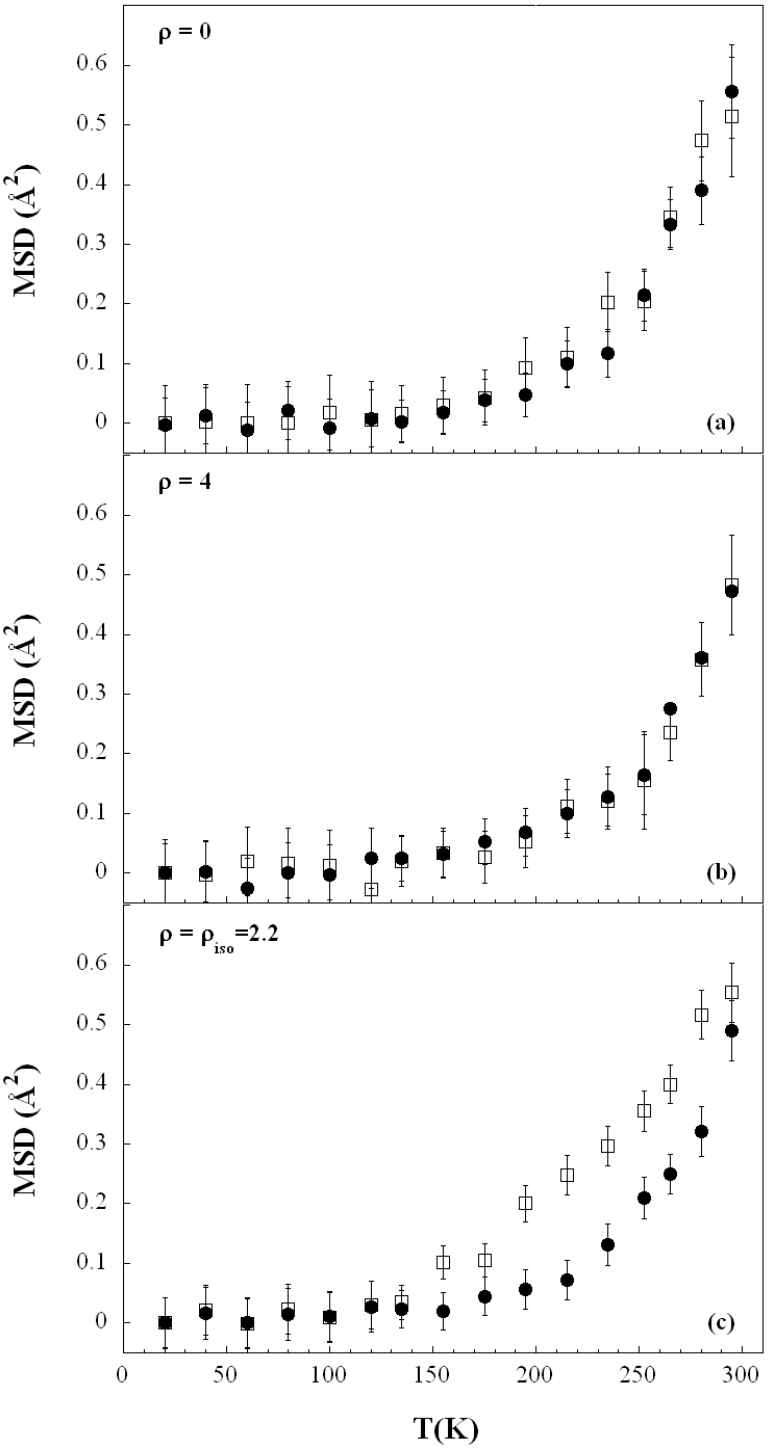

Fig. 4: Normalised MSD of the CLs-DNA mixed multilayers *vs.* T, as a function of the cationic lipid/DNA molar weight ratio ρ. Panel a: pure lipids (ρ=0); panel b: excess of liposomes (ρ=4); panel c: isoelectric point ($\rho=\rho_{iso}=2.2$). Open squares: out-of-plane direction; filled circles: in-plane direction. Incoherent elastic neutron scattering data have been acquired at IN13-ILL, with an energy resolution of 8μeV [31].

More recently [32], the investigation was extended to DOTAP-DOPC model membranes as a function of the DOTAP/(DOPC+DOTAP) ratio ϕ (Fig. 5), revealing a reduction of the dynamics along the direction normal to the membrane induced by increasing the neutral lipid (DOPC) concentration from ϕ = 0.5 to 0.8.

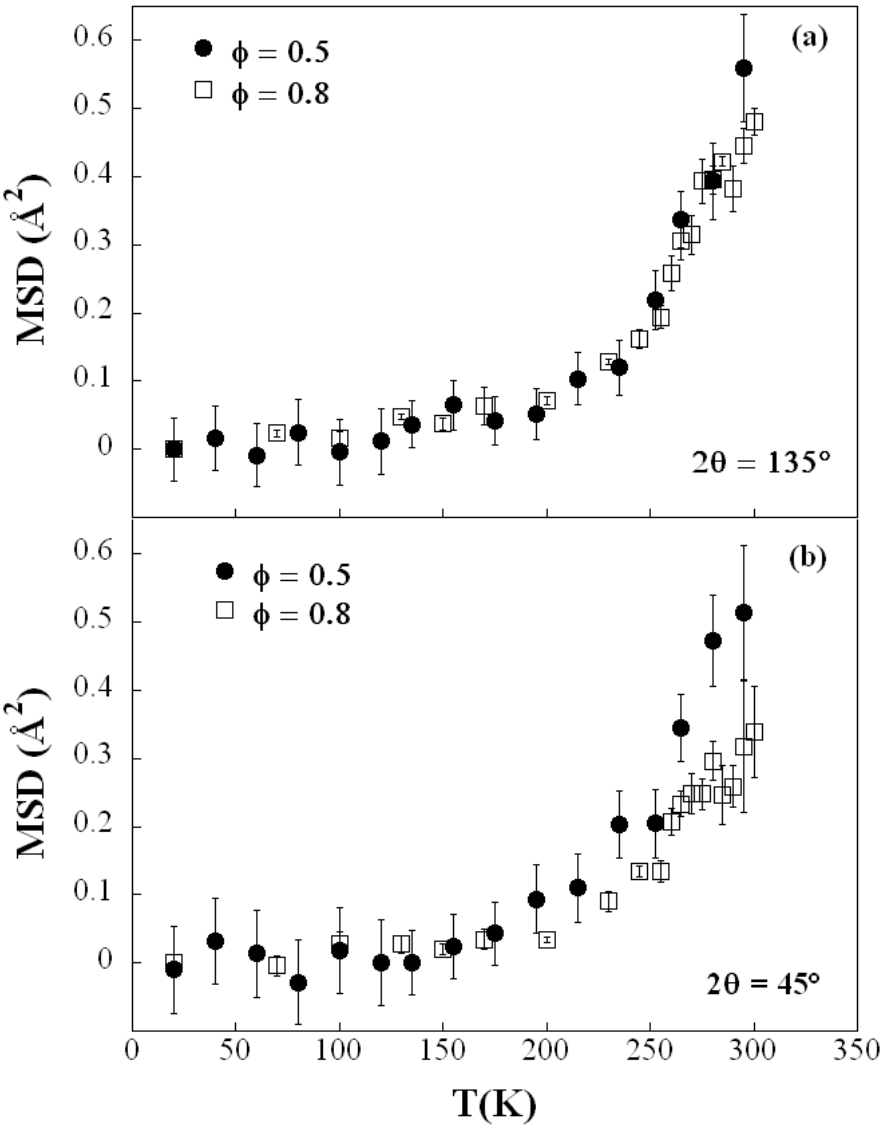

Fig. 5: Temperature dependences of MSD for ϕ = 0.5 (filled circles) and ϕ = 0.8 (empty squares), measured at 135° (a) and 45° (b) with respect to the membrane normal. Incoherent elastic neutron scattering data have been acquired at IN13-ILL, with an energy resolution of 8μeV [32].

The explanation of the observed behaviour has to take into account the origin of the detected elastic intensity. While in the case of ϕ = 0.5 equal contributions arise from DOPC and DOTAP scattering, the ϕ = 0.8 sample reflects a difference of the relative weight in the total revealed signal. Indeed, the 0.8 lipid ratio refers to the increasing of

DOPC concentration of a factor of 4 with respect to the DOTAP. Thus, being the density cross section comparable for the lipids, in the $\phi = 0.8$ case the 80 % contribution to the total signal is assigned to the DOPC, while only 20 % arises from DOTAP.
On the other hand, DOPC has greater hydrophilic heads, characterized by the presence of a phosphate PO_4^- group not present in the cationic DOTAP where there is only the aminic one NH_3^+. Thus, the decrease of the out-of-plane mean square displacements correlated to the increasing DOPC concentration may be interpreted in terms of more localized vertical diffusion due to less free space accessible (Fig. 6).

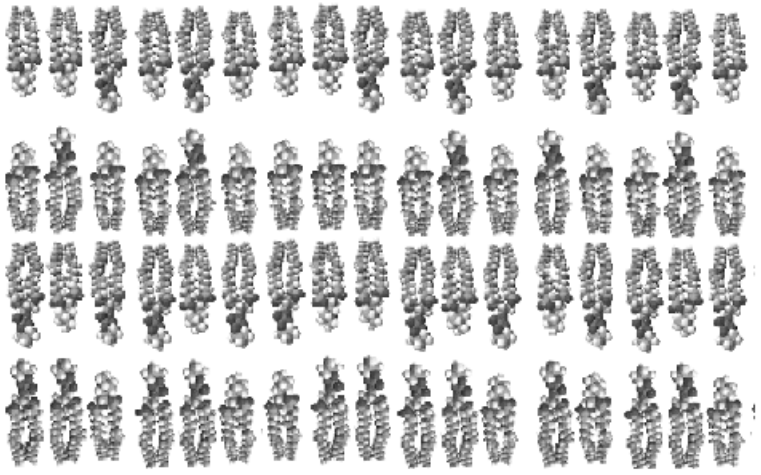

Fig. 6. Schematic representation of the DOTAP+DOPC oriented lipid mixture. The greater occupation of the interbilayer free space assigned to the DOPC, is evident.

Moreover, the ϕ independent in-plane dynamics confirms that the key-role in the changes of membrane dynamics is mainly governed by the different size of the lipid heads.

3. *The dynamics of the gangliosides in bilayer domains*

Many macromolecules of biological relevance are characterized by the presence of sugar moieties with different degrees of complexity. A particular class of sugar-containing molecules is that of gangliosides, glycosphingolipids abundant in neuronal plasma membranes, which are believed to play a role in a number of cellular functions, including cell recognition, adhesion, regulation, signal transduction, and development of tissues. They are predominantly located on the outer leaflet of the membrane and may act to protect the membrane from harsh conditions such as low pH or degradative enzymes [33, 34]. Ganglioside are amphiphilic molecules constituted of a ceramide and a saccharidic headgroup including one or more charged sugars (sialic acid). The mechanical properties and biological functions of gangliosides are strongly dependent on the behaviour of the lipids to which they are bound [35-38]. The properties of lipids are then likely to be strongly affected by the microdomain presence and arrangement.

One of the most commonly studied gangliosides is galactosyl-Nacetylgalactosaminyl(N-acetyl-neuraminyl)galactosylglucosylceramide (GM1) [39]. GM1 is a member of the glycosphingolipids family and contains four neutral sugar residues and a negatively charged sialic acid residue. The glycolipid monosialoganglioside GM1 is widely distributed in all tissues and reaches its highest concentrations in the central nervous system. It is primarily located in the outer surface of the mammalian cell's plasma membrane and in synaptic membranes of the CNS. GM1 ganglioside modulates a number of cell surface and receptor activities as well as neuronal differentiation and development, protein phosphorilation and synaptic function.

Recently the formation of ganglioside GM1-rich domains in monolayers and bilayers is an area of increased scientific interest. In particular, specialized membrane domains composed of phospholipids, glycolipids, and cholesterol-so called lipid rafts-are thought to play a role in a diverse range of processes ranging from membrane trafficking to signaling through specific membrane protein interactions where the raft microdomain acts as a platform for various cellular events [40-48].

The first investigation on the dynamics of low-hydration lamellar systems containing gangliosides concerned the effect induced by the presence of minority amount of GM1 molecules on the dynamics of oriented lamellar DMPC assemblies deposited on Si flat substrate [49].

A strong gap in the incoherent elastic neutron intensity, measured on IN13 at ILL, was observed across the gel-to-liquid lipid phase transition region (T_c ~ 320K, at the given membrane hydration) (Fig. 7).

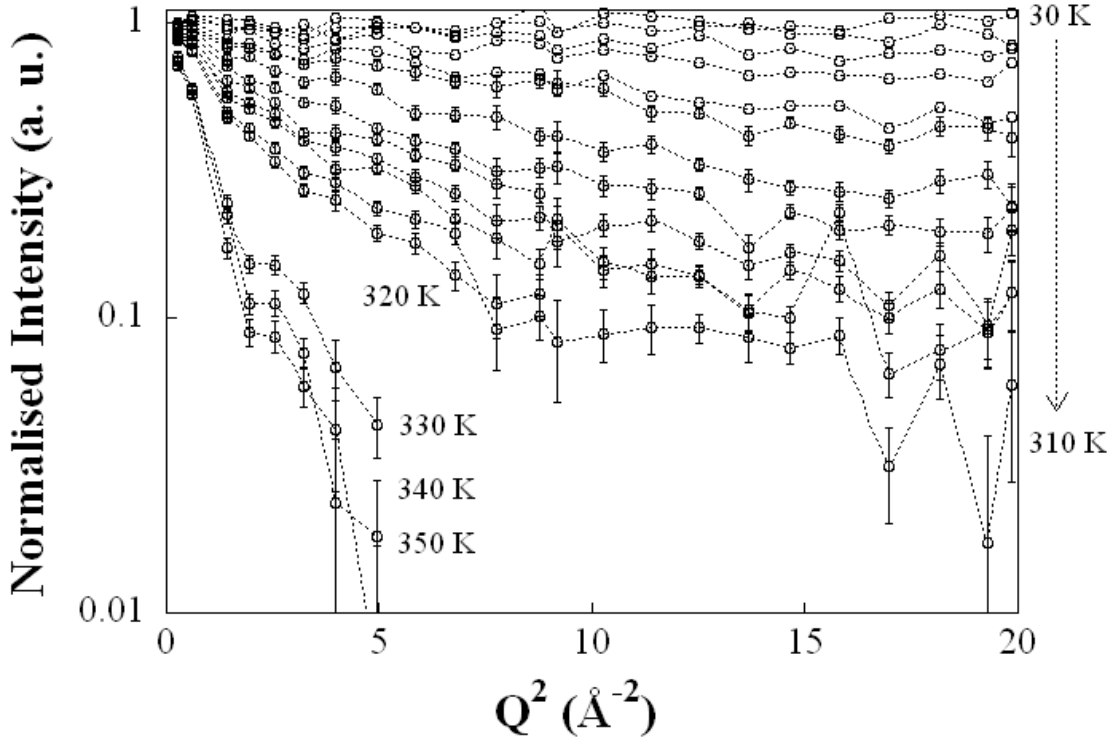

Fig. 7: Normalised elastic intensity of in-plane DMPC *vs.* Q^2, measured on IN13-ILL. Temperatures from 30 K to 350 K are reported. High temperature data points at high Q values are omitted for clarity, due to the large error bars associated to the low signals recorded [49].

Below the lipid phase transition, the in-plane lipid dynamics is sensibly increased upon addition of GM1, while a strong reduction of the out of plane mobility is observed across the phase transtion (data not shown, publication in progress, [49]).

At a glance, the presence of GM1 results in a clear increase in anisotropy, damping the mean square displacement in out-of-plane direction a $T > T_c$, and in a kink mainly affecting the in-plane curve at temperatures slightly lower than 300 K, as if a double process is taking place. The presence of domains enriched in gangliosides could provide the clue for a reasonable interpretation of these results. Moreover, the present results would support the hypothesis, drawn on the basis of past experiments with various techniques evidencing their ability to establish an extended network of interactions, that gangliosides play a central role in the coordination of the structure and dynamics of their environment.

4. Influence of hydration on the dynamics of model membrane systems

Biological membranes are composed not only of different kinds of lipids but also of membrane proteins and molecules like e.g. cholesterol and ethanol. Lipid membranes consisting of only one type of lipid such as 1,2-Dimyristoyl-*sn*-Glycero-3-Phosphocholine (DMPC) serve as role models for their more complex counterparts in biological systems. The phase behaviour is strongly dependent on the hydration level of the membranes [50]. Inelastic neutron scattering (INS) [51], quasi elastic neutron scattering (QENS) [2,52-53] and neutron spin echo spectroscopy (NSE) [54] have already been employed to study local as well as collective dynamics of these membranes. However, most of these studies lack a systematic investigation of the behaviour of the model membranes in dependence on their hydration.

By hydrating the mulilayer stack using pure D_2O or saturated salt solutions, the relative humidity (rh) can be adjusted and thus the level of hydration of the membranes.

From structural investigations [50] it is known that a lower degree of hydration causes a shift of the main phase transition to higher temperatures. As a result of the lower water content the repeating distance of the bilayers is reduced. The effect can be seen e.g. by neutron diffraction as a shift in the distance of the Bragg peaks originating from the lipid bilayers as shown in Fig. 8. Via the relation $d=\lambda/2*\sin(\theta)$ (λ=neutron wavelength, θ=scattering angle) the repeating distance d can easily be calculated. For a fully hydrated DMPC bilayer the d-spacing lies in the order of 63 Ångstroms [55]. While the influence of the hydration on the structural properties of the membranes is well investigated, the knowledge about this influence on the lipid dynamics of these model systems is rather poor. From quasi-elastic neutron scattering investigations on pure lipid multilayer systems, the diffusive motions of lipids within the bilayer have been estimated. Consistent values for the diffusion constant in the order of $D=11*10^{-10}$ m^2/s [51-53] have been obtained. However, none of them take into account hydration effects.

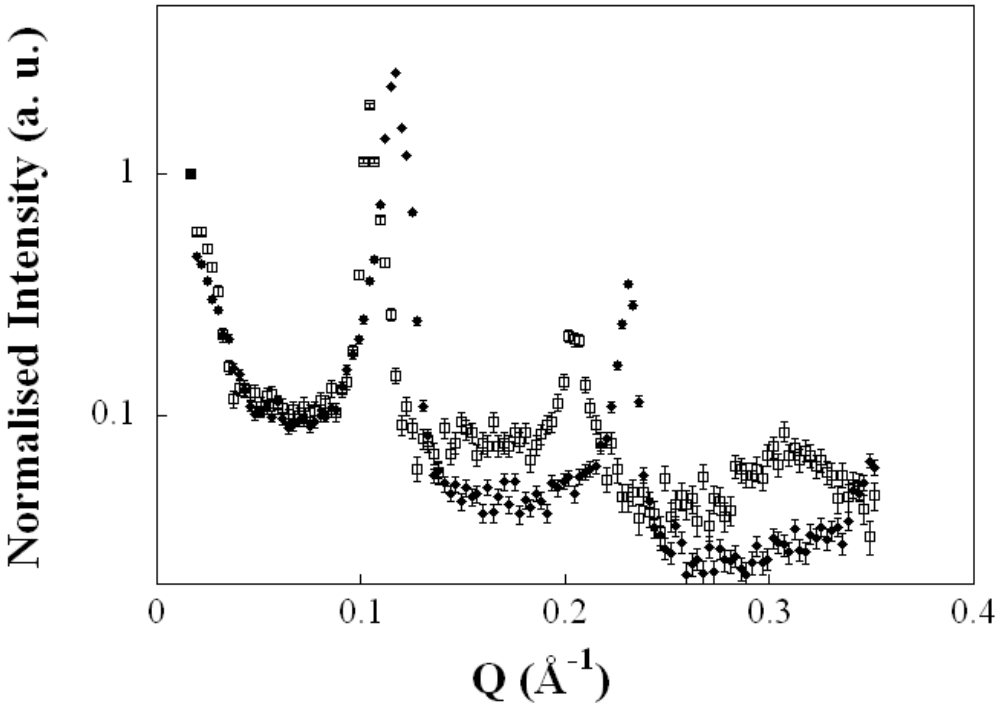

Fig. 8: Diffraction data taken on D16 at ILL to evaluate the d-spacing for two samples with different hydrations levels [56]. Open squares: 100 % rh (pure D_2O atmosphere); filled diamonds: 75% rh (D_2O in saturated NaCl salt solution). The experimental d-spacing are 62.5 Å and 54.9 Å, respectively [56].

Only recently, a neutron scattering investigation, performed on highly oriented DMPC multibilayers, at two different rh levels, enhanced the strong influence of hydration effect on the membrane dynamics [56] (Fig. 9).

The investigated temperature range covers both the main phase transition from the P_β ripple to the liquid-crystalline L_α phase which occurs around 296K for DMPC, at the hydration here investigated, and also the pre-transition from the L_β gel phase to the P_β ripple phase about 10 degrees below the main phase transition. The higher hydrated sample (100 % rh) shows a clear bend at the main lipid phase transition around 300K, in agreement with an increased mobility of the alkyl chain in the liquid phase, whereas a clear shift of the phase transition temperatures for the less hydrated sample (75 % rh) is evident.

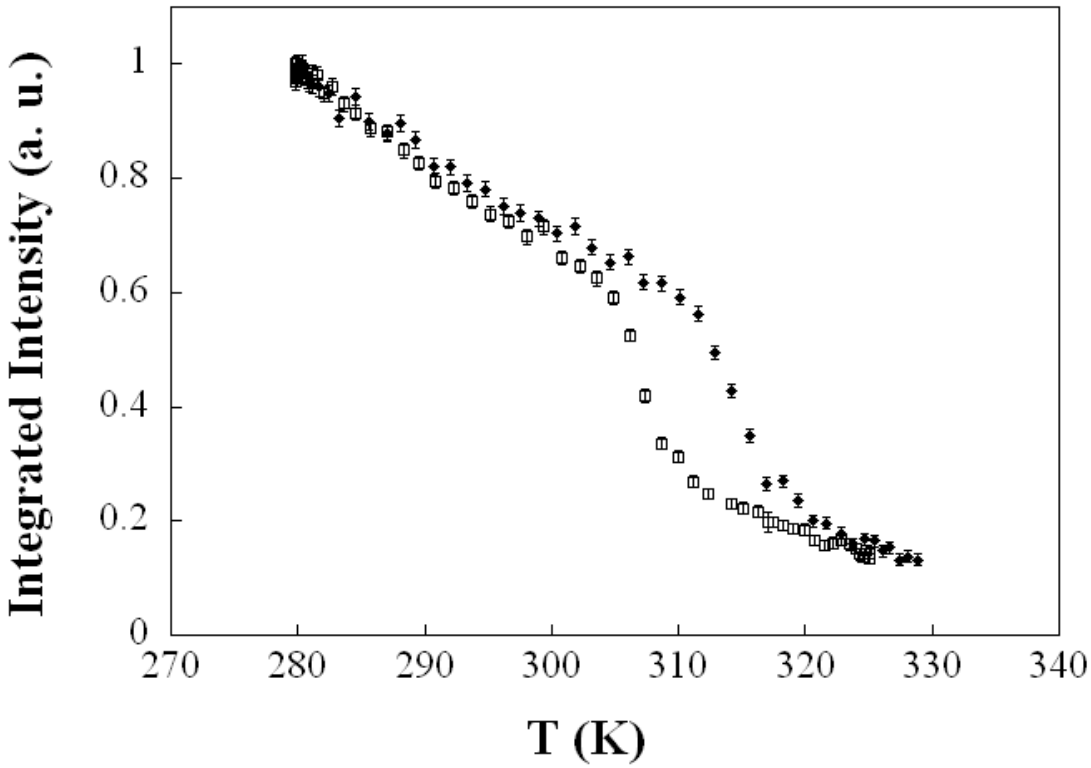

Fig. 9 Integrated elastic intensity of DMPC, measured at 135°, on the cold neutron backscattering spectrometer IN16 at ILL with an energy resolution of 0.9 μeV. Data are binned over the Q range 0.43 – 1.93 $Å^{-1}$ to gain in statistic. Empty symbols: h=100 % rh; filled symbols: h=75 % rh [56].

The study reveals the strong influence hydration, not only on the structure but also on the dynamics on membrane systems.

References

[1] Henkel T, Mittler S, Pfeiffer W, Rotzer H, Apell HJ, Knoll W. Lateral order in mixed lipid bilayers and its influence on ion translocation by gramicidin: a model for the structure-function relationship in membranes. Biochimie 1989; 71: 89-98.

[2] Pfeiffer W, Henkel TH, Sackmann E, Knoll W, Richter D. Local Dynamics of Lipid Bilayers Studied by Incoherent Quasi-Elastic Neutron Scattering. Europhys Lett 1989; 8: 201-6.

[3] Deriu, A. 1993. The power of quasielastic neutron scattering to probe biophysical systems. Phys. Rev. B. 183:331–342

[4] Doster, W., S. Cusack, and W. Petry. 1989. Dynamical transition of myoglobin revealed by inelastic neutron scattering. Nature. 337:754–756.

[5] Zaccai, G. 2000. How soft is a protein? A protein dynamics force constant measured by neutron scattering. Science. 288:1604–1607.

[6] Martenson RE. Myelin: Biology and Chemistry, CRC Press, Boca Raton, 1992.

[7] Luzzati V, Mateu L. Order-disorder phenomena in myelinated nerve sheaths. I. A physical model and its parametrization: exact and approximate determination of the parameters. J Mol Biol 1990; 215: 373-84.

[8] Smith R. The basic protein of CNS myelin: its structure and ligand binding. J Neurochem 1992; 59: 1589-608.

[9] Riccio P, Masotti L, Cavatorta P, De Santis A, Juretic D, Bobba A, Pasquali-Ronchetti I, Quagliarello E. Myelin basic protein ability to organize lipid bilayers: structural transition in bilayers of lysophosphatidylcholine micelles. Biochem Biophys Res Commun 1986; 134: 313-9.

[10] Carnegie PR, Dunkley PR, in: B.W. Agranoff, M.H. Aprison (Eds.), Advances in Neurochemistry, Plenum Press, New York, 1975..

[11] Omlin FX, deH. Webster F, Palkovits CG, Cohen S. Immunocytochemical localization of basic protein in major dense line regions of central and peripheral myelin. J Cell Biol 1982; 95: 242-8.

[12] Boggs MJ. Lipid–Protein Interactions, P.C. Jost, O.H. Griffith 2, 1982.

[13] Inouye H, Karthigasan J, Kirschner DA. Membrane structure in isolated and intact myelins. Biophys J 1989; 56: 129-37.

[14] Haas H, Torrielli M, Steitz R, Cavatorta P, Sorbi R, Fasano A, Riccio P, Gliozzi A. Myelin model membranes on solid substrates. Thin Solid Films 1998; 627: 327–329.

[15] Facci P, Cavatorta P, Cristofolini L, Fontana MP, Fasano A, Riccio P. Kinetic and structural study of the interaction of myelin basic protein with dipalmitoylphosphatidylglycerol layers. Biophys J 2000; 78: 1413-9.

[16] Natali F, Relini A, Gliozzi A, Rolandi R, Cavatorta P, Deriu A, Fasano A, Riccio P. Protein-membrane interaction: effect of myelin basic protein on the dynamics of oriented lipids. Chem Phys 2003; 292: 455-64.

[17] Friedmann T. Overcoming obstacles to gene therapy. Sci Am 1997; 276: 96–101.

[18] Rubanyi GM. The future of human gene therapy. Mol Aspects Med 2001; 22: 113–42.

[19] Felgner PL, Gadek TR, Holm M, Roman R, Chan RW, Wenz M, Northrop JP, Ringold GM, Danielsen M. Lipofection: a highly efficient, lipid-mediated DNA-transfection procedure. Proc Natl Acad Sci 1987; 84: 7413–7.

[20] Cullis PR, de Kruijff B. Lipid polymorphism and the functional roles of lipids in biological membranes. Biochim Biophys Acta 1979; 559: 399–420.

[21] Farhood H, Serbina N, Huang L. The role of dioleoyl phosphatidylethanolamine in cationic liposome mediated gene transfer. Biochim Biophys Acta 1995; 1235: 289–95.

[22] Liu Y, Mounkes LC, Liggitt HD, Brown CS, Solodin I, Heath TD, Debs RJ. Factors influencing the efficiency of cationic liposome-mediated intravenous gene delivery. Nat Biotechnol 1997; 15: 167–73.

[23] Radler JO, Koltover I, Salditt T, Safinya CR. Structure of DNA-cationic liposome complexes: DNA intercalation in multilamellar membranes in distinct interhelical packing regimes. Science 1997; 275: 810– 4.

[24] Crook K, Stevenson BJ, Dubouchet M, Porteous DJ. Inclusion of cholesterol in DOTAP transfection complexes increases the delivery of DNA to cells in vitro in the presence of serum. Gene Ther 1998; 5: 137–43.

[25] Hirsch-Lerner D, Barenholz Y. Hydration of lipoplexes commonly used in gene delivery: follow-up by laurdan fluorescence changes and quantification by differential scanning calorimetry. Biochim Biophys Acta 1999; 1461: 47–57.

[26] Kennedy MT, Pozharski EV, Rakhmanova VA, MacDonanld RC. Factors governing the assembly of cationic phospholipid-DNA complexes. Biophys J 2000; 78: 1620–33.

[27] Regelin AE, Fankhaenel S., Gurtesch L., Prinz C., von Kiedrowski G., Massing. U. Biophysical and lipofection studies of DOTAP analogs. Biochim Biophys Acta 2000: 1464: 151–64.

[28] Choosakoonkriang S, Wiethoff CM, Anchordoquy TJ, Koe GS, Smith JG, Middaugh CR. Infrared spectroscopic characterization of the interaction of cationic lipids with plasmid DNA. J Biol Chem 2001; 276: 8037–43.

[29] Braun CS, Jas GS, Choosakoonkriang S, Koe GS, Smith JG, Middaugh CR. The structure of DNA within cationic lipid/DNA complexes. Biophys J 2003; 84: 1114–23.

[30] Zuhorn IS, Oberle V, Visser WH, Engberts JBN, Bakowsky U, Polushkin E, Hoechkstra D. Phase behavior of cationic amphiphiles and their mixtures with

helper lipid influences lipoplex shape, DNA translocation, and transfection efficiency. Biophys J 2002; 83: 2096–108.

[31] Natali F, Pozzi D, Castellano C, Caracciolo G, Congiu Castellano A. DNA-lipoplex: a non-invasive method for gene delivery. A neutron scattering investigation. Biophys J 2005; 88(2):1081-90.

[32] Castellano C, Natali F, Pozzi D, Caracciolo G, Congiu Castellano A. Dynamical properties of oriented lipid membranes studied by elastic incoherent neutron scattering. Physica B 2004; 350: 955-8.

[33] Alberts B. Molecular Biology of the Cell., 3rd Ed; Garland Publishing Inc., New York, 1994.

[34] Beitinger H, Vogel V, Möbius D, Rahmann H. Surface potentials and electric dipole moments of ganglioside and phospholipid bilayers: contribution of the polar headgroup at the water/lipid interface. Biochim Biophys Acta 1989; 984: 293–300.

[35] Brocca P, Cantù L, Corti M, Del Favero E, Raudino A. Cooperative behavior of ganglioside molecules in model systems. Neurochem Res 2002; 27: 559–63.

[36] Cantu' L, Corti M, Del Favero E, Muller E, Raudino A, Sonnino S. Thermal Hysteresis in Ganglioside Micelles Investigated by Differential Scanning Calorimetry and Light-Scattering. Langmuir 1999; 15: 4975–80.

[37] Cantu' L, Corti M, Del Favero E, Raudino A. Tightly Packed Lipid Lamellae with Large Conformational Flexibility in the Interfacial Region May Exhibit Multiple Periodicity in Their Repeat Distance. A Theoretical Analysis and X-ray Verification. Langmuir 2000; 16: 8903–11.

[38] Boretta M, Cantu' L, Corti M, Del Favero E. Cubic phases of gangliosides in water: Possible role of the conformational bistability of the headgroup. Physica A 1997; 236: 162–76.

[39] Maggio B. The surface behavior of glycosphingolipids in biomembranes: a new frontier of molecular ecology. Prog Biophys Mol Biol 1994; 62: 55–117.

[40] Simons K, Ikonen E. Functional rafts in cell membranes. Nature 1997; 387: 569–72.

[41] Yuan C, Johnston LJ. Distribution of ganglioside GM1 in L-alpha-dipalmitoylphosphatidylcholine/cholesterol monolayers: a model for lipid rafts Biophys J 2000; 79: 2768–81.

[42] Sharom FJ, Grant CW. A model for ganglioside behaviour in cell membranes. Biochim Biophys Acta 1978, 507, 280–93.

[43] Peters M, Mehlhorn I, Barber K, Grant C. Evidence of a distribution difference between two gangliosides in bilayer membranes. Biochim Biophys Acta 1984; 778: 419–28.

[44] Delmelle M, Dufrane SP, Brasseur R, Ruysschaert JM. Clustering of gangliosides in phospholipid bilayers. FEBS Lett 1980; 121: 11–4.

[45] McIntosh TJ, Simon SA. Long- and short-range interactions between phospholipid/ganglioside GM1 bilayers. Biochemistry 1994; 33: 10477–86.

[46] Bunow MR, Bunow B. Phase behavior of ganglioside-lecithin mixtures. Relation to dispersion of gangliosides in membranes. Biophys J 1979; 27: 325–37.

[47] Sela BA, Bach D. Calorimetric studies on the interaction of gangliosides with phospholipids and myelin basic protein. Biochim Biophys Acta 1984, 771, 177–182.

[48] Thompson TE, Allietta M, Brown RE, Johnson ML, Tillack TW. Organization of ganglioside GM1 in phosphatidylcholine bilayers. Biochim Biophys Acta 1985; 817: 229–37.

[49] Natali F, Caronna C, Del Favero E, Deriu A, Cantu' L. Directional dynamics in DMPC membranes containing gangliosides. In preparation.

[50] Smith GS, Sirota EB, Safinya CR, Clark NA. Structure of the L beta phases in a hydrated phosphatidylcholine multimembrane. Phys Rev Lett 1988; 60: 813-6.

[51] Rheinstädter MC, Ollinger C, Fragneto G, Demmel F, Salditt T, Collective Dynamics of Lipid Membranes Studied by Inelastic Neutron Scattering, Phys Rev. Lett., 2004; 93: 108107

[52] König S, Pfeiffer W, Bayerl T, Richter D, Sackmann E. Molecular dynamics of lipid bilayers studied by incoherent quasi-elastic neutron scattering. J Phys II France 1992; 2: 1589-615.

[53] Swenson J, Kargl F, Berntsen P, Svanberg C. Solvent and lipid dynamics of hydrated lipid bilayers by incoherent quasielastic neutron scattering. J Chem Phys 2008; 129: 045101.

[54] Rheinstädter MC, Häußler W, Salditt T, Dispersion Relation of Lipid Membrane Shape Fluctuations by Neutron Spin-Echo Spectrometry, Phys. Rev. Lett., 2006; 97: 048103

[55] Kucerka N, Liu Y, Chu N, Petrache HI, Tristram-Nagle S, Nagle JF. Structure of fully hydrated fluid phase DMPC and DLPC lipid bilayers using X-ray scattering from oriented multilamellar arrays and from unilamellar vesicles. Biophys J 2005; 88: 2626-37.

[56] Trapp M, Juranyi F, Unruh T, Tehei M, Gutberlet T, Peters J. To be submitted.

List of Tables

List of Figures

Bibliography

[1] J. Chadwick. Possible existence of a neutron. *Nature*, 129:312, Feb 1932.

[2] Amsler, C. et al. (Particle Data Group). Review of particle physics. *Physics Letters B*, 667(1-5):1–6, September 2008.

[3] B. N. Brockhouse. Lattice vibrations in silicon and germanium. *Phys. Rev. Lett.*, 2(6):256–258, Mar 1959.

[4] http://nobelprize.org/nobel_prizes/physics/laureates/1994/.

[5] M. Trapp, T. Gutberlet, F. Juranyi, T. Unruh, B. Demé, M. Tehei, and J. Peters. Hydration dependent studies of highly aligned multilayer lipid membranes by neutron scattering. *J. Chem. Phys.*, 133(16):164505–7, October 2010.

[6] J.H. Roh, J.E. Curtis, S. Azzam, V.N. Novikov, I. Peral, Z. Chowdhuri, R.B. Gregory, and A.P. Sokolov. Influence of hydration on the dynamics of lysozyme. *Biophys. J.*, 91:2573–2588, Oct 2006.

[7] M. Jasnin, M. Moulin, M. Haertlein, G. Zaccai, and M. Tehei. In Vivo Measurement of Internal and Global Macromolecular Motions in *Escherichia coli*. *Biophysical Journal*, 95(2):857–864, July 2008.

[8] A. Paciaroni, A. Orecchini, E. Cornicchi, M. Marconi, C. Petrillo, M. Haertlein, M. Moulin, H. Schober, M. Tarek, and F. Sacchetti. Fingerprints of amorphous icelike behavior in the vibrational density of states of protein hydration water. *Physical Review Letters*, 101(14):148104, 2008.

[9] W. Doster, S. Cusack, and W. Petry. Dynamical transition of myoglobin revealed by inelastic neutron scattering. *Nature*, 337(6209):754–756, February 1989.

[10] M. Tehei, B. Franzetti, D. Madern, M. Ginzburg, B. Z. Ginzburg, M.-T. Giudici-Orticoni, M. Bruschi, and G. Zaccai. Adaptation to extreme environments: macromolecular dynamics in bacteria compared in vivo by neutron scattering. *EMBO reports*, 5(1):66–70, 2004.

[11] Neutron data booklet, 2004. Institut Laue-Langevin.

[12] G. Squires. *Introduction to the Theory of Thermal Neutron Scatering*. Dover Publications, 1978.

[13] L. Van Hove. Correlations in space and time and born approximation scattering in systems of interacting particles. *Phys. Rev.*, 95(1):249–262, Jul 1954.

[14] A. Taylor, M. Dunne, S. Bennington, S. Ansell, I. Gardner, P. Norreys, T. Broome, D. Findlay, and R. Nelmes. A route to the brightest possible neutron source? *Science*, 315(5815):1092–1095, February 2007.

[15] H. F. Bohn, K. Clausen, A. Claver, R. Cywinsky, F. Frick, W. Rögener, B. Stahl-Busse, U. Steigenberger, H. Tietze-Jaensch, and P. Tindemans. European source of science. In *The ESS Project, Volume 1*. ESS council, 2002.

[16] H. Maier-Leibnitz and T. Springer. The use of neutron optical devices on beam-hole experiments on beam-hole experiments. *Journal of Nuclear Energy. Parts A/B. Reactor Science and Technology*, 17(4-5):217–225, July 1963.

[17] C. F. Majkrzak, V. Nunez, J. R. D. Copley, J. F. Ankner, and G. L. Greene. Supermirror transmission polarizers for neutrons. In *Proc. SPIE*, volume 1738, pages 90–106, San Diego, CA, USA, November 1992. SPIE.

[18] F. Mezei. Neutron spin echo: A new concept in polarized thermal neutron techniques. *Zeitschrift für Physik A Hadrons and Nuclei*, 255:146–160, Apr 1972.

[19] H. Maier-Leibnitz. Grundlagen für die Beurteilung von Intensitäts- und Genauigkeitsfragen bei Neutronenstreumessungen. *Nukleonik*, 8(2):61–67, 1966.

[20] http://www.ill.eu/instruments-support/instruments-groups/instruments/in16/characteristics/.

[21] http://www.frm2.tum.de/wissenschaftliche-nutzung/spektrometrie/toftof/prinzip-primaerspectrometer/index.html.

[22] http://www.ill.eu/instruments-support/instruments-groups/instruments/in6/characteristics/.

[23] T. Unruh, J. Neuhaus, and W. Petry. The high-resolution time-of-flight spectrometer TOFTOF. *Nuclear Instruments and Methods in*

Physics Research Section A: Accelerators, Spectrometers, Detectors and Associated Equipment, 580(3):1414–1422, Oct 2007.

[24] M. Bée. *Quasielastic Neutron Scattering:Principles and Applications in Solid State Chemistry, Biology and Materials Science*. Adam Hilger, Philadelphia, 1988.

[25] M. C. Rheinstädter, C. Ollinger, G. Fragneto, F. Demmel, and T. Salditt. Collective Dynamics of Lipid Membranes Studied by Inelastic Neutron Scattering. *Physical Review Letters*, 93(10):108107, 2004.

[26] J. Fitter and R.E. Lechner. Incoherent neutron scattering (INS), 1998.

[27] A. Rahman, K. S. Singwi, and A. Sjölander. Theory of slow neutron scattering by liquids. *Phys. Rev.*, 126(3):986–996, May 1962.

[28] J. C. Smith. Protein dynamics: comparison of simulations with inelastic neutron scattering experiments. *Quarterly Reviews of Biophysics*, 24(03):227–291, 1991.

[29] A. Guinier and G. Fournier. *Small-angle scattering of X-rays*. John Wiley & Sons, Inc, Hoboken, New Jersey, USA, 1955.

[30] V. Réat, G. Zaccai, C. Ferrand, and C. Pfister. Functional dynamics in purple membranes. In *Biological Macromolecular Dynamcis, Proceedings of a Workshop on Inelastic and Quasielastic Neutron Scattering in Biology*, pages 117–122, 1997.

[31] F. Volino and A. J. Dianoux. Neutron incoherent scattering law for diffusion in a potential of spherical symmetry: general formalism and application to diffusion inside a sphere. *Molecular Physics*, 41:271–279, Oct 1980.

[32] M.-C. Bellissent-Funel, J. Teixeira, K.F. Bradley, and S. H. Chen. Dynamics of hydration water in protein. *J. Phys. I France*, 2(6):995–1001, jun 1992.

[33] P. L. Hall and D. K. Ross. Incoherent neutron scattering functions for random jump diffusion in bounded and infinite media. *Molecular Physics*, 42:673–682, Feb 1981.

[34] K. S. Singwi and Alf Sjölander. Diffusive motions in water and cold neutron scattering. *Phys. Rev.*, 119(3):863–871, Aug 1960.

[35] L. Carpentier, M. Bée, A. M. Giroud-Godquin, P. Maldivi, and J. C. Marchon. Alkyl chain motions in columnar mesophases. *Molecular Physics*, 68(6):1367–1378, Dec 1989.

[36] S. König, W. Pfeiffer, T. Bayerl, D. Richter, and E. Sackmann. Molecular dynamics of lipid bilayers studied by incoherent quasi-elastic neutron scattering. *J. Phys. II France 2*, 2(8):1589–1615, Aug 1992.

[37] M. Doxastakis, V. Garcia Sakai, S. Ohtake, J. K. Maranas, and J. J. de Pablo. A Molecular View of Melting in Anhydrous Phospholipidic Membranes. *Biophys. J.*, 92(1):147–161, 2007.

[38] M. Prager and A. Heidemann. Rotational tunneling and neutron spectroscopy : a compilation. Technical Report ILL95PR20T, ILL, 1995.

[39] A. Deriu, A. Paciaroni, J. Zaccai, and C. Pfister. First experimental results from the IN13-Collaborative Research Group (CRG) at the ILL. *Physica B: Condensed Matter*, 276-278:512–513, March 2000.

[40] http://www.ill.eu/instruments-support/instruments-groups/instruments/in13/characteristics/.

[41] http://www.neutronoptics.com/index.html.

[42] M. S. Appavou, G. Gibrat, M.-C. Bellissent-Funel, M. Plazanet, J. Pieper, A. Buchsteiner, and B. Annighöfer. The influence of a medium pressure on the structure and dynamics of a bovine pancreatic trypsin inhibitor protein. *Journal of Physics: Condensed Matter*, 17(40):S3093–3099, 2005.

[43] W. H. Freeman. *Lehninger Principles of Biochemistry*. Freeman, W. H. and Company, 2005.

[44] W. Pfeffer. *Osmotische Untersuchungen. Studien zur Zellmechanik*. Engelmann, W., 1877.

[45] E. Gorter and F. Grendel. On bimolecular layers of lipid on the chromacytes of the blood. *J. Exp. Med.*, 41:439–443, 1925.

[46] S. J. Singer and G. L. Nicolson. The fluid mosaic model of the structure of cell membranes. *Science*, 175(4023):720–731, February 1972.

[47] O.G. Mouritsen and M. Bloom. Mattress model of lipid-protein interactions in membranes. *Biophysical Journal*, 46(2):141–153, August 1984.

[48] S. König, T. M. Bayerl, G. Coddens, D. Richter, and E. Sackmann. Hydration dependence of chain dynamics and local diffusion in L-alpha-dipalmitoylphosphtidylcholine multilayers studied by incoherent quasi-elastic neutron scattering. *Biophys. J.*, 68(5):1871–1880, 1995.

[49] B. W. Koenig, H. H. Strey, and K. Gawrisch. Membrane lateral compressibility determined by NMR and x-ray diffraction: effect of acyl chain polyunsaturation. *Biophys. J.*, 73(4):1954–1966, 1997.

[50] S. König, E. Sackmann, D. Richter, R. Zorn, C. Carlile, and T. M. Bayerl. Molecular dynamics of water in oriented DPPC multilayers studied by quasielastic neutron scattering and deuterium-nuclear magnetic resonance relaxation. *The Journal of Chemical Physics*, 100(4):3307–3316, 1994.

[51] S. Busch, C. Smuda, L. C. Pardo, and T. Unruh. Molecular mechanism of long-range diffusion in phospholipid membranes studied by quasielastic neutron scattering. *Journal of the American Chemical Society*, 132:3232 – 3233, 2010.

[52] M. C. Rheinstädter, W. Häußler, and T. Salditt. Dispersion Relation of Lipid Membrane Shape Fluctuations by Neutron Spin-Echo Spectrometry. *Physical Review Letters*, 97(4):048103, 2006.

[53] R. H. Pearson and I. Pascher. The molecular structure of lecithin dihydrate. *Nature*, 281(5731):499–501, October 1979.

[54] T. Heimburg. *Thermal Biophysics of Membranes*. Wiley-VCH, Weinheim, Germany, 2007.

[55] G. S. Smith, E. B. Sirota, C. R. Safinya, and N. A. Clark. Structure of the L_β phases in a hydrated phosphatidylcholine multimembrane. *Phys. Rev. Lett.*, 60(9):813–816, Feb 1988.

[56] D. Guard-Friar, C. H. Chen, and A. S. Engle. Deuterium isotope effect on the stability of molecules: phospholipids. *The Journal of Physical Chemistry*, 89:1810–1813, 1985.

[57] http://www.avantilipids.com.

[58] T. Heimburg. A model for the lipid pretransition: Coupling of ripple formation with the chain-melting transition. *Biophysical Journal*, 78(3):1154–1165, March 2000.

[59] L. Ding, T.M. Weiss, G. Fragneto, W. Liu, L. Yang, and H.W. Huang. Distorted Hexagonal Phase Studied by Neutron Diffraction: Lipid Components Demixed in a Bent Monolayer. *Langmuir*, 21(1):203–210, 2005.

[60] J. Fitter, S. A. W. Verclas, R. E. Lechner, H. Seelert, and N. A. Dencher. Function and picosecond dynamics of bacteriorhodopsin in purple membrane at different lipidation and hydration. *FEBS Letters*, 433(3):321 – 325, 1998.

[61] J. Zanotti, M.-C. Bellissent-Funel, and J. Parello. Hydration-Coupled Dynamics in Proteins Studied by Neutron Scattering and NMR: The Case of the Typical EF-Hand Calcium-Binding Parvalbumin. *Biophysical Journal*, 76(5):2390 – 2411, 1999.

[62] F. Gabel, D. Bicout, U. Lehnert, M. Tehei, M. Weik, and G. Zaccai. Protein dynamics studied by neutron scattering. *Quarterly Reviews of Biophysics*, 35(04):327–367, 2003.

[63] J. Pieper, T. Hauß, A. Buchsteiner, and G. Renger. The effect of hydration on protein flexibility in photosystem II of green plants studied by quasielastic neutron scattering. *European Biophysics Journal*, 37:657–663, 2008.

[64] K. Wood, U Lehnert, B. Kessler, G. Zaccai, and D. Oesterhelt. Hydration dependence of active core fluctuations in bacteriorhodopsin. *Biophysical Journal*, 95(1):194 – 202, 2008.

[65] P. J. Steinbach and B.R. Brooks. Protein hydration elucidated by molecular dynamics simulation. *Proceedings of the National Academy of Sciences*, 90:9135–9139, 1993.

[66] M. Tarek and D. J. Tobias. Role of Protein-Water Hydrogen Bond Dynamics in the Protein Dynamical Transition. *Phys. Rev. Lett.*, 88(13):138101, Mar 2002.

[67] C.-J. Högberg and A. P. Lyubartsev. A molecular dynamics investigation of the influence of hydration and temperature on structural and dynamical properties of a dimyristoylphosphatidylcholine bilayer. *The Journal of Physical Chemistry B*, 110:14326–14336, 2006.

[68] E. G. Brandt and O. Edholm. Stretched exponential dynamics in lipid bilayer simulations. *J. Chem. Phys.*, 133(11):115101–12, September 2010.

[69] W. Pfeiffer, Th. Henkel, E. Sackmann, W. Knoll, and D. Richter. Local Dynamics of Lipid Bilayers Studied by Incoherent Quasi-Elastic Neutron Scattering. *EPL (Europhysics Letters)*, 8(2):201–206, 1989.

[70] M. Rheinstädter, J. Das, E. Flenner, B. Brüning, T. Seydel, and I. Kosztin. Motional coherence in fluid phospholipid membranes. *Physical Review Letters*, 101(24):248106, 2008.

[71] A. A. Nevzorov and M. F. Brown. Dynamics of lipid bilayers from comparative analysis of ^{2}H and ^{13}C nuclear magnetic resonance relaxation data as a function of frequency and temperature. *The Journal of Chemical Physics*, 107(23):10288–10310, 1997.

[72] S. H. Chen, C. Y. Liao, H. W. Huang, T. M. Weiss, M.-C. Bellisent-Funel, and F. Sette. Collective Dynamics in Fully Hydrated Phospholipid Bilayers Studied by Inelastic X-Ray Scattering. *Phys. Rev. Lett.*, 86(4):740–743, Jan 2001.

[73] B. Klösgen, C. Reichle, S. Kohlsmann, and K.D. Kramer. Dielectric spectroscopy as a sensor of membrane headgroup mobility and hydration. *Biophysical Journal*, 71:3251 – 3260, 1996.

[74] E. Y. Shalaev and P. L. Steponkus. Glass transition of a synthetic phospholipid in the lamellar phase. *The Journal of Physical Chemistry B*, 107:8734–8737, Aug 2003.

[75] R. Hirn, T. M. Bayerl, J. O. Rädler, and E. Sackmann. Collective membrane motions of high and low amplitude, studied by dynamic light scattering and micro-interferometry. *Faraday Discuss.*, 111:17–30, 1999.

[76] C. Eggeling, C. Ringemann, R. Medda, G. Schwarzmann, K. Sandhoff, S. Polyakova, V.N. Belov, B. Hein, C. von Middendorff, A. Schonle, and S.W. Hell. Direct observation of the nanoscale dynamics of membrane lipids in a living cell. *Nature*, 457:1159–1162, Feb 2009.

[77] http://www.ill.eu/d16/.

[78] N. Kucerka, Y. Liu, N. Chu, H. I. Petrache, S. Tristram-Nagle, and J. F. Nagle. Structure of Fully Hydrated Fluid Phase DMPC and DLPC Lipid Bilayers Using X-Ray Scattering from Oriented Multilamellar Arrays and from Unilamellar Vesicles. *Biophys. J.*, 88(4):2626–2637, 2005.

[79] M. C. Rheinstädter, T. Seydel, F. Demmel, and T. Salditt. Molecular motions in lipid bilayers studied by the neutron backscattering technique. *Physical Review E (Statistical, Nonlinear, and Soft Matter Physics)*, 71(6):061908, 2005.

[80] http://www.ill.eu/instruments-support/computing-for-science/cs-software/all-software/lamp/.

[81] B. Frick and L. J. Fetters. Methyl group dynamics in glassy polyisoprene: A neutron backscattering investigation. *Macromolecules*, 27:974–980, 1994.

[82] H. Pfeiffer, H. Binder, G. Klose, and K. Heremans. Hydration pressure and phase transitions of phospholipids: I. Piezotropic approach. *Biochimica et Biophysica Acta (BBA) - Biomembranes*, 1609(2):144–147, Jan 2003.

[83] H. Pfeiffer, H. Binder, G. Klose, and K. Heremans. Hydration pressure and phase transitions of phospholipids: II. Thermotropic approach. *Biochimica et Biophysica Acta (BBA) - Biomembranes*, 1609(2):148–152, Jan 2003.

[84] M. Trapp, F. Juranyi, M. Tehei, L. van Eijck, B. Demé, T. Gutberlet, and J. Peters. Elastic scattering studies of aligned dmpc multilayers on different hydrations. *Spectroscopy*, 24(5):461–466, January 2010.

[85] F. Natali, A. Relini, A. Gliozzi, R. Rolandi, P. Cavatorta, A. Deriu, A. Fasano, and P. Riccio. The influence of the lipid-protein interaction on the membrane dynamics. *Physica B: Condensed Matter*, 350(1-3, Supplement 1):E623 – E626, 2004. Proceedings of the Third European Conference on Neutron Scattering.

[86] E. Flenner, J. Das, M. C. Rheinstadter, and I. Kosztin. Subdiffusion and lateral diffusion coefficient of lipid atoms and molecules in phospholipid bilayers. *Physical Review E (Statistical, Nonlinear, and Soft Matter Physics)*, 79(1):011907, 2009.

[87] J. Peters, M. C. Rheinstädter, T. Seydel, and M. Trapp. A memory function to measure difusion in membranes by elastic and quasielastic neutron scattering. ILL report CRG 1584.

[88] http://sourceforge.net/projects/frida/.

[89] http://www.ncnr.nist.gov/dave.

[90] J. Swenson, F. Kargl, P. Berntsen, and C. Svanberg. Solvent and lipid dynamics of hydrated lipid bilayers by incoherent quasielastic neutron scattering. *The Journal of Chemical Physics*, 129(4):045101, 2008.

[91] F. Natali, A. Relini, A. Gliozzi, R. Rolandi, P. Cavatorta, A. Deriu, A. Fasano, and P. Riccio. Protein-membrane interaction: effect of myelin basic protein on the dynamics of oriented lipids. *Chemical Physics*, 292(2-3):455 – 464, 2003. Quasielastic Neutron Scattering of Structural Dynamics in Condensed Matter.

[92] M. Bée, H. Jobic, and C. Sourisseau. Neutron scattering study of methyl group reorientations in trimethyloxosulphonioum iodide, $(CH_3)_3SOI$. *Journal of Physics C: Solid State Physics*, 18(31):5771–5781, 1985.

[93] M. Tehei, J. C. Smith, C. Monk, J. Ollivier, M. Oettl, V. Kurkal, J. L. Finney, and R. M. Daniel. Dynamics of immobilized and native escherichia coli dihydrofolate reductase by quasielastic neutron scattering. *Biophysical Journal*, 90(3):1090–1097, February 2006.

[94] Z. Bu, D. A. Neumann, S.-H. Lee, C. M. Brown, D. M. Engelman, and C. C. Han. A view of dynamics changes in the molten globule-native folding step by quasielastic neutron scattering. *Journal of Molecular Biology*, 301(2):525–536, August 2000.

[95] P. A. Egelstaff. *An introduction to the liquid state*. Academic Press, New York, USA, 1967.

[96] R. Winter and W. Dzwolak. Exploring the temperature-pressure configurational landscape of biomolecules: from lipid membranes to proteins. *Philosophical Transactions of the Royal Society A: Mathematical, Physical and Engineering Sciences*, 363:537–563, Feb 2005.

[97] R. Winter. High pressure nmr studies on lyotropic lipid mesophases and model biomembranes. In G. A. WEBB, editor, *Annual Reports on NMR Spectroscopy*, volume 50 of *Annual Reports on NMR Spectroscopy*, pages 163 – 200. Academic Press, 2003.

[98] G. N. Somero. Adaptations to high hydrostatic pressure. *Annual Review of Physiology*, 54(1):557–577, October 1992.

[99] M. L. M. Lopes, V. L. Valente Mesquita, A. C. N. Chiaradia, A. A. R. Fernandes, and P. M. B. Fernandes. High hydrostatic pressure processing of tropical fruits. *Annals of the New York Academy of Sciences*, 1189(1):6–15, 2010.

[100] J. P. P. M. Smelt. Recent advances in the microbiology of high pressure processing. *Trends in Food Science & Technology*, 9(4):152–158, April 1998.

[101] E. F. DeLong and A. A. Yayanos. Adaptation of the membrane lipids of a deep-sea bacterium to changes in hydrostatic pressure. *Science*, 228(4703):1101–1103, May 1985.

[102] http://www.coml.org/.

[103] C. R. Woese, O. Kandler, and M. L. Wheelis. Towards a natural system of organisms: proposal for the domains archaea, bacteria, and eucarya. *Proceedings of the National Academy of Sciences of the United States of America*, 87(12):4576–4579, June 1990.

[104] J. R. Hazel and E. E. Williams. The role of alterations in membrane lipid composition in enabling physiological adaptation of organisms to their physical environment. *Progress in Lipid Research*, 29(3):167–227, 1990.

[105] I. D. Skanes, J. Stewart, K. M. W. Keough, and M. R. Morrow. Effect of chain unsaturation on bilayer response to pressure. *Phys. Rev. E*, 74(5):051913–, November 2006.

[106] L. F. Braganza and David L. Worcester. Hydrostatic pressure induces hydrocarbon chain interdigitation in single-component phospholipid bilayers. *Biochemistry*, 25:2591–2596, 1986.

[107] F. H. Johnson and E. A. Flagler. Hydrostatic pressure reversal of narcosis in tadpoles. *Science*, 112:91–92, 1950.

[108] T. Heimburg and A. D. Jackson. The thermodynamics of general anesthesia. *Biophysical Journal*, 92(9):3159–3165, May 2007.

[109] D. H. Bartlett. Pressure effects on in vivo microbial processes. *Biochimica et Biophysica Acta (BBA) - Protein Structure and Molecular Enzymology*, 1595(1-2):367–381, March 2002.

[110] H. Dvir, I. Silman, M. Harel, T. L. Rosenberry, and J. L. Sussman. Acetylcholinesterase: From 3d structure to function. *Chemico-Biological Interactions*, 187(1-3):10–22, September 2010.

[111] P. Masson and O. Lockridge. Butyrylcholinesterase for protection from organophosphorus poisons: Catalytic complexities and hysteretic behavior. *Archives of Biochemistry and Biophysics*, 494(2):107 – 120, 2010.

[112] F. Zheng, W. Yang, M.-C. Ko, J. Liu, H. Cho, D. Gao, M. Tong, H.-H. Tai, J. H. Woods, and C.-G. Zhan. Most efficient cocaine hydrolase designed by virtual screening of transition states. *Journal of the American Chemical Society*, 130(36):12148–12155, September 2008.

[113] D. M. Quinn. Acetylcholinesterase: enzyme structure, reaction dynamics, and virtual transition states. *Chemical Reviews*, 87(5):955–979, October 1987.

[114] J.L. Sussman, M. Harel, F. Frolow, C. Oefner, A. Goldman, L. Toker, and I. Silman. Atomic structure of acetylcholinesterase from *Torpedo californica*: a prototypic acetylcholine-binding protein. *Science*, 253(5022):872–879, August 1991.

[115] M. Monkenbusch, D. Richter, and R. Biehl. Observation of protein domain motions by neutron spectroscopy. *Chem. Eur. J. of Chem. Phys.*, 11(6):1188–1194, 2010.

[116] R. Biehl, B. Hoffmann, M. Monkenbusch, P. Falus, S. Préost, R. Merkel, and D. Richter. Direct observation of correlated interdomain motion in alcohol dehydrogenase. *Phys. Rev. Lett.*, 101(13):138102–, September 2008.

[117] J.A. McCammon and S.C. Harvey. *Dynamics of proteins and nucleic acids*, volume 17, page 220. Cambridge University Press, Cambridge, 1987.

[118] H.-X. Zhou, S. T. Wlodek, and J. A. McCammon. Conformation gating as a mechanism for enzyme specificity. *Proceedings of the National Academy of Sciences of the United States of America*, 95(16):9280–9283, August 1998.

[119] S. V. Lushchekina, A. V. Nemukhin, D. I. Morozov, and S. D. Varfolomeev. Correlation between the substrate structure and the rate of acetylcholinesterase hydrolysis modeled with the combined quantum mechanical/molecular mechanical studies. *Chemico-Biological Interactions*, 187(1-3):59–63, September 2010.

[120] Y. Xu, J. P. Colletier, H. Jiang, I. Silman, J. L. Sussman, and M. Weik. Induced-fit or preexisting equilibrium dynamics? lessons from protein crystallography and md simulations on acetylcholinesterase and implications for structure-based drug design. *Protein Science*, 17(4):601–605, 2008.

[121] S. Tara, V. Helms, T. P. Straatsma, and J. A. McCammon. Molecular dynamics of mouse acetylcholinesterase complexed with huperzine a. *Biopolymers*, 50:347–359, 1999.

[122] S. Tara, T. P. Straatsma, and J. A. McCammon. Mouse acetylcholinesterase unliganded and in complex with huperzine a: A comparison of molecular dynamics simulations. *Biopolymers*, 50(1):35–43, 1999.

[123] T. Shen, K. Tai, R. H. Henchman, and J. A. McCammon. Molecular dynamics of acetylcholinesterase. *Accounts of Chemical Research*, 35(6):332–340, June 2002.

[124] Y. Xu, J. Shen, X. Luo, I. Silman, J. L. Sussman, K. Chen, and H. Jiang. How does huperzine a enter and leave the binding gorge of acetylcholinesterase? steered molecular dynamics simulations. *Journal of the American Chemical Society*, 125(37):11340–11349, 2003.

[125] K. Henzler-Wildman and D. Kern. Dynamic personalities of proteins. *Nature*, 450(7172):964–972, dec 2007.

[126] G. R. Kneller. Quasielastic neutron scattering and relaxation processes in proteins: analytical and simulation-based models. *Phys. Chem. Chem. Phys.*, 7(13):2641–2655, 2005.

[127] L. Larini, A. Ottochian, C. De Michele, and D. Leporini. Universal scaling between structural relaxation and vibrational dynamics in glass-forming liquids and polymers. *Nature Physics*, 4(1):42–45, January 2008.

[128] A. Ottochian, C. De Michele, and D. Leporini. Universal divergenceless scaling between structural relaxation and caged dynamics in glass-forming systems. *J. Chem. Phys.*, 131(22):224517–10, December 2009.

[129] Y. Nicolet, O. Lockridge, P. Masson, J. C. Fontecilla-Camps, and F. Nachon. Crystal Structure of Human Butyrylcholinesterase and of Its Complexes with Substrate and Products. *Journal of Biological Chemistry*, 278(42):41141–41147, 2003.

[130] R.M. Daniel, R.V. Dunn, J.L. Finney, and J.C. Smith. The role of dynamics in enzyme activity. *Annual Review of Biophysics and Biomolecular Structure*, 32(1):69–92, June 2003.

[131] F. Natali, J. Peters, D. Russo, S. Barbieri, C. Chiapponi, A. Cupane, A. Deriu, M. T. Di Bari, E. Farhi, Y. Gerelli, P. Mariani, A. Paciaroni, C. Rivasseau, G. Schiró, and F. Sonvico. IN13 Backscattering Spectrometer at ILL: Looking for Motions in Biological Macromolecules and Organisms. *Neutron News*, 19:14–18, 2008.

[132] E. Carletti, H. Li, B. Li, F. Ekstrom, Y. Nicolet, M. Loiodice, E. Gillon, M. T. Froment, O. Lockridge, L. M. Schopfer, P. Masson, and F. Nachon. Aging of cholinesterases phosphylated by tabun proceeds through o-dealkylation. *Journal of the American Chemical Society*, 130(47):16011–16020, November 2008.

[133] T. L. Rosenberry and D. M. Scoggin. Structure of human erythrocyte acetylcholinesterase. characterization of intersubunit disulfide bonding and detergent interaction. *Journal of Biological Chemistry*, 259(9):5643–5652, May 1984.

[134] G. L. Ellman, K.D. Courtney, V. Andres jr., and R. M. Featherstone. A new and rapid colorimetric determination of acetylcholinesterase activity. *Biochemical Pharmacology*, 7(2):88–90, IN1, 91–95, July 1961.

[135] R. Zorn. On the evaluation of neutron scattering elastic scan data. *Nuclear Instruments and Methods in Physics Research Section A: Accelerators, Spectrometers, Detectors and Associated Equipment*, 603(3):439–445, May 2009.

[136] M. Bée. Localized and long-range diffusion in condensed matter: state of the art of QENS studies and future prospects. *Chemical Physics*, 292(2-3):121–141, Mar 2003.

[137] G. Zaccai. The case for an empirical high-throughput neutron scattering approach to protein dynamics. *Acta Cryst D*, 2010.

[138] H. H. Paalman and C. J. Pings. Numerical evaluation of x-ray absorption factors for cylindrical samples and annular sample cells. *J. Appl. Phys.*, 33(8):2635–2639, August 1962.

[139] M. Tehei, R. Daniel, and G. Zaccai. Fundamental and biotechnological applications of neutron scattering measurements for macromolecular dynamics. *European Biophysics Journal*, 35(7):551–558, 2006.

[140] E. Carletti, J.-P. Colletier, F. Dupeux, M. Trovaslet, P. Masson, and F. Nachon. Structural evidence that human acetylcholinesterase inhibited by tabun ages through o-dealkylation. *Journal of Medicinal Chemistry*, 53(10):4002–4008, May 2010.

[141] P. Masson, S. Rey, C. Cléry, N. Fontaine, C. Kronman, B. Velan, and A. Shafferman. Stability of aged phosphylated cholinesterases and chymotrypsin. *Proceedings of the Medical Defense Bioscience Review*, 1:43–52, 1996.

[142] F. Gabel, M. Weik, P. Masson, F. Renault, D. Fournier, L. Brochier, B. P. Doctor, A. Saxena, I. Silman, and G. Zaccai. Effects of Soman Inhibition and of Structural Differences on Cholinesterase Molecular Dynamics: A Neutron Scattering Study. *Biophys. J.*, 89(5):3303–3311, 2005.

[143] P. Masson, C. Cléry, P. Guerra, A. Redslob, C. Albaret, and P. L. Fortier. Hydration change during the aging of phosphorylated human butyrylcholinesterase: importance of residues aspartate-70 and glutamate-197 in the water network as probed by hydrostatic and osmotic pressures. *Biochem. J.*, 343(2):361–369, October 1999.

[144] F. Gabel, P. Masson, M.-T. Froment, B.P. Doctor, A. Saxena, I. Silman, G. Zaccai, and M. Weik. Direct correlation between molecular dynamics and enzymatic stability: A comparative neutron scattering study of native human butyrylcholinesterase and its aged soman conjugate. *Biophys. J.*, 96:1489–1494, 2009.

[145] D. Rochu, C. Cléry-Barraud, F. Renault, A. Chevalier, C. Bon, and P. Masson. Capillary electrophoresisversus differential scanning calorimetry for the analysis of free enzyme versus enzyme-ligand complexes: In the search of the ligand-free status of cholinesterases. *Electrophoresis*, 27(2):442–451, 2006.

[146] S. Sacquin-Mora, P. Sebban, V. Derrien, B. Frick, R. Lavery, and C. Alba-Simionesco. Probing the flexibility of the bacterial reaction center: The wild-type protein is more rigid than two site-specific mutants. *Biochemistry*, 46(51):14960–14968, December 2007.

[147] M. Jasnin, L. van Eijck, M. M. Koza, J. Peters, C. Laguri, H. Lortat-Jacob, and G Zaccai. Dynamics of heparan sulfate explored by neutron scattering. *Physical Chemistry Chemical Physics*, 12(14):3360–3362, 2010.

[148] L. Cordone, M. Ferrand, E. Vitrano, and G. Zaccai. Harmonic behavior of trehalose-coated carbon-monoxy-myoglobin at high temperature. *Biophysical Journal*, 76(2):1043–1047, February 1999.

[149] W. Doster. The protein-solvent glass transition. *Biochimica et Biophysica Acta (BBA) - Proteins & Proteomics*, 1804(1):3 – 14, 2010. Includes Special Section: Protein-Water Interactions.

[150] R. M. Daniel, J. L. Finney, and J. C. Smith. The dynamic transition in proteins may have a simple explanation. *Faraday Disc.*, 122:163–169, 2002.

[151] R. M. Daniel, J. L. Finney, V. Réat, R. Dunn, M. Ferrand, and J. C. Smith. Enzyme dynamics and activity: Time-scale dependence of dynamical transitions in glutamate dehydrogenase solution. *Biophysical Journal*, 77(4):2184 – 2190, 1999.

[152] T. Becker, J. A. Hayward, J. L. Finney, R. M. Daniel, and J. C. Smith. Neutron frequency windows and the protein dynamical transition. *Biophysical Journal*, 87(3):1436 – 1444, 2004.

[153] G. Zaccai. How soft is a protein? a protein dynamics force constant measured by neutron scattering. *Science*, 288(5471):1604–1607, June 2000.

[154] T. Becker and J. C. Smith. Energy resolution and dynamical heterogeneity effects on elastic incoherent neutron scattering from molecular systems. *Phys. Rev. E*, 67(2):021904, Feb 2003.

[155] M Trovalet. privat communications.

[156] B. Varga, F. Migliardo, E. Takacs, B. Vertessy, S. Magazù, and C. Mondelli. Neutron scattering studies on dutpase complex in the presence of bioprotectant systems. *Chemical Physics*, 345(2-3):250–258, April 2008.

Summary

Incoherent elastic and quasi-elastic neutron scattering were used to measure membrane and protein dynamics in the nano- to picosecond time and Ångstrom length scale.
The hydration dependent dynamics of DMPC model membranes was studied using elastic and quasi-elastic neutron scattering. The elastic experiments showed a clear shift of the temperature of the main phase transition to higher temperatures with decreasing hydration level.
The performed quasi-elastic measurements demonstrated nicely the influence, hydration has on the diffusive motions of the head lipid groups. Different models are necessary to fit the Q-dependence of the elastic incoherent structure factor and show therefore the reduced mobility as a result of reduced water content.
In addition to temperature, pressure as a second thermodynamical variable was used to explore dynamics of DMPC membranes. The ordering introduced by applying pressure has similar effect to decreased hydration, therefore both approaches are complementary.
Covering three orders of magnitude in observation time, the dynamics of native AChE and its complexed counterpart in presence of Huperzin A was investigated in the range from 1 ns to 100 ps. The mean square displacements obtained from the elastic data allowed the determination of activation energies and gave evidence that a hierarchy of motions contributes to the enzymatic activity. Diffusion constants and residence times were extracted from the quasi-elastic broadening.

Key words: neutron scattering, dynamics, model membranes, hydration, AChE, BChE, high hydrostatic pressure

Résumé

La diffusion incohérente élastique et quasi-élastique de neutrons a été utilisée pour mesurer la dynamique de membranes et de protéines à l'échelle de la pico- à la nanoseconde et de la longueur de l'Ångstrom.
La dynamique de membranes modèles DMPC, en fonction de l'hydratation a été étudiée par diffusion neutronique. Les expériences élastiques ont, clairement montré un décalage de la température de transition de phase principale vers une température plus haute pour une diminution du niveau d'hydratation.
Les mesures quasi-élastiques effectuées ont montré l'influence de l'hydratation sur les mouvements diffusifs des têtes lipidiques. Différents modèles ont été nécessaires pour affiner les dépendances en Q des facteurs de structure élastiques incohérents et montrent donc la mobilité réduite due à l'hydratation inférieure.
En plus de la température, la pression comme deuxième variable thermodynamique a été utilisée pour étudier la dynamique des membranes DMPC. L'ordre induit par l'application d'une pression a un effet similaire à une hydratation diminuée, donc les deux approches sont complémentaires.
Couvrant trois ordres de grandeur, la dynamique d'AChE libre ou complexée avec de l'Huperzine A a été étudiée dans le domaine allant de 1 ns à 100 ps. Les déplacements carrés moyens obtenues à partir des données élastiques ont permis la détermination des énergies d'activation et prouvent que toute une hiérarchie de mouvements contribue a l'activité enzymatique. Les constantes de diffusion et les temps de corrélation ont été extraits de l'élargissement quasi-élastique.

mots clefs : diffusion de neutrons, dynamique, membranes modèles, hydratation, AChE, BChE, pression hydrostatique